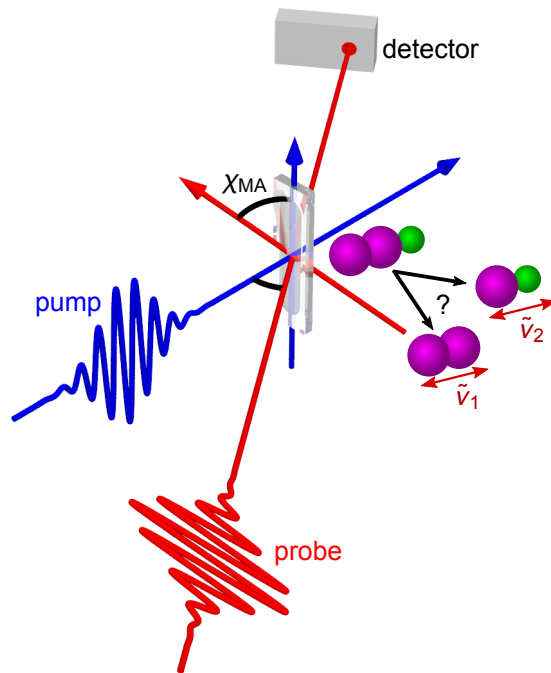


Identification of trihalide photodissociation patterns by global vibrational wavepacket analysis of broadband magic-angle transient absorption data



Dissertation zur Erlangung
des naturwissenschaftlichen Doktorgrades
der Julius-Maximilians-Universität Würzburg

vorgelegt von
Sebastian Schott
aus Werneck

Würzburg 2017

Eingereicht bei der Fakultät für Chemie und Pharmazie am

Gutachter der schriftlichen Arbeit

1. Gutachter: Prof. Dr. T. Brixner

2. Gutachter: _____

Prüfer des öffentlichen Promotionskolloquiums

1. Prüfer: Prof. Dr. T. Brixner

2. Prüfer: _____

3. Prüfer: _____

Datum des öffentlichen Promotionskolloquiums

Doktorurkunde ausgehändigt am

List of publications

- [1] A. Steinbacher, H. Hildenbrand, S. Schott, J. Buback, M. Schmid, P. Nuernberger, and T. Brixner. *Generating laser-pulse enantiomers*. *Opt. Express*, **25**, 21735–21752 (2017). doi:10.1364/OE.25.021735.
- [2] J. Knorr, P. Sokkar, S. Schott, P. Costa, W. Thiel, W. Sander, E. Sanchez-Garcia, and P. Nuernberger. *Competitive solvent-molecule interactions govern primary processes of diphenylcarbene in solvent mixtures*. *Nat Commun*, **7**, 12968 (2016). doi:10.1038/ncomms12968.
- [3] S. Schott, L. Röss, J. Hrušák, P. Nuernberger, and T. Brixner. *Identification of photofragmentation patterns in trihalide anions by global analysis of vibrational wavepacket dynamics in broadband transient absorption data*. *Phys. Chem. Chem. Phys.*, **18**, 33287–33302 (2016). doi:10.1039/C6CP06729H.
- [4] S. Schott, A. Steinbacher, J. Buback, P. Nuernberger, and T. Brixner. *Generalized magic angle for time-resolved spectroscopy with laser pulses of arbitrary ellipticity*. *J. Phys. B: At. Mol. Opt. Phys.*, **47**, 124014 (2014). doi:10.1088/0953-4075/47/12/124014.

Parts of this thesis were adapted from Ref. [3] with permission from the PCCP Owner Societies or from Ref. [4] © IOP Publishing. Reproduced with permission. All rights reserved:

- Sec. 2.2.3, pp. 28–29 was adapted from [4], Sec. 4, p. 7.
- Sec. 2.3, pp. 36–39 was adapted from [3], Sec. 4.3, pp. 33299.
- Sec. 3, pp. 45–61 was adapted from [4], pp. 1–10 and pp. 11–12.
- Sec. 3.6, pp. 61–64 was adapted from [4], Sec. 7, p. 2 and pp. 10–11.
- Sec. 4.1, pp. 65–66 was adapted from [3], Sec. 4.3, pp. 33299–33300.
- Sec. 5, pp. 79–109 was adapted from [3], pp. 33287–33299 and the corresponding supplementary.
- Sec. 6, pp. 111–112 was adapted from [3], Sec. 3, pp. 33297–33298 and [4], Sec. 8, p. 11

In addition to this list, the caption of each adapted figure references the original source.

Contents

1. Introduction	11
2. Transient absorption spectroscopy	15
2.1. Difference absorbance signal	15
2.2. Underlying quantum mechanics	18
2.2.1. Light–matter interaction	18
2.2.2. Wavepacket dynamics	20
2.2.3. Macroscopic polarization	25
2.2.4. First-order signal	29
2.2.5. Third-order signal	34
2.3. Modelling the reaction kinetics	36
2.4. Data fitting with the variable projection algorithm	40
3. Generalized magic angle	45
3.1. Electric-field polarization	46
3.2. Transition-probability approach	47
3.3. Response-theory approach	55
3.4. Generalized magic-angle condition for transient absorption	57
3.5. Magic-angle condition for 2D spectroscopy	60
3.6. Anisotropy	61
3.6.1. Single signal contribution	62
3.6.2. Overlapping signal contributions	62
3.6.3. Degenerate transition dipole moments	63
4. Variable projection algorithm	65
4.1. Modelling vibrational wavepacket oscillations	65
4.2. Mathematica implementation	66
4.3. Examples	71
5. Trihalide photodissociation pathways	79
5.1. Sample preparation	81
5.2. Transient absorption setup	83
5.3. Transient absorption signals: the case of triiodide	88
5.4. Transient absorption signals of the other five trihalides	94
5.5. Ab-initio frequency calculations	102
5.6. Reactant and fragment identification	104
5.7. Conclusion	108

6. Summary	111
7. Outlook for quantum control	113
A. femtoTools package collection	115
A.1. Kernel/init.m	115
A.2. parVarPro.nb	116
A.3. gaussTrace.nb	122
A.4. imagePlot.nb	125
A.5. framePlot.nb	130
A.6. plotOptions.nb	133
A.7. fourier.nb	136
A.8. io.nb	138

Kurzfassung

Die Erfindung von Laserpulsformern ermöglichte eine Vielzahl von Quantenkontrollexperimenten, bei denen eine chemische Reaktionen mittels maßgeschneiderten Laserpulsen gelenkt wird. Allerdings wurde trotz der bedeutenden Rolle der flüssigen Phase in der Chemie bis heute kein erfolgreicher Versuch publiziert in diesem Aggregatzustand die Selektivität bei der Spaltung chemischer Bindungen zu kontrollieren. Vielversprechende Kandidaten für ein derartiges Experiment sind $C_{\infty v}$ -symmetrische Trihalidanionen mit zwei verschiedenen chemischen Bindungen, wie z.B. I_2Cl^- , da diese Moleküle prinzipiell das einfachste Kontrollszenario, in dem entweder die eine oder die andere Bindung gespalten wird, ermöglichen und, wie vom meist untersuchten Trihalid I_3^- bekannt, eine Dissoziationsreaktion unter ultravioletter (UV) Bestrahlung erwartet wird.

Um im Rahmen dieser Arbeit zu untersuchen, ob sich die Dissoziationsreaktion solcher Trihalide in zwei verschiedene Photofragmente aufzweigt, wurde die ultraschnelle Photodissoziationdynamik von I_3^- , Br_3^- , IBr_2^- und ICl_2^- (Punktgruppe $D_{\infty h}$) sowie von I_2Br^- und I_2Cl^- (Punktgruppe $C_{\infty v}$) in Dichlormethanolösung mittels breitbandiger transientser Absorptionsspektroskopie in der Magischer-Winkel-Konfiguration gemessen. Die Identifikation der Reaktionspfade stützt sich auf die Oszillation von Schwingungswellenpaketen, die den Dissoziationsprozess überstehen und folglich nicht nur Informationen über die Trihalidedukte sondern auch über die Dihalidprodukte tragen.

Diese charakteristischen Schwingungswellenzahlen wurden aus jedem gemessenen transientsen Absorptionsspektrum durch einen globalen Fit der Populationsdynamik zusammen mit der Wellenpaketdynamik extrahiert. Bis vor Kurzem war solch eine kombinierte Modellfunktion in dem gängigen Fitwerkzeug Glotaran nicht verfügbar. Dies machte es erforderlich eine eigene Implementation des zugrunde liegenden Fitalgorithmus der variablen Projektionen zu entwickeln, wofür die Computeralgebrasoftware Mathematica gewählt wurde. Mathematicas Funktionsumfang erlaubt nicht nur eine große Flexibilität bei der Konstruktion beliebiger Modellfunktionen, sondern bietet auch die Möglichkeit, die Ableitungen einer Modellfunktion automatisch zu berechnen. Dies erlaubt der Fitprozedur die exakte Jacobi-Matrix zu verwenden, anstatt diese mittels der Finite-Differenzen-Methode zu approximieren.

Wider den Erwartungen wurde für jedes der untersuchten $C_{\infty v}$ Trihalide nur einer der zwei denkbaren Photodissoziationskanäle beobachtet. Da die Photofragmente rekombinieren, klingen deren Absorptionssignal und das Grundzustandsausbleichen des Edukts wieder ab. Dies passiert stets in biexponentieller Form, was im Fall von I_3^- von Ruhman und Kollegen mit der direkten Bildung von neutralen Dihalogenfragmenten I_2 neben den negativ geladenen Dihalidfragmenten I_2^- interpretiert wurde. Im Rahmen dieser Arbeit ließ sich ein solcher direkter Reaktionskanal nicht beobachten. Stattdessen wird die schnelle Komponente des biexponentiellen Zerfalls mit überschüssiger Vibrati-

onsenergie erklärt, die den der Rekombination vorangehenden Elektrontransferprozess $I_2^- + I \longrightarrow I_2 + I^-$ begünstigt, während die langsame Komponente abgekühlten Fragmenten zugeordnet wird.

Zusätzlich zu den Tihalidexperimenten wurde durch Herleitung Magischer-Winkel-Bedingungen für Antwortsignale aus elektrischer Dipolwechselwirkung dritter Ordnung mit beliebig polarisierten Laserpulsen theoretisch untersucht, ob eine Magischer-Winkel-Konfiguration für Polarisationsformungs-Kontrollexperimente möglich ist. Weiterhing wurden die Feinheiten anisotroper Signale, die den gut bekannten Bereich von -0.2 bis 0.4 verletzen, untersucht.

Abstract

The invention of laser pulse shapers allowed for various quantum control experiments, where a chemical reaction is guided by specifically tailored laser pulses. However, despite of the prominent role of the liquid phase in chemistry, no successful attempt for controlling the selectivity of a bond-fission reaction has yet been reported in this state of matter. Promising candidates for such an experiment are $C_{\infty v}$ -symmetric trihalide anions with two different chemical bonds like I_2Cl^- , because these molecules notionally offer the most simplest selectivity-control scenario of breaking either the one or the other bond and they are expected to dissociate under ultraviolet (UV) irradiation like it is known for the most-studied trihalide I_3^- .

In order to investigate in this thesis the possibility that the dissociation reaction of such trihalides branches into two different photofragments, the ultrafast photodissociation dynamics of I_3^- , Br_3^- , IBr_2^- and ICl_2^- (point group $D_{\infty h}$) as well as of I_2Br^- and I_2Cl^- (point group $C_{\infty v}$) in dichloromethane solution were measured with broadband transient absorption spectroscopy in magic-angle configuration. The identification of the reaction pathway(s) relies on vibrational wavepacket oscillations, which survive the dissociation process and therefore carry not only informations about the reactant trihalides but also about the fragment dihalides.

These characteristic vibrational wavenumbers were extracted from the measured transient absorption spectra by globally fitting the population dynamics together with the wavepacket dynamics. Until recently, such a combined model function was not available in the well-established fitting tool Glotaran. This made it inevitable to develop a custom implementation of the underlying variable-projection fitting algorithm, for which the computer-algebra software Mathematica was chosen. Mathematica's sophisticated built-in functions allow not only for a high flexibility in constructing arbitrary model functions, but also offer the possibility to automatically calculate the derivative(s) of a model function. This allows the fitting procedure to use the exact Jacobian matrix instead of approximating it with the finite difference method.

Against the expectation, only one of the two thinkable photodissociation channels was found for each of the investigated $C_{\infty v}$ trihalides. Since the photofragments recombine, their absorption signal as well as the reactant ground state bleach recover. This happens in a biexponential manner, which in the case of I_3^- was interpreted by Ruhman and coworkers with the direct formation of a neutral dihalogen fragment I_2 beside the negatively charged dihalide fragment I_2^- . In this thesis, such a direct reaction channel was not found and instead the fast component of the biexponential decay is explained with vibrational excess energy mediating the recombination-preceding electron transfer process $I_2^- + I \longrightarrow I_2 + I^-$, while the slow component is attributed to cooled-down fragments.

In addition to the trihalide experiments, the possibility of a magic-angle configuration for polarization-shaping control experiments was theoretically investigated in this thesis by deriving magic-angle conditions for the third-order electric-dipole response signal of arbitrarily polarized laser pulses. Furthermore, the subtleties of anisotropy signals violating the well-known range of -0.2 to 0.4 were studied.

1. Introduction

A central task of chemistry is molecular synthesis, where a desired product is created by successively forming and breaking chemical bonds. Each of these reaction steps is controlled by the amount (or concentration) of reactants (possibly with protective groups) and catalysts, the temperature, the pressure, protective gas, applied voltages/currents and irradiation. With the invention of laser pulse shapers, this tool chain got extended by a new control knob: Ultrashort laser pulses that are specifically tailored to guide reaction pathways [5–11] were successfully used in gas phase experiments to control the formation and fission of chemical bonds [12, 13].

However, for the liquid phase, which is the most important state of matter for chemical synthesis, no successful photodissociation control attempt has been reported yet. The simplest possible model system to try this kind of experiment would be a molecule that consists of only three atoms but offers two distinct chemical bonds, which one then seeks to break selectively by a tailored pump pulse shape as illustrated in Fig. 1.1. Promising molecules of this type are trihalide anions like I_2Cl^- , because each trihalide is expected to undergo a photodissociation reaction under ultra-violet (UV) irradiation, as is well known for the trihalide I_3^- [14]. The outcome of the photoreaction is observed by measuring the intensity of a probe laser pulse that passed the sample cell after the pump pulse. From this intensity, one can then extract a feedback signal to test the bond-selectivity and efficiency of the applied pump pulse shapes. However, the identification of a suitable feedback signal is not a trivial task and requires further knowledge about the dynamics of the molecular system under study.

Therefore, the first step towards controlling the photodissociation reaction of dissolved trihalides and the main goal of this thesis is to investigate the ultrafast photochemical behaviour of the trihalide series I_3^- , Br_3^- , IBr_2^- , ICl_2^- , I_2Br^- , and I_2Cl^- with broadband transient absorption spectroscopy (Sec. 2), for which an "unshaped", i.e., temporally compressed, pump pulse is used. Interpreting the sample's effect on the probe intensity with the Bouguer–Lambert–Beer law (Sec. 2.1) allows to identify reactant and photodissociation-fragment concentrations, whose time-dependent behaviour can be determined by repeating the experiment with different time delays between the pump pulse and the probe pulse. In general the signal contributions from different molecular species and different molecular quantum states overlap and therefore a fitting procedure is required to separate the individual concentrations.

A common open-source software tool for the fitting procedure is Glotaran (global and target analysis) [15], which implements the variable projection algorithm [16] to effectively exploit the structure of the model function (Sec. 2.3) that consists of a linear combination of non-linear basis functions, typically decaying exponentials. However, until recently [17], it was not possible to include the pronounced vibrational oscillations of the

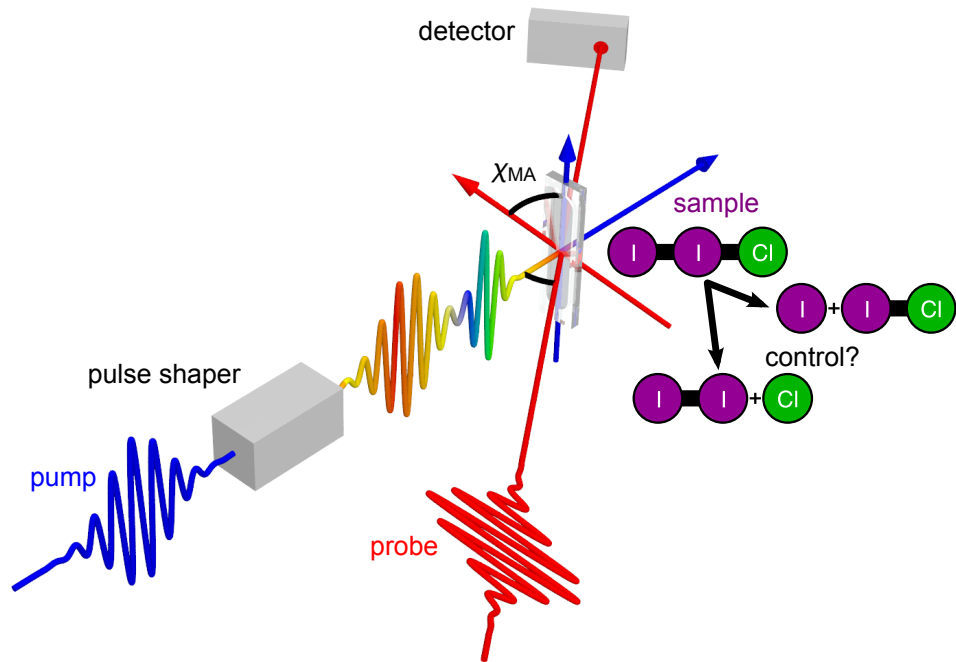


Figure 1.1.: Quantum control scheme. Can a pump laser pulse be shaped in such a way that one controls which chemical bond of dissolved I_2Cl^- (or a similar trihalide) breaks, while detecting the reaction with a probe laser pulse? By tuning the laser pulse polarization to a relative angle of $\chi_{MA} \approx 54.7^\circ$, also called magic angle, the influence of the molecules' orientation onto the signal can be suppressed.

trihalides as oscillating cosine functions beside the decaying exponentials and therefore a custom Mathematica [18] implementation of the variable projection algorithm (Sec. 2.4) was developed within this thesis (Sec. 4). This implementation has the advantage that Mathematica is equipped with sophisticated computer-algebra tools, which allow the user to design her or his own customized model function. Furthermore, Mathematica can automatically calculate the model function's partial derivatives and thus construct the exact Jacobian matrix instead of approximating it with the finite-difference method.

Having separated the concentrations of the quantum states of the molecular species under study, one still lacks an explanation for the dynamical behaviour of each individual concentration and its corresponding signal, which is the key element to design a promising quantum-control strategy. Understanding the sample's microscopic behaviour and how this results in the macroscopic signal is far beyond the scope of the Bouguer–Lambert–Beer law but requires quantum electrodynamics, which is therefore introduced and discussed in Sec. 2.2. Especially, quantum-mechanical wavepacket (WP) dynamics (Sec. 2.2.2) are of interest to explain oscillating signal contributions.

Furthermore, the signal's dependence on the pump and probe polarization lies in the focus of this thesis. In the so-called magic-angle configuration $\chi_{MA} = \arccos(1/\sqrt{3}) \approx 54.7^\circ$ [19] illustrated in Fig. 1.1, one can suppress the influence of the molecules' orien-

tation on the signal to exclusively measure the concentration (or population) changes of the molecular quantum states. In contrast, anisotropy spectroscopy utilizes this very effect to extract informations about the molecule structure and reorientation dynamics. Beside this magic-angle condition for linearly polarized pump and probe pulses, also the case of circularly polarized pump and linearly polarized probe pulses is well known, but no generalized magic-angle condition for arbitrarily polarized pump and probe pulses has been reported so far (except [4], which is adapted in this thesis). This theory extension presented in Sec. 3 is the second goal of this thesis, which might help to understand future experiments based on polarization-controlled spectroscopy, optical-activity spectroscopy [circular dichroism (CD) and optical rotatory dispersion (ORD)] or corresponding quantum control attempts. In Sec. 3.6, the discussion about the general magic-angle condition is then complemented about the explanation how the anisotropy signal can exceed in transient absorption spectroscopy the well-known range of -0.4 to 0.2 [see eq. (3.50)].

With the above-mentioned data evaluation tools and the theory about the signal formation at hand, the broadband transient absorption data of the trihalide series is finally evaluated and discussed in Sec. 5. Despite the fact that some trihalides have distinct chemical bonds, always only one major, possibly sole photodissociation fragment was found. This result, summarized in Sec. 6, complicates the search for a suitable control strategy (Sec. 7), because instead of disturbing a fragile balance between two photoproducts, one needs to find out how one photodissociation pathway can be so dominant and what would be a suitable control knob to force the system in the opposite direction.

Besides the question about a promising quantum control attempt, the findings of this thesis might also be of interest for the various applications that employ trihalide anions. In synthetic chemistry these molecules serve as halogenating agents but play also important roles in catalysis, electrochemistry, and solar cell technology. For instance, the most famous trihalide I_3^- is part of the redox electrolyte in the original Grätzel cell [20] and other dye-sensitized solar cells [21]. Despite being heavily investigated with ultrafast spectroscopy since 1992 [14], I_3^- did still not reveal all its photodynamical secrets. Ruhman and coworkers [22] found an unknown photodissociation intermediate and their explanation for this signal is confirmed and extended by the new data collected within this thesis.

2. Transient absorption spectroscopy

All experiments done within this thesis rely on transient absorption (TA) spectroscopy, of which the basic concepts and the data interpretation within the Bouguer–Lambert–Beer law are reviewed in the following Sec. 2.1. In addition, potential sources for signal artefacts are discussed. To understand TA signals beyond the Bouguer–Lambert–Beer law, Sec. 2.2 looks on TA spectroscopy from a quantum mechanical perspective. Then, in Sec. 2.3, it is explained how a global model function can be constructed for trihalide samples consisting of a mixture of photofragmenting molecules. Finally, Sec. 2.4 introduces the variable projection algorithm (VPA), which is ideally suited to fit this kind of model functions.

2.1. Difference absorbance signal

As depicted in Fig. 1.1, the pathways of a pump (blue) and a probe (red) laser pulse are spatially overlapped inside a sample cell, but in contrast to a control experiment, the pulse shaper is now used to temporally compress the pump pulse for an optimal time resolution. Initially, the reactant sample molecules R are in a thermal equilibrium with the solvent environment, but then, as illustrated in Fig. 2.1a, a UV, visible (VIS) or near-infrared (NIR) pump pulse excites (blue arrow) the valence electron configuration of some of the reactant sample molecules to a state of higher energy $R \rightarrow R^*$ and therefore the pump initiates molecular dynamics (black arrows), i.e., depending on time T , the excited molecules distribute their excess energy towards the solvent until they reach again a thermal equilibrium. During this relaxation process, the molecules may pass through different intermediate electronic states like R^* , which are called product states P , P^* , ... if not only the physical but also the chemical properties change due to ionization, isomerization or due to the formation or fission of chemical bonds. In addition, all changes of the electronic structure are always accompanied by changes of the nuclear vibrations leading to signal oscillations, as exemplified in Fig. 2.1b. The overall relaxation or reaction pathway that is taken depends on the specific sample molecules and it may branch into several routes, which do not necessarily end at the initial state, but might lead to stable product states.

In order to elucidate the underlying reaction mechanism, the effect of the transient intermediates on the absorbance

$$A(\lambda, T) = -\lg \left[\frac{I(\lambda, T)}{I_0(\lambda)} \right] = \sum_{i=0}^{n-1} \epsilon_i(\lambda) c_i(T) l \quad (2.1)$$

of the sample is observed as a function of the wavelength λ and the time $T = t - t_0$ that elapsed since the pump excitation at t_0 . This is done by detecting the transmitted

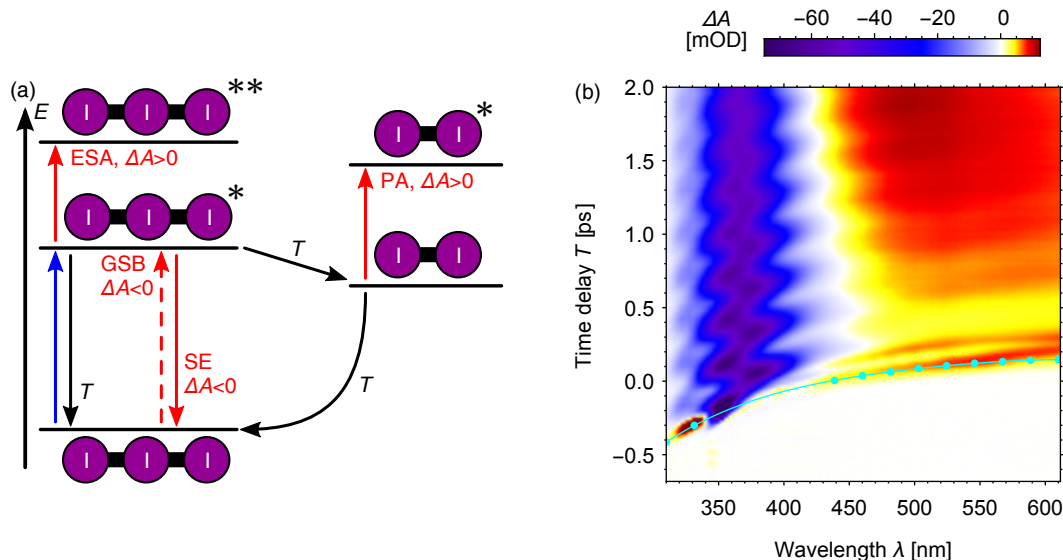


Figure 2.1.: Basic concept of transient absorption spectroscopy exemplified by I_3^- . (a) A 348 nm pump pulse (blue arrow) excites the sample molecules $R \rightarrow R^*$ and therefore initiates molecular dynamics (black arrows), which are detected by the absorbance change ΔA of a subsequent probe pulse (red arrows) that is temporally delayed about T . Thinkable processes are the absorbance-increasing ESA and PA ($\Delta A > 0$) and the absorbance-decreasing GSB and SE ($\Delta A < 0$). (b) The negative signal was found to be the I_3^- GSB, while the positive signal until 0.4 ps was identified as I_3^- ESA (Sec. 5.3). After 0.4 ps the chemical bond breaks and later positive signals were attributed to the I_2^- PA. In addition, one can observe pronounced oscillations, which stem from the molecules' vibrations and thus allow for their identification (Sec. 5.6). Unfortunately, these oscillations cannot be explained with the Bouguer–Lambert–Beer law, but require a more sophisticated theory considering quantum-mechanically wavepacket dynamics (Sec. 2.2.2). Note that the probe WL is chirped in such a way that the red part of its spectrum arrives before the blue part. To correct this wavelength-dependent time axis, a fourth-order polynomial (cyan curve) was fitted to manually selected t_0 points (cyan dots) and the transient absorption spectrum was shifted accordingly, resulting in Fig. 5.7. [3, Fig. S5] - Reproduced by permission of the PCCP Owner Societies

spectral intensity $I(\lambda, T)$ of the probe pulse, which follows the pump pulse with the time delay T . While the use of a supercontinuum white-light probe pulse (Sec. 5.2) allows to cover a broad spectral range with a single laser shot, the temporal changes must be scanned step-by-step by repeating the whole experiment with different time delays T in a refreshed sample volume.

Assuming the validity of the Bouguer–Lambert–Beer law [23, Chap. 5.1.3], the decrease of the initial probe spectrum $I_0(\lambda)$ to $I(\lambda, T)$ depends on the length l of the probe beam path through the sample, the decadic molar absorption coefficients $\epsilon_i(\lambda)$ and the time-dependent concentrations (or populations) $c_i(T)$ of the n components, i.e., the n energy states that belong to the molecular species, being present inside the probed sample volume. This includes also the molecules that remained unaffected by the pump and therefore to extract the weaker transient signal from this stronger static background, a

reference spectrum $I_{\text{ref}}(\lambda)$ resulting from the absorbance

$$A_{\text{ref}}(\lambda) = -\lg \left[\frac{I_{\text{ref}}(\lambda)}{I_{\text{ref},0}(\lambda)} \right] = \sum_{i=0}^{n-1} \epsilon_i(\lambda) c_i l \quad (2.2)$$

of the static concentrations c_i is measured by repeating the experiment without the pump pulse in a refreshed sample volume. Then, the difference absorbance

$$\Delta A(\lambda, T) = A(\lambda, T) - A_{\text{ref}}(\lambda) = -\lg \left[\frac{I(\lambda, T)}{I_0(\lambda)} \right] + \lg \left[\frac{I_{\text{ref}}(\lambda)}{I_{\text{ref},0}(\lambda)} \right] \quad (2.3)$$

$$\approx -\lg \left[\frac{I(\lambda, T)}{I_{\text{ref}}(\lambda)} \right] \quad (2.4)$$

is calculated from the negative decadic logarithm of the ratio of the probe spectrum $I(\lambda, T)$ and the reference probe spectrum $I_{\text{ref}}(\lambda)$ by assuming equal initial spectra $I_0(\lambda) \approx I_{\text{ref},0}(\lambda)$ for both measurements, i.e., neglecting power fluctuations of the laser source.

To fulfil this assumption, both measurements should be temporally as close as possible. For the used laser source (Sec. 5.2), which delivers pump–probe pulse pairs at a repetition rate of 1 kHz, the closest time between two measurements is 1 ms and by blocking every other pump pulse, a single difference spectrum $\Delta A(\lambda, T)$ for a given time delay T can be measured in a shot-to-shot manner within this 1 ms, a time window too small for distortions due to long-term power fluctuations. To achieve a good signal-to-noise ratio, $\Delta A(\lambda, T)$ is measured at least a thousand times for each time delay T . However, fluctuations of the pump power or the pump–probe overlap, which distort the effective transient concentration $c_i(T)$ seen by the probe pulse, are not corrected by the shot-to-shot technique. While the pump power fluctuations can be monitored, the pump–probe overlap fluctuations have to be minimized by choosing a larger pump beam diameter in comparison to the probe beam diameter.

Having considered the artefacts due to fluctuations of the laser source, the interpretation of the measured difference absorbance

$$\Delta A(\lambda, T) = A(\lambda, T) - A_{\text{ref}}(\lambda) = \sum_{i=0}^{n-1} \epsilon_i(\lambda) c_i(T) l - \sum_{i=0}^{n-1} \epsilon_i(\lambda) c_i l \quad (2.5)$$

can be addressed. As illustrated by the red arrows in Fig. 2.1a, different processes either decrease ($\Delta A < 0$) or increase ($\Delta A > 0$) the measured absorbance depicted in Fig. 2.1b. Since the pump pulse excites part of the sample, the number of ground state molecules is reduced ($c_i(T) < c_i$) and therefore the ground state absorption decreases, leading to a negative difference absorbance ($\Delta A < 0$), called ground state bleach (GSB). In contrast, the appearance of excited state molecules that were not present before ($c_i(T) > c_i$) gives rise to a positive excited state absorption (ESA) ($\Delta A > 0$). If the molecules' excitation results in a chemically new product, then the ESA is also called product absorption (PA). Finally, the probe pulse can also trigger an excited molecule to emit its excess energy in form of light that amplifies the probe pulse intensity (also $c_i(T) > c_i$ but $\epsilon_i(\lambda) < 0$).

This so-called stimulated emission (SE) appears as negative absorbance ($\Delta A < 0$) in the data, because an amplification of the probe light can also be interpreted as reduced absorption.

2.2. Underlying quantum mechanics

Obviously, the Bouguer–Lambert–Beer law, introduced in the last Sec. 2.1, does not explain every signal contribution occurring inside the TA spectrum depicted in Fig. 2.1b: The TA signal starts with a sharp peak that occurs at larger time delays T for longer wavelengths λ . This so-called coherent artefact (CA) results when the pump and the probe laser pulse temporally overlap $T = 0$ and thus the time ordering of the light–matter interaction (Sec. 2.2.1) is lost. If, as in this case, the probe pulse is chirped in such a way that the red part of its spectrum arrives before the blue part, then the time axis becomes wavelength dependent and the time-zero defining CA shifts with λ . Furthermore, the pronounced oscillatory behaviour stems from vibrational WPs which travel back and forth on an electronic potential energy surface (PES) of the molecules under study (Sec. 2.2.2). Finally and less obvious, Fig. 2.1b contains only signals caused by changes in the population (concentration) of the molecular quantum states. This filtering was achieved by suppressing orientation effects (Sec. 2.2.3) from the TA-relevant first- and third-order signals (Sects. 2.2.4 and 2.2.5) with the so-called magic-angle configuration (Sec. 3).

2.2.1. Light–matter interaction

Following the Refs. [24] and [25], each molecule n inside the sample volume can be described by a Hamiltonian

$$\begin{aligned} \hat{H}_n &\approx \hat{H}_{\text{mol},n} + \hat{H}_{\text{bath},n} - \overbrace{\int_{-\infty}^{\infty} \hat{\mathbf{P}}_n(\mathbf{r}) \cdot \mathbf{E}_\perp(\mathbf{r}, t)}^{\hat{H}_{\text{int},n}(t)} \\ &\approx \hat{H}_{\text{mol},n} + \hat{H}_{\text{bath},n} - \int_{-\infty}^{\infty} \delta(\mathbf{r} - \mathbf{R}_n) \hat{\boldsymbol{\mu}}_n \cdot \mathbf{E}_\perp(\mathbf{r}, t), \end{aligned} \quad (2.6)$$

which consists of a molecular Hamiltonian $\hat{H}_{\text{mol},n}$ representing the isolated molecule, a bath Hamiltonian $\hat{H}_{\text{bath},n}$ approximating the molecule’s interaction with the solvent environment and an interaction Hamiltonian $\hat{H}_{\text{int},n}(t)$ approximating the molecule’s interaction with a classical external electromagnetic laser field. For the latter it is usually sufficient to consider only the interaction between the transverse electric laser field $\mathbf{E}_\perp(\mathbf{r}, t)$ and the molecule’s polarization $\hat{\mathbf{P}}_n(\mathbf{r})$, which can often be simplified with the electric-dipole approximation utilizing the electric dipole moment $\hat{\boldsymbol{\mu}}_n$ and the Dirac delta function $\delta(\mathbf{r} - \mathbf{R}_n)$.

Since the pure quantum state of each molecule is unknown, one uses the density operator, whose time evolution under the influence of the electric field $\mathbf{E}_\perp(\mathbf{r}, t)$ can be approximated by a perturbative series

$$\hat{\rho}_n(t) \approx \hat{\rho}_n^{(0)}(t) + \hat{\rho}_n^{(1)}(t) + \hat{\rho}_n^{(2)}(t) + \hat{\rho}_n^{(3)}(t) + \dots \quad (2.7)$$

if $\mathbf{E}_\perp(\mathbf{r}, t)$ is sufficiently weak compared to the electric field strength inside the molecule. The zeroth-order term

$$\hat{\rho}_n^{(0)}(t) = \hat{U}_{0,n}(t, t_0)\hat{\rho}_n(t_0)\hat{U}_{0,n}^\dagger(t, t_0) = \hat{\mathcal{U}}_{0,n}(t, t_0)\hat{\rho}_n(t_0) \quad (2.8)$$

represents the time evolution of the unperturbed, isolated molecule. The density-operator notation can further be shortened by switching from Hilbert space to Liouville space, in which the density operator $\hat{\rho}(t_0)$ takes the form of a vector, whose time evolution is described by the time evolution superoperator $\hat{\mathcal{U}}_0(t, t_0)$. For more details on the Liouville space concept, see, e.g., [24, Chap. 3] and [25, Chap. 2.5]. A single interaction can either act from the left (bra) side or the right (ket) side on the density operator as described by the commutator inside the first-order term

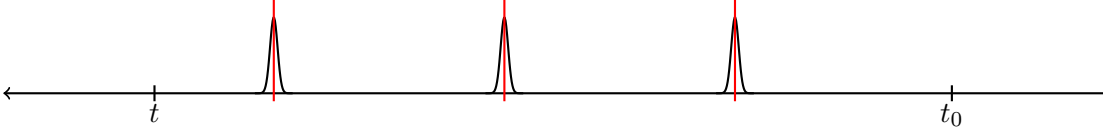
$$\begin{aligned} \hat{\rho}_n^{(1)}(t) &= -\frac{i}{\hbar} \int_{t_0}^t d\tau_1 \hat{\mathcal{U}}_{0,n}(t, \tau_1) \left[\hat{H}'_n(\tau_1), \hat{\mathcal{U}}_{0,n}(\tau_1, t_0) \hat{\rho}_n(t_0) \right] \\ &= -\frac{i}{\hbar} \int_{t_0}^t d\tau_1 \hat{\mathcal{U}}_{0,n}(t, \tau_1) \hat{\mathcal{L}}'_n(\tau_1) \hat{\mathcal{U}}_{0,n}(\tau_1, t_0) \hat{\rho}_n(t_0), \end{aligned} \quad (2.9)$$

which can be compactly reformulated by introducing the superoperator $\hat{\mathcal{L}}'_n(\tau_1)$. Similarly, one receives the density operator's time evolution for two

$$\hat{\rho}_n^{(2)}(t) = \left(-\frac{i}{\hbar}\right)^2 \int_{t_0}^t d\tau_2 \int_{t_0}^{\tau_2} d\tau_1 \hat{\mathcal{U}}_{0,n}(t, \tau_2) \hat{\mathcal{L}}'_n(\tau_2) \hat{\mathcal{U}}_{0,n}(\tau_2, \tau_1) \hat{\mathcal{L}}'_n(\tau_1) \hat{\mathcal{U}}_{0,n}(\tau_1, t_0) \hat{\rho}_n(t_0) \quad (2.10)$$

and for three

$$\hat{\rho}_n^{(3)}(t) = \left(-\frac{i}{\hbar}\right)^3 \int_{t_0}^t d\tau_3 \int_{t_0}^{\tau_3} d\tau_2 \int_{t_0}^{\tau_2} d\tau_1$$

$$\hat{\mathcal{U}}_{0,n}(t, \tau_3) \hat{\mathcal{L}}'_n(\tau_3) \hat{\mathcal{U}}_{0,n}(\tau_3, \tau_1) \hat{\mathcal{L}}'_n(\tau_2) \hat{\mathcal{U}}_{0,n}(\tau_2, \tau_1) \hat{\mathcal{L}}'_n(\tau_1) \hat{\mathcal{U}}_{0,n}(\tau_1, t_0) \hat{\rho}_n(t_0)$$


(2.11)

light-matter interactions et cetera. Each interaction is interpreted such that a part of the current quantum state is projected into a different energy eigenstate, when the laser's photon energy matches the energy gap in between. The interactions can happen at any time, at which the electromagnetic field amplitude is not zero, which is illustrated by the three Gaussian-shaped laser pulses below (2.11). However, the interactions are time ordered, i.e., $\tau_1 \leq \tau_2$ and $\tau_2 \leq \tau_3$ and with the three time integrals every possible combination for these time-ordered interactions is considered. This includes also the case when all three interactions happen during the first laser pulse. If one is explicitly interested in the spectroscopic signal resulting from the interaction of three different laser pulses, e.g., to control the delay times in between the interactions, then one needs to separate this signal from the signal contributions of all other first-, second-, third- or higher-order processes as explained in Sec. 2.2.5.

Together with the evolution of the density operator, also the polarization changes, of which the expectation value

$$\mathbf{P}(\mathbf{r}, t) = \underbrace{\sum_n \text{Tr}[\hat{\mathbf{P}}_n(\mathbf{r}) \hat{\rho}_n^{(1)}(t)]}_{\mathbf{P}^{(1)}} + \underbrace{\sum_n \text{Tr}[\hat{\mathbf{P}}_n(\mathbf{r}) \hat{\rho}_n^{(2)}(t)]}_{\mathbf{P}^{(2)}} + \underbrace{\sum_n \text{Tr}[\hat{\mathbf{P}}_n(\mathbf{r}) \hat{\rho}_n^{(3)}(t)]}_{\mathbf{P}^{(3)}} + \dots, \quad (2.12)$$

especially the transverse part serves as source for an electric signal field

$$\nabla^2 \mathbf{E}_\perp(\mathbf{r}, t) - \frac{1}{c^2} \frac{\partial^2}{\partial t^2} \mathbf{E}_\perp(\mathbf{r}, t) = \frac{1}{\epsilon_0 c^2} \frac{\partial^2}{\partial t^2} \mathbf{P}_\perp(\mathbf{r}, t), \quad (2.13)$$

which is then measured by the detector, e.g., a spectrometer and can be interpreted to elucidate the molecules' quantum mechanical properties and behaviour.

2.2.2. Wavepacket dynamics

Having generally discussed how a quantum system is perturbed by an electromagnetic field (Sec. 2.2.1), a closer look to the specific behaviour of molecular quantum systems will reveal the origin of the oscillatory WP signal inside Fig. 2.1b: The first step is to distinguish the atomic nuclei with mass $m_{N,n}$ and charge $Z_n e$ ($Z_n \in \mathbb{N}$) from the nuclei-orbiting electrons with mass m_e and elementary charge $-e$, which "glue" the atoms

together and thus form the molecular structure. Then, the position-space representation of the molecular Hamiltonian

$$H_{\text{mol}} = \underbrace{-\sum_n \frac{\hbar^2 \nabla_{\mathbf{e},n}^2}{2m_e}}_{T_e} + \underbrace{\frac{1}{4\pi\epsilon_0} \sum_{m>n} \frac{e^2}{|\mathbf{r}_{e,n} - \mathbf{r}_{e,m}|}}_{V_e} - \underbrace{\sum_n \frac{\hbar^2 \nabla_{\mathbf{N},n}^2}{2m_{\mathbf{N},n}}}_{T_{\mathbf{N}}} + \underbrace{\frac{1}{4\pi\epsilon_0} \sum_{m>n} \frac{Z_n Z_m e^2}{|\mathbf{r}_{\mathbf{N},n} - \mathbf{r}_{\mathbf{N},m}|}}_{V_{\mathbf{N}}} - \underbrace{\frac{1}{4\pi\epsilon_0} \sum_{n,m} \frac{Z_m e^2}{|\mathbf{r}_{e,n} - \mathbf{r}_{\mathbf{N},m}|}}_{V_{e\mathbf{N}}} \quad (2.14)$$

from (2.6) splits into the electron kinetic energy T_e , electron–electron potential energy V_e , nuclear kinetic energy $T_{\mathbf{N}}$, nuclear–nuclear potential energy $V_{\mathbf{N}}$ and electron–nuclear potential energy $V_{e\mathbf{N}}$, depending on the electron coordinates

$$\mathbf{r}_e = \{\mathbf{r}_{e,1}, \mathbf{r}_{e,2}, \dots\} \quad (2.15)$$

and momenta $-i\hbar\nabla_{\mathbf{e},n}$ and the nuclear coordinates

$$\mathbf{r}_{\mathbf{N}} = \{\mathbf{r}_{\mathbf{N},1}, \mathbf{r}_{\mathbf{N},2}, \dots\} \quad (2.16)$$

and momenta $-i\hbar\nabla_{\mathbf{N},n}$ [26, Chap. 12]. Note that the typically weak magnetic effects are neglected and the particle momentum operator becomes $\hat{\mathbf{p}}_{\mathbf{M}} \approx \hat{\mathbf{p}} = -i\hbar\nabla$ in the position-space representation. Furthermore, note that also the self interaction is neglected by choosing $m > n$ for the summation indices.

Since the nuclei are much heavier than the electrons $m_{\mathbf{N},n} \gg m_e$, they react much slower on any interaction force. From the perspective of the quickly reacting electrons it seems that the nuclei stand still. This allows to approximate the electron Hamiltonian

$$H_e(\mathbf{r}_{\mathbf{N}}) \approx T_e + V_e + V_{e\mathbf{N}}(\mathbf{r}_{\mathbf{N}}) \quad (2.17)$$

by choosing a fixed nuclear geometry $\mathbf{r}_{\mathbf{N}}$ for the electron–nuclear potential energy $V_{e\mathbf{N}}(\mathbf{r}_{\mathbf{N}})$ and by neglecting the nuclear kinetic energy $T_{\mathbf{N}}$ as well as the nuclear–nuclear potential energy $V_{\mathbf{N}}$. Solving the corresponding electronic eigenequation

$$H_e(\mathbf{r}_{\mathbf{N}})\psi_{e,i}(\mathbf{r}_e; \mathbf{r}_{\mathbf{N}}) = E_i(\mathbf{r}_{\mathbf{N}})\psi_{e,i}(\mathbf{r}_e; \mathbf{r}_{\mathbf{N}}) \quad (2.18)$$

leads then to a set of electronic wavefunctions $\psi_{e,i}(\mathbf{r}_e; \mathbf{r}_{\mathbf{N}})$ of eigenenergy $E_i(\mathbf{r}_{\mathbf{N}})$, which both depend on the chosen nuclear configuration $\mathbf{r}_{\mathbf{N}}$. With this results and under the assumption that the full electronic–nuclear wavefunction

$$\psi_{i,j}(\mathbf{r}_e, \mathbf{r}_{\mathbf{N}}) = \psi_{e,i}(\mathbf{r}_e; \mathbf{r}_{\mathbf{N}})\psi_{\mathbf{N},i,j}(\mathbf{r}_{\mathbf{N}}) \quad (2.19)$$

can be constructed by multiplying the afore-mentioned electronic wavefunction with a nuclear wavefunction $\psi_{\mathbf{N},i,j}(\mathbf{r}_{\mathbf{N}})$, the left-hand side of the full eigenequation

$$H\psi_{i,j}(\mathbf{r}_e, \mathbf{r}_{\mathbf{N}}) = E_{i,j}\psi_{i,j}(\mathbf{r}_e, \mathbf{r}_{\mathbf{N}}) \quad (2.20)$$

takes the form

$$\begin{aligned}
H\psi_{i,j}(\mathbf{r}_e, \mathbf{r}_N) = & [E_i(\mathbf{r}_N) + V_N]\psi_{e,i}(\mathbf{r}_e; \mathbf{r}_N)\psi_{N,i,j}(\mathbf{r}_N) \\
& - \sum_n \frac{\hbar^2}{2m_{N,n}} \left[\psi_{e,i}(\mathbf{r}_e; \mathbf{r}_N) \nabla_{N,n}^2 \psi_{N,i,j}(\mathbf{r}_N) \right. \\
& \left. + \nabla_{N,n} \psi_{e,i}(\mathbf{r}_e; \mathbf{r}_N) \cdot \nabla_{N,n} \psi_{N,i,j}(\mathbf{r}_N) + \psi_{N,i,j}(\mathbf{r}_N) \nabla_{N,n}^2 \psi_{e,i}(\mathbf{r}_e; \mathbf{r}_N) \right] \quad (2.21)
\end{aligned}$$

containing nuclear-coordinate derivatives of the electronic wavefunction in the last two terms [26, Chap. 12]. Typically, these terms are much smaller than the other terms and can be neglected, which is known as the Born–Oppenheimer approximation. Without an operator that acts on the electronic part of the wavefunction, $\psi_{e,i}(\mathbf{r}_e; \mathbf{r}_N)$ can be dropped and the full eigenequation (2.20) simplifies to an eigenequation

$$\underbrace{[T_N + E_i(\mathbf{r}_N) + V_N]}_{V_{\text{PES},i}(\mathbf{r}_N)} \psi_{N,i,j}(\mathbf{r}_N) = E_{i,j} \psi_{N,i,j}(\mathbf{r}_N) \quad (2.22)$$

for the nuclear wavefunction $\psi_{N,i,j}(\mathbf{r}_N)$. This equation is mathematically equivalent to the eigenequation of a particle that propagates on the PES, which is defined by the attractive or repulsive electronic potential energies $E_i(\mathbf{r}_N)$ and the repulsive nuclear potential energy V_N .

For the simplest case of a diatomic molecule, the generally multidimensional coordinate space \mathbf{r}_N reduces to one dimension: The internuclear distance r_N . In such a scenario, the i th PES [also named potential energy curve (PEC) in the one-dimensional case] can often be approximated by a Morse potential [29]

$$V_{\text{PES},i}(r_N) = D_{e,i} e^{-2a_i(r_N - r_{e,i})} - 2D_{e,i} e^{-a_i(r_N - r_{e,i})} - E_{0,i} \quad (2.23)$$

with dissociation energy (or depth) $D_{e,i}$, width a_i , equilibrium distance $r_{e,i}$ and energy offset $E_{0,i}$ placing the i th PES relative to the other PES. One possibility to receive these PES-determining quantities is to derive them from experimental data, like it was done for various dihalide molecules [27, 28], of which the result for diiodide is illustrated in Fig. 2.2a. The vibrational energies and nuclear wavefunctions of Morse PESs take the form

$$E_{i,j} = h\nu_{0,i} \left(j + \frac{1}{2} \right) - \frac{(h\nu_{0,i})^2}{4D_{e,i}} \left(j + \frac{1}{2} \right)^2 - D_{e,i} - E_{0,i} \quad (2.24)$$

and

$$\begin{aligned}
\psi_{N,i,j}(r_N) = & \sqrt{a_i(k_i - 2j - 1) \frac{\Gamma(j+1)}{\Gamma(k_i - j)}} e^{-k_i e^{-a_i(r_N - r_{e,i})}/2} \\
& \left[k_i e^{-a_i(r_N - r_{e,i})} \right]^{(k_i - 2j - 1)/2} L_j^{(k_i - 2j - 1)} \left[k_i e^{-a_i(r_N - r_{e,i})} \right], \quad (2.25)
\end{aligned}$$

respectively [30–32], where h is the Planck constant,

$$\nu_{0,i} = \frac{a_i}{2\pi} \sqrt{\frac{2D_{e,i}}{\mu}} \quad (2.26)$$

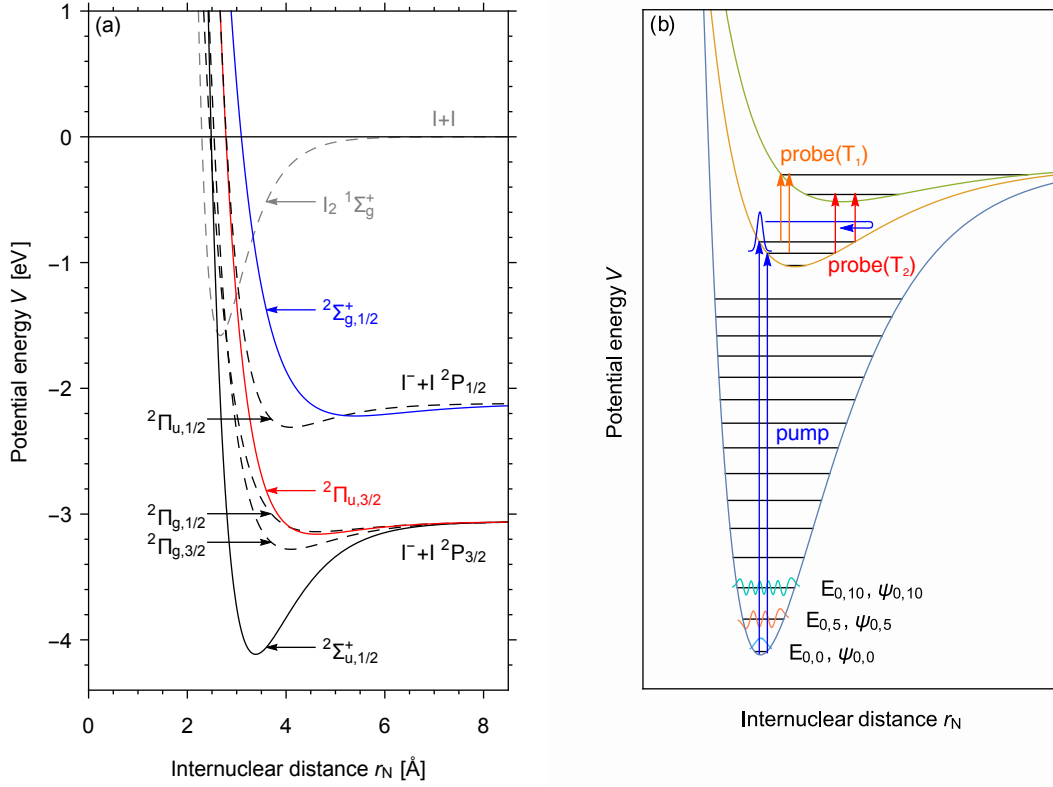


Figure 2.2.: Wavepackets travelling on PESs. One possibility to characterize the PESs of a diatomic molecule, e.g., iodine or diiodide (a), is to calculate Morse potential energy curves from experimental data [27, 28]. Each PES i gives a nuclear vibrational eigenequation, which yields a set of vibrational eigenenergies $E_{i,j}$ and vibrational wavefunctions $\psi_{N,i,j}(\mathbf{r}_N)$ (b). An ultrashort and therefore broadband pump laser pulse typically excites multiple vibrational states simultaneously, which then add up to a vibrational wavepacket oscillating between a minimal and a maximal internuclear distance r_N . Therefore, the spectral position of the probed ESA shifts depending on the time delay between pump and probe pulse, e.g., T_1 and T_2 .

is the fundamental frequency,

$$\mu = \frac{m_{N,1}m_{N,2}}{m_{N,1} + m_{N,2}} \quad (2.27)$$

is the reduced mass of the diatomic molecule,

$$k_i = 4\pi \frac{\sqrt{2\mu D_{e,i}}}{a_i \hbar} \quad (2.28)$$

and $L_j^{(k_i-2j-1)}[\dots]$ are the generalized Laguerre polynomials. Both $E_{i,j}$ and $\psi_{N,i,j}(r_N)$ are qualitatively exemplified in Fig. 2.2b.

These nuclear states $\psi_{N,i,j}(r_N)$ combined with the electronic states $\psi_{e,i}(\mathbf{r}_e; r_N)$ form the quantum states $\psi_{i,j}(\mathbf{r}_e, r_N)$ between which the molecular system jumps under the perturbation of a laser pulse, as described in Sec. 2.2.1. For example, a molecule initially being in the electronic–vibrational ground state $\psi_{0,0}(\mathbf{r}_e, r_N)$ can be excited by a

pump pulse in such a way that a part of the molecular wavefunction is projected into an electronically and possibly vibrationally excited state $\psi_{1,j}(\mathbf{r}_e, r_N)$, as illustrated in Fig. 2.2b. Such a transition between two quantum states requires that the electromagnetic field of the pump pulse oscillates with an optical frequency ν that is in resonance with the molecular energy gap $h\nu = E_{1,j} - E_{0,0}$. Since an ultrashort laser pulse is created by overlapping a multitude of monochromatic waves with different optical frequencies, the pump pulse is capable to simultaneously excite multiple nuclear states $\psi_{N,1,j}(r_N)$, which therefore add up to a vibrational wavepacket oscillating between a minimal and a maximal internuclear distance [26, Chap. 13]. Consequently, the ESA signal, which is measured with a subsequent probe pulse, oscillates between two spectral positions following the wavepacket dynamic. Beyond the effect of the wavepacket position, the ESA is also influenced by the wavepacket broadening and narrowing around the equilibrium position $r_{e,i}$ and the turning points, respectively. This effect stems from the Morse potential’s anharmonicity, which also results in a varying energy spacing between consecutive vibrational states: For lower vibrational energy levels, the energy spacing increases, which also increases the oscillation frequency of a wavepacket that climbs down the vibrational energy ladder while the molecule cools down by distributing the vibrational energy into the environment. For the I_2 system, these effects were extensively simulated and discussed by Vöhringer [33, Sec. 3.3].

Staying with iodine-based molecules, the next level of complexity is reached with triiodide I_3^- . Under the assumption that I_3^- has a fixed bond angle of 180° and therefore stays always linear, the nuclear coordinates \mathbf{r}_N reduce to the two bond lengths r_{ab} and r_{bc} , which lead to the two-dimensional PESs depicted in Fig. 2.3. The bottom of the electronic ground state is approximated by a two-dimensional harmonic potential [Fig. 2.3, (purple)], while the excited states reached after 365 nm excitation [Fig. 2.3, (blue)] and 266 nm excitation [Fig. 2.3, (green)] are approximated by London–Eyring–Polanyi–Sato (LEPS) potentials [34], but also ab-initio calculations are available [35, 36]. Again, the shape-defining parameters were extracted from experimental data [37]. In contrast to the one-dimensional case, an excited state wavepacket has now three possibilities: Either it propagates along one of the valleys or over the hill in between, increasing the bond length r_{ab} , r_{bc} or both, respectively. Since a chemical bond breaks at a certain bond length, the route over the hill results in three-body dissociation, while the routes along the valleys result in two-body dissociation yielding a radical iodine atom and a diiodide I_2^- fragment. Therefore, the cross profile of both valleys smoothly turns into the diiodide’s electronic ground state PES $^2\Sigma_{u,1/2}^+$ [Fig. 2.2a], where then the wavepacket oscillates at a characteristic I_2^- wavenumber. This allows to identify the diatomic fragment, especially in the case of heteronuclear trihalides, which have distinguishable valleys leading to different fragments. Note that the wavepacket’s ”choice” of a dissociation channel is a simplification. In fact, as long as the wavepacket is energetically over the valley-separating barrier, it can spread into both valleys and thus enter both dissociation channels simultaneously, like a particle in the double-slit experiment. Furthermore, to quantify the wavepacket motion, first one needs to transform the (r_{ab}, r_{bc}) coordinate system into a so-called skewed coordinate system [26, 12.3.3].

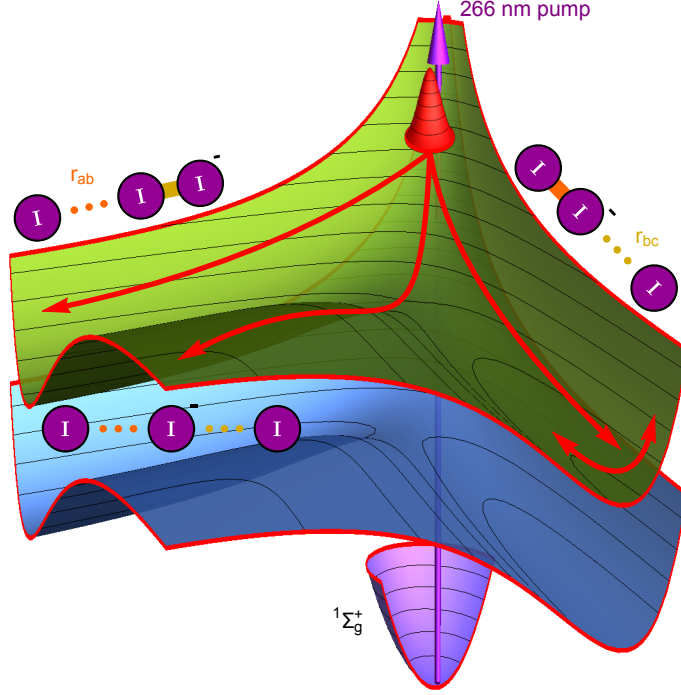


Figure 2.3.: Wavepacket dynamics on I_3^- LEPS potentials. A 365 nm or 266 nm pump laser pulse excites an I_3^- molecule from the purple electronic ground state PES to the blue or green LEPS PES, respectively. The wavepacket created in this manner has three options: Either it enters one of the two valleys or it propagates over the hill in between. In the first two cases, only one bond length, r_{ab} or r_{bc} , increases, leading to two-body dissociation, while the route over the hill results in three-body dissociation. Along both valleys, the PES smoothly turns into the diiodide's electronic ground state PES, where therefore the wavepacket oscillates at a characteristic diiodide wavenumber, as illustrated by the double headed arrow.

Detailed simulations of the triiodide wavepacket dynamics following an ultrashort pump pulse excitation can be found in the literature [37–40] [33, Sec. 2.5].

2.2.3. Macroscopic polarization

Starting with the overall polarization $\mathbf{P}(\mathbf{r}, t)$ instead of its transverse part $\mathbf{P}_\perp(\mathbf{r}, t)$ required for the signal field (2.13), the first-order term in (2.12) takes the form

$$\mathbf{P}^{(1)}(\mathbf{r}, t) = \frac{i}{\hbar} \sum_n \int_{-\infty}^{\infty} d^3 r_1 \int_{t_0}^t d\tau_1 \text{Tr} \left\{ \hat{\mathbf{P}}_n(\mathbf{r}) \hat{\mathcal{U}}_{0,n}(t, \tau_1) \otimes \left[\hat{\mathbf{P}}_n(\mathbf{r}_1), \hat{\mathcal{U}}_{0,n}(\tau_1, t_0) \hat{\rho}_n(t_0) \right] \right\} \cdot \mathbf{E}_\perp(\mathbf{r}_1, \tau_1) \quad (2.29)$$

if the electric interaction Hamiltonian from (2.6) is inserted inside the definition of the first-order density operator (2.9). Since the transverse electric field $\mathbf{E}_\perp(\mathbf{r}, t)$ is not an

operator, it can be factored out of the trace, using the scalar (dot) product and the tensor product \otimes .

If the sample molecules are in equilibrium at time t_0 , the density operator

$$\hat{\mathcal{U}}_{0,n}(\tau_1, t_0) \hat{\rho}_n^{(1)}(t_0) = \hat{\rho}_n^{(1)}(t_0) \quad (2.30)$$

does not evolve with the unperturbed time evolution superoperator $\hat{\mathcal{U}}_{0,n}(\tau_1, t_0)$, not even for an infinite time interval $t_0 = -\infty$ [24, Chap. 5] and thus the polarization simplifies to

$$\mathbf{P}^{(1)}(\mathbf{r}, t) = \frac{i}{\hbar} \sum_n \int_{-\infty}^{\infty} d^3 r_1 \int_{-\infty}^t d\tau_1 \text{Tr} \left\{ \hat{\mathbf{P}}_n(\mathbf{r}) \hat{\mathcal{U}}_{0,n}(t - \tau_1) \otimes [\hat{\mathbf{P}}_n(\mathbf{r}_1), \hat{\rho}_n(-\infty)] \right\} \cdot \mathbf{E}_{\perp}(\mathbf{r}_1, \tau_1), \quad (2.31)$$

using also the fact that the remaining $\hat{\mathcal{U}}_{0,n}(t, \tau_1)$ does not depend on the absolute times t and τ_1 but on the difference $t - \tau_1$.

Within the electric dipole approximation given in eq. (2.6), the polarization

$$\mathbf{P}^{(1)}(\mathbf{r}, t) \approx \frac{i}{\hbar} \sum_n \int_{-\infty}^{\infty} d^3 r_1 \int_{-\infty}^t d\tau_1 \text{Tr} \left\{ \hat{\boldsymbol{\mu}}_n \delta(\mathbf{r} - \mathbf{R}_n) \hat{\mathcal{U}}_{0,n}(t - \tau_1) \otimes [\hat{\boldsymbol{\mu}}_n \delta(\mathbf{r}_1 - \mathbf{R}_n), \hat{\rho}_n(-\infty)] \right\} \cdot \mathbf{E}_{\perp}(\mathbf{r}_1, \tau_1) \quad (2.32)$$

becomes local due to $\delta(\mathbf{r} - \mathbf{R}_n)$, which can be replaced by $\delta(\mathbf{r} - \mathbf{r}_1)$, because \mathbf{r}_1 must equal the position \mathbf{R}_n of the n th molecule due to $\delta(\mathbf{r}_1 - \mathbf{R}_n)$. However, one cannot know the position of every molecule in a gaseous or a liquid sample, which therefore needs to be approximated by a simplified macroscopic structure. Assuming a homogeneous sample, $\delta(\mathbf{r}_1 - \mathbf{R}_n)$ can be replaced

$$\mathbf{P}^{(1)}(\mathbf{r}, t) = \frac{i}{\hbar} \sum_n \int_{-\infty}^{\infty} d^3 r_1 \int_{-\infty}^t d\tau_1 c_n \text{Tr} \left\{ \hat{\boldsymbol{\mu}}_n \delta(\mathbf{r} - \mathbf{r}_1) \hat{\mathcal{G}}_{0,n}(t - \tau_1) \otimes [\hat{\boldsymbol{\mu}}_n, \hat{\rho}_n(-\infty)] \right\} \cdot \mathbf{E}_{\perp}(\mathbf{r}_1, \tau_1) \quad (2.33)$$

by the concentration

$$c_n = \frac{n_n}{V} \quad (2.34)$$

of each molecular species n defined by the amount of substance n_n per sample volume V , which can be interpreted as the probability density to find a molecule of type n in an infinitesimal small volume $d^3 r_1$ located at an arbitrary position \mathbf{r}_1 . Note that this assumption does not allow to calculate reflection and transmission at interfaces, which, for example, can be calculated according to Ref. [41, Chap. II:33]. The introduction of the Liouville space retarded Green function [24, Chap. 3]

$$\hat{\mathcal{G}}_{0,n}(t - \tau_1) = \theta(t - \tau_1) \hat{\mathcal{U}}_{0,n}(t - \tau_1) \quad (2.35)$$

allows to extend the upper limit of the time integral to ∞ and thus simplifies the Fourier transformation applied in the next Sec. 2.2.4. Solving the spatial integral reveals that the spatial dependence of the polarization

$$\mathbf{P}_{\perp}^{(1)}(\mathbf{r}, t) = \frac{i}{\hbar} \sum_n \int_{-\infty}^{\infty} d\tau_1 c_n \text{Tr} \{ \hat{\boldsymbol{\mu}}_n \hat{\mathcal{G}}_{0,n}(t - \tau_1) \otimes [\hat{\boldsymbol{\mu}}_n, \hat{\rho}_n(-\infty)] \} \cdot \mathbf{E}_{\perp}(\mathbf{r}, \tau_1) \quad (2.36)$$

stems solely from the electric field but not from the sample. Consequently, the polarization inherits its spatial properties from the transverse electric field and thus becomes also transverse, as required for (2.13).

Note that n now indexes the molecular species instead of the individual molecules. The simplest scenario

$$\mathbf{P}_{\perp}^{(1)}(\mathbf{r}, t) = \int_{-\infty}^{\infty} d\tau_1 c \frac{i}{\hbar} \underbrace{\text{Tr} \{ \hat{\boldsymbol{\mu}} \hat{\mathcal{G}}_0(t - \tau_1) \otimes [\hat{\boldsymbol{\mu}}, \hat{\rho}(-\infty)] \}}_{\mathbf{t}^{(2)}(t - \tau_1)} \cdot \mathbf{E}_{\perp}(\mathbf{r}, \tau_1) \quad (2.37)$$

consists of only one type of molecules, whose orientations can be concisely expressed by the second-rank tensor $\mathbf{t}^{(2)}(t - \tau_1)$, but since the possibility of individual molecular orientations was not considered during the spatial averaging, $\mathbf{t}^{(2)}(t - \tau_1)$ describes molecules that are all oriented in the same direction. However, like for the positions, also the precise orientations of all molecules are unknown, but for a liquid sample one can assume that the molecules are randomly oriented, i.e., each orientation occurs with the same probability. Consequently, no preferred orientation exists and the sample is isotropic. The information about the orientation of the molecules is contained in the tensor properties of $\mathbf{t}^{(2)}(t - \tau_1)$. To get the rotationally averaged (denoted below by a ring accent) tensor $\overset{\circ}{\mathbf{T}}^{(2)}(t - \tau_1)$ in the laboratory-fixed frame $A, B \in \{X, Y, Z\}$, one has to average each element

$$\overset{\circ}{T}_{AB}^{(2)} = \sum_{ab} I_{AB:ab}^{(2)} t_{ab}^{(2)} \quad (2.38)$$

of the single-molecule tensor $\mathbf{t}^{(2)}(t - \tau_1)$ in the molecule-fixed frame $a, b \in \{x, y, z\}$, using the weighting factor

$$I_{AB:ab}^{(2)} = \frac{1}{3} \delta_{AB} \delta_{ab}, \quad (2.39)$$

which is known from the literature [42] [25, Chap. 3.3] with δ_{ij} being the Kronecker delta. Note that for concise equations, the time dependence of the tensor elements is hidden. Since the only remaining tensor property of the result

$$\overset{\circ}{\mathbf{T}}^{(2)}(t - \tau_1) = \frac{1}{3} (t_{xx}^{(2)} + t_{yy}^{(2)} + t_{zz}^{(2)}) \begin{pmatrix} 1 & 0 & 0 \\ 0 & 1 & 0 \\ 0 & 0 & 1 \end{pmatrix} \quad (2.40)$$

is the identity matrix, the first-order polarization

$$\mathbf{P}_{\perp}^{(1)}(\mathbf{r}, t) = \int_{-\infty}^{\infty} d\tau_1 n \frac{i}{\hbar} \overset{\circ}{\mathbf{T}}^{(2)}(t - \tau_1) \cdot \mathbf{E}_{\perp}(\mathbf{r}, \tau_1) = \int_{-\infty}^{\infty} d\tau_1 S^{(1)}(t - \tau_1) \mathbf{E}_{\perp}(\mathbf{r}, \tau_1) \quad (2.41)$$

can be expressed in terms of a scalar first-order response function $S^{(1)}(t - \tau_1)$.

In a similar way, one can define the second-order polarization

$$\mathbf{P}_\perp^{(2)}(\mathbf{r}, t) = \int_{-\infty}^{\infty} d\tau_2 \int_{-\infty}^{\infty} d\tau_1 \mathbf{S}^{(2)}(t - \tau_2, \tau_2 - \tau_1) : [\mathbf{E}_\perp(\mathbf{r}, \tau_2) \otimes \mathbf{E}_\perp(\mathbf{r}, \tau_1)] \quad (2.42)$$

with the second-order response function

$$\mathbf{S}^{(2)}(t - \tau_2, \tau_2 - \tau_1) = n \frac{i}{\hbar} \overset{\circ}{\mathbf{T}}^{(3)}(t - \tau_2, \tau_2 - \tau_1), \quad (2.43)$$

which is now a rotationally averaged third-rank tensor $\overset{\circ}{\mathbf{T}}^{(3)}(t - \tau_2, \tau_2 - \tau_1)$, whose two interactions with the electric field are expressed by the double dot product $:$ and the tensor product \otimes . Again, the single-molecule tensor

$$\mathbf{t}^{(3)}(t - \tau_2, \tau_2 - \tau_1) = \text{Tr} \left\{ \hat{\boldsymbol{\mu}} \hat{\mathcal{G}}_0(t - \tau_2) \otimes [\hat{\boldsymbol{\mu}}, \hat{\mathcal{G}}_0(\tau_2 - \tau_1) [\hat{\boldsymbol{\mu}}, \hat{\rho}(-\infty)]] \right\} \quad (2.44)$$

is averaged element-by-element

$$\overset{\circ}{T}_{ABC}^{(3)} = \sum_{abc} I_{ABC:abc}^{(3)} t_{abc}^{(3)}, \quad (2.45)$$

for which now the weighting factor

$$I_{ABC:abc}^{(3)} = \frac{1}{6} \varepsilon_{ABC} \varepsilon_{abc} \quad (2.46)$$

is used with ε_{ijk} being the Levi-Civita epsilon ($\varepsilon_{XYZ} = \varepsilon_{ZXY} = \varepsilon_{YZX} = -\varepsilon_{XZY} = -\varepsilon_{YXZ} = -\varepsilon_{ZYX} = 1$ and $\varepsilon_{ijk} = 0$ for all other cases). Note that the multiplications implied by the commutators in (2.44) are tensor products. It can be shown that the second-order polarization must vanish for isotropic samples [43, Chap. 9.1] [44, Chap. 1.5.10] and thus this term is only important for anisotropic samples like birefringent crystals.

Therefore, for dissolved molecules, the lowest-order non-linear signal stems from the third-order polarization

$$\mathbf{P}_\perp^{(3)}(\mathbf{r}, t) = \int_{-\infty}^{\infty} d\tau_3 \int_{-\infty}^{\infty} d\tau_2 \int_{-\infty}^{\infty} d\tau_1 \mathbf{S}^{(3)}(t - \tau_3, \tau_3 - \tau_2, \tau_2 - \tau_1) \vdots [\mathbf{E}_\perp(\mathbf{r}, \tau_3) \otimes \mathbf{E}_\perp(\mathbf{r}, \tau_2) \otimes \mathbf{E}_\perp(\mathbf{r}, \tau_1)] \quad (2.47)$$

depending on the third-order response function

$$\mathbf{S}^{(3)}(t - \tau_3, \tau_3 - \tau_2, \tau_2 - \tau_1) = n \frac{i}{\hbar} \overset{\circ}{\mathbf{T}}^{(4)}(t - \tau_3, \tau_3 - \tau_2, \tau_2 - \tau_1), \quad (2.48)$$

which is now a rotationally averaged fourth-rank tensor $\overset{\circ}{\mathbf{T}}^{(4)}(t - \tau_3, \tau_3 - \tau_2, \tau_2 - \tau_1)$, whose three interactions with the electric field are expressed by the triple dot product. Because of the averaging

$$\overset{\circ}{T}_{ABCD}^{(4)} = \sum_{abcd} I_{ABCD:abcd}^{(4)} t_{abcd}^{(4)} \quad (2.49)$$

using now the weighting factor

$$I_{ABCD:abcd}^{(4)} = \frac{1}{30} \begin{pmatrix} \delta_{AB}\delta_{CD} & \delta_{AC}\delta_{BD} & \delta_{AD}\delta_{BC} \end{pmatrix} \begin{pmatrix} 4 & -1 & -1 \\ -1 & 4 & -1 \\ -1 & -1 & 4 \end{pmatrix} \begin{pmatrix} \delta_{ab}\delta_{cd} \\ \delta_{ac}\delta_{bd} \\ \delta_{ad}\delta_{bc} \end{pmatrix}, \quad (2.50)$$

the 81 tensor elements of an arbitrary rank-four single-molecule tensor

$$\mathbf{t}^{(4)}(t-\tau_3, \tau_3-\tau_2, \tau_2-\tau_1) = \text{Tr} \left\{ \hat{\boldsymbol{\mu}} \hat{\mathcal{G}}_0(t-\tau_3) \otimes [\hat{\boldsymbol{\mu}}, \hat{\mathcal{G}}_0(\tau_3-\tau_2)[\hat{\boldsymbol{\mu}}, \hat{\mathcal{G}}_0(\tau_2-\tau_1)[\hat{\boldsymbol{\mu}}, \hat{\rho}(-\infty)]]] \right\} \quad (2.51)$$

in the molecule-fixed frame $a, b, c, d \in \{x, y, z\}$ decrease down to 21 non-zero elements

$$\mathring{T}_{iiii}^{(4)} = \sum_{abcd} \frac{1}{15} (\delta_{ab}\delta_{cd} + \delta_{ac}\delta_{bd} + \delta_{ad}\delta_{bc}) t_{abcd}^{(4)}, \quad (2.52)$$

$$\mathring{T}_{ijjj}^{(4)} = \sum_{abcd} \frac{1}{30} (4\delta_{ab}\delta_{cd} - \delta_{ac}\delta_{bd} - \delta_{ad}\delta_{bc}) t_{abcd}^{(4)} \quad (i \neq j), \quad (2.53)$$

$$\mathring{T}_{ijij}^{(4)} = \sum_{abcd} \frac{1}{30} (-\delta_{ab}\delta_{cd} + 4\delta_{ac}\delta_{bd} - \delta_{ad}\delta_{bc}) t_{abcd}^{(4)} \quad (i \neq j), \quad (2.54)$$

$$\mathring{T}_{ijji}^{(4)} = \sum_{abcd} \frac{1}{30} (-\delta_{ab}\delta_{cd} - \delta_{ac}\delta_{bd} + 4\delta_{ad}\delta_{bc}) t_{abcd}^{(4)} \quad (i \neq j), \quad (2.55)$$

for the tensor $\mathring{\mathbf{T}}^{(4)}(t-\tau_3, \tau_3-\tau_2, \tau_2-\tau_1)$ in the laboratory-fixed frame $A, B, C, D \in \{X, Y, Z\}$. But because of

$$\mathring{T}_{iiii}^{(4)} = \mathring{T}_{ijjj}^{(4)} + \mathring{T}_{ijij}^{(4)} + \mathring{T}_{ijji}^{(4)} \quad (2.56)$$

only three of these elements are independent [44, 45].

2.2.4. First-order signal

The macroscopic polarization derived in the last Sec. 2.2.3 is the only signal-radiating source term inside the electromagnetic wave eq. (2.13) if solely electric-dipole light-matter interaction is considered. Splitting the polarization into the perturbative series defined by (2.12), allows to combine the linear first-order term $\mathbf{P}_{\perp}^{(1)}(\mathbf{r}, t)$ with the electric field on the left-hand side of eq. 2.13 [24, Chap. 4]

$$\nabla^2 \mathbf{E}_{\perp}(\mathbf{r}, t) - \frac{1}{c^2} \frac{\partial^2}{\partial t^2} \left[\mathbf{E}_{\perp}(\mathbf{r}, t) - \frac{1}{\epsilon_0} \mathbf{P}_{\perp}^{(1)}(\mathbf{r}, t) \right] = \frac{1}{\epsilon_0 c^2} \frac{\partial^2}{\partial t^2} \sum_{n=2}^{\infty} \mathbf{P}_{\perp}^{(n)}(\mathbf{r}, t), \quad (2.57)$$

which then can be rewritten

$$\nabla^2 \mathbf{E}_{\perp}(\mathbf{r}, t) - \frac{1}{c^2} \frac{\partial^2}{\partial t^2} \int_{-\infty}^{\infty} d\tau_1 \underbrace{\left[\delta(t-\tau_1) + \frac{1}{\epsilon_0} \mathbf{S}^{(1)}(t-\tau_1) \right]}_{\epsilon_r(t-\tau_1)} \mathbf{E}_{\perp}(\mathbf{r}, \tau_1) = \frac{1}{\epsilon_0 c^2} \frac{\partial^2}{\partial t^2} \sum_{n=2}^{\infty} \mathbf{P}_{\perp}^{(n)}(\mathbf{r}, t) \quad (2.58)$$

using the response function $\mathbf{S}^{(1)}(t - \tau_1)$ from (2.41) or the relative dielectric function $\epsilon_r(t - \tau_1)$. In general, both functions are second-rank tensors, which reduce to scalar quantities for an isotropic sample [see eq. (2.40)].

The higher the electric-field amplitude, the higher the order of the polarization terms that become relevant to the light-matter interaction. Therefore, all non-linear terms $\mathbf{P}_\perp^{(n \geq 2)}(\mathbf{r}, t)$ can be neglected for sufficiently low field amplitudes. Starting with such a scenario, the wave equation reduces to

$$\nabla^2 \mathbf{E}_\perp(\mathbf{r}, t) - \frac{1}{c^2} \frac{\partial^2}{\partial t^2} \int_{-\infty}^{\infty} d\tau_1 \epsilon_r(t - \tau_1) \cdot \mathbf{E}_\perp(\mathbf{r}, \tau_1) = 0, \quad (2.59)$$

of which the convolution of $\epsilon_r(t)$ and $\mathbf{E}_\perp(\mathbf{r}, t)$ can be simplified to a (dot) product by switching from the time domain to the (angular) frequency domain

$$\nabla^2 \mathbf{E}_\perp(\mathbf{r}, t) - \frac{1}{c^2} \frac{\partial^2}{\partial t^2} \int_{-\infty}^{\infty} d\tau_1 \epsilon_r(t - \tau_1) \cdot \int_{-\infty}^{\infty} \frac{d\omega}{2\pi} \mathbf{E}_\perp(\mathbf{r}, \omega) e^{-i\omega\tau_1} = 0, \quad (2.60)$$

using the Fourier transformation of the electric field. With

$$t_1 = t - \tau_1 \quad (2.61)$$

and a reordered integration sequence

$$\nabla^2 \mathbf{E}_\perp(\mathbf{r}, t) - \frac{1}{c^2} \frac{\partial^2}{\partial t^2} \int_{-\infty}^{\infty} \frac{d\omega}{2\pi} \int_{-\infty}^{\infty} dt_1 \epsilon_r(t_1) \cdot \mathbf{E}_\perp(\mathbf{r}, \omega) e^{-i\omega(t-t_1)} = 0 \quad (2.62)$$

the time integral can be solved

$$\nabla^2 \mathbf{E}_\perp(\mathbf{r}, t) - \frac{1}{c^2} \frac{\partial^2}{\partial t^2} \int_{-\infty}^{\infty} \frac{d\omega}{2\pi} \epsilon_r(\omega) \cdot \mathbf{E}_\perp(\mathbf{r}, \omega) e^{-i\omega t} = 0 \quad (2.63)$$

yielding the Fourier transformation of the relative dielectric function $\epsilon_r(\omega)$. (For an inhomogeneous sample $\epsilon_r(\mathbf{r}, t)$, also the spatial Fourier transformation needs to be considered, resulting in a \mathbf{k} -dependent $\epsilon_r(\mathbf{k}, \omega)$ [24, Chap. 4].) Since the time dependence remains only in the exponential function, now the time derivative

$$\nabla^2 \mathbf{E}_\perp(\mathbf{r}, t) + \int_{-\infty}^{\infty} \frac{d\omega}{2\pi} \frac{\omega^2}{c^2} \epsilon_r(\omega) \cdot \mathbf{E}_\perp(\mathbf{r}, \omega) e^{-i\omega t} = 0 \quad (2.64)$$

can be calculated. Furthermore, if one applies the spatial Fourier transformation and rewrites the full equation in the (\mathbf{k}, ω) -space

$$\nabla^2 \int_{-\infty}^{\infty} \frac{d^3k}{(2\pi)^3} \int_{-\infty}^{\infty} \frac{d\omega}{2\pi} \mathbf{E}_\perp(\mathbf{k}, \omega) e^{i\mathbf{k}\cdot\mathbf{r} - i\omega t} + \int_{-\infty}^{\infty} \frac{d^3k}{(2\pi)^3} \int_{-\infty}^{\infty} \frac{d\omega}{2\pi} \frac{\omega^2}{c^2} \epsilon_r(\omega) \cdot \mathbf{E}_\perp(\mathbf{k}, \omega) e^{i\mathbf{k}\cdot\mathbf{r} - i\omega t} = 0, \quad (2.65)$$

it becomes obvious that the integrand must vanish

$$\int_{-\infty}^{\infty} \frac{d^3k}{(2\pi)^3} \int_{-\infty}^{\infty} \frac{d\omega}{2\pi} \underbrace{\left[-|\mathbf{k}|^2 \mathbf{E}_{\perp}(\mathbf{k}, \omega) + \frac{\omega^2}{c^2} \boldsymbol{\epsilon}_r(\omega) \cdot \mathbf{E}_{\perp}(\mathbf{k}, \omega) \right]}_{\stackrel{!}{=}0} e^{i\mathbf{k}\cdot\mathbf{r}-i\omega t} = 0 \quad (2.66)$$

to fulfil the wave equation. For isotropic samples $\boldsymbol{\epsilon}_r(\omega)$ simplifies to a scalar quantity $\epsilon_r(\omega)$ and the relation

$$k(\omega) = \frac{\omega}{c} \sqrt{\epsilon_r(\omega)} = \frac{\omega}{c} n(\omega) + i \frac{\alpha(\omega)}{2} \quad (2.67)$$

must hold to fulfil (2.66). Usually, the real and imaginary part of the root of the dielectric function are distinguished by the refractive index $n(\omega)$ and the absorption coefficient $\alpha(\omega)$.

The interpretation of the above results is that the Fourier transformation applied in eq. (2.65) decomposes an arbitrary electromagnetic wave $\mathbf{E}_{\perp}(\mathbf{r}, t)$ into a continuous sum of (\mathbf{k}, ω) -dependent, monochromatic plane waves

$$\mathbf{E}_{\perp}(\mathbf{k}, \omega) e^{i\mathbf{k}\cdot\mathbf{r}-i\omega t}, \quad (2.68)$$

whose wave vector amplitude

$$k(\omega) = \frac{\omega}{c} \sqrt{\epsilon_r(\omega)} \quad (2.69)$$

is determined by the angular frequency ω and the dielectric function $\epsilon_r(\omega)$, which in turn depends on the sample's properties. Therefore, also a single monochromatic plane wave

$$\mathbf{E}_{\perp}(\mathbf{r}, t) = \mathbf{E}_0 e^{i\mathbf{k}_0\cdot\mathbf{r}-i\omega_0 t} \quad (2.70)$$

of angular frequency ω_0 with

$$k_0 = \frac{\omega_0}{c} \sqrt{\epsilon_r(\omega_0)} \quad (2.71)$$

fulfils the wave eq. (2.13). In order to reshape this spatially and temporally infinitely wide, complex-valued wave into a real-valued pulse,

$$\mathbf{E}_{\perp}(\mathbf{r}, t) = \mathbf{e}_0 E_0(\mathbf{r}, t) e^{i\mathbf{k}_0\cdot\mathbf{r}-i\omega_0 t} + \text{c.c.} \quad (2.72)$$

one introduces a spatio-temporal-dependent envelope $E_0(\mathbf{r}, t)$ with, like in the Jones formalism [46], a fixed polarization \mathbf{e}_0 [not to confuse with the material polarization $\mathbf{P}(\mathbf{r}, t)$] and adds the complex conjugate. In the most general case

$$\mathbf{E}_{\perp}(\mathbf{r}, t) = \mathbf{e}_0(\mathbf{r}, t) E_0(\mathbf{r}, t) e^{i\mathbf{k}_0\cdot\mathbf{r}-i\omega_0 t} + \text{c.c.} = \sum_{i \in \{x, y, z\}} \mathbf{e}_{0,i} A_i(\mathbf{r}, t) e^{i\mathbf{k}_0\cdot\mathbf{r}-i\omega_0 t} + \text{c.c.}, \quad (2.73)$$

both the envelope and the polarization vector depend on time t [47] and space \mathbf{r} . Such pulses can be generated by a polarization pulse shaper [48, 49]. However, this thesis

focuses on laser pulses with static polarization. In the frequency domain, the pulse takes the form

$$\mathbf{E}_\perp(\mathbf{r}, \omega) = \int_{-\infty}^{\infty} dt \mathbf{E}_\perp(\mathbf{r}, t) e^{i\omega t} \quad (2.74)$$

$$= \int_{-\infty}^{\infty} dt \left[\mathbf{e}_0 E_0(\mathbf{r}, t) e^{i\mathbf{k}_0 \cdot \mathbf{r} - i\omega_0 t} + \text{c.c.} \right] e^{i\omega t} \quad (2.75)$$

$$= \int_{-\infty}^{\infty} dt \mathbf{e}_0 E_0(\mathbf{r}, t) e^{i\mathbf{k}_0 \cdot \mathbf{r}} e^{i(\omega - \omega_0)t} + \int_{-\infty}^{\infty} dt \mathbf{e}_0^* A^*(\mathbf{r}, t) e^{-i\mathbf{k}_0 \cdot \mathbf{r}} e^{i(\omega + \omega_0)t} \quad (2.76)$$

$$= \mathbf{e}_0 E_0(\mathbf{r}, \omega - \omega_0) e^{i\mathbf{k}_0 \cdot \mathbf{r}} + \mathbf{e}_0^* A^*(\mathbf{r}, \omega + \omega_0) e^{-i\mathbf{k}_0 \cdot \mathbf{r}}, \quad (2.77)$$

which is then inserted into the (frequency-domain) wave eq. (2.64)

$$\int_{-\infty}^{\infty} \frac{d\omega}{2\pi} \left[\nabla^2 + \underbrace{\frac{\omega^2}{c^2} \epsilon_r(\omega)}_{k^2(\omega)} \right] \mathbf{e}_0 E_0(\mathbf{r}, \omega - \omega_0) e^{i\mathbf{k}_0 \cdot \mathbf{r}} e^{-i\omega t} + \text{c.c.} = 0. \quad (2.78)$$

Applying the Laplacian

$$\nabla^2 \mathbf{e}_0 E_0(\mathbf{r}, \omega - \omega_0) e^{i\mathbf{k}_0 \cdot \mathbf{r}} = e^{i\mathbf{k}_0 \cdot \mathbf{r}} \left[\nabla^2 + (2i\mathbf{k}_0 \cdot \nabla) - |\mathbf{k}_0|^2 \right] \mathbf{e}_0 E_0(\mathbf{r}, \omega - \omega_0) \quad (2.79)$$

leads to

$$\int_{-\infty}^{\infty} \frac{d\omega}{2\pi} e^{i\mathbf{k}_0 \cdot \mathbf{r}} \left[\nabla^2 + 2i\mathbf{k}_0 \cdot \nabla + k^2(\omega) - k_0^2 \right] \mathbf{e}_0 E_0(\mathbf{r}, \omega - \omega_0) e^{-i\omega t} + \text{c.c.} = 0, \quad (2.80)$$

where the wavenumber difference

$$k^2(\omega) - k_0^2 = [k(\omega) + k_0][k(\omega) - k_0] \approx 2k_0[k(\omega) - k_0] \quad (2.81)$$

can be approximated. This allows to expand the wavenumber

$$k(\omega) = \sum_{n=0}^{\infty} \frac{1}{n!} \frac{d^n k}{d\omega^n}(\omega_0) (\omega - \omega_0)^n = k_0 + k'_0(\omega - \omega_0) + \frac{1}{2} k''_0(\omega - \omega_0)^2 + \dots \quad (2.82)$$

into a Taylor series around the center frequency ω_0 , where

$$k'_0 = \frac{1}{v_0} \quad (2.83)$$

represents the inverse group velocity v_0 and k''_0 describes the group velocity dispersion. For this expansion, in combination with

$$w = \omega - \omega_0 \quad (2.84)$$

and

$$\mathbf{s}_0 = \frac{\mathbf{k}_0}{|\mathbf{k}_0|} \quad (2.85)$$

the wave equation takes the form

$$\int_{-\infty}^{\infty} \frac{dw}{2\pi} 2ik_0 e^{ik_0 \cdot \mathbf{r}} \left(\frac{\nabla^2}{2ik_0} + \mathbf{s}_0 \cdot \nabla - ik'_0 w - \frac{i}{2} k''_0 w^2 + \dots \right) \mathbf{e}_0 E_0(\mathbf{r}, w) e^{-i(w+\omega_0)t} + \text{c.c.} = 0. \quad (2.86)$$

Finally, one can rewrite the factors $-iw$ and $-w^2$ as temporal derivatives of e^{-iwt} and execute the inverse Fourier transformation resulting in the time domain differential equation (DE)

$$2ik_0 e^{ik_0 \cdot \mathbf{r} - i\omega_0 t} \left(\frac{\nabla^2}{2ik_0} + \mathbf{s}_0 \cdot \nabla + k'_0 \frac{\partial}{\partial t} + \frac{i}{2} k''_0 \frac{\partial^2}{\partial t^2} + \dots \right) \mathbf{e}_0 E_0(\mathbf{r}, t) + \text{c.c.} = 0 \quad (2.87)$$

for the pulse envelope $E_0(\mathbf{r}, t)$.

From the perspective of a small molecule placed inside the focus of the typically Gaussian laser beam [50, Chap. 17.1], the beam profile

$$E_0(\mathbf{r}, t) = E_0(z, t) \quad (2.88)$$

seems to be flat and one can neglect the envelope's second-order spatial variations

$$\nabla^2 E_0(z, t) \ll \frac{\partial E_0}{\partial z}(z, t). \quad (2.89)$$

If, in addition, the temporal variation of the envelope $E_0(z, t)$ is small compared to the oscillations $\exp(ik_0 z - i\omega_0 t)$, one can furthermore neglect the envelope's second- and higher-order temporal variations

$$\frac{i}{2} k''_0 \frac{\partial^2 E_0}{\partial t^2}(z, t) \ll k'_0 \frac{\partial E_0}{\partial t}(z, t). \quad (2.90)$$

With these so-called slowly-varying envelope approximation (SVEA) [44, Chap. 7.5.2], the wave equation simplifies to

$$2ik_0 e^{ik_0 z - i\omega_0 t} \left(\frac{\partial}{\partial z} + \frac{1}{v_0} \frac{\partial}{\partial t} \right) \mathbf{e}_0 E_0(z, t) + \text{c.c.} = 0, \quad (2.91)$$

where $k'_0 = 1/v_0$ is rewritten in terms of the group velocity v_0 . This quantity is often identified as the velocity with which the laser pulse travels, but the interpretation of v_0 might also be more complex depending on the medium, which is passed by the laser pulse [51]. In the first case one can switch to a retarded frame of reference

$$E_0(z, t) \rightarrow E_0(\xi, \eta), \quad (2.92)$$

where one sits at any place

$$\xi = z \quad (2.93)$$

on top of the laser pulse if $t = 0$ in

$$\eta = t - \frac{z}{v_0} \quad (2.94)$$

equals zero [52, Chap. 1.2.1]. By also transforming the spatial derivative

$$\frac{\partial}{\partial z} E_0(\xi, \eta) = \frac{\partial E_0}{\partial \xi} \frac{\partial \xi}{\partial z} + \frac{\partial E_0}{\partial \eta} \frac{\partial \eta}{\partial z} = \left(\frac{\partial}{\partial \xi} - \frac{1}{v_0} \frac{\partial}{\partial \eta} \right) E_0(\xi, \eta) \quad (2.95)$$

and the temporal derivative

$$\frac{\partial}{\partial t} E_0(\xi, \eta) = \frac{\partial E_0}{\partial \xi} \frac{\partial \xi}{\partial t} + \frac{\partial E_0}{\partial \eta} \frac{\partial \eta}{\partial t} = \frac{\partial}{\partial \eta} E_0(\xi, \eta), \quad (2.96)$$

the wave equation simplifies to

$$2ik_0 e^{ik_0 \xi - i\omega_0 \eta} \frac{\partial}{\partial \xi} e_0 E_0(\xi, \eta) + \text{c.c.} = 0, \quad (2.97)$$

where the remaining spatial derivative of the envelope $\partial E_0 / \partial \xi (\xi, \eta) = 0$ equals zero. Therefore, the shape of the envelope $E_0(\xi, \eta)$ stays constant while the pulse travels at the group velocity v_0 . This is a result of neglecting the higher-order terms of $k(\omega)$, which would add the description of the laser pulse's dispersion.

2.2.5. Third-order signal

For strong electric fields, like in ultrashort laser pulses with high peak intensities, one also needs to consider the higher-order polarization terms $\mathbf{P}_\perp^{(n)}(\mathbf{r}, t)$, as described in eq. (2.57). Since the second order polarization $\mathbf{P}_\perp^{(2)}(\mathbf{r}, t)$ vanishes for isotropic samples [43, Chap. 9.1] [44, Chap. 1.5.10], the next term of interest is the third-order polarization $\mathbf{P}_\perp^{(3)}(\mathbf{r}, t)$, which is defined in (2.47) and stems from three interactions between the electric field (2.72)

$$\mathbf{E}_\perp(\mathbf{r}, t) = \sum_i \mathbf{E}_i(\mathbf{r}, t) = \sum_i \mathbf{e}_i E_i(\mathbf{r}, t) e^{i\mathbf{k}_i \cdot \mathbf{r} - i\omega_i t} + \text{c.c.} \quad (2.98)$$

and a molecule. Therefore, up to three different laser pulses, $\mathbf{E}_i(\mathbf{r}, t)$, $\mathbf{E}_j(\mathbf{r}, t)$ and $\mathbf{E}_l(\mathbf{r}, t)$, may contribute to $\mathbf{P}_\perp^{(3)}(\mathbf{r}, t)$. Each of these laser pulses is again described within the SVEA, but in contrast to the pulse defined in Sec. 2.2.4, the propagation direction \mathbf{k}_i can be arbitrarily chosen. Altogether, the SVEA wave equation (2.91) takes now the form

$$\sum_i 2ik_i e^{i\mathbf{k}_i \cdot \mathbf{r} - i\omega_i t} \left(\mathbf{s}_i \cdot \nabla + \frac{1}{v_i} \frac{\partial}{\partial t} \right) \mathbf{e}_i E_i(\mathbf{r}, t) + \text{c.c.} = \frac{1}{\epsilon_0 c^2} \frac{\partial^2}{\partial t^2} \mathbf{P}_\perp^{(3)}(\mathbf{r}, t). \quad (2.99)$$

Note that despite of neglecting the spatial beam profile by applying the SVEA, the two laser pulses must spatially overlap at the molecule position to generate a $\mathbf{P}_\perp^{(3)}(\mathbf{r}, t)$ term.

Substituting the time coordinates in (2.47) with

$$t_3 = t - \tau_3 \quad (2.100)$$

$$t_2 = \tau_3 - \tau_2 \quad (2.101)$$

$$t_1 = \tau_2 - \tau_1 \quad (2.102)$$

leads to

$$\mathbf{P}_\perp^{(3)}(\mathbf{r}, t) = \int_{-\infty}^{\infty} dt_3 \int_{-\infty}^{\infty} dt_2 \int_{-\infty}^{\infty} dt_1 \mathbf{S}^{(3)}(t_3, t_2, t_1) \dot{:} [\mathbf{E}_\perp(\mathbf{r}, t - t_3) \otimes \mathbf{E}_\perp(\mathbf{r}, t - t_3 - t_2) \otimes \mathbf{E}_\perp(\mathbf{r}, t - t_3 - t_2 - t_1)] \quad (2.103)$$

from which one can factor out the oscillating $\exp[i(\mathbf{k}_i \pm \mathbf{k}_j \pm \mathbf{k}_l) \cdot \mathbf{r} - i(\omega_i \pm \omega_j \pm \omega_l)t]$ terms to distinguish the different polarization-generating laser pulse combinations

$$\mathbf{P}_\perp^{(3)}(\mathbf{r}, t) = \sum_{i,j,l} \tilde{\mathbf{P}}_{i,j,l}(\mathbf{r}, t) e^{i(\mathbf{k}_i \pm \mathbf{k}_j \pm \mathbf{k}_l) \cdot \mathbf{r} - i(\omega_i \pm \omega_j \pm \omega_l)t} + \text{c.c.} \quad (2.104)$$

for third-order spectroscopy. Each of these polarization terms represents a radiation source inside the wave eq. (2.99) and thus may emit a signal pulse that oscillates at the corresponding sum or difference frequency. This signal pulse in turn may generate another radiating polarization term et cetera. Therefore, one might expect that the number of generated signal pulses diverge. However, this is avoided by two effects: First, signal pulses have weaker electric fields, which do not generate measureable third-order effects. Second, a signal pulse is only created if the so-called phase matching condition is fulfilled: In the case of transient absorption spectroscopy, the signal pulse $\mathbf{E}_3(\mathbf{r}, t)$ needs to propagate into the same direction

$$\mathbf{k}_3 = \mathbf{k}_2 + \mathbf{k}_1 - \mathbf{k}_1 \quad (2.105)$$

as the probe pulse $\mathbf{E}_2(\mathbf{r}, t)$ to hit the detector (spectrometer). Thus, from all possible third-order signals only those remain which interact twice with the pump pulse $\mathbf{E}_1(\mathbf{r}, t)$ and once with the probe pulse $\mathbf{E}_2(\mathbf{r}, t)$ such that

$$\omega_3 = \omega_1 - \omega_1 + \omega_2. \quad (2.106)$$

The corresponding polarization amplitude [25, Chap.5.5] is

$$\begin{aligned} \tilde{\mathbf{P}}_{2,1,1}^{\text{TA}}(\xi, \eta) = & \int_{-\infty}^{\infty} dt_3 \int_{-\infty}^{\infty} dt_2 \int_{-\infty}^{\infty} dt_1 \\ & \left[\mathbf{S}^{(3)}(t_3, t_2, t_1) \dot{:} (\mathbf{e}_2 \otimes \mathbf{e}_1 \otimes \mathbf{e}_1^*) \right. \\ & \quad E_2(\mathbf{r}, t - t_3) e^{i\omega_2 t_3} E_1(\mathbf{r}, t - t_3 - t_2) E_1^*(\mathbf{r}, t - t_3 - t_2 - t_1) e^{-i\omega_1 t_1} \\ & \quad + \mathbf{S}^{(3)}(t_3, t_2, t_1) \dot{:} (\mathbf{e}_2 \otimes \mathbf{e}_1^* \otimes \mathbf{e}_1) \\ & \quad \left. E_2(\mathbf{r}, t - t_3) e^{i\omega_2 t_3} E_1^*(\mathbf{r}, t - t_3 - t_2) E_1(\mathbf{r}, t - t_3 - t_2 - t_1) e^{i\omega_1 t_1} \right] \quad (2.107) \end{aligned}$$

and the wave equation of the third-order signal pulse $\mathbf{E}_3(\mathbf{r}, t)$ takes the form

$$\frac{\partial}{\partial \xi} e_3 E_3(\xi, \eta) + \text{c.c.} = \frac{i\omega_3^2}{2k_3 \epsilon_0 c^2} \tilde{\mathbf{P}}_{2,1,1}^{\text{TA}}(\eta) e^{i\Delta k \xi} + \text{c.c.} \quad (2.108)$$

if the assumption of a small angle $\mathbf{k}_1 \angle \mathbf{k}_2 \approx 0$ and similar group velocities $v_1 \approx v_2 \approx v_3$ allows to move into the retarded frame of reference defined in Sec. 2.2.4. In addition, it is assumed that $\tilde{\mathbf{P}}_{2,1,1}^{\text{TA}}(\eta)$ does not change with ξ , which allows to solve the wave equation by integration yielding a signal pulse

$$\mathbf{E}_3(L, \eta) \propto i\mathbf{P}_{2,1,1}^{\text{TA}}(\eta) \quad (2.109)$$

at the end L of the sample cell. Since signal pulse $\mathbf{E}_3(\mathbf{r}, t)$ and probe pulse $\mathbf{E}_2(\mathbf{r}, t)$ propagate in the same direction, the spectrometer detects the intensity

$$\begin{aligned} |\mathbf{E}_3(\mathbf{r}, t) + \mathbf{E}_2(\mathbf{r}, t)|^2 &= |\mathbf{E}_3(\mathbf{r}, t)|^2 + |\mathbf{E}_2(\mathbf{r}, t)|^2 + 2 \text{Re} [\mathbf{E}_3(\mathbf{r}, t) \mathbf{E}_2^*(\mathbf{r}, t)] \\ &\approx |\mathbf{E}_2(\mathbf{r}, t)|^2 + 2 \text{Re} [\mathbf{E}_3(\mathbf{r}, t) \mathbf{E}_2^*(\mathbf{r}, t)] \end{aligned} \quad (2.110)$$

of the interference of both laser pulses, of which the pure signal term $|\mathbf{E}_3(\mathbf{r}, t)|^2$ can be neglected, because the signal pulse is typically much weaker than the probe pulse $E_3(\mathbf{r}, t) \ll E_2(\mathbf{r}, t)$. Finally, the two remaining terms can be separated if $|\mathbf{E}_2(\mathbf{r}, t)|^2$ is measured on its own by repeating the experiment without the pump pulse and thus without generating a third-order signal pulse.

2.3. Modelling the reaction kinetics

To separate the GSB, ESA, PA and SE signal contributions described in Sec. 2.1 and to quantify the underlying molecular dynamics, a model function for the difference absorbance

$$\begin{aligned} \Delta A_{\text{kin}}(\lambda, T) &= \sum_{i=0}^{n-1} \epsilon_i(\lambda) c_i(T) l - \sum_{i=0}^{n-1} \epsilon_i(\lambda) c_i l \\ &= \sum_{i=0}^{n-1} \epsilon_i(\lambda) c_i(T) l - \bar{\epsilon}(\lambda) \sum_{i=0}^{n-1} c_i(T) l \\ &= \sum_{i=0}^{n-1} \Delta \epsilon_i(\lambda) c_i(T) l \end{aligned} \quad (2.111)$$

has to be fitted to the measured data. Since one cannot extract absolute concentrations $c_i(T)$ and absolute absorption coefficients $\epsilon_i(\lambda)$ from a difference signal $\Delta A(\lambda, T)$, eq. (2.5) is rewritten in terms of the difference absorption coefficient

$$\Delta \epsilon_i(\lambda) = \epsilon_i(\lambda) - \bar{\epsilon}(\lambda), \quad (2.112)$$

using the averaged absorption coefficient

$$\bar{\epsilon}(\lambda) = \frac{\sum_{i=0}^{n-1} \epsilon_i(\lambda) c_i}{\sum_{i=0}^{n-1} c_i} \quad (2.113)$$

to also consider the most general scenario of multiple starting components, which, e.g., is the case for heteronuclear trihalides (Fig. 5.1). Then, the sum over the static c_i can be replaced by the sum over the dynamic $c_i(T)$. This step is only valid if the overall number of components stays constant, which is obviously not the case for a photodissociation reaction. Nevertheless, this simplification is possible for the trihalides, because only one of the two fragments, e.g., I_2^- but not I, is measured within the spectral detection window, so the number of observed components stays constant.

The temporal behaviour of the concentrations $c_i(T)$ can be described with a compartment model [53] that is based on a reaction scheme, which, as introduced in Sec. 2.1, describes how the pump-excited molecules evolve to states of lower energy or undergo chemical reactions until the initial ground state is reached or a stable product is formed. Assuming that the transition from a state j to a lower energy state $i < j$ ($E_i < E_j$) is a stochastic process that happens at a probability linearly depending on the amount of molecules in the higher energy state, the concentration change

$$\frac{dc_i}{dT}(T) = \sum_{j>i} \varphi_{ij} k_j c_j(T) - k_i c_i(T) \quad (2.114)$$

in the lower energy state can be written in form of a first-order DE, in which all higher energy states j populate the lower energy state i at a characteristic rate k_j . Since the reaction pathway does not need to be straightforward but might branch into different routes, only the percentage $0 \leq \varphi_{ij} \leq 1$ ($\sum_i \varphi_{ij} = 1$) reaches the state i . If the state i is not stable but has a finite lifetime $\tau_i = 1/k_i$, it further decays at a rate k_i to states of even lower energy. However, the probability for a state transition does not need to depend linearly on the molecules' concentration [53] but might be quadratic if two molecules are involved in a reaction [2] et cetera. Despite these additional possibilities, the focus of this thesis lies on the linear processes and solving the whole system of linear DEs results in a so-called linear kinetic model, in which the concentrations rise and decay exponentially. Such a model is called homogeneous if it consists of a discrete number of exponential functions. In contrast, the model is called inhomogeneous if a continuous sum of exponentials

$$\int_{-\infty}^{\infty} dk P(k) e^{-kT} \quad (2.115)$$

is required to describe the molecular dynamics [53]. This is the case when, for example, an environment-sensitive decay rate k meets a large variety of molecule–solvent configurations. The result of the continuous sum depends on the specific form of the probability distribution $P(k)$. A prominent example is the stretched exponential [54, 55]

$$e^{-(k'T)^\beta} = \int_0^{\infty} ds P(s, \beta) e^{-sk'T}, \quad (2.116)$$

where

$$s = \frac{k}{k'} \quad (2.117)$$

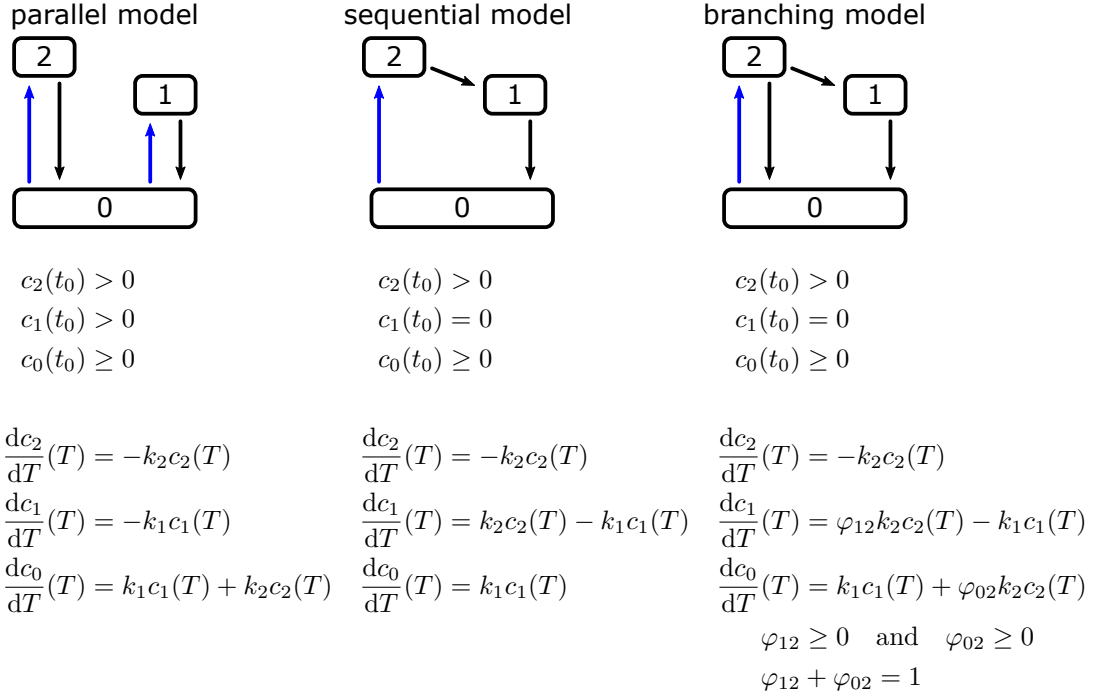


Figure 2.4.: Basic kinetic models. After being excited by a pump pulse (blue arrows), the excited states 1 and 2 decay to the ground state 0 (black arrows) following a parallel model (left), a sequential model (center) or a branching model (right) often referred to as target model. The vertical displacement illustrates the state's energy. Below the reaction scheme, the corresponding initial concentrations and the DE systems are given.

is the normalization of the exponential decay rate k with respect to the stretched-exponential rate k' .

Concentrating on the homogeneous case, one distinguishes three basic kinetic models, which are illustrated in Fig. 2.4 with the help of the simplest scenario consisting of only three components: Either the energy decay happens in parallel (Fig. 2.4, left), sequentially (Fig. 2.4, center) or in a branching manner (Fig. 2.4, right). Actually, the parallel model ($\varphi_{12} = 0$, $\varphi_{02} = 1$) and the sequential model ($\varphi_{12} = 1$, $\varphi_{02} = 0$) are just special cases of the more general branching model, also called target model. Since one cannot separate the initial concentration $c_i(t_0) = c_{i,0}$ from $\Delta\epsilon_i(\lambda)$ without additional knowledge, these parameters plus the sample cell's length l are combined to one

$$\Delta A_{\text{kin}}(\lambda, T) = \sum_{i=0}^{n-1} \left[\text{DADS}_i(\lambda) c_i^{\text{DADS}}(T) \quad \text{or} \quad \text{EADS}_i(\lambda) c_i^{\text{EADS}}(T) \right. \\ \left. \quad \text{or} \quad \text{SADS}_i(\lambda) c_i^{\text{SADS}}(T) \right], \quad (2.118)$$

called decay associated difference spectra (DADS) for the parallel model, evolution-associated difference spectra (EADS) for the sequential model, species-associated differ-

ence spectra (SADS) for the target model or X associated difference spectra (XADS) to reference in the following all three cases simultaneously. The remaining $c_i^{\text{XADS}}(T)$ ranging from 0 to 1 describes the concentration profile. However, all three models fit the data with the same accuracy [53] [56, Sec. 3.2]. Therefore, it is impossible to judge by the fit result which of the reaction schemes is the correct one, but further information from complementary measurements or from theoretical considerations are required.

Furthermore, one needs to be careful about which concentration functions are fed into the fit algorithm. If, for example, only one component is present before the pump excitation $\bar{\epsilon}(\lambda) = \epsilon_0(\lambda)$, then the difference absorption coefficient $\Delta\epsilon_0(\lambda) = 0$ and the $\text{XADS}_i(\lambda)$ vanishes and therefore fitting the corresponding ground state concentration profile $c_0^{\text{XADS}}(T)$ does not make sense. Actually, the excited state concentrations $c_{i>0}^{\text{XADS}}(T)$ ultimately decay into the ground state $c_0^{\text{XADS}}(T)$ and thus already contain the dynamics of $c_0^{\text{XADS}}(T)$. (This is also valid if a stable product is formed, except that the product's decay rate towards the ground state becomes zero.)

To fit the non-vanishing $\text{XADS}_i(\lambda)$, first their wavelength dependence has to be considered. Within a kinetic model, this is achieved by defining an individual amplitude $\text{XADS}_i(\lambda_j)$ for each component i and each measured wavelength data point j . Alternatively, it would also be possible to model the spectrum $\text{XADS}_i(\lambda)$ and define an individual amplitude $c_i^{\text{XADS}}(T_j)$ for each component i and each measured time data point j or to construct a spectrotemporal model $\text{XADS}_i(\lambda) \cdot c_i^{\text{XADS}}(T)$. However, spectral models are typically more phenomenological and require more fit parameters. While an extensive discussion about this topic can be found, e.g., in Ref. [53], the present thesis focuses on the kinetic model, which, from the perspective of a fit algorithm, contains two types of fit parameters: The rate constants k_i determine the decaying exponentials and are thus non-linear fit parameters. In contrast, the individual amplitudes $\text{XADS}_i(\lambda_j)$ determine the linear combination of the decaying exponentials and are therefore linear fit parameters. For example, using three non-linear kinetic fit parameters to model a typical transient absorption dataset with 256 measured wavelengths requires $3 \times 256 = 768$ linear XADS fit parameters. This example also illustrates a difficulty of global or target kinetic models for broadband transient absorption spectra. The large number of parameters would not only slow down the fit algorithm, but also increase the probability for getting trapped in a local minimum. Such a scenario can be avoided by using the variable projection algorithm (VPA) (Sec. 2.4) [16, 53], which exploits the specific form of the model function, a linear combination of non-linear functions, called separable non-linear model or partially non-linear model. Based on the finding that a given set of non-linear parameters already imply the solution of the linear parameters, the dimensionality of the parameter search space can be reduced by removing the linear parameters.

A generalization of the kinetic model (2.118) that includes oscillating signals optimized for the VPA was developed in this thesis and will be presented in Sec. 4.1

2.4. Data fitting with the variable projection algorithm

The VPA of Golub and Pereyra [16, 57] is a fit algorithm which exploits the structure of model functions

$$\eta(\boldsymbol{\alpha}, \mathbf{c}, t) = \sum_{j=1}^n c_j \phi_j(\boldsymbol{\alpha}, t) \quad (2.119)$$

consisting of a linear combination of non-linear functions $\phi_j(\boldsymbol{\alpha}, t)$: By eliminating the n linear parameters

$$\mathbf{c} = (c_1, \dots, c_n)^T, \quad (2.120)$$

the parameter space is reduced to the q non-linear parameters

$$\boldsymbol{\alpha} = (\alpha_1, \dots, \alpha_q)^T, \quad (2.121)$$

resulting in a faster convergence and a higher probability to find the global minimum due to a possibly reduced number of local minima. In particular, the VPA is ideally suited to globally fit kinetic models of transient absorption spectra, which typically consists of a large number of linear parameters \mathbf{c} , one for each component and each wavelength pixel of the DADS, EADS or SADS (Sec. 2.3). An alternative to the VPA would be the reduction of data points by singular-value decomposition (SVD) filtering, which however is prone to noise [53]. This drawback can be avoided by the use of the VPA and furthermore, a variant of the VPA, the partitioned VPA [58], reduces the memory consumption if the dataset and the model function allow a partitioning, e.g., transient absorption spectra can be partitioned into single transients (time-dependent signal for single wavelength), each of which represents the time-dependent signal at a specific wavelength.

For understanding the basic concept of the VPA, it is sufficient to focus on a one-dimensional dataset, e.g., a single transient,

$$\mathbf{y} = (y_1, \dots, y_m)^T, \quad (2.122)$$

measured at m time steps

$$\mathbf{t} = (t_1, \dots, t_m)^T, \quad (2.123)$$

for which the deviation to the model function (2.119) is described by the residuals

$$r_i(\boldsymbol{\alpha}, \mathbf{c}) = y_i - \sum_{j=1}^n c_j \phi_j(\boldsymbol{\alpha}, t_i). \quad (2.124)$$

Being a least-square algorithm, the VPA optimizes the parameters $\boldsymbol{\alpha}$ and \mathbf{c} to minimize the l^2 -norm [16]

$$\min_{\boldsymbol{\alpha}, \mathbf{c}} f(\boldsymbol{\alpha}, \mathbf{c}) = \min_{\boldsymbol{\alpha}, \mathbf{c}} \frac{1}{2} \|\mathbf{r}(\boldsymbol{\alpha}, \mathbf{c})\|_2^2 = \min_{\boldsymbol{\alpha}, \mathbf{c}} \frac{1}{2} \|\mathbf{y} - \boldsymbol{\phi}(\boldsymbol{\alpha}) \cdot \mathbf{c}\|_2^2 \quad (2.125)$$

of the residuals, here rewritten in the vector notation using the model matrix

$$\phi_{ij}(\boldsymbol{\alpha}) = \phi_j(\boldsymbol{\alpha}, t_i). \quad (2.126)$$

For a given set of non-linear parameters α , this optimization procedure reduces to finding the linear parameters

$$\mathbf{c}(\alpha) = \phi^+(\alpha) \cdot \mathbf{y}, \quad (2.127)$$

which can be calculated with the Moore–Penrose pseudoinverse $\phi^+(\alpha)$ [16] [see eq. (2.153)] uncovering the α -dependency of $\mathbf{c}(\alpha)$. Therefore, the fit "problem must become increasingly ill-conditioned as (and if) it converges to the optimal parameters" [16, p. R4]. On the other hand, this property can be used to convert the fit problem into a well-conditioned one: Being already determined by the non-linear parameters α , the linear parameters $\mathbf{c}(\alpha)$ can be eliminated from the residuals' norm

$$\min_{\alpha} f(\alpha) = \min_{\alpha} \frac{1}{2} \|\mathbf{r}(\alpha)\|_2^2 = \min_{\alpha} \frac{1}{2} \left\| \mathbf{y} - \phi(\alpha) [\phi^+(\alpha) \cdot \mathbf{y}] \right\|_2^2 \quad (2.128)$$

at the cost of calculating the pseudoinverse $\phi^+(\alpha)$ but with the advantage that only the typically much smaller set of non-linear parameters α is left to be optimized by the fit algorithm [16]. The new residual form

$$\mathbf{r}(\alpha) = [\mathbf{I} - \phi(\alpha) \cdot \phi^+(\alpha)] \mathbf{y} = \mathbf{P}(\alpha) \cdot \mathbf{y}, \quad (2.129)$$

here rewritten with the help of the identity matrix \mathbf{I} , is called the variable projection of \mathbf{y} , because $\mathbf{P}(\alpha)$ is the projector on the orthogonal complement of the column space of $\phi(\alpha)$, varying with the non-linear parameters α [16].

In contrast to the linear parameters, which can be directly calculated with the pseudoinverse, the optimization of the non-linear parameters requires an iterative algorithm, for which Mathematica's built-in Levenberg–Marquardt–algorithm was chosen in this thesis (Sec. 4.2). The origin of this algorithm dates back to the Newton–Raphson method [59] for numerically approximating the zeros (or roots)

$$f(\alpha) \stackrel{!}{=} 0 \quad (2.130)$$

of a real-valued function, which, for this purpose, is expanded into a first-order Taylor series

$$f(\alpha_s) + \frac{df}{d\alpha}(\alpha_s)(\alpha_{s+1} - \alpha_s) = 0 \quad (2.131)$$

around a chosen starting point α_s . Then, this linear approximation is iteratively evaluated

$$\alpha_{s+1} = \alpha_s - \left[\frac{df}{d\alpha}(\alpha_s) \right]^{-1} f(\alpha_s), \quad (2.132)$$

following the function's gradient $df/d\alpha(\alpha_s)$ until α_{s+1} converges to one of $f(\alpha)$ roots.

In the same way, one can apply this algorithm to the gradient

$$\frac{df}{d\alpha}(\alpha) \stackrel{!}{=} 0, \quad (2.133)$$

to search for the function's minimum (or maximum)

$$\min_{\alpha} f(\alpha) \quad (2.134)$$

by iteratively

$$\alpha_{s+1} = \alpha_s - \left[\frac{d^2 f}{d\alpha^2}(\alpha_s) \right]^{-1} \frac{df}{d\alpha}(\alpha_s) \quad (2.135)$$

following the gradient's gradient $d^2 f/d\alpha^2(\alpha_s)$.

For multidimensional functions like the above defined l^2 -norm (2.128), the gradient

$$\mathbf{g}(\boldsymbol{\alpha}) = \nabla f(\boldsymbol{\alpha}) = \begin{pmatrix} \frac{\partial f}{\partial \alpha_1}(\boldsymbol{\alpha}) \\ \vdots \\ \frac{\partial f}{\partial \alpha_q}(\boldsymbol{\alpha}) \end{pmatrix} \stackrel{!}{=} 0 \quad (2.136)$$

becomes a vector quantity, whose roots can be approximated in analogy to the one-dimensional case by iteratively

$$\boldsymbol{\alpha}_{s+1} = \boldsymbol{\alpha}_s - [\mathbf{J}_g(\boldsymbol{\alpha}_s)]^{-1} \mathbf{g}(\boldsymbol{\alpha}_s) \quad (2.137)$$

$$= \boldsymbol{\alpha}_s - [\mathbf{H}_f(\boldsymbol{\alpha}_s)]^{-1} \nabla f(\boldsymbol{\alpha}_s) \quad (2.138)$$

following the gradient's derivatives, which are concisely expressed in form of the Jacobian matrix

$$\mathbf{J}_g(\boldsymbol{\alpha}) = \begin{pmatrix} \frac{\partial g_1}{\partial \alpha_1}(\boldsymbol{\alpha}) & \cdots & \frac{\partial g_1}{\partial \alpha_q}(\boldsymbol{\alpha}) \\ \vdots & \ddots & \vdots \\ \frac{\partial g_q}{\partial \alpha_1}(\boldsymbol{\alpha}) & \cdots & \frac{\partial g_q}{\partial \alpha_q}(\boldsymbol{\alpha}) \end{pmatrix} = \mathbf{H}_f(\boldsymbol{\alpha}) = \begin{pmatrix} \frac{\partial^2 f}{\partial \alpha_1^2}(\boldsymbol{\alpha}) & \cdots & \frac{\partial^2 f}{\partial \alpha_1 \partial \alpha_q}(\boldsymbol{\alpha}) \\ \vdots & \ddots & \vdots \\ \frac{\partial^2 f}{\partial \alpha_q \partial \alpha_1}(\boldsymbol{\alpha}) & \cdots & \frac{\partial^2 f}{\partial \alpha_q^2}(\boldsymbol{\alpha}) \end{pmatrix}, \quad (2.139)$$

also known as Hessian matrix $\mathbf{H}_f(\boldsymbol{\alpha})$ in relation to the scalar function $f(\boldsymbol{\alpha})$. The calculation of the gradient and the Hessian matrix can either be done directly (Ref. [60] shows how this is combined with the variable projection method) or by exploiting the l^2 -norm's specific dependence on the residual vector

$$f(\boldsymbol{\alpha}) = \sum_{i=1}^m r_i^2(\boldsymbol{\alpha}), \quad (2.140)$$

which allows to rewrite the gradient

$$g_j(\boldsymbol{\alpha}) = \sum_{i=1}^m r_i(\boldsymbol{\alpha}) \frac{\partial r_i}{\partial \alpha_j}(\boldsymbol{\alpha}) \quad (2.141)$$

or

$$\mathbf{g}(\boldsymbol{\alpha}) = \mathbf{J}_r^T(\boldsymbol{\alpha}) \cdot \mathbf{r}(\boldsymbol{\alpha}) \quad (2.142)$$

and the Hessian matrix

$$H_{jk}(\boldsymbol{\alpha}) = \sum_{i=1}^m \left[\frac{\partial r_i}{\partial \alpha_k}(\boldsymbol{\alpha}) \frac{\partial r_i}{\partial \alpha_j}(\boldsymbol{\alpha}) + r_i(\boldsymbol{\alpha}) \frac{\partial^2 r_i}{\partial \alpha_j \partial \alpha_k}(\boldsymbol{\alpha}) \right] \approx \sum_{i=1}^m \frac{\partial r_i}{\partial \alpha_k}(\boldsymbol{\alpha}) \frac{\partial r_i}{\partial \alpha_j}(\boldsymbol{\alpha}) \quad (2.143)$$

or

$$\mathbf{H}_f(\boldsymbol{\alpha}) \approx \mathbf{J}_r^\Gamma(\boldsymbol{\alpha}) \cdot \mathbf{J}_r(\boldsymbol{\alpha}) \quad (2.144)$$

in terms of the residuals $\mathbf{r}(\boldsymbol{\alpha})$ and their Jacobian matrix $\mathbf{J}_r(\boldsymbol{\alpha})$, resulting in the well-known Gauss–Newton algorithm [61]

$$\boldsymbol{\alpha}_{s+1} = \boldsymbol{\alpha}_s - \left[\mathbf{J}_r^\Gamma(\boldsymbol{\alpha}_s) \cdot \mathbf{J}_r(\boldsymbol{\alpha}_s) \right]^{-1} \mathbf{J}_r^\Gamma(\boldsymbol{\alpha}_s) \cdot \mathbf{r}(\boldsymbol{\alpha}_s), \quad (2.145)$$

for which the Hessian’s second-order derivatives are neglected. Improving the algorithm’s convergence control with a damping factor λ , either combined with the identity matrix,

$$\boldsymbol{\alpha}_{s+1} = \boldsymbol{\alpha}_s - \left\{ \mathbf{J}_r^\Gamma(\boldsymbol{\alpha}_s) \cdot \mathbf{J}_r(\boldsymbol{\alpha}_s) + \lambda \mathbf{I} \right\}^{-1} \mathbf{J}_r^\Gamma(\boldsymbol{\alpha}_s) \cdot \mathbf{r}(\boldsymbol{\alpha}_s), \quad (2.146)$$

or the diagonal part of the approximated Hessian matrix,

$$\boldsymbol{\alpha}_{s+1} = \boldsymbol{\alpha}_s - \left\{ \mathbf{J}_r^\Gamma(\boldsymbol{\alpha}_s) \cdot \mathbf{J}_r(\boldsymbol{\alpha}_s) + \lambda \text{diag} \left[\mathbf{J}_r^\Gamma(\boldsymbol{\alpha}_s) \cdot \mathbf{J}_r(\boldsymbol{\alpha}_s) \right] \right\}^{-1} \mathbf{J}_r^\Gamma(\boldsymbol{\alpha}_s) \cdot \mathbf{r}(\boldsymbol{\alpha}_s), \quad (2.147)$$

leads finally to the Levenberg–Marquardt algorithm [16, 62, 63].

The advantage that is added by the VPA is how one calculates the residual vector $\mathbf{r}(\boldsymbol{\alpha})$ [see eq. (2.129)] and the Jacobian matrix $\mathbf{J}_r(\boldsymbol{\alpha})$, of which the k th column was found to be

$$\begin{aligned} \mathbf{J}_{\cdot k} &= - \left[\left(\mathbf{P} \frac{\partial \phi}{\partial \alpha_k} \phi^+ \right) + \left(\mathbf{P} \frac{\partial \phi}{\partial \alpha_k} \phi^+ \right)^\top \right] \mathbf{y} \\ &= \underbrace{-\mathbf{D}_k \phi^+ \mathbf{y} + \phi \phi^+ \mathbf{D}_k \phi^+ \mathbf{y}}_{=-\mathbf{A}_{\cdot k}} - \underbrace{\phi^{+\top} \mathbf{D}_k^\top \mathbf{y} + \phi^{+\top} \mathbf{D}_k^\top \phi \phi^+ \mathbf{y}}_{=-\mathbf{B}_{\cdot k}}, \end{aligned} \quad (2.148)$$

using the projector property $\mathbf{P}^\top = \mathbf{P}$ [16, 57]. Here, the notation is lightened by the abbreviation of the model matrix’s element-by-element differentiation

$$\mathbf{D}_k = \frac{\partial \phi}{\partial \alpha_k} \quad (2.149)$$

and the omission of the matrices’ $\boldsymbol{\alpha}$ -dependence. Altogether, the VPA boils down to efficiently compute the model matrix $\phi(\boldsymbol{\alpha}_s)$, its derivatives $\mathbf{D}_k(\boldsymbol{\alpha}_s)$ and pseudoinverse $\phi^+(\boldsymbol{\alpha}_s)$ to numerically calculate the residuals $\mathbf{r}(\boldsymbol{\alpha})$ and their Jacobian $\mathbf{J}_r(\boldsymbol{\alpha})$ for each step s until the Levenberg–Marquardt algorithm (2.146) or (2.147) converges to a set of non-linear parameters $\boldsymbol{\alpha}_s$ that correctly fits the measured data.

While $\phi(\boldsymbol{\alpha}_s)$ can be received from the straightforward evaluation of each part of the model function $\phi_j(t_i)$ at each time step t_i , $\mathbf{D}_k(\boldsymbol{\alpha}_s)$ requires the user to also provide the model function derivatives, as, for example, in O’Leary’s Matlab implementation of the VPA [57]. Thus, and probably because of the complicated computation of the residual Jacobian (2.148), many VPA implementations, also the package (TIMP) [58], directly approximate

$$J_{ij}(\boldsymbol{\alpha}) = \frac{\partial r_i}{\partial \alpha_j}(\boldsymbol{\alpha}) \approx \frac{r_i \left(\left(\cdots \alpha_j + h \cdots \right)^\top \right) - r_i \left(\left(\cdots \alpha_j \cdots \right)^\top \right)}{h} \quad (2.150)$$

with the finite difference method, which can cause inefficiency and unreliability [57]. On the other hand, the manual preparation of the model function derivatives is time-consuming and error-prone. This issue can be solved with Mathematica's computer algebra tools, which allow the VPA implementation developed in this thesis (Sec. 4.2) to automatically calculate the model function derivatives.

For the numerical calculation of the pseudoinverse $\phi^+(\alpha_s)$, a variety of algorithms exists, of which the two most successful are, on the one hand, the QR decomposition, which is fast and reliable for well-conditioned linear least-squares problems, and, on the other hand, the SVD, which is slower but numerically more stable, especially in the case of ill-conditioned problems [57, 64]. Preferring stability, the latter was chosen for the Mathematica implementation (Sec. 4.2) of the VPA. The SVD factorizes the $m \times n$ matrix

$$\phi(\alpha_s) = \mathbf{U}\mathbf{S}\mathbf{V}^\dagger \quad (2.151)$$

into the unitary $m \times m$ matrix \mathbf{U} , the unitary $n \times n$ matrix \mathbf{V} and the $m \times n$ rectangular diagonal matrix

$$\mathbf{S} = \text{diag}(\sigma_1, \sigma_2, \dots, \sigma_n) \quad (2.152)$$

containing the so-called singular values σ_j on the diagonal. Note that the number of measured time steps m is typically much larger than the number of the fit function components n and therefore the number of σ_j is limited by n . Exploiting the fact that the complex-conjugate transpose of a unitary matrix is also its inverse $\mathbf{U}^\dagger = \mathbf{U}^{-1}$, the pseudoinverse of the model matrix takes the form

$$\phi^+(\alpha_s) = \mathbf{V}\mathbf{S}^+\mathbf{U}^\dagger, \quad (2.153)$$

in which the $n \times m$ pseudoinverse

$$\mathbf{S}^+ = \text{diag}(\sigma_1^{-1}, \sigma_2^{-1}, \dots, \sigma_n^{-1}) \quad (2.154)$$

is received by inverting the singular values on the diagonal and transposing the off-diagonal zeros. Since a small singular value $\sigma_j \approx 0$ has a large reciprocal, a small noise amplitude can have a huge effect in \mathbf{S}^+ . Therefore, the list of reciprocal singular values is typically truncated

$$\sigma_j^{-1} = \begin{cases} \sigma_j^{-1} & \text{if } \sigma_j > t \\ 0 & \text{otherwise} \end{cases} \quad (2.155)$$

at a certain threshold t . This is one possible form of regularization, which improves the numerical stability of the SVD [64].

3. Generalized magic angle

In transient absorption experiments (Sec. 2), an anisotropic distribution of transition dipole moments (TDMs) is created by the pump pulse depending on its polarization [19]. Hence, the differential absorbance signal (2.4) depends on the polarizations and the propagation directions of the pump and the probe pulse. Employing ultrahigh time resolution, the anisotropic distribution of TDMs that is generated by the pump pulse evolves because of population and orientation changes [53, 65–68]. Both processes influence the anisotropy of the distribution. On the one hand, states with a molecular structure different from the initial state may be populated. Thus, anisotropy measurements (Sec. 3.6) can be used to determine the relative orientation of TDMs with respect to the molecular structure [69–71] and to reveal time constants and reaction paths of, e.g., energy transfer in reaction centers [72, 73], exciton delocalization in dendrimers [74, 75], ligand docking [76–78], or electron hopping in proteins [79, 80]. On the other hand, the molecules may rotate. In solution, rotational diffusion makes the excited subensemble isotropic with time [71, 81].

If only population changes are of interest, all these anisotropy-changing effects and their associated decays complicate the measured signal. Therefore, experimental conditions have been derived under which a spectroscopic signal contains contributions neither from molecular structural changes nor from rotational diffusion but reflects the pure population dynamics. The most prominent condition is the “magic-angle” configuration for linearly polarized pump and probe pulses in which the two polarization directions subtend a relative angle of $\chi_{\text{MA}} = \arccos(1/\sqrt{3}) \approx 54.7^\circ$ [19]. The case of circularly polarized pump pulses and linearly polarized probe pulses was treated by Cho [82] who showed that by choosing an angle of $90^\circ - \chi_{\text{MA}} \approx 35.3^\circ$ between the propagation directions of pump and probe one can suppress contributions from electric quadrupole transition moments allowing for a selective measurement of the combined electric-dipole–magnetic-dipole nonlinear response terms contributing to the circularly polarized two-dimensional pump-probe signal.

In order to generalize these known conditions and to analyse the geometry of arbitrary pulse propagation directions and polarizations with arbitrary ellipticity (Sec. 3.1), the probability $P_j(T, \lambda)$ that a single molecule contributes to the difference absorbance signal

$$\Delta A(T, \lambda) = \sum_j \Delta A_j(T, \lambda) = \sum_j cVP_j(T, \lambda) \quad (3.1)$$

is derived either with the transition-probability approach (Sec. 3.2) or the response-theory approach (Sec. 3.3). In both cases it is assumed that the molecules form an isotropic sample having the particle concentration c (2.34), i.e., the molecules are assumed to be randomly oriented inside the volume V that is illuminated by both the pump

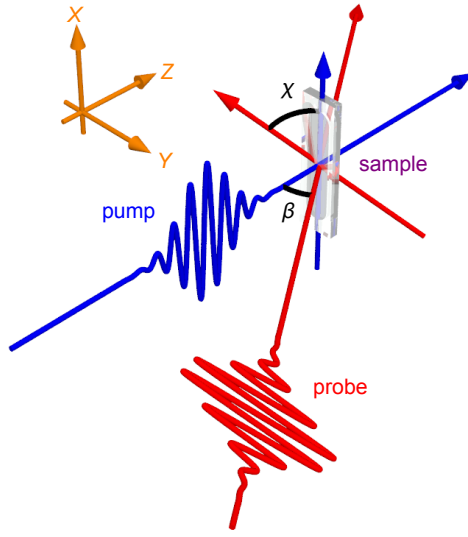


Figure 3.1.: Pump–probe transient absorption geometry. Pump and probe beam are spatially overlapped in the sample and their wave vectors enclose the angle β . Adjusting the angle χ between the linear polarization vectors of the pump and probe pulses to the magic angle of $\chi_{MA} = \arccos(1/\sqrt{3}) \approx 54.7^\circ$ suppresses structural information and orientation dynamics in the measured signal. The coordinate system used throughout this section is shown on the left. The pump wave vector is always assumed to be parallel to the Z direction. [4, Fig. 1] © IOP Publishing. Reproduced with permission. All rights reserved

and the probe beam. As explained in Sec. 3.4, it was discovered that anisotropic contributions in transient absorption signals can also be suppressed for elliptical polarization. Finally, Sec. 3.5 extends the discussion to two-dimensional spectroscopy.

3.1. Electric-field polarization

The pump and probe pulses are spatially overlapped in the sample, as shown exemplarily in Fig. 3.1. Therefore, the electric field interacting with the sample consists of two laser pulses in the case of transient absorption spectroscopy. Each laser pulse is described as a plane polychromatic wave according to (2.72). Despite the fact that the polarization vector $\mathbf{e}(\mathbf{r}, t)$ may depend on space \mathbf{r} and time t [see eq. (2.73)], the focus of this section lies on laser pulses with static polarization but variable ellipticity, as e.g. generated with a broadband wave-plate. In general, these pulses do not propagate collinearly, but their wave vectors \mathbf{k}_{pu} and \mathbf{k}_{pr} enclose an angle β . The linear polarization vectors \mathbf{e}_{pu} and \mathbf{e}_{pr} of the pulses in Fig. 3.1 also enclose an arbitrary angle χ .

Without loss of generality the laboratory Z axis can be chosen as propagation direction of one of the beams, say the pump, and therefore the polarization vector

$$\mathbf{e}_{pu} = \begin{pmatrix} \cos(\chi_{pu}) \\ e^{i\delta_{pu}} \sin(\chi_{pu}) \\ 0 \end{pmatrix} \quad (3.2)$$

lies in the XY plane perpendicular to the propagation direction as depicted in Fig. 3.1. The ratio of the polarization amplitudes in X and Y direction is described by the angle

$$\chi_{pu} = \arctan \left(\frac{|e_{pu,Y}|}{|e_{pu,X}|} \right) \quad (3.3)$$

and the phase difference between the X and Y polarization components by the angle δ_{pr} . The probe polarization in the laboratory frame

$$\mathbf{e}_{\text{pr}} = \mathbf{R}_X(\beta) \cdot \begin{pmatrix} \cos(\chi_{\text{pr}}) \\ e^{i\delta_{\text{pr}}} \sin(\chi_{\text{pr}}) \\ 0 \end{pmatrix} = \begin{pmatrix} \cos(\chi_{\text{pr}}) \\ e^{i\delta_{\text{pr}}} \cos(\beta) \sin(\chi_{\text{pr}}) \\ e^{i\delta_{\text{pr}}} \sin(\beta) \sin(\chi_{\text{pr}}) \end{pmatrix} \quad (3.4)$$

is described analogously, but in addition the rotation matrix $\mathbf{R}_X(\beta)$ performs a rotation about the laboratory X axis with the angle β to take into account the different propagation direction.

To measure only population changes, the magic angle [19] of $\chi_{\text{MA}} = \arccos(1/\sqrt{3}) \approx 54.7^\circ$ is applied. As any polarization vector lies in a plane perpendicular to the propagation direction, the angle β affects the polarization vector in the laboratory coordinate system. To maintain the magic-angle configuration for any β it is necessary to choose either the pump or the probe polarization parallel to the rotation axis of β , which is chosen as the X axis in Fig. 3.1.

3.2. Transition-probability approach

In order to determine P_j in (3.1), time-dependent perturbation theory (Sec. 2.2.1) is used to calculate the transition probability (superscript ‘‘T’’)

$$P_{fi}^{(\text{T})}(t) = \frac{1}{\hbar^2} \left| \int_{t_0}^t d\tau e^{i\omega_{fi}\tau} H'_{fi}(\tau) \right|^2 \quad (3.5)$$

for a transition from an initial state $|i\rangle$ to a final state $|f\rangle$ of a molecular system due to the perturbative electric field of the laser pulses [25, 83]. After applying the electric-dipole interaction Hamiltonian from (2.6)

$$H'_{fi}(\tau) = \langle f | H'(\tau) | i \rangle = \langle f | -\boldsymbol{\mu} \cdot \mathbf{E}_\perp(\mathbf{r}, \tau) | i \rangle = -\boldsymbol{\mu}_{fi} \cdot \mathbf{E}_\perp(\mathbf{r}, \tau) = -\mu_{fi} \tilde{\boldsymbol{\mu}}_{fi} \cdot \mathbf{E}_\perp(\mathbf{r}, \tau) \quad (3.6)$$

with the electric field of a single laser pulse from (2.72) and the amplitude and the orientation of the TDM μ_{fi} and $\tilde{\boldsymbol{\mu}}_{fi}$, respectively, the resulting transition probability

$$P_{fi}^{(\text{T})}(t) = \frac{1}{4\hbar^2} \left| \tilde{\boldsymbol{\mu}}_{fi} \cdot \mathbf{e} \int_{t_0}^t d\tau e^{i\omega_{fi}\tau} \mu_{fi} E(\mathbf{r}, \tau) e^{i(\mathbf{k}_0 \cdot \mathbf{r} - \omega_0 \tau)} + \tilde{\boldsymbol{\mu}}_{fi} \cdot \mathbf{e}^* \int_{t_0}^t d\tau e^{i\omega_{fi}\tau} \mu_{fi} E^*(\mathbf{r}, \tau) e^{-i(\mathbf{k}_0 \cdot \mathbf{r} - \omega_0 \tau)} \right|^2 \quad (3.7)$$

can be simplified in the rotating-wave approximation, in which the first of the two terms in (3.7) dominates near the resonance $\omega_0 \rightarrow \omega_{fi}$. The transition probability for times t after the end of the laser-pulse interaction is then the product of an orientation factor and an amplitude factor. While the amplitude describes in fact the population evolution that one ultimately wants to measure, the goal of this section is to find anisotropy-free conditions irrespective of those dynamics. Thus, specifically the orientation factor

$$P_{fi}^{(\text{T})} = |\tilde{\boldsymbol{\mu}}_{fi} \cdot \mathbf{e}|^2 \quad (3.8)$$

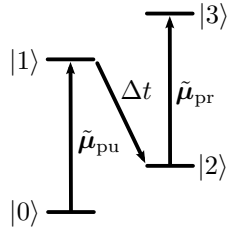


Figure 3.2.: Pump–probe dynamics. One possibility of how the system may evolve and interact with the light pulses in transient absorption: The pump pulse induces the first transition $|0\rangle \rightarrow |1\rangle$ and after the evolution of the system $|1\rangle \rightarrow |2\rangle$ during time Δt , the subsequent probe pulse causes the transition $|2\rangle \rightarrow |3\rangle$. The pump and probe transitions have their TDMs, $\tilde{\boldsymbol{\mu}}_{\text{pu}}$ and $\tilde{\boldsymbol{\mu}}_{\text{pr}}$, oriented in a certain direction, enclosing the angle α . [4, Fig. 2] © IOP Publishing. Reproduced with permission. All rights reserved

that depends explicitly on vectorial properties is considered in the following. One finds that $P_{fi}^{(T)}$ is proportional to the squared projection of the complex electric-field polarization vector \mathbf{e} onto the normalized TDM direction $\tilde{\boldsymbol{\mu}}_{fi}$.

In a transient absorption experiment the system under study may behave as depicted in Fig. 3.2. The pump pulse excites a system from the initial (ground) state $|0\rangle$ to an excited state $|1\rangle$; during time Δt the system evolves from $|1\rangle$ to $|2\rangle$; finally, the probe pulse triggers the transition from $|2\rangle$ to $|3\rangle$. Without loss of generality, one can use this representative signal path to derive the orientation dependence of a single signal contribution P_j (3.1). First, the transition probabilities,

$$P_{\text{pu}}^{(T)} = |\tilde{\boldsymbol{\mu}}_{\text{pu}} \cdot \mathbf{e}_{\text{pu}}|^2, \quad (3.9)$$

$$P_{\text{pr}}^{(T)} = |\tilde{\boldsymbol{\mu}}_{\text{pr}} \cdot \mathbf{e}_{\text{pr}}|^2, \quad (3.10)$$

for both the pump and the probe interaction are calculated based on (3.8). From here on the TDM directions ($\tilde{\boldsymbol{\mu}}_{\text{pu}}$, $\tilde{\boldsymbol{\mu}}_{\text{pr}}$) and the transition probabilities ($P_{\text{pu}}^{(T)}$, $P_{\text{pr}}^{(T)}$) are labelled with the corresponding pulse rather than the involved states. For deriving anisotropy-free conditions, it is relevant that the pump and the probe pulses can interact with different TDM directions $\tilde{\boldsymbol{\mu}}_{\text{pu}}$ and $\tilde{\boldsymbol{\mu}}_{\text{pr}}$, respectively, which enclose in general an arbitrary angle α .

The derivation of P_j in eq. (3.1) can be divided into three steps. In contrast to the chronological order in Fig. 3.2, one first considers a probe TDM pointing in direction (θ, ϕ) and calculates the probability P_{pu} that a corresponding pump TDM was excited by the pump pulse. In the second step the probability $P_{\text{pr}}^{(T)}$ of probing an excited molecule with such a probe TDM is determined. Finally the results for P_{pu} and $P_{\text{pr}}^{(T)}$ are combined to derive the probability P_j for a single signal contribution.

To calculate P_{pu} one has to define the normalized pump and probe TDM directions $\tilde{\boldsymbol{\mu}}_{\text{pu}}$ and $\tilde{\boldsymbol{\mu}}_{\text{pr}}$, respectively. Arbitrary but real-valued TDMs enclosing an angle α are assumed. The orientation of the TDMs is described in spherical coordinates with the polar angle θ and the azimuthal angle ϕ . In the cartesian coordinate system of Fig. 3.1 the Z direction corresponds to $\theta = 0^\circ$, the X direction to $(\theta = 90^\circ, \phi = 0^\circ)$, and the Y

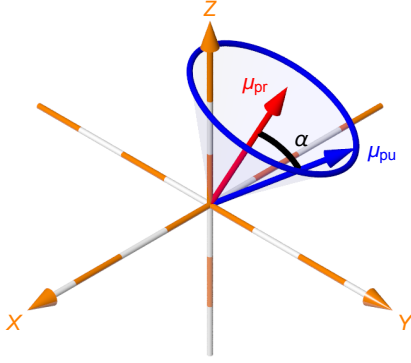


Figure 3.3.: Pump-probe TDM relation. If the probe TDM of an excited molecule is oriented in direction $\tilde{\boldsymbol{\mu}}_{\text{pr}}$ (red arrow), a pump TDM $\tilde{\boldsymbol{\mu}}_{\text{pu}}$ pointing onto the blue circle was excited, because all these pump TDMs enclose the angle α with the probe TDM. [4, Fig. 3] © IOP Publishing. Reproduced with permission. All rights reserved

direction to $(\theta = 90^\circ, \phi = 90^\circ)$. First one defines a probe TDM

$$\tilde{\boldsymbol{\mu}}_{\text{pr}}(\theta, \phi) = \begin{pmatrix} \sin(\theta) \cos(\phi) \\ \sin(\theta) \sin(\phi) \\ \cos(\theta) \end{pmatrix} \quad (3.11)$$

pointing in the direction (θ, ϕ) , which is depicted as red arrow in Fig. 3.3. The corresponding pump TDM then has to point to somewhere on the blue circle around $\tilde{\boldsymbol{\mu}}_{\text{pr}}$ because of the assumption that the pump and probe TDMs enclose the angle α . To describe all possible pump TDM directions one can choose an initial element

$$\tilde{\boldsymbol{\mu}}_{\text{pu,ini}}(\theta, \phi, \alpha) = \begin{pmatrix} \sin(\theta - \alpha) \cos(\phi) \\ \sin(\theta - \alpha) \sin(\phi) \\ \cos(\theta - \alpha) \end{pmatrix} \quad (3.12)$$

and rotate it around $\tilde{\boldsymbol{\mu}}_{\text{pr}}$ by using the three-dimensional rotation matrix $\mathbf{R}_{\mathbf{n}}(\gamma)$ which rotates counter-clock-wise around the unit vector \mathbf{n} by the angle γ resulting in the pump TDM direction

$$\tilde{\boldsymbol{\mu}}_{\text{pu}}(\theta, \phi, \alpha, \gamma) = \mathbf{R}_{\tilde{\boldsymbol{\mu}}_{\text{pr}}}(\gamma) \cdot \tilde{\boldsymbol{\mu}}_{\text{pu,ini}}(\theta, \phi, \alpha). \quad (3.13)$$

In an isotropic sample each of the pump TDMs on the blue circle in Fig. 3.3 contributes to the signal for a given $\tilde{\boldsymbol{\mu}}_{\text{pr}}$ with the same probability. Therefore, the pump TDMs point on each infinitesimal line element

$$dl = \sin(\alpha) d\gamma \quad (3.14)$$

of the circle with the same orientation probability density (superscript “O”) $P_{\text{pu}}^{(\text{O})}$ given by

$$\frac{1}{2\pi \sin(\alpha)} dl = \frac{1}{2\pi} d\gamma = P_{\text{pu}}^{(\text{O})} d\gamma. \quad (3.15)$$

If any anisotropy were present before excitation, for example due to an orientation or alignment process [84–88] not considered here, the probability distribution for $\tilde{\boldsymbol{\mu}}_{\text{pu}}$ would depend on direction.

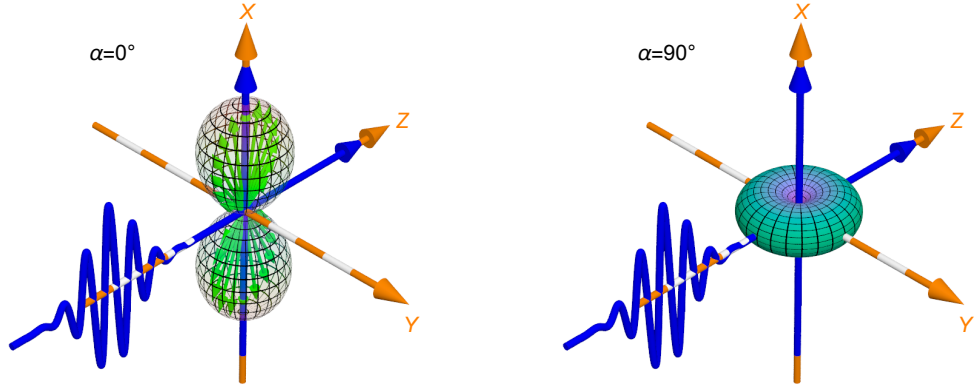


Figure 3.4.: Pump distribution $P_{\text{pu}}(\theta, \phi)$ for a linearly polarized pump pulse. For each direction (θ, ϕ) a vector is drawn with length $P_{\text{pu}}(\theta, \phi)$ as illustrated by the green arrows in the left image. All these vectors point on a three-dimensional surface. This pump distribution $P_{\text{pu}}(\theta, \phi)$ is depicted here for a linearly polarized pump pulse ($\chi_{\text{pu}} = 0^\circ$, $\delta_{\text{pu}} = 0^\circ$). The case $\alpha = 0^\circ$ is shown on the left, while the right hand side depicts the case for $\alpha = 90^\circ$. [4, Fig. 4] © IOP Publishing. Reproduced with permission. All rights reserved

Now one can multiply the orientation probability $P_{\text{pu}}^{(O)}$ of (3.15) with the transition probability $P_{\text{pu}}^{(T)}$ of (3.9), insert the pump TDM direction of (3.13) and the pump polarization vector of (3.2) and integrate over all possible pump TDMs pointing on the blue circle. As a result derived with Mathematica [89] one gets the pump probability

$$\begin{aligned}
P_{\text{pu}}(\theta, \phi, \alpha, \chi_{\text{pu}}, \delta_{\text{pu}}) &= \int_0^{2\pi} d\gamma P_{\text{pu}}^{(O)} P_{\text{pu}}^{(T)} = \frac{1}{2\pi} \int_0^{2\pi} d\gamma |\tilde{\mu}_{\text{pu}} \cdot \mathbf{e}_{\text{pu}}|^2 \\
&= \frac{1}{2\pi} \int_0^{2\pi} d\gamma \left| \cos(\chi_{\text{pu}}) [\cos(\theta) \cos(\phi) \cos(\gamma) \sin(\alpha) \right. \\
&\quad \left. - \cos(\alpha) \cos(\phi) \sin(\theta) - \sin(\alpha) \sin(\phi) \sin(\gamma)] \right. \\
&\quad \left. + e^{i\delta_{\text{pu}}} \sin(\chi_{\text{pu}}) [\cos(\theta) \cos(\gamma) \sin(\alpha) \sin(\phi) \right. \\
&\quad \left. - \cos(\alpha) \sin(\theta) \sin(\phi) + \cos(\phi) \sin(\alpha) \sin(\gamma)] \right|^2 \\
&= \frac{1}{8} \sin^2(\alpha) [3 + \cos(2\theta) - 2 \cos(2\phi) \cos(2\chi_{\text{pu}}) \sin^2(\theta)] \\
&\quad + \frac{1}{8} \sin^2(\theta) [1 + 3 \cos(2\alpha)] \cos(\delta_{\text{pu}}) \sin(2\phi) \sin(2\chi_{\text{pu}}) \quad (3.16) \\
&\quad + \frac{1}{2} \sin^2(\theta) \cos^2(\alpha) [1 + \cos(2\phi) \cos(2\chi_{\text{pu}})]
\end{aligned}$$

depending on the chosen direction (θ, ϕ) for the probe TDM, the angle α between the pump and probe TDMs and the electric-field polarization $(\chi_{\text{pu}}, \delta_{\text{pu}})$ of the pump pulse.

For an illustration, one can draw a vector for every probe TDM orientation (θ, ϕ) , choosing the corresponding pump probability P_{pu} as its length. All these vectors (Fig. 3.4,

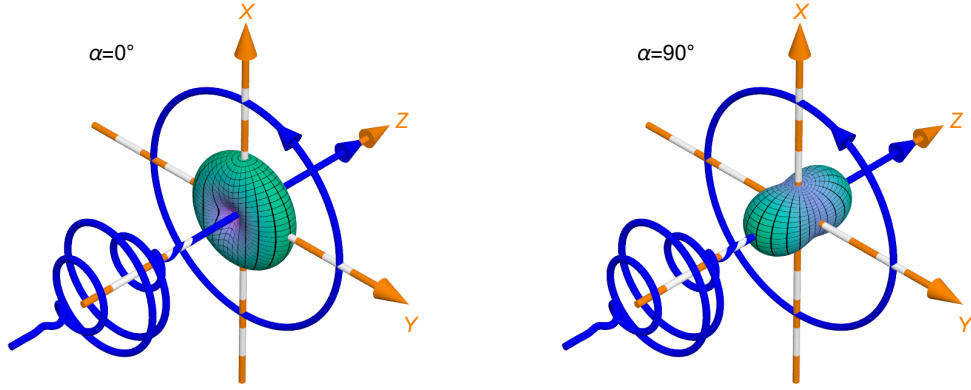


Figure 3.5.: Pump distribution $P_{\text{pu}}(\theta, \phi)$ for a circularly polarized pump pulse ($\chi_{\text{pu}} = 45^\circ$, $\delta_{\text{pu}} = 90^\circ$) with $\alpha = 0^\circ$ (left) and $\alpha = 90^\circ$ (right). [4, Fig. 5] © IOP Publishing. Reproduced with permission. All rights reserved

left, green) point on a three-dimensional surface. This surface illustrates the angular (θ, ϕ) distribution of the pump probability P_{pu} . Such a distribution is exemplarily depicted for a pump pulse propagating in the Z direction with linear (Fig. 3.4), circular (Fig. 3.5) and elliptical (Fig. 3.6) polarization. In each figure the left image refers to an angle of $\alpha = 0^\circ$ and the right image to an angle of $\alpha = 90^\circ$ between the pump and probe TDMs.

In Fig. 3.4 the linearly polarized ($\chi_{\text{pu}} = 0^\circ$, $\delta_{\text{pu}} = 0^\circ$) pump pulse leads to the commonly known \cos^2 distribution for parallel ($\alpha = 0^\circ$) and a torus-shaped distribution for perpendicular ($\alpha = 90^\circ$) TDMs. Both distributions inherit the symmetry of the three-dimensional polarization vector \mathbf{e}_{pu} . In the case of linear polarization in X direction the distribution is rotationally symmetric around the X axis and has mirror-plane symmetry with respect to the YZ plane.

Circular polarization ($\chi_{\text{pu}} = 45^\circ$, $\delta_{\text{pu}} = 90^\circ$) as indicated by the blue circle in Fig. 3.5 leads to rotation symmetry around the propagation direction (Z axis) instead of the polarization direction and to mirror-plane symmetry with respect to the XY plane [90, 91].

In the case of elliptically polarized light ($\chi_{\text{pu}} = 45^\circ$, $\delta_{\text{pu}} = 70^\circ$) in Fig. 3.6 only the XY mirror-plane symmetry is maintained independent of α , but no rotation symmetry remains.

Now one can proceed with the second step and insert the probe TDM direction (3.11) and the probe polarization (3.4) into (3.10) to calculate the probability

$$P_{\text{pr}}^{(\text{T})}(\theta, \phi, \chi_{\text{pr}}, \delta_{\text{pr}}, \beta) = |\tilde{\boldsymbol{\mu}}_{\text{pr}} \cdot \mathbf{e}_{\text{pr}}|^2 = \left| \sin(\theta) \cos(\phi) \cos(\chi_{\text{pr}}) + \cos(\theta) \sin(\chi_{\text{pr}}) e^{i\delta_{\text{pr}}} \sin(\beta) + \sin(\theta) \sin(\phi) \sin(\chi_{\text{pr}}) e^{i\delta_{\text{pr}}} \cos(\beta) \right|^2 \quad (3.17)$$

to probe an excited molecule with its probe TDM pointing into the chosen direction

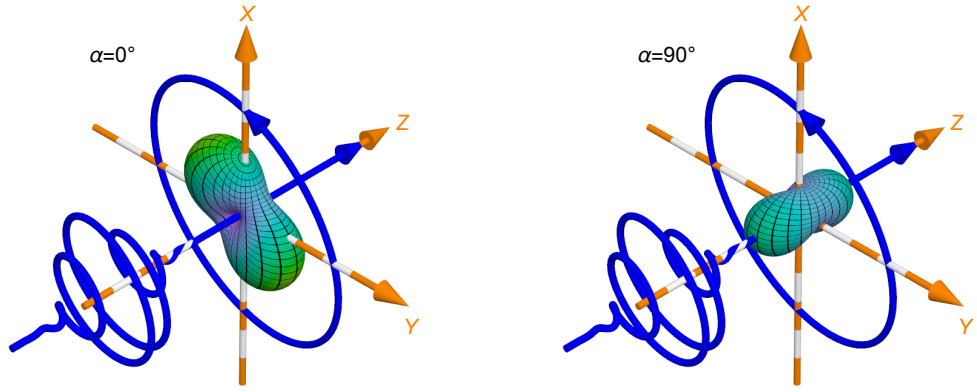


Figure 3.6.: Pump distribution $P_{\text{pu}}(\theta, \phi)$ for an elliptically polarized pump pulse ($\chi_{\text{pu}} = -45^\circ$, $\delta_{\text{pu}} = -70^\circ$) with $\alpha = 0^\circ$ (left) and $\alpha = 90^\circ$ (right). [4, Fig. 6] © IOP Publishing. Reproduced with permission. All rights reserved

(θ, ϕ) . Again, each direction vector (θ, ϕ) with length $P_{\text{pr}}^{(\text{T})}$ is used to construct a surface that illustrates the probe distribution as depicted in Fig. 3.7 (left, red) for a linearly polarized probe pulse.

In the last step one has to consider the probability that the probe TDM of a molecule points into the chosen direction (θ, ϕ) . In an isotropic sample this probability is independent of direction. Therefore, the probe TDM points on each infinitesimal small area

$$dA = \sin(\theta) d\theta d\phi \quad (3.18)$$

of the unit sphere with the same orientation probability density $P_{\text{pr}}^{(\text{O})}$ given by

$$\frac{1}{4\pi} dA = \frac{1}{4\pi} \sin(\theta) d\theta d\phi = P_{\text{pr}}^{(\text{O})} d\theta d\phi. \quad (3.19)$$

Finally one multiplies the pump probability P_{pu} (3.16) with the probe orientation probability $P_{\text{pr}}^{(\text{O})}$ (3.19) and the probe transition probability $P_{\text{pr}}^{(\text{T})}$ (3.17) and integrates

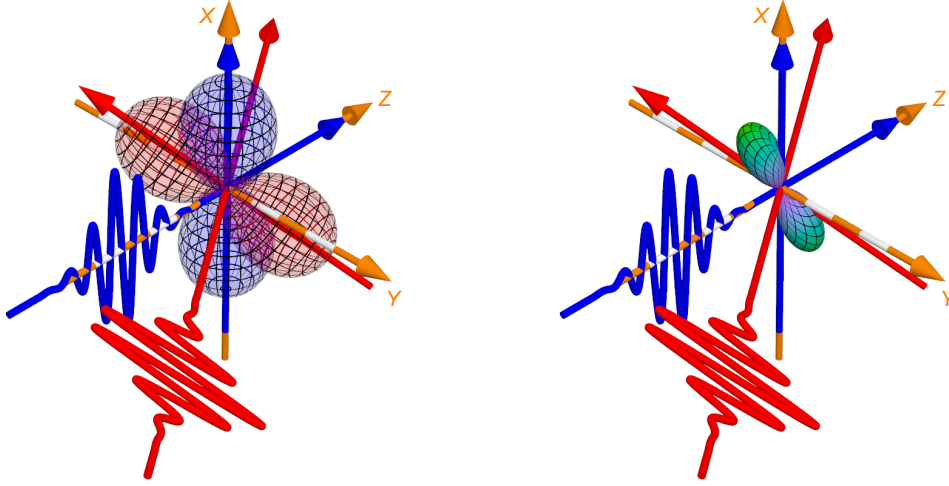


Figure 3.7.: Pump and probe distributions. The left side depicts the pump distribution P_{pu} (blue, $\chi_{\text{pu}} = 0^\circ$, $\delta_{\text{pu}} = 0^\circ$, $\alpha = 0^\circ$) and the probe distribution $P_{\text{pr}}^{(\text{T})}$ (red, $\chi_{\text{pr}} = -54.7^\circ$, $\delta_{\text{pr}} = 0^\circ$) separately, whereas the right side illustrates the overlap distribution $P_{\text{pu}}P_{\text{pr}}^{(\text{T})}$. [4, Fig. 7] © IOP Publishing. Reproduced with permission. All rights reserved

over all possible orientations (θ, ϕ) . As a result one gets the probability

$$\begin{aligned}
 P_j(\alpha, \chi_{\text{pu}}, \delta_{\text{pu}}, \chi_{\text{pr}}, \delta_{\text{pr}}, \beta) &= \int_0^{2\pi} d\phi \int_0^\pi d\theta P_{\text{pu}} P_{\text{pr}}^{(\text{T})} P_{\text{pr}}^{(\text{O})} \\
 &= \frac{1}{60} \left\{ -2 \cos^2(\chi_{\text{pr}}) [-3 + \cos(2\chi_{\text{pu}})] \right. \\
 &\quad + [7 - \cos(2\beta) + 2 \cos^2(\beta) \cos(2\chi_{\text{pu}})] \sin^2(\chi_{\text{pr}}) \\
 &\quad \left. - 2 \cos(\beta) \cos(\delta_{\text{pr}}) \cos(\delta_{\text{pu}}) \sin(2\chi_{\text{pr}}) \sin(2\chi_{\text{pu}}) \right\} \\
 &\quad + \frac{1}{60} \cos^2(\alpha) \left\{ 2 \cos^2(\chi_{\text{pr}}) [1 + 3 \cos(2\chi_{\text{pu}})] \right. \\
 &\quad + [-1 + 3 \cos(2\beta) - 6 \cos^2(\beta) \cos(2\chi_{\text{pu}})] \sin^2(\chi_{\text{pr}}) \\
 &\quad \left. + 6 \cos(\beta) \cos(\delta_{\text{pr}}) \cos(\delta_{\text{pu}}) \sin(2\chi_{\text{pr}}) \sin(2\chi_{\text{pu}}) \right\} \quad (3.20)
 \end{aligned}$$

that a single molecule contributes to the pump–probe signal ΔA_j depending on the angle α between the pump and probe TDMS and the electric-field polarization of the pump ($\chi_{\text{pu}}, \delta_{\text{pu}}$) and the probe pulse ($\chi_{\text{pr}}, \delta_{\text{pr}}, \beta$). For multiple spectrally overlapping signals it is necessary to repeat the calculation above for all pump and probe TDMS combinations of the involved signal paths and to sum the signals according to (3.1).

To validate the correctness of the rotational averaging procedure in the transition-probability approach (see Sec. 3.2), one can apply an alternative approach using Euler

rotations. Again one assumes arbitrary but real-valued TDMs

$$\tilde{\boldsymbol{\mu}}_{\text{pu}}(\phi, \theta, \gamma) = \mathbf{R}(\phi, \theta, \gamma) \cdot \begin{pmatrix} 0 \\ 0 \\ 1 \end{pmatrix}, \quad (3.21)$$

$$\tilde{\boldsymbol{\mu}}_{\text{pr}}(\phi, \theta, \gamma, \alpha) = \mathbf{R}(\phi, \theta, \gamma) \cdot \mathbf{R}_Y(-\alpha) \cdot \begin{pmatrix} 0 \\ 0 \\ 1 \end{pmatrix}, \quad (3.22)$$

enclosing an angle α , here achieved by a rotation matrix \mathbf{R}_Y rotating the initial vector around the Y axis. The Euler rotation matrix [92]

$$\mathbf{R}(\phi, \theta, \gamma) = \mathbf{R}_Z(\phi) \cdot \mathbf{R}_Y(\theta) \cdot \mathbf{R}_Z(\gamma) \quad (3.23)$$

allows to choose an arbitrary orientation. Now the definition of the pump (3.21) and probe (3.22) TDM directions and the definition of the pump (3.2) and probe (3.4) electric-field polarization vectors are applied to the corresponding equations of the transition probability (3.9) and (3.10) and rotational averaging [42, 93–97],

$$P_j = \frac{1}{8\pi^2} \int_0^{2\pi} d\phi \int_0^\pi d\theta \int_0^{2\pi} d\gamma P_{\text{pu}}^{(\text{T})} P_{\text{pr}}^{(\text{T})} \sin(\theta), \quad (3.24)$$

is performed over the product of the pump and probe transition probabilities to calculate the probability P_j . The result is the same as in (3.20).

A graphical interpretation of (3.20) is shown in Fig. 3.7. The pump pulse generates an excited distribution shaped by the pump polarization and the angle α (Fig. 3.7, left, blue). The probe pulse queries a distribution shaped by the probe polarization (Fig. 3.7, left, red). Therefore, the probability P_j depends on the product of both distributions (Fig. 3.7, right, green) over which one has to integrate, i.e., their overlap.

The α dependence of the pump-induced distribution P_{pu} connects the probability P_j to the molecular structure. On the one hand, one can exploit this property to extract structural information from anisotropy measurements; on the other hand, one can suppress the structure dependence of the signal to extract information on population dynamics. Removing the structure dependence is possible if the α -related deformation of the pump-induced distribution does not affect the intersection volume between the pump and probe distribution.

To find magic-angle configurations for arbitrarily polarized pump and probe pulses, thus, the α dependence of the probability P_j has to vanish. According to (3.20), this is the case for each configuration that fulfills

$$\left\{ 2 \cos^2(\chi_{\text{pr}}) [1 + 3 \cos(2\chi_{\text{pu}})] \right. \\ \left. + [-1 + 3 \cos(2\beta) - 6 \cos^2(\beta) \cos(2\chi_{\text{pu}})] \sin^2(\chi_{\text{pr}}) \right. \\ \left. + 6 \cos(\beta) \cos(\delta_{\text{pr}}) \cos(\delta_{\text{pu}}) \sin(2\chi_{\text{pr}}) \sin(2\chi_{\text{pu}}) \right\} = 0, \quad (3.25)$$

because α occurs in (3.20) only in the second term. (3.25) is a central result of the present work as it provides the most general magic-angle condition for arbitrary excitation geometry and static pulse polarizations. Examples for particular realizations of (3.25) and their relation to the known magic-angle limiting cases will be discussed in Sec. 3.4.

3.3. Response-theory approach

Compared to the transition-probability approach, the response-theory approach is less illustrative but more general. It fits into the general framework of nonlinear response functions [24, 25, 45, 98] and therefore allows to discuss magic-angle conditions not only for transient absorption, but also for 2D spectroscopy and third-order spectroscopy in general. These techniques are based on the third-order polarization (2.103) [24, 25]. Being interested in orientation effects, one can focus on the tensor properties of the response function $\mathbf{S}^{(3)}$ and the vector properties of the electric field \mathbf{E} . The third-order response function $\mathbf{S}^{(3)}$ is a tensor $\mathcal{T}^{(4)}$ of rank four that interacts three times with the complex polarization vector of the electric field

$$\mathcal{T}^{(4)} : (\mathbf{e}_3 \otimes \mathbf{e}_2 \otimes \mathbf{e}_1). \quad (3.26)$$

The three polarization vectors \mathbf{e}_1 , \mathbf{e}_2 and \mathbf{e}_3 are assigned to individual laser pulses with different but constant polarization. This approximation is possible if the electric field $\mathbf{E}(\mathbf{r}, t)$ consists of temporally separated laser pulses. In third-order spectroscopy, the information contained in the measured signal is filtered by the phase matching, phase cycling and time ordering applied in the specific experiment (see Sec. 2.2.5). These filter conditions also affect the orientation effects in the signal, e.g., the time ordering defines the order of the polarization vectors in (3.26) and therefore the outcome of this equation. For transient absorption no phase cycling is applied. According to the phase matching conditions

$$\mathbf{k}_S = \mathbf{k}_{\text{pu}} - \mathbf{k}_{\text{pu}} + \mathbf{k}_{\text{pr}} \quad \text{and} \quad \mathbf{k}_S = -\mathbf{k}_{\text{pu}} + \mathbf{k}_{\text{pu}} + \mathbf{k}_{\text{pr}} \quad (3.27)$$

for a pump–probe signal detected along direction \mathbf{k}_S the sample interacts twice with the pump and once with the probe pulse. These experimental conditions result in the two combinations

$$\mathcal{T}^{(4)} : (\mathbf{e}_{\text{pr}} \otimes \mathbf{e}_{\text{pu}}^* \otimes \mathbf{e}_{\text{pu}}) \quad \text{and} \quad \mathcal{T}^{(4)} : (\mathbf{e}_{\text{pr}} \otimes \mathbf{e}_{\text{pu}} \otimes \mathbf{e}_{\text{pu}}^*), \quad (3.28)$$

respectively, one has to consider [25]. Like the filter conditions, mentioned above, the polarization sequence is an additional filter parameter, which allows to measure specific elements of the tensor $\mathcal{T}^{(4)}$.

For isotropic samples, like randomly oriented noninteracting molecules in solution, which are the focus of this thesis, the tensor $\mathcal{T}^{(4)}$ needs to be rotationally averaged according to (2.49). As in (3.26), the rotationally averaged tensor (denoted by the ring accent) interacts three times with the electric field of the laser pulses,

$$\overset{\circ}{\mathcal{T}}^{(4)} : (\mathbf{e}_3 \otimes \mathbf{e}_2 \otimes \mathbf{e}_1) = \mathcal{T}^{(3)} : (\mathbf{e}_3 \otimes \mathbf{e}_2) = \mathcal{T}^{(2)} \cdot \mathbf{e}_3 = \mathcal{T}^{(1)}. \quad (3.29)$$

The vanishing ring accent denotes that the contracted tensors are not isotropic since the electric-field polarization introduces a preferred direction. Each interaction such as in

$$\mathbf{T}^{(3)} = \overset{\circ}{\mathbf{T}}^{(4)} \cdot \mathbf{e} = \sum_D \overset{\circ}{T}_{ABCD}^{(4)} \cdot e_D \quad (3.30)$$

results in a tensor contraction and finally the remaining tensor of rank one, $\mathbf{T}^{(1)}$, carries the vector property of the third-order polarization $\mathbf{P}_\perp^{(3)}$.

A different interpretation of the interactions in (3.29) is as follows. The polarization of the electric field is used to select the combination of the tensor elements being measured. Therefore, the question arises which tensor elements are relevant for a magic-angle condition. Because the magic angle is applied to suppress orientation effects and retain only isotropic signals, one has to search for the isotropic part of $\mathbf{T}^{(2)}$, i.e., after two pump-pulse interactions. Again rotational averaging

$$\overset{\circ}{T}_{AB}^{(2)} = \sum_{ab} I_{AB:ab}^{(2)} T_{ab}^{(2)} \quad (3.31)$$

provides the answer. The tensor $\overset{\circ}{\mathbf{T}}^{(2)}$ contains the isotropic part of $\mathbf{T}^{(2)}$. Using the weighting factor (2.39) known from the literature [25, 42], rotational averaging results in a tensor

$$\overset{\circ}{\mathbf{T}}^{(2)} = \begin{pmatrix} d & 0 & 0 \\ 0 & d & 0 \\ 0 & 0 & d \end{pmatrix} \quad (3.32)$$

described by a diagonal matrix consisting of nine elements

$$d = \frac{1}{9} \left(t_{xxxx}^{(4)} + t_{xxyy}^{(4)} + t_{xxzz}^{(4)} + t_{yyxx}^{(4)} + t_{yyyy}^{(4)} + t_{yyzz}^{(4)} + t_{zzxx}^{(4)} + t_{zzyy}^{(4)} + t_{zzzz}^{(4)} \right) \quad (3.33)$$

that belong to the tensor $\mathbf{t}^{(4)}$ [see (2.51)] in the molecule-fixed frame. Therefore, to perform a third-order response experiment under magic-angle condition, one has to select electric field polarization vectors for which the measured signal contains only the mentioned nine tensor elements of $\mathbf{t}^{(4)}$.

Under ideal phase matching, the third-order polarization emits a signal field

$$\mathbf{E}_S \propto i\omega_S \mathbf{P}_\perp^{(3)}(t) \quad (3.34)$$

with the center frequency ω_S [compare (2.109)] that is in a transient absorption experiment self-heterodyne detected [24, 25],

$$I(t) \propto \text{Re} [\mathbf{E}_{\text{LO}}^*(t) \mathbf{E}_S(t)], \quad (3.35)$$

using the probe pulse as the local oscillator $\mathbf{E}_{\text{LO}}^*(t)$ [compare (2.110)]. Therefore the projections

$$\overset{\circ}{\mathbf{T}}^{(4)} \vdots \left(\mathbf{e}_{\text{pr}}^* \otimes \mathbf{e}_{\text{pr}} \otimes \mathbf{e}_{\text{pu}}^* \otimes \mathbf{e}_{\text{pu}} \right) \quad \text{and} \quad \overset{\circ}{\mathbf{T}}^{(4)} \vdots \left(\mathbf{e}_{\text{pr}}^* \otimes \mathbf{e}_{\text{pr}} \otimes \mathbf{e}_{\text{pu}} \otimes \mathbf{e}_{\text{pu}}^* \right) \quad (3.36)$$

of the emitted signal field onto the polarization \mathbf{e}_{pr}^* reach the detector.

In the final step, the definitions of the electric-field polarizations (3.2) and (3.4) are applied to solve the equation

$$\overset{\circ}{\mathbf{T}}^{(4)} \vdots \left(\mathbf{e}_{\text{pr}}^* \otimes \mathbf{e}_{\text{pr}} \otimes \mathbf{e}_{\text{pu}}^* \otimes \mathbf{e}_{\text{pu}} + \mathbf{e}_{\text{pr}}^* \otimes \mathbf{e}_{\text{pr}} \otimes \mathbf{e}_{\text{pu}} \otimes \mathbf{e}_{\text{pu}}^* \right) = 2d \quad (3.37)$$

with d given by (3.33) to find an experimental configuration fulfilling the magic-angle condition, i.e., a configuration for measuring only the isotropic signal d (3.33). This procedure is simplified by the following approach. First, the isotropic contribution from the general tensor $\overset{\circ}{\mathbf{T}}^{(4)}$ is removed by setting each individual tensor element in (3.33) equal to zero. Then, with the remaining tensor $\overset{\circ}{\mathbf{T}}_{\text{aniso}}^{(4)}$, the anisotropy signal results in

$$\begin{aligned} \overset{\circ}{\mathbf{T}}_{\text{aniso}}^{(4)} \vdots \left(\mathbf{e}_{\text{pr}}^* \otimes \mathbf{e}_{\text{pr}} \otimes \mathbf{e}_{\text{pu}}^* \otimes \mathbf{e}_{\text{pu}} + \mathbf{e}_{\text{pr}}^* \otimes \mathbf{e}_{\text{pr}} \otimes \mathbf{e}_{\text{pu}} \otimes \mathbf{e}_{\text{pu}}^* \right) = \\ \left\{ 2 \cos^2(\chi_{\text{pr}})[1 + 3 \cos(2\chi_{\text{pu}})] + [-1 + 3 \cos(2\beta) - 6 \cos^2(\beta) \cos(2\chi_{\text{pu}})] \sin(2\chi_{\text{pu}}) \right. \\ \left. + 6 \cos(\beta) \cos(\delta_{\text{pr}}) \cos(\delta_{\text{pu}}) \sin(2\chi_{\text{pr}}) \sin(2\chi_{\text{pu}}) \right\} \\ \times \left(t_{xyxy}^{(4)} + t_{xyyx}^{(4)} + t_{xzxz}^{(4)} + t_{xzzx}^{(4)} + t_{yxyx}^{(4)} + t_{yxyx}^{(4)} \right. \\ \left. + t_{yzyz}^{(4)} + t_{yzyz}^{(4)} + t_{zxxz}^{(4)} + t_{zxxz}^{(4)} + t_{zyyz}^{(4)} + t_{zyyz}^{(4)} \right). \quad (3.38) \end{aligned}$$

To measure under magic-angle conditions, the anisotropic signal contribution (3.38) has to vanish. This is achieved for each configuration that fulfills (3.25), i.e., the same condition is retrieved here as in the transition-probability approach. Apart from this confirmation of the transition-probability approach (Sec. 3.2), the response-theory approach can also be used to derive magic-angle conditions for geometries other than pump–probe spectroscopy (see, e.g., Sec. 3.5 for 2D spectroscopy).

3.4. Generalized magic-angle condition for transient absorption

As concluded in Sec. 3.2 and Sec. 3.3, an anisotropy-free pump–probe measurement requires an experimental configuration in which the pump polarization $(\chi_{\text{pu}}, \delta_{\text{pu}})$, the probe polarization $(\chi_{\text{pr}}, \delta_{\text{pr}})$ and the probe direction angle β fulfill the magic-angle condition (3.25). Interestingly, the phase differences δ_{pu} and δ_{pr} occur only in the last of the three terms of (3.25). Thus if one demands for this term

$$\cos(\beta) \cos(\delta_{\text{pr}}) \cos(\delta_{\text{pu}}) \sin(2\chi_{\text{pr}}) \sin(2\chi_{\text{pu}}) = 0, \quad (3.39)$$

the remaining magic-angle condition

$$\left\{ 2 \cos^2(\chi_{\text{pr}})[1 + 3 \cos(2\chi_{\text{pu}})] + [-1 + 3 \cos(2\beta) - 6 \cos^2(\beta) \cos(2\chi_{\text{pu}})] \sin^2(\chi_{\text{pr}}) \right\} = 0 \quad (3.40)$$

is valid for any phase difference δ_{pu} and δ_{pr} , i.e., it is valid for any ellipticity that can be achieved for a given angle χ_{pu} and χ_{pr} . However, these angles still have to fulfill (3.40).

(3.39) offers five possibilities for how any dependence of (3.25) onto the phase differences δ_{pu} and δ_{pr} can be eliminated.

Case 1: The amplitude ratio of the pump pulse χ_{pu} could be set to 0° such that $\sin(2\chi_{\text{pu}}) = 0$. This corresponds to selecting a linear pump polarization along the X axis and it is intuitively clear that the phase difference δ_{pu} is not relevant if the pump polarization consists only of an X component. The resulting rotation symmetry with respect to the X axis (see Fig. 3.4) cancels the β dependence and simplifies (3.40) to

$$\chi_{\text{pr}} = \arccos\left(\frac{1}{\sqrt{3}}\right) \approx 54.7^\circ. \quad (3.41)$$

For a linearly polarized probe pulse ($\delta_{\text{pr}} = 0^\circ$) this is the well-known magic-angle condition [19], but the condition is also valid for an elliptical polarized probe pulse with any phase difference δ_{pr} , because the δ_{pr} dependence vanishes from the general magic-angle condition (3.25) due to fulfillment of (3.39).

Case 2: To fulfill (3.39), the probe polarization is chosen to be parallel to the X axis, $\chi_{\text{pr}} = 0^\circ$, such that $\sin(2\chi_{\text{pr}}) = 0$. The β dependence vanishes due to rotation symmetry with respect to the X axis. Then the phase difference δ_{pr} is not relevant because the probe polarization consists only of an X component. (3.40) then simplifies to

$$\chi_{\text{pu}} = \arccos\left(\frac{1}{\sqrt{3}}\right) \approx 54.7^\circ. \quad (3.42)$$

Similar to the first case, for linearly polarized pump pulses, $\delta_{\text{pu}} = 0^\circ$, this is the well-known magic-angle condition and the general approach extends this condition to elliptically polarized pump pulses with any phase difference δ_{pu} .

Case 3: Now the pump polarization is chosen to be parallel to the Y axis, $\chi_{\text{pu}} = 90^\circ$, such that $\sin(2\chi_{\text{pu}}) = 0$. With only the Y polarization component, the phase difference δ_{pu} is again not relevant. In contrast to cases 1 and 2, the configuration shows no rotation symmetry around the X axis and β does not vanish, but is connected to χ_{pr} via the magic-angle condition

$$-1 - 3 \cos(2\chi_{\text{pr}}) + 6 \cos(2\beta) \sin^2(\chi_{\text{pr}}) = 0 \quad (3.43)$$

that remains from (3.40). This condition is again valid for elliptically polarized probe pulses with any phase difference δ_{pr} .

Case 4: A horizontal probe polarization located in the YZ plane is chosen, $\chi_{\text{pr}} = 90^\circ$, such that $\sin(2\chi_{\text{pr}}) = 0$. Without the vertical X part, the polarization does again not depend on the phase difference δ_{pr} . Similar to case 3, the rotation symmetry with respect to the X axis vanishes. Now the angle β is connected to χ_{pu} via the magic-angle condition

$$-1 + 3 \cos(2\beta) - 6 \cos^2(\beta) \cos(2\chi_{\text{pu}}) = 0 \quad (3.44)$$

remaining from (3.40), which is valid for an elliptically polarized pump pulse with any phase difference δ_{pu} .

Case 5: The last possibility to fulfill (3.39) for any δ_{pu} and δ_{pr} dependence is to set $\beta = 90^\circ$, such that $\cos(\beta) = 0$. Such a perpendicular configuration is not very practical

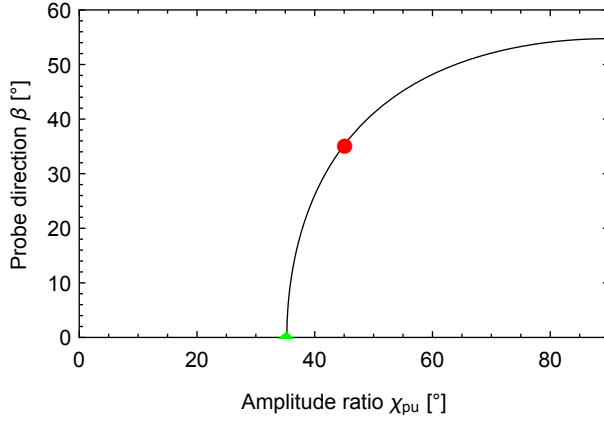


Figure 3.8.: Generalized magic-angle condition. The black curve represents the relationship (3.46) between the propagation angle β of the probe beam and the amplitude ratio χ_{pu} of the pump polarization vector for an arbitrarily polarized pump pulse and a probe pulse with a linear polarization vector in the YZ plane ($\chi_{\text{pr}} = 90^\circ$). Below $\chi_{\text{pu}} = 35.3^\circ$ no solution exists and therefore no magic-angle configuration can be found. The colored plot markers highlight three special cases: Circular (red \circ) pump polarization and linear pump polarization for collinear (green \diamond) and noncollinear (blue \square) propagation direction. [4, Fig. 8] © IOP Publishing. Reproduced with permission. All rights reserved

for the thin-film cuvettes used in most time-resolved liquid-phase measurements although it may be an option in the gas phase. The magic-angle condition (3.40) then simplifies to

$$-1 + 3 \cos(2\chi_{\text{pr}}) + 6 \cos^2(\chi_{\text{pr}}) \cos(2\chi_{\text{pu}}) = 0 \quad (3.45)$$

and is valid for elliptically polarized pump and probe pulses with any phase difference δ_{pu} and δ_{pr} , respectively.

In case 1 and case 2 discussed above, the polarizations of the pump and the probe pulses are given by the magic-angle conditions (3.41) and (3.42), respectively. It is possible to choose any phase difference δ_{pr} or δ_{pu} , respectively, but the amplitude-ratio angle is determined by the magic angle of $\arccos(1/\sqrt{3}) \approx 54.7^\circ$. To find a magic-angle configuration for an arbitrary pump or probe polarization, one of the options from cases 3-5 has to be applied. If one, e.g., wants to excite the system under study with an arbitrarily polarized pump pulse in the common nonperpendicular geometry, case 4 would lead to an anisotropy-free configuration. Solving (3.44) for β results in

$$\beta = \pm \arccos \frac{1}{\sqrt{3}|\sin(\chi_{\text{pu}})|} \quad (3.46)$$

and connects the amplitude ratio χ_{pu} of the pump pulse to the propagation angle β of the probe pulse. This relationship is depicted by the black curve in Fig. 3.8 and three special cases of (3.46) are shown as coloured plot markers.

Case 4a: For collinear pump and probe pulses propagating along the Z direction ($\beta = 90^\circ$) the amplitude ratio becomes $\chi_{\text{pu}} = 35.3^\circ$ (Fig. 3.8, green \diamond). Subtracting both

amplitude-ratio angles,

$$\chi_{\text{pr}} - \chi_{\text{pu}} = 90^\circ - 35.3^\circ = 54.7^\circ = \chi_{\text{MA}}, \quad (3.47)$$

reveals that the angle of 35.3° is the known magic angle, just measured with respect to the X axis instead of the Y axis. This is only valid for a collinear geometry ($\beta = 0^\circ$). For the commonly used noncollinear geometry ($\beta > 0^\circ$), it is necessary to adjust the angles β and χ_{pu} according to (3.46). If one chooses, for example, $\beta = 10^\circ$ as often employed in pump-probe experiments a corrected angle of $\chi_{\text{pu}} \approx 35.9^\circ$ is required. Thus, in contrast to (3.41) and (3.42) it is not sufficient to rotate the polarization of one of the pulses about 54.7° to achieve the magic-angle configuration if one starts with horizontally polarized pump and probe pulses ($\chi_{\text{pu}} = 90^\circ$ and $\chi_{\text{pr}} = 90^\circ$), because of the lacking rotation symmetry around the X axis.

Case 4b: In the second special limit of case 4, a linearly polarized pump pulse ($\delta_{\text{pu}} = 0$) whose polarization is contained in the YZ plane ($\chi_{\text{pu}} = 90^\circ$) results in an angle $\beta = 54.7^\circ$ (Fig. 3.8, blue \square).

Case 4c: Finally for a circularly polarized pump pulse ($\chi_{\text{pu}} = 45^\circ$, $\delta_{\text{pu}} = \pi/2$) one derives an angle of $\beta = 35.3^\circ = 90^\circ - \chi_{\text{MA}}$ (Fig. 3.8, red \circ) also found by Cho [82] for a transient circular dichroism experiment.

Below an amplitude ratio of $\chi_{\text{pu}} = 35.3^\circ = 90^\circ - \chi_{\text{MA}}$ no solution exists for the limitation of a probe pulse with a linear polarization vector ($\delta_{\text{pr}} = 0^\circ$) located in the YZ plane ($\chi_{\text{pr}} = 90^\circ$) and therefore no magic-angle configuration.

The result generalizes the known anisotropy-free condition of linearly and circularly polarized pulses (colored plot markers in Fig. 3.8) to elliptically polarized pulses (black line in Fig. 3.8).

By design, the signal fulfilling (3.39) does not depend on the phase difference δ_{pu} as resulting from the third-order interaction within the electric dipole approximation. This means that any remaining experimentally detected presence of a δ_{pu} -dependent signal indicates either higher-order interactions or violation of the electric dipole approximation. Thus, such an arrangement allows access exclusively to signals of fifth- or higher-order interaction or it can be used as a sensitive probe for nondipolar transitions like chiral signals that stem from the combined electric dipole, magnetic dipole and electric quadrupole interaction [25]. Applications of phase-cycling methods should be compatible with the generalized magic angle as well.

3.5. Magic-angle condition for 2D spectroscopy

Concerning the electric-field polarization, one advantage of 2D spectroscopy compared to transient absorption spectroscopy is the possibility to control the polarization state of up to four instead of two laser pulses. Therefore more polarization combinations are accessible to filter out the desired information from the measured signal as Hochstrasser [45] and Zanni and coworkers [98] demonstrated. They found polarization sequences that enhance weak cross peaks that would ordinarily be covered by dominating diagonal peaks. Several sample applications are available in the literature [99–107].

In the literature on 2D spectroscopy specific polarization sequences are often recorded and combined linearly to obtain derived quantities. However, for anisotropy-free dynamics, the magic-angle condition could also be employed [108], because the response-theory approach in Sec. 3.3 is not restricted to transient absorption spectroscopy. If one considers linear polarization and chooses for 2D spectroscopy in pump–probe geometry the first two pulses to be in parallel polarization, then the known angle of $(\mathbf{e}_1 \parallel \mathbf{e}_2) \angle \mathbf{e}_3 = 54.7^\circ$ between the first two and the third pulse fulfils the magic-angle condition. The same angle $(\mathbf{e}_1 \parallel \mathbf{e}_2) \angle (\mathbf{e}_3 \parallel \mathbf{e}_4) = 54.7^\circ$ is valid for 2D spectroscopy in phase-matched box geometry if the polarization vectors of the four pulses are selected to be pairwise parallel.

At least two ways exist to implement such a configuration. On the one hand, the \mathbf{k} vectors of the four laser beams may enclose small angles with respect to each other and enter the sample approximately collinearly. Thus, the influence of the propagation vectors onto the polarization vectors may be neglected and in this near-collinear geometry, the polarization vectors $\mathbf{e}_3 \parallel \mathbf{e}_4$ are rotated by 54.7° with respect to $\mathbf{e}_1 \parallel \mathbf{e}_2$. On the other hand, when the four beams enclose a larger mutual angle and the near-collinear approximation is not valid, the propagation vectors of the first two pulses \mathbf{k}_1 and \mathbf{k}_2 can be considered to define a plane, and the corresponding polarization vectors \mathbf{e}_1 and \mathbf{e}_2 can be chosen to be perpendicular with respect to that plane. Likewise, the last two pulses \mathbf{k}_3 and \mathbf{k}_4 can be considered to define a plane with \mathbf{e}_3 and \mathbf{e}_4 being perpendicular to that plane. To fulfill the magic-angle condition, it is then necessary to choose propagation vectors for which both planes enclose the magic angle of 54.7° . This geometry thus works for larger inter-beam angles.

3.6. Anisotropy

The magic-angle conditions discussed so far allow to exclusively measure population changes, because the anisotropy signal is suppressed. In contrast to that, one can also use a particular polarization configuration of the experimental setup to measure specifically the anisotropy signal. Two measurements are required, one with mutually parallel pump and probe polarizations (ΔA_{\parallel}), i.e., $\chi = 0^\circ$, and one with mutually perpendicular polarizations (ΔA_{\perp}), i.e. $\chi = 90^\circ$. Again it is necessary to choose one of the polarizations parallel to the X axis to maintain the parallel configuration for any angle β . The anisotropy defined as

$$r = \frac{\Delta A_{\parallel} - \Delta A_{\perp}}{\Delta A_{\parallel} + 2\Delta A_{\perp}} \quad (3.48)$$

allows determining the angle between the participating pump and probe TDMs if their degeneracy is known. For example, if the pumped and probed TDMs μ_{pu} and μ_{pr} , respectively, are non-degenerate, one can determine from r the angle

$$\alpha = \arccos \frac{\sqrt{1+5r}}{\sqrt{3}} \quad (3.49)$$

that they enclose [71]. However, overlapping and/or degenerate bands might impede such a straightforward analysis; only for special cases of degenerate TDMs an equivalent

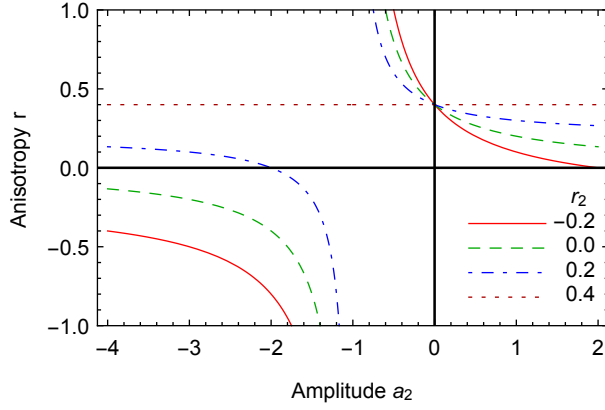


Figure 3.9.: Diverging anisotropy. The plotted curves $r(a_2) = a_1 r_1 / (a_1 + a_2) + a_2 r_2 / (a_1 + a_2)$ of the overlapping signals a_1 and a_2 exemplify the effect of overlapping anisotropy signals. The amplitude $a_1 = 1$ and the anisotropy $r_1 = 0.4$ of one signal are fixed, whereas a_2 and r_2 of the other signal vary. [4, Fig. 9] © IOP Publishing. Reproduced with permission. All rights reserved

relation can be given [68, 77, 109].

3.6.1. Single signal contribution

Like for deriving the magic-angle conditions, one can apply the general model from Sec. 3.2 to connect the measured anisotropy to informations about the molecular structure, i.e., the angle α between the pump and probe TDMS. Using the anisotropy definition (3.48) for measured absorbance changes (3.1) and the probability P_j (3.20) one can calculate the anisotropy according to

$$r_j(\alpha) = \frac{P_j(\alpha, 0, 0, 0, 0, \beta) - P_j(\alpha, 0, 0, 90^\circ, 0, \beta)}{P_j(\alpha, 0, 0, 0, 0, \beta) + 2P_j(\alpha, 0, 0, 90^\circ, 0, \beta)} = \frac{1}{10}[1 + 3 \cos(2\alpha)], \quad (3.50)$$

which is in agreement with the literature result for linearly polarized pulses [110]. According to (3.50), the valid range for the anisotropy is $-0.2 \leq r_j \leq 0.4$. As the system evolves with the time delay Δt , the structural information α and its dynamic behavior is masked by rotational diffusion, which results finally in randomly oriented molecules. Therefore, the anisotropy decays to zero.

3.6.2. Overlapping signal contributions

If the signals of multiple combinations of pump and probe TDMS overlap, the measurable anisotropy

$$r = \frac{\sum_j \Delta A_{\parallel,j} - \sum_j \Delta A_{\perp,j}}{\sum_j \Delta A_{\parallel,j} + 2 \sum_j \Delta A_{\perp,j}} \quad (3.51)$$

depends on all signal contributions. With the relation [19]

$$\Delta A_{\text{MA},j} = \frac{\Delta A_{\parallel,j} + 2\Delta A_{\perp,j}}{3} \quad (3.52)$$

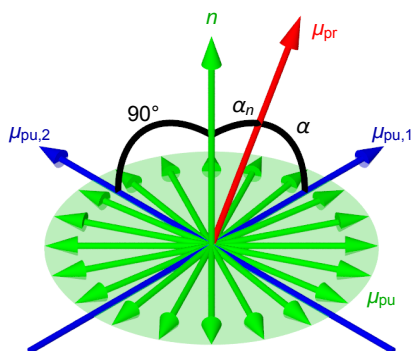


Figure 3.10.: Degenerate TDM. In a molecule with a two-fold degenerate pump TDM μ_{pu} , each orientation (green arrows in the disk) contributes to the measured signal. One can describe all possibilities with two basis vectors ($\mu_{pu,1}, \mu_{pu,2}$) and one basis vector can always include an angle of 90° with the corresponding probe TDM μ_{pr} . The other basis vector encloses the angle α and the surface normal \mathbf{n} the angle α_n with the probe TDM. [4, Fig. 10] © IOP Publishing. Reproduced with permission. All rights reserved

for absorbance changes detected in magic-angle configuration, it is possible to rewrite (3.51) to obtain

$$r = \frac{\sum_j r_j \Delta A_{MA,j}}{\sum_j \Delta A_{MA,j}}, \quad (3.53)$$

and thus the anisotropy is the average over the anisotropies r_j of each single signal contribution with the corresponding magic-angle signal $\Delta A_{MA,j}$ as a weighting factor. Therefore, the averaged anisotropy $-\infty < r < \infty$ clearly deviates from the range $-0.2 \leq r_j \leq 0.4$ of a single signal contribution, e.g., if the magic-angle signals $\Delta A_{MA,j}$ have differing signs. In Fig. 3.9 this behaviour of the anisotropy

$$r(a_2) = \frac{a_1 r_1}{a_1 + a_2} + \frac{a_2 r_2}{a_1 + a_2} \quad (3.54)$$

is visualized for two overlapping signals $a_1 = 1$ and a_2 with anisotropies of $r_1 = 0.4$ and r_2 . Both, changes in the signal amplitude a_2 and changes in the anisotropy r_2 influence the measured anisotropy r . At $a_2 = -a_1$, (3.54) has a pole and the anisotropy r diverges. Experimental anisotropy data which actually diverge because of overlapping signal contributions can be found in the literature [111–113].

3.6.3. Degenerate transition dipole moments

An example for overlapping anisotropy contributions are molecules with degenerate TDMs. In such a system [68, 77, 109], the orientation of the TDM is not defined by a single vector. Instead it is possible to draw a three-dimensional surface shaped depending on the degeneracy and every vector pointing to any point of this surface represents a valid orientation of the degenerate TDM. A set of suitable basis vectors can be used to describe all these directions. Such degenerate TDMs occur typically in highly symmetric molecules such as porphyrin or benzene. These molecules have a two-fold degeneracy composed of two perpendicular basis vectors, which form a disk as depicted in Fig. 3.10. Assuming that the pump TDM is degenerate, one can always choose one of the two basis vectors to enclose an angle of 90° with the probe TDM. The other basis vector encloses

in general an arbitrary angle α with the probe TDM. According to (3.50) and (3.53) one can calculate the anisotropy

$$r(\alpha) = \frac{1}{2}r_1(90^\circ) + \frac{1}{2}r_2(\alpha) = \frac{1}{20}[3 \cos(2\alpha) - 1] \quad (3.55)$$

as the average over both signal contributions [109]. The weighting factor of 1/2 is the same for both pump TDMs because both are pumped with the same probability and both signals have the same sign. It is also possible to express the anisotropy

$$r(\alpha_n) = \frac{1}{20}\{3 \cos[2(90^\circ - \alpha_n)] - 1\} = -\frac{1}{20}[3 \cos(2\alpha_n) + 1] \quad (3.56)$$

dependent on the angle $\alpha_n = 90^\circ - \alpha$ between the normal of the disk-shaped surface in Fig. 3.10 and the probe TDM. The result (3.56), derived with the general approach, is in agreement with the literature [68, 77, 109].

4. Variable projection algorithm

A valuable tool utilizing the VPA (Sec. 2.4) for data analysis is the open-source TIMP [58], which can be operated via the graphical user interface Glotaran [15]. However, until recently [17], this software package did not allow for fitting the pronounced vibrational oscillations of the trihalide molecules according to eq. (4.1). Therefore, a custom version of the partitioned VPA, capable to process the complex-valued, linear oscillation-associated difference spectra (OADS) fit parameters from eq. (4.2), was implemented in Mathematica [18] on top of the built-in Levenberg–Marquardt algorithm by following a recent Matlab implementation [57] and the R package TIMP [58]. Furthermore, this new implementation allows to use the sophisticated computer-algebra tools of Mathematica to flexibly design new customized model functions. Another advantage of the computer-algebra tools is that Mathematica can automatically calculate the model function’s partial derivatives and thus construct the exact Jacobian matrix instead of approximating it with the finite-difference method.

4.1. Modelling vibrational wavepacket oscillations

For taking the vibrational WP signals (Sec. 2.2.2) in Fig. 2.1 into account, each of the m vibrational modes

$$\begin{aligned} \Delta A_{\text{osc}}(\lambda, T) &= \sum_{j=0}^{m-1} 2A_j(\lambda) \cos[\omega_j T + \phi_j(\lambda)] e^{-\delta_j T} \\ &= \sum_{j=0}^{m-1} [\text{OADS}_j(\lambda) e^{i\omega_j T - \delta_j T} + \text{OADS}_j^*(\lambda) e^{-i\omega_j T - \delta_j T}] \end{aligned} \quad (4.1)$$

is modelled as a component with a spectrum $A_j(\lambda)$ and a concentration profile, which oscillates with angular frequency ω_j and decays with a damping factor δ_j . In general, this temporal oscillation is accompanied by a spectral oscillation, which is considered by the wavelength-dependent phase $\phi_j(\lambda)$. By switching to the exponential representation of the cosine, the non-linear fit parameter $\phi_j(\lambda)$ is combined with $A_j(\lambda)$ and therefore transformed into a single, complex linear fit parameter: the OADS

$$\text{OADS}_j(\lambda) = A_j(\lambda) e^{i\phi_j(\lambda)}, \quad (4.2)$$

which matches ideally the concept of the VPA, but requires an algorithm designed for complex numbers [114]. To have a fit algorithm fulfilling all the above-mentioned requirements and to be as flexible as possible in extending the fit function, a custom version

of the complex partitioned VPA was implemented in Mathematica [18], as described in the next Sec. 4.2. Analogous to this implementation, global fitting of kinetic and oscillating signals was also developed independently and simultaneously by van Stokkum and coworkers [17], who use the sum of a sine and cosine function instead of the exponential cosine representation.

In addition to the molecular kinetics and oscillations, the coherent artefact (CA)

$$CA(\lambda, T) = \sum_{j=0}^2 CAADS_j(\lambda) \frac{\partial^j}{\partial T^j} IRF(\lambda, T) \quad (4.3)$$

is modelled by multiplying the CA-associated difference spectra (CAADS) $CAADS_j(\lambda)$ with the instrumental response function (IRF)

$$IRF(\lambda, T) = \frac{1}{\sqrt{2\pi}} \frac{2\sqrt{2 \ln 2}}{\Delta T(\lambda)} e^{-4 \ln(2) [T - t_0(\lambda)]^2 / \Delta T(\lambda)^2} \quad (4.4)$$

and its first and second derivative. The Gaussian shape is based on the assumption that the IRF stems from the convolution of Gaussian-shaped pump and probe pulses. If the chirp is corrected as described in Fig. 2.1b, the wavelength dependence of time zero $t_0(\lambda)$ can be removed. Additionally, the minor wavelength dependence of the full width at half maximum (FWHM) $\Delta T(\lambda)$ can often be neglected.

Since a second Gaussian-shaped peak occurs in Fig. 2.1b right after the CA due to a WP on the excited I_3^- PES (Sec. 2.2.2), the flexibility of the custom VPA implementation (Sec. 4) is exploited to add another model function, which describes this WP

$$WP(\lambda, T) = WPADS_j(\lambda) e^{-4 \ln(2) [T - t_{WP,0}(\lambda)]^2 / \Delta t_{WP}(\lambda)^2} \quad (4.5)$$

with the WP-associated difference spectra $WPADS_j(\lambda)$ and a Gaussian function similar to the CA model. Despite the small wavelength-dependent shift $t_{WP,0}(\lambda)$ visible in the dataset, the WP was sufficiently approximated by neglecting the wavelength dependence for $t_{WP,0}(\lambda)$ and $\Delta t_{WP}(\lambda)$. Analogous to modelling this Gaussian-shaped WP, it is possible with the mentioned VPA implementation to consider other signals that deviate from the extended model consisting of kinetics, oscillations and CA.

Finally, all parts are combined to the overall model function

$$\Delta A_{\text{model}}(\lambda, T) = CA(\lambda, T) + \{[\Delta A_{\text{kin}}(\lambda) + \Delta A_{\text{osc}}(\lambda) + WP(\lambda)] * IRF\}(T) \quad (4.6)$$

in which the kinetic model (2.118), the oscillation model and the WP model are convolved * with the IRF to consider the limited temporal resolution of the experimental setup.

4.2. Mathematica implementation

The Mathematica VPA implementation developed in this thesis is based on Mathematica's built-in function minimizer

```
{fmin, amin} = FindMinimum[f @@ asym, ainit];,
```

which can be used to numerically iterate the fit parameters

```
 $\alpha_{\text{sym}} = \{\alpha_1, \alpha_2, \dots\};$ 
```

of the variable projection norm f @@ α_{sym} (2.128) until a local minimum f_{min} at

```
 $\alpha_{\text{min}} = \{\alpha_1 \rightarrow \alpha_{1,\text{min}}, \alpha_2 \rightarrow \alpha_{2,\text{min}}, \dots\};$ 
```

is found in the region around the initialization point

```
 $\alpha_{\text{init}} = \{\{\alpha_1, \alpha_{1,0}\}, \{\alpha_2, \alpha_{2,0}\}, \dots\};$ 
```

Selecting the Levenberg–Marquardt algorithm

```
1 {fmin,  $\alpha_{\text{min}}$ } = FindMinimum[Null,  $\alpha_{\text{init}}$ ,
2   Method -> {
3     "LevenbergMarquardt",
4     "Residual" -> rfunc @@  $\alpha_{\text{sym}}$ ,
5     "Jacobian" -> jfunc @@  $\alpha_{\text{sym}}$  (*or "FiniteDifference"*)
6   }
7   ];
```

allows to directly use the residual function $rfunc$ @@ α_{sym} (2.129) and the Jacobian matrix $jfunc$ @@ α_{sym} (2.148) of the variable projection norm f @@ α_{sym} , which therefore can be neglected by passing `Null` to `FindMinimum[...]`. Furthermore, one can easily switch between the exact Jacobian and its finite difference approximation by replacing $jfunc$ @@ α_{sym} with the `"FiniteDifference"` option and vice versa. This approximation is a quite useful backup strategy if, for some reason, the calculation of the exact Jacobian fails. In addition, the finite-difference method allows a step-by-step development of the VPA, because, first, one can focus on the implementation of the residual function

```
1 rfunc[ $\alpha$ ?NumericQ] := Module[
2   { $\phi$ ,  $\phi_{\text{pinv}}$ , c},
3    $\phi$  = Compile[{{xvec, _Real, 1}},
4     Evaluate[ $\phi_{\text{vec}}$  /. Thread[xsym -> (Indexed[xvec, #] & /@ Range@Length@xsym)]],
5     Parallelization -> True,
6     RuntimeAttributes -> {Listable},
7     RuntimeOptions -> "Speed"] @ x;
8    $\phi_{\text{pinv}}$  = PseudoInverse@ $\phi$ ;
9   c =  $\phi_{\text{pinv}}$ .y;
10  Re[y -  $\phi$ .c]
11  ];
```

without worrying about the Jacobian. For each iteration step i of the Levenberg–Marquardt algorithm (2.146) or (2.147), `FindMinimum[...]` calls the residual function with the current numeric fit parameters

```
 $\alpha = \{\alpha_{1,i}, \alpha_{2,i}, \dots\};$ 
```

which are automatically inserted into each model function (2.119)

```
 $\phi_{\text{vec}} = \{\phi_1$  @@ xsym,  $\phi_2$  @@ xsym, ...};,
```

leaving only the functions' dependency on the coordinates

```
xsym = {x1, x2, ...};.
```

Note that in contrast to the simplified one-dimensional case `xsym = {t}` of eq. (2.119), the fit functions might be multi-dimensional, e.g., `xsym = {λ, t}` in the case of a spectrotemporal model (see Sec. 2.3) or an uncorrected chirp in eq. (4.4). To receive the model matrix ϕ (2.126), each function in `φvec` needs to be evaluated at all measured coordinate tuples

```
x = {{x1,1, x2,1, ...}, {x1,1, x2,2, ...}, ...,
      {x1,2, x2,1, ...}, {x1,2, x2,2, ...}, ...};,
```

e.g., `x = Tuples[{{λ1, λ2, ...}, {t1, t2, ...}}]` in the aforementioned (λ, t) -dependent case. To speed up this bottleneck, the model functions are compiled via the function `Compile[... φvec ...] @ x` before they are applied to `x`. For this purpose, the custom coordinate names, e.g., `xsym = {λ, t}`, need to be replaced by the vector

```
xvec = {xvec1, xvec2, ...};.
```

With Mathematica's built-in, SVD-based pseudoinverse function `PseudoInverse[...]` the remaining calculations become straightforward following eq. (2.129), except for taking the real part `Re[...]`, which is required to ensure that the fit model `φ.c` always has a real-valued output but can consist of complex-valued fit parameters, e.g., the OADS (4.2).

If the non-linear fit functions `φvec` depend on less coordinates than the linear fit parameters `c`, it would be a waste of computation time to re-evaluate `φvec` for every coordinate tuple. For example, this is the case in the model introduced in Sec. 4.1: When the chirp in eq. (4.4) is corrected, `φvec` depends only on `t` but not on `λ` and one should evaluate `φvec` once for the `t`-coordinates and reuse the result for every `λ`-coordinate. The residual function `rfunc` already provides this feature, all one has to do is to use a one-dimensional coordinate set `xsym = {t}` with `x = {t1, t2, ...}` and replace the before vectorized measurement data

```
y = {y[λ1, t1], y[λ1, t2], ..., y[λ2, t1], y[λ2, t2], ...};
```

with its actual two-dimensional form

```
y = {{y[λ1, t1], y[λ2, t1], ...},
      {y[λ1, t2], y[λ2, t2], ...},
      ...};.
```

Since, `FindMinimum[...]` expects a residual vector, one has to check for this optimized fitting procedure

```
1  rfunc[α_?NumericQ] := Module[
2      {φ, φpinv, c, r},
3      φ = Compile[{{xvec, _Real, 1}},
4          Evaluate[φvec /. Thread[xsym -> (Indexed[xvec, #] & /@ Range@Length@xsym)]],
5          Parallelization -> True,
6          RuntimeAttributes -> {Listable},
7          RuntimeOptions -> "Speed"] @ x;
8      φpinv = PseudoInverse@φ;
9      c = φpinv.y;
10     r = Re[y - φ.c];
11     If[VectorQ@y, r, Join @@ Transpose@r]
12 ];
```

and vectorize the then two-dimensional array of residuals r by `Join @@ Transpose@r`.

Even if the latter optimization cannot be applied, it is possible to further improve the calculation of the residuals

```

1  rfunc[α_?NumericQ] := Module[
2    {x, φ, φpinv, c, r},
3    x = If[xpar === None || Depth[y] > 3,
4      Flatten /@ Tuples[xvar, 1],
5      Flatten /@ Tuples[{xpar, xvar}]];
6    φ = Compile[{{xvec, _Real, 1}},
7      Evaluate[φvec /. Thread[xsym -> (Indexed[xvec, #] & /@ Range@Length@xsym)],
8      Parallelization -> True,
9      RuntimeAttributes -> {Listable},
10     RuntimeOptions -> "Speed"]@x;
11    φ = If[xpar === None || Depth[y] > 3, {φ}, Partition[φ, Length@xvar]];
12    φpinv = PseudoInverse /@ φ;
13    Join @@ MapThread[(
14      φ = #1; φpinv = #2; y = #3;
15      c = φpinv.y;
16      r = Re[y - φ.c];
17      If[VectorQ[#3, r, Join @@ Transpose@r]) &,
18      {φ, φpinv, y}]
19  ];

```

for multidimensional datasets, for which the evaluation of the model functions ϕ_{vec} at each coordinate tuple, e.g., $\{\lambda_i, t_j\}$, is not only time consuming, but leads also to huge ϕ -matrices, for which the calculation of the pseudoinverse requires a lot of memory and long computation times. To circumvent the latter issue, one splits the coordinate tuples into two groups $xpar$ and $xvar$ and partitions $\phi = \text{Partition}[\phi, \text{Length}@xvar]$ the ϕ -matrix in such a way that one receives for each coordinate tuple in $xpar$ a separate matrix in $\phi = \{\phi_1, \phi_2, \dots\}$. For example, a transient absorption spectrum can be partitioned into the transients

$$y = \{\{y[\lambda_1, t_1], y[\lambda_1, t_2], \dots\}, \{y[\lambda_2, t_1], y[\lambda_2, t_2], \dots\}, \dots\};$$

with $xvar = \{t_1, t_2, \dots\}$ for each wavelength $xpar = \{\lambda_1, \lambda_2, \dots\}$, to which therefore an individual matrix ϕ_i is assigned. Then, the pseudoinverse function $\phi_{pinv} = \text{PseudoInverse} /@ \phi$ is applied separately on each ϕ_i via the map operator `/@` and the individual residuals r are calculated with the help of `MapThread[...]`. This third and final version of the residual function `rfunc` can also be applied to the first two scenarios, whose above defined datasets require now an additional surrounding curly bracket, e.g.,

$$y = \{\{y[\lambda_1, t_1], y[\lambda_1, t_2], \dots, y[\lambda_2, t_1], y[\lambda_2, t_2], \dots\}\};$$

and

$$y = \{\{\{y[\lambda_1, t_1], y[\lambda_2, t_1], \dots\}, \{y[\lambda_1, t_2], y[\lambda_2, t_2], \dots\}, \dots\}\};$$

to inform `rfunc` that only one partition needs to be evaluated. In addition, the partition coordinates $xpar = \text{None}$ need to be `None` for the first case.

Based on the residual function `rfunc`, one can develop the Jacobian function

```

1  jfunc[α_?NumericQ] := Module[
2      {x, d, φ, φpinv, c, atr, btr, jtr},
3      x = If[xpar === None || Depth[y] > 3,
4          Flatten /@ Tuples[xvar, 1],
5          Flatten /@ Tuples[{xpar, xvar}]];
6      d = Compile[{{xvec, _Real, 1}},
7          Evaluate[# /. Thread[xsym -> (Indexed[xvec, #] & /@ Range@Length@xsym)],
8          Parallelization -> True,
9          RuntimeAttributes -> {Listable},
10         RuntimeOptions -> "Speed"]@x & /@ dφset;
11     φ = Compile[{{xvec, _Real, 1}},
12         Evaluate[φvec /. Thread[xsym -> (Indexed[xvec, #] & /@ Range@Length@xsym)],
13         Parallelization -> True,
14         RuntimeAttributes -> {Listable},
15         RuntimeOptions -> "Speed"]@x;
16     d = If[xpar === None || Depth[y] > 3, {d}, Transpose[#, {1, 3, 2, 4}]& @
↪ Partition[Transpose[d, {2, 1, 3}], Length@xvar]];
17     φ = If[xpar === None || Depth[y] > 3, {φ}, Partition[φ, Length@xvar]];
18     φpinv = PseudoInverse /@ φ;
19     Join @@ MapThread[(
20         φ = #1; φpinv = #2; y = #3; d = #4;
21         c = φpinv.y;
22         atr = #.c - φ.(φpinv.(#.c)) & /@ d;
23         btr = φpinv†.(#†.y) - φpinv†.(#†.(φ.c)) & /@ d;
24         jtr = Re[-atr - btr];
25         If[VectorQ@y, Transpose[jtr], Join @@ (Transpose[jtr, {3, 2, 1}])] &,
26         {φ, φpinv, y, d}]
27 ];

```

according to eq. (2.148). The calculation of x , ϕ and ϕpinv remains exactly the same, but, in addition, the model functions' derivatives

```
dφset = Transpose[D[φvec, {αsym}]];
```

need to be evaluated at every coordinate tuple to receive the derivative matrix d (2.149) in analogy to the calculation of ϕ . Note that Mathematica's built-in function `D[...]` allows for an automatic derivation of the model functions ϕvec with respect to the non-linear fit parameters αsym . Finally, the (transposed) Jacobian $j\text{tr}$ is computed via the (transposed) auxiliary matrices $a\text{tr}$ and $b\text{tr}$ as defined in eq. (2.148).

The complete source code of the implemented `parVarPro.nb` package can be found in Sec. A.2. It combines the above-explained core functions into one fit function `parVarPro[...]`, which also allows to compute multiple datasets simultaneously. Also, the number of iteration steps, the number of residual and Jacobian function calls and the overall required computation time is provided. Furthermore, the sum squared residual (SSR), the weighted residual mean square σ , the corrected total sum of squares (CTSS) and the square of the multiple correlation coefficient R^2 are computed according to Ref. [57]. To allow for a comfortable access to this multitude of information, `parVarPro[...]` returns the custom data format `fittedModel[...]`. However, features like weighting of data points, constraining fit parameters and calculating error bars for the fit parameters are not available yet and require further development work.

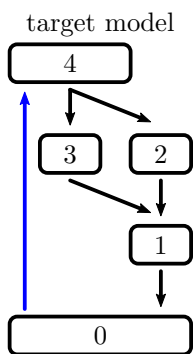


Figure 4.1.: Glotaran demo target model. The pump pulse populates state four (blue arrow), whose decay (black arrows) branches into state three and two, which decay into state one, which in turn decays into the ground state zero.

4.3. Examples

To prove the afore-mentioned features of the Mathematica VPA implementation and to demonstrate its handling, the fit function `parVarPro[...]` is first applied to Glotaran's demo dataset. Then, the capability to fit spectro-temporal oscillations is shown with a second, specifically tailored test dataset.

Following Glotaran's demo project, the temporal concentration profiles

```

1  cModel[t_] = {c4[t], c3[t], c2[t], c1[t]} /. Flatten@DSolve[
2    {c4[0] == 1, c4'[t] == -k4 c4[t],
3    c3[0] == 0, c3'[t] == -k3 c3[t] + phi43 k4 c4[t],
4    c2[0] == 0, c2'[t] == -k2 c2[t] + phi42 k4 c4[t],
5    c1[0] == 0, c1'[t] == -k1 c1[t] + k2 c2[t] + k3 c3[t],
6    c0[0] == 1, c0'[t] == +k1 c1[t]},
7    {c4[t], c3[t], c2[t], c1[t], c0[t]}, t] /.
8    {k4 -> 9.49943878184853, phi43 -> 0.087, phi42 -> 0.913};
  
```

are modelled (compare Fig. 2.4) in such a way that, as depicted in Fig. 4.1, the concentration (population) decay $c_4[t]$ of the initially pump-populated state four branches into state three $c_3[t]$ and two $c_2[t]$, which both decay into state one $c_1[t]$, which in turn decays into the ground state $c_0[t]$. Here, one can already see a great advantage of using Mathematica: It allows the user to directly write the target model in form of a set of DE for the temporal concentration derivatives $c_i'[t]$ (compare with Fig. 2.4) and automatically calculates the corresponding model functions via `DSolve[...]`. Note that in this example the value of the decay rate k_4 and the branching ratio $\phi_{43} = 1 - \phi_{42}$ are fixed. Furthermore, note that one can chose arbitrary initial concentration amplitudes $c_4[0] == 1$ and $c_0[0] == 1$, because the fit algorithm compensates them by scaling the corresponding DADS, EADS or SADS.

The limited temporal resolution of the experimental setup is considered by convolving [compare eq. (4.6)]

```

1  fitModel = Flatten@{
2    Convolve[cModel[t] UnitStep[t], irfModel[t], t, t],
3    irfModel[t]} /. t0 -> t0Model;
  
```

the instantly occurring kinetic signal (`cModel[t] UnitStep[t]`) with a Δt -broad, Gaussian-shaped IRF [compare eq. (4.4)]

```

irfModel[t_] = 2. Sqrt[Log[2.]/pi]/Delta Exp[-4. Log[2.] (t - t0)^2/Delta^2];,
  
```

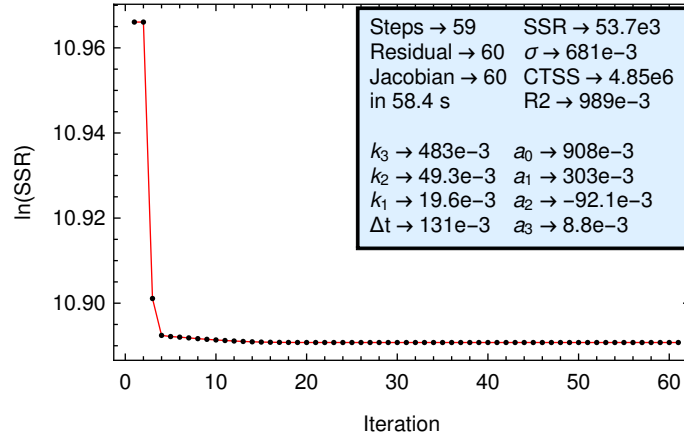


Figure 4.2.: Summary of the fit result. The SSR converged within 59 iteration steps requiring 60 residual function calls and 60 Jacobian function calls, which altogether took ≈ 60.0 s. The finally achieved fit quality is described by the SSR, the weighted residual mean square σ , the CTSS and the square of the multiple correlation coefficient R^2 , while all remaining parameters represents the resulting nonlinear fit parameters.

which is also used to describe the CA around time zero t_0 [compare eq. (4.3) without the derivatives]. To take care of the chirp, t_0 is replaced with the wavelength-dependent polynomial function

$$t0Model = a_0 + a_1(\lambda - \lambda_c)/100. + a_2((\lambda - \lambda_c)/100.)^2 + a_3((\lambda - \lambda_c)/100.)^3 / .\lambda_c \rightarrow 550;$$

having the center wavelength $\lambda_c \rightarrow 550$.

The complete model function `fitModel`, its variables $\{\lambda, t\}$ and initial fit parameters $\{k_3, 0.35\}, \{k_2, 0.04\}, \dots\}$ are passed to the fit function

```
1  vpm = parVarPro[
2      {{wavelength, time, transient, {\lambda, t}, fitModel}},
3      {{k3, 0.35}, {k2, 0.04}, {k1, 0.02},
4      {\Delta t, 0.06}, {a0, 0.91}, {a1, 0.31}, {a2, -0.10}, {a3, 0.01}}]
```

together with the wavelength axis

$$wavelength = \{\lambda_1, \lambda_2, \dots\};,$$

the time axis

$$time = \{t_1, t_2, \dots\};$$

and the dataset in form of a list of transients

$$transient = \{ \{y[\lambda_1, t_1], y[\lambda_1, t_2], \dots\}, \\ \{y[\lambda_2, t_1], y[\lambda_2, t_2], \dots\}, \\ \dots \};.$$

As result `parVarPro[...]` returns a `vpm = fittedModel[...]` object, which is visually summarized as shown in Fig. 4.2. The graph illustrates how the natural logarithm of the SSR converges, while the blue info tells that the convergence criterion was reached after

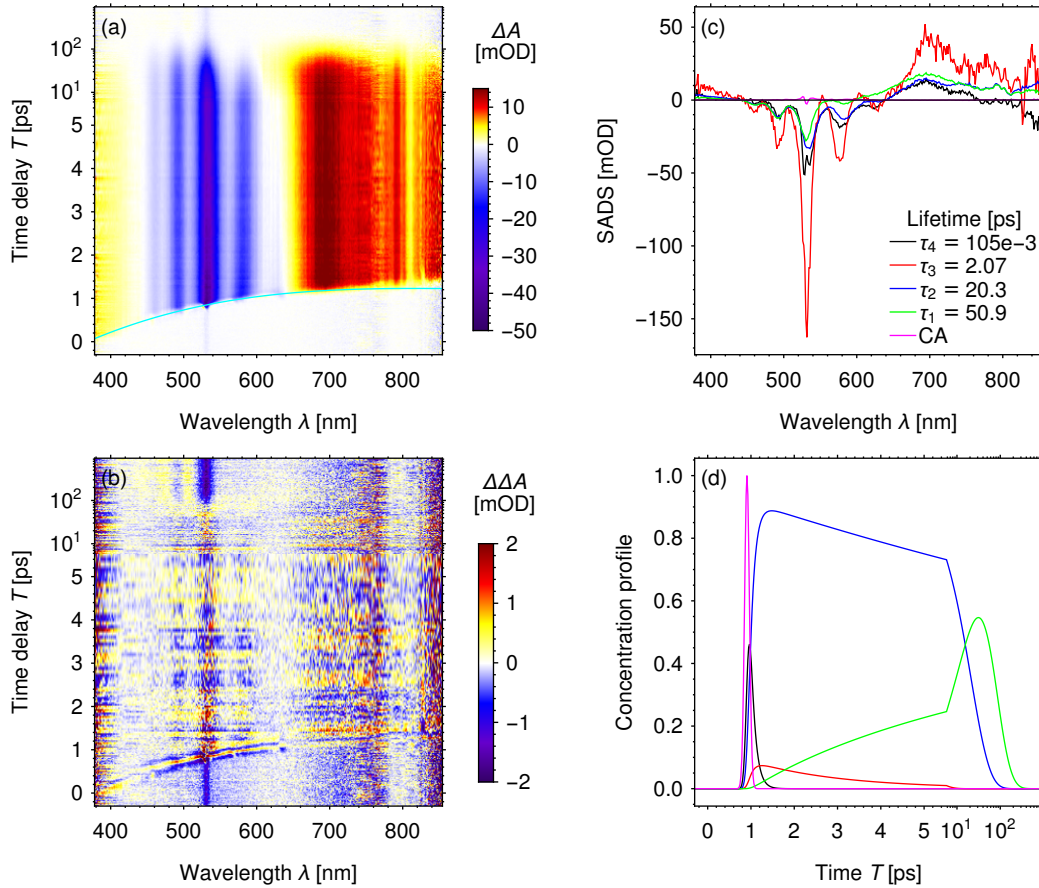


Figure 4.3.: Details of the fit result. For a given dataset (a), the fit algorithm identifies the chimp curvature (cyan curve) and splits the measured transient absorption spectrum into the fit residuals (b) and a model spectrum, which is defined by the SADS (c) and the temporal concentration profiles (d).

59 steps with 60 residual and Jacobian function calls, for which a Win7-operated Intel Core i7-4790 CPU with 3.6 GHz and 16 GB of RAM required ≈ 60.0 s (≈ 1 s/step). In addition, the box informs about the optimized nonlinear fit parameters as well as the SSR, the weighted residual mean square σ , the CTSS and the square of the multiple correlation coefficient R^2 that were achieved with the last iteration step according to Ref. [57]. Beyond this summary, one can access every information inside the `fittedModel[...]` object by using one of the following key words:

```
vpm[#]& /@ {"Data", "DataSets", "FitResiduals", "Function", "LinearParameters",
  ↪ "NonlinearParameters", "Monitor", "Statistic"};
```

This allows to inspect all details, as shown in Fig. 4.3, where (a) depicts the original dataset plus the fitted chimp, (b) the fit residuals, (c) the linear fit parameters, i.e., the SADS, and (d) the corresponding temporal concentrations profiles.

For comparison, Fig. 4.4 shows the fit result of Glotaran, which found after 54 steps



Figure 4.4.: Details of Glotaran's fit result. Within the fit error, the SADS (c) and the concentration profiles (d) equal those of the Mathematica result in Fig. 4.3.

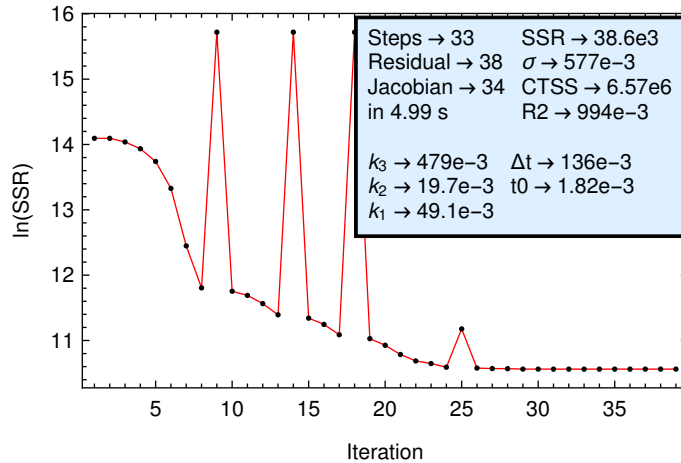


Figure 4.5.: Summary of the chirp-corrected fit. The fit parameters equal the result of the uncorrected fit from Fig. 4.2, but were achieved within only ≈ 5 s.

taking ≈ 145 s (≈ 2.7 s/step on the same computer) the same nonlinear fit parameters within the fit error (bracketed values in the upper-right parameter table of Fig. 4.4). The Mathematica Δt value needs to be divided by $2\sqrt{2\ln 2}$ before it can be compared to the Glotaran `irf2` value. Furthermore, Glotaran’s root mean square (RMS) value is a thousand times smaller than the equivalent Mathematica R^2 value, because OD instead of mOD was used for the absorption amplitude. Finally, it should be mentioned that, in contrast to the parameter table legend of Fig. 4.4, Glotaran presents the lifetimes in ps and not in s. In fact, both, Glotaran and the Mathematica VPA implementation, do not process units of measurements and the user has to deduce the units of the fit parameters from the units of the input dataset, which had a ps time axis in the present example. Note that Mathematica seems to be faster than Glotaran, but one should not forget that Glotaran performs an error calculation, which is still a missing feature in the Mathematica VPA implementation. Furthermore, this single measurement gives only a rough estimation of the consumed computation time, but cannot identify a trend, which in addition might heavily depend on the chosen model function and the chosen dataset.

A significant reduction of computation time can be achieved by performing a chirp correction, i.e., by temporally shifting each transient in such a way that all transients start at the same time zero. Then, the `t0Model` function can be replaced with a single fit parameter t_0 and the overall fit model becomes wavelength-independent. Consequently, the fit algorithm does not need to evaluate the model function for every (λ_i, t_j) -tuple but only for the time steps t_j . The required individual time offset

```
t0Corr = t0Func /@ wavelength;
```

for each transient stems from applying the chirp function `t0Func` to every wavelength. Here, the already fitted `t0Model` was used for `t0Func`, but actually one wants to do the chirp correction before the fit procedure. A reliable strategy is to fit the chirp model function `t0Model` with Mathematica’s default `LinearModelFit[...]` to a manually selected

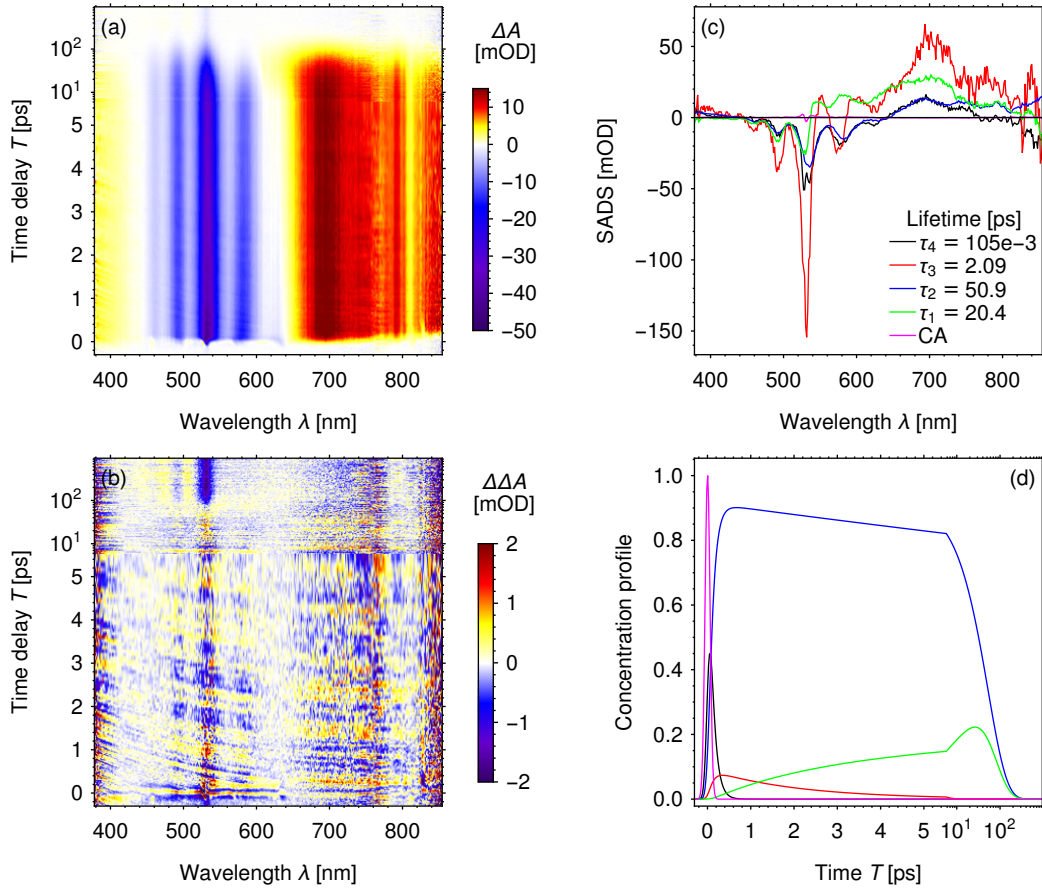


Figure 4.6.: Details of the chirp-corrected fit. For a given dataset (a), the fit algorithm splits the measured transient absorption spectrum into the fit residuals (b) and a model spectrum, which is defined by the SADS (c) and the temporal concentration profiles (d).

set of t_0 -values, which can comfortably be extracted from any Mathematica plot: Right-click the plot, select "Get Coordinates", click at the positions of t_0 (center of the coherent artefact for a set of different transients) and strg-c / strg-v copy them to the notebook.

In order to shift the transients about an arbitrary time offset, they need to be interpolated:

```

1 pad = 100;
2 transientFunc = Interpolation[
3   Transpose@{ArrayPad[time, pad, "Extrapolated"],
4             ArrayPad[ArrayPad[#, {0, pad}, "Fixed"], {pad, 0}, 0]},
5   InterpolationOrder -> 1] & /@ transient;.

```

Since the temporally shifted transients would cover different time ranges, one either needs to cut away the nonoverlapping region or to extrapolate this gap. Here the latter option was chosen and the time axis was padded with `pad = 100 "Extrapolated"` entries at both ends, while the transients were extended with 100 zeros before t_0 and 100 "Fixed" values at the end, i.e., the last signal value was attached a 100 times. The latter assumption

of a constant signal is valid if the end of the time axis lies in the ns-region, where the ps-shift of the chirp correction can be neglected.

With the such-prepared interpolation functions one can finally shift the transients

```
1 cctas = Transpose@Table[transientFunc[[i]][time + t0Corr[[i]],
2   {i, 1, Length@t0Corr, 1}];
```

and transpose the result to get a chirp-corrected transient absorption spectrum

```
cctas = {{y[λ1, t1], y[λ2, t1], ...},
        {y[λ1, t2], y[λ2, t2], ...},
        ...};,
```

i.e., a list of difference spectra, which is then fed into the fit function

```
1 vpm = parVarPro[
2   {{wavelength, time, {cctas}, {t}, fitModel}},
3   {{k3, 0.5}, {k2, 0.05}, {k1, 0.01},
4   {Δt, 0.2}, {t0, 0.7}}]
```

yielding the same result as the uncorrected dataset but much faster, as can be seen in the Fig. 4.5 and 4.6. Again, Glotaran (≈ 0.44 s/step) and Mathematica (≈ 0.15 s/step) are similarly fast. Note that the used Glotaran version did not allow for fitting the CA without defining a chirp function. However, even with fixed parameters, the chirp function cancels the above-described gain in computation speed. Therefore, this function was neglected for the calculation speed comparison with Mathematica at the cost of getting an incorrect fit result.

If the transient absorption signal shows dynamics that can not be explained with the so-far discussed models, Mathematica allows for a comfortable adaption of the model function. For example, the afore-mentioned wavepacket oscillations can be fitted with the two complex conjugate decaying exponentials [compare eq. (4.1)]

```
fitModel = {Exp[-I ω t] Exp[-δ t], Exp[I ω t] Exp[-δ t]}/2;,
```

which add up to a real-valued cosine function, but allow the fit function

```
1 vpm = parVarPro[
2   {{wavelength, time, {dataset}, {t}, fitModel}},
3   {{ω, 22.}, {δ, 1/5.}}]
```

to search for complex-valued linear fit parameters, which then form the OADS amplitude and phase in Fig. 4.7c, while Fig. 4.7d shows the corresponding damped oscillation profile. As can be seen from Fig. 4.7b, the residuals consist solely of noise, i.e., the fit function perfectly matches the oscillations.

In the case that the fit algorithm fails, because the model functions' derivatives can not be calculated by Mathematica, the option

```
parVarPro[... , "Jacobian" -> "FiniteDifference"]
```

allows to fall back to the finite difference method. Finally, like in Glotaran, it is also possible to simultaneously fit

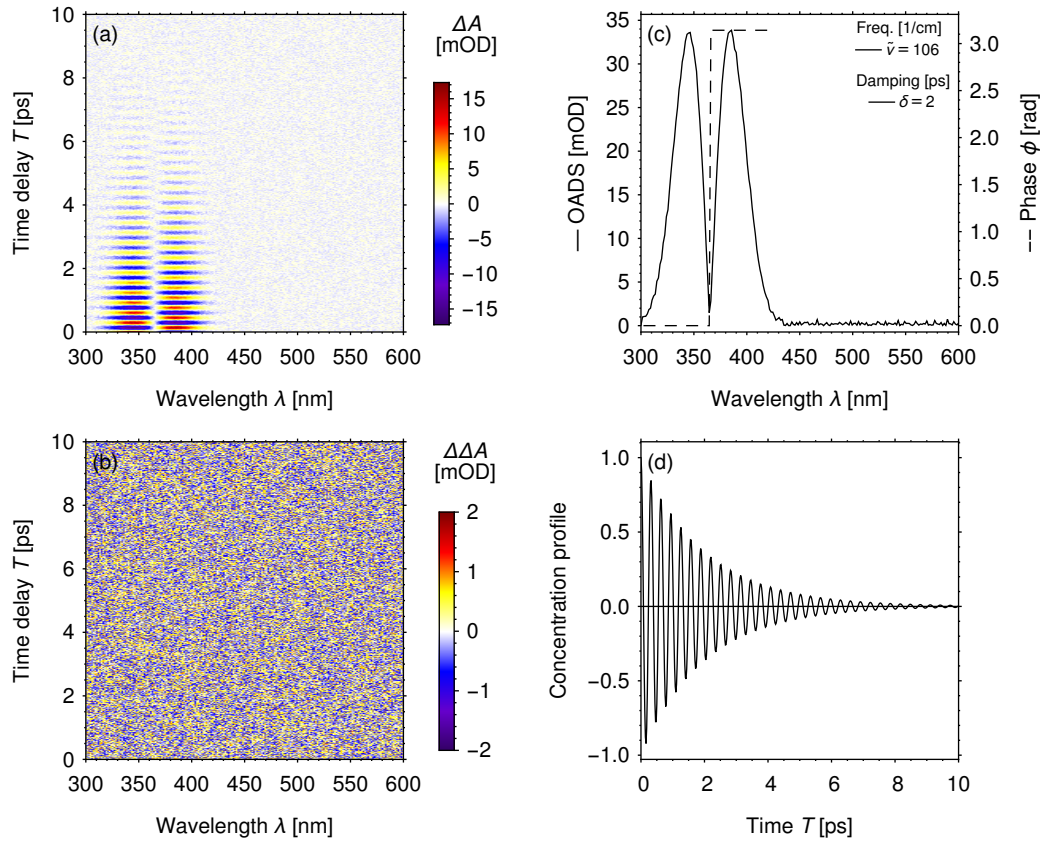


Figure 4.7.: Damped oscillation fit with wavelength-dependent phase. The wavepacket dynamics of I_3^- were mimicked in the test dataset (a) by a damped oscillation with a phase jump around 363 nm. The fit algorithm perfectly separated the noise, which remains in the residuals (b), from the oscillation, whose OADS amplitude and phase are shown in (c), while the temporal oscillation profile can be seen in (d).

```

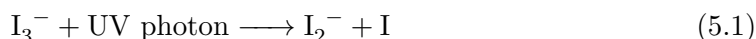
1  vpm = parVarPro[
2      {{wavelength1, time1, {dataset1}, {t}, fitModel1},
3       {wavelength2, time2, {dataset2}, {t}, fitModel2}.
4       ...},
5       {{kn, 0.5}, ...}]

```

multiple datasets `dataset1`, `dataset2`, ... with different fit models `fitModel1`, `fitModel2`, ... sharing the nonlinear fit parameters k_n .

5. Trihalide photodissociation pathways

Investigations of I_3^- with femtosecond spectroscopy were pioneered by Ruhman and coworkers [14, 22, 37, 115–125] and by the Vöhringer group [33, 39, 111, 126–130]. With ultrashort pulses, the nanosecond time resolution of flash photolysis experiments [131–135] could be improved, and the primary processes in the photodissociation reaction



were unraveled.

Ruhman’s group found that when I_3^- is excited with pump pulses at 308 nm, the spectral signature of I_2^- fragments absorbing around 740 nm [133, 135, 136] appears within 300 fs. Since this photodissociation process is faster than the dephasing of the photoinduced coherent reactant vibrations, the I_2^- fragments inherit these vibrations which give rise to a transient signal oscillating with a wavenumber of $(94 \pm 5) \text{ cm}^{-1}$. The transient oscillations at the blue and the red edge of the I_2^- absorption band show a phase difference of π as expected for an oscillating vibrational WP (Sec. 2.2.2) [137–140]. With (450 ± 50) fs, the dephasing of the coherent oscillation is about ten times faster than the ≈ 4 ps narrowing of the I_2^- PA band due to vibrational cooling. The GSB of I_3^- decays biexponentially [(5 ± 1) ps and (75 ± 10) ps] and is accompanied by a 110 cm^{-1} oscillation lasting for ≈ 1.5 ps which is assigned to the symmetric stretch vibration of I_3^- excited via resonant impulsive stimulated Raman scattering.

Vöhringer’s group [39, 126, 128] excited I_3^- with femtosecond pulses at 400 nm or 266 nm and observed three-body dissociation at the higher pump energy. Furthermore, the first 300 fs of the WP evolution from excited I_3^- towards the $\text{I}_2^- + \text{I}$ fragments could be resolved and by probing at various wavelengths between 400 nm and 960 nm, a wavelength dependence for the wavenumber of the I_2^- oscillation was identified and explained by a filter effect of the Franck–Condon window which limits the accessible vibrational states depending on the optical transition wavelength. By reconstructing the I_2^- PA spectrum, the vibrational cooling and the associated spectral band narrowing and shifting could be separated from the biexponential decay (≈ 2.45 ps and ≈ 73 ps).

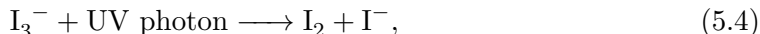
Since the I_3^- GSB as well as the I_2^- PA decay biexponentially with basically identical time constants, this process stems most likely from recombination of the $\text{I}_2^- + \text{I}$ fragments. The biexponential behaviour was first explained by a diffusion model, [126] but the observation of an additional PA band [22, 121] required the consideration of a second product species X in addition to or instead of the diffusion concept. The X species were identified as $\text{I}_2^- + \text{I}$ contact pairs [22] which are trapped in the solvent cage and give rise to a disturbed I_2^- signal because of the small interfragment distance. The slow decay of this signal was explained with an electron transfer (ET)



preceding the recombination process



while the fast decay of the PA was attributed to an alternative photodissociation channel



which results in directly recombining fragment pairs and was also observed in gas-phase experiments [35, 141, 142]. To test the latter assignment, in the present thesis TA measurements with broadband probing in the spectral region of the 505 nm absorption band of I_2 and the 445 nm absorption band of the I_2 -ethanol complex [143] are performed.

An important factor for the efficiency of the competing photofragmentation channels is the symmetry of the two bonds, which also has an impact on the molecular vibrations and hence on the oscillating signal contribution. Kühne et al. deconvolved the I_3^- GSB oscillation via linear-prediction singular-value decomposition [39, 126] and uncovered not only higher harmonics of the I_3^- symmetric stretch vibration but also a weak signal at 140 cm^{-1} , from the asymmetric stretch vibration of I_3^- . Gershgoren et al. also observed the combination band at $(253 \pm 2) \text{ cm}^{-1}$ which they extracted with the filter diagonalization method [124]. The asymmetric stretch vibration was also evident in earlier Raman experiments [144–149] with a strong solvent dependence [150]. Since the asymmetric stretch vibration is not Raman-active for the $\text{D}_{\infty\text{h}}$ -symmetric I_3^- , some solvents must break the $\text{D}_{\infty\text{h}}$ symmetry into $\text{C}_{\infty\text{v}}$ by lengthening one bond, or into $\text{C}_{2\text{v}}$ by bending the molecule, or into C_S by doing both. A series of theoretical papers [129, 151–158] addressed this issue and recently structural information was obtained directly by time-resolved X-ray liquidography (TRXL) [159, 160] or extracted from X-ray photoelectron spectroscopy (XPS) supported by ab-initio molecular dynamics simulations [161–163]. The TRXL data revealed $\text{D}_{\infty\text{h}}$ symmetry for I_3^- in acetonitrile, $\text{C}_{\infty\text{v}}$ in methanol, and C_S in water.

The effect of a broken symmetry on the photodissociation reaction on an ultrafast time scale was investigated by Ruhman and coworkers by applying transient absorption spectroscopy to I_3^- in acetonitrile and ethanol and to I_2Br^- in acetonitrile [119, 120]. In all three cases, the formation of coherently oscillating I_2^- fragments was observed, but for the broken symmetry, achieved either by the ethanol solvent or by substituting I_3^- with I_2Br^- , the I_2^- fragments are cooler and have a more compact and localized WP, so that the transient oscillation is more pronounced. Furthermore, I_2^- was found to be the major, possibly sole dihalide product of I_2Br^- photodissociation, because no indication for IBr^- formation was found, even not in measurements utilizing broadband probe pulses [164]. However, the existence of competing photodissociation channels in trihalide molecules was shown in gas-phase experiments, where photoexcitation of IBrCl^- yielded both IBr^- and ICl^- fragments [165] and photoexcitation of I_2Br^- yielded I_2 , I_2^- , IBr and IBr^- fragments [166] as well as I^- fragments [167]. Nevertheless, these findings do not guarantee the existence of branching photodissociation channels in the liquid phase, but rather demonstrate the significant impact of a solvent environment on the efficiency of the different reaction channels as it is discussed for the case of I_3^- [35, 40, 141, 168, 169].

Table 5.1.: Reactant concentrations in mmol l^{-1} for trihalide samples prepared in DCM

sample name	(inter)halogen	+	halide
$\text{I}_2 + \text{I}^-$	I_2 (2.5)	+	I^- (5)
Br_3^-	-	+	-
$\text{IBr} + \text{Br}^-$	IBr (10)	+	Br^- (40)
$\text{ICl} + \text{Cl}^-$	ICl (50)	+	Cl^- (200)
$\text{I}_2 + \text{Br}^-$	I_2 (2.5)	+	Br^- (10)
$\text{I}_2 + \text{Cl}^-$	I_2 (2.5)	+	Cl^- (2.5)

In this study, the photodissociation channels of I_3^- , Br_3^- , IBr_2^- , ICl_2^- , I_2Br^- , and I_2Cl^- are investigated by ultrafast transient absorption spectroscopy with broadband probing covering the UV-VIS spectral ranges 310 nm to 610 nm and 270 nm to 515 nm. The key element in identifying photodissociation channels is the characteristic vibrational frequency of the resulting diatomic fragments, which can be extracted from the transient oscillations of the PA. For a general treatment, a global analysis implementation is developed for broadband transient absorption data, so that both coherent vibrational and exponential decay dynamics can be modelled simultaneously. This systematic approach, demonstrated for six trihalide anions, provides extensive information on whether competing fragmentation patterns are accessible for trihalides in solution or whether the presence of the environment might prevent this possibility.

5.1. Sample preparation

The trihalide anions I_3^- , IBr_2^- , ICl_2^- , I_2Br^- , I_2Cl^- were prepared by mixing the halogen I_2 (CAS 7553-56-2, AR grade) or the interhalogen IBr or ICl (CAS 7789-33-5 or 7790-99-0, respectively, Sigma-Aldrich: 1 mol l^{-1} in dichloromethane (DCM)) with the corresponding tetrabutylammonium iodide, bromide or chloride salt (CAS 311-28-4, reagent 98 %, CAS 1643-19-2, ACS ≥ 98 %, or CAS 1112-67-0, ≥ 97 %, respectively, Sigma-Aldrich) in DCM (CAS 75-09-2, ≥ 99.9 %, Merck Millipore) as listed in Tab. 5.1. Since within the chemical equilibrium, multiple trihalide molecules may coexist (see Fig. 5.1), the samples are named after the reactant combination. The Br_3^- anion was prepared by dissolving tetrabutylammonium tribromide (CAS 38932-80-8, 98 %, Sigma-Aldrich) in DCM. Instead of the solvent ethanol (most commonly used for TA studies on I_3^-) [14, 22, 33, 39, 111, 115–117, 119–128, 130, 170] or room-temperature ionic liquids [171, 172] anhydrous DCM was preferred in this paper, as it ensures the stability of the starting materials I_2 , IBr and ICl , which dissociate in ethanol in the presence of slightest traces of water [143]. To ensure the solubility of the halide salts in DCM, an organic cation like tetrabutylammonium Bu_4N^+ is required.

Concentrations of the different trihalides were chosen in such a way as to guarantee an absorbance of at least 0.3 OD at the excitation wavelength for a sample flow cell of 200 μm optical path length. To measure with each laser shot (each 1 ms) a completely refreshed sample, the solution was circulated with a micro annular gear pump (mzr-4605,

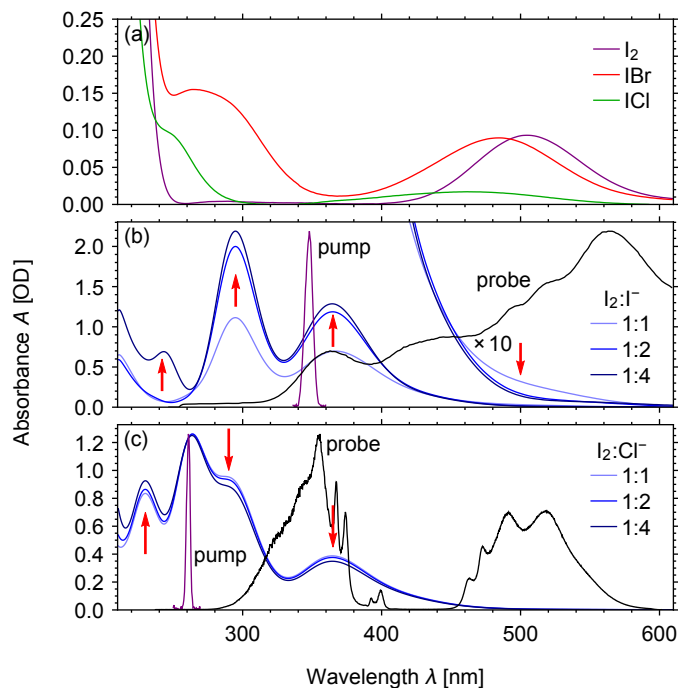


Figure 5.1.: Absorption spectra of different trihalide-forming (inter)halogen-halide equilibria in DCM plus pump and probe spectra. (a) Without a halide salt, the halogen I_2 (505 nm) and the interhalogens IBr (485 nm) and ICl (465 nm) are stable in DCM. (b) $I_2 + I^-$: An increasing I^- (244 nm) concentration decreases the amount of I_2 (505 nm) and increases the I_3^- (295 nm D-band and 365 nm C-band) concentration (red arrows). (c) $I_2 + Cl^-$: A mixture of trihalides is formed. With an increasing Cl^- (below 210 nm) concentration, the amount of ICl_2^- (230 nm) increases, while the I_3^- (295 nm D-band and 365 nm C-band) concentration decreases and the amount of I_2Cl^- (264 nm, probably D-band) stays nearly constant. [3, Fig. 1] - Reproduced by permission of the PCCP Owner Societies

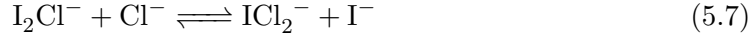
HNP Mikrosysteme).

The heteronuclear trihalides are expected to form only one isomer with the heaviest element located at the center position. Hence, if Y is heavier than X, $[X-Y-X]^-$ is preferred over $[Y-X-X]^-$, whereas $[Y-Y-X]^-$ is preferred over $[Y-X-Y]^-$ [151, 152]. In solution, the yield of the homonuclear trihalides is determined by an equilibrium reaction, e.g.



which allows to control the balance between I_2 and I_3^- by the concentration of I^- , as seen in the absorption spectrum (Fig. 5.1b). Since the I^- absorption (244 nm) [173] lies outside the range of the transient absorption setup, the halide concentration is increased to minimize the I_2 (505 nm, Fig. 5.1a) amount, in which case also the I_3^- (295 nm D-band and 365 nm C-band) [174] concentration increases. To avoid three-body dissociation observed when pumping at 266 nm, [39, 160] an excitation wavelength of 348 nm was chosen.

Balancing the equilibrium reactions of the heteronuclear trihalides is more delicate, because multiple pathways, e.g.



lead to a mixture of various trihalides [175] which can be identified in the absorption spectrum (Fig. 5.1c) [174–178]. The amount of ICl_2^- (230 nm D-band) increases with the Cl^- (below 210 nm) [173] concentration, while the amount of I_3^- (295 nm D-band and 365 nm C-band) decreases and the I_2Cl^- (264 nm, probably D-band) concentration stays nearly constant. Using a high excess of Cl^- , even the I_2Cl^- vanishes and a predominant ICl_2^- solution is prepared. I_2Cl^- cannot be purified this way, because it requires a balance between Cl^- and I^- anions and therefore also ICl_2^- and I_3^- is present. To measure primarily the transient absorption of I_2Cl^- , an excitation wavelength of 261 nm (at the cost of probably entering the three-body dissociation channel) was chosen.

By exchanging Cl with Br, the reactions (5.6) to (5.9) are also valid for iodine-bromine systems. However, in these cases different trihalides cannot be separated by their spectroscopic signatures because all absorption bands are merged into a single band that shifts if the balance between the trihalides changes. Therefore, it is not possible to selectively excite I_2Br^- only. The excitation wavelengths 348 nm and 261 nm, selected for I_3^- and I_2Cl^- experiments, are not in resonance with the remaining trihalides Br_3^- , IBr_2^- , ICl_2^- and I_2Br^- , except for IBr_2^- , which absorbs at 260 nm. Therefore, these trihalides are excited at either the blue or the red edge of their C-/D-absorption band (261 nm) or at the A-/B-band (348 nm), [174] for which the low absorption efficiency was compensated by a higher sample concentration.

5.2. Transient absorption setup

The TA setup (Fig. 5.2a) was driven by a regenerative titanium-sapphire (Ti:Sa) amplifier system (Solstice, Spectra-Physics: 797 nm, 100 fs, 1 kHz) whose output was split into a pump and a probe beam.

To excite the trihalide samples, the pump was converted to the UV spectral range [348 nm (261 nm) for the first (second) measurement series] via a noncollinear optical parametric amplifier (NOPA) followed by second-harmonic generation in a β -barium borate crystal (TOPAS-White, Light Conversion). The UV pump passed a Keplerian telescope consisting of two spherical mirrors (SMs) (focal lengths: $f_1 = 500$ mm and $f_2 = 300$ mm), which adapted the beam diameter for the following UV pulse shaper, an acousto-optic programmable dispersive filter (Dazzler UV-250-400, Fastlite) [179–182]. The shaper was used to optimize the temporal resolution by compressing the UV pump pulses to a FWHM duration of 70 fs at 261 nm and 40 fs at 348 nm (see Figs. 5.3 and 5.4 for XFROG [180,181,183–186] measurements). An SM ($f = 175$ mm) was used to focus

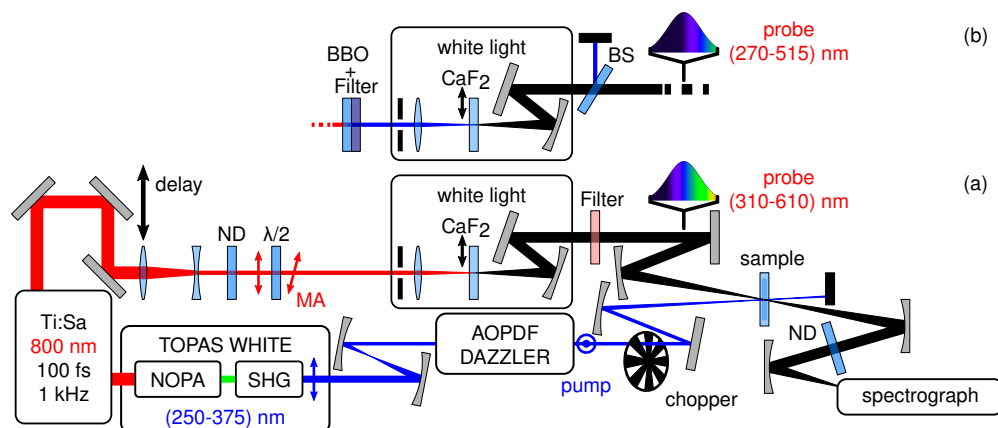


Figure 5.2.: Schematic transient absorption setup for (310–610) nm WL (a) and (270–515) nm WL (b). (a) The output of a Ti:Sa amplifier is split into two beams, which are focussed and overlapped inside the sample. A pump pulse excites the sample molecules and a snapshot of the subsequent decay dynamics is observed via a probe pulse. To scan the full dynamics, the experiment needs to be repeated for different pump–probe time delays. Probe power fluctuations and the static background are removed with the help of reference measurements for which every other pump pulse is blocked by a chopper wheel. A NOPA (TOPAS WHITE) in combination with a SHG crystal is used to tune the pump wavelength to the sample’s absorption wavelength, while WL generation in the probe beam allows to measure multiple wavelengths at once, when the intense 800 nm fundamental is blocked by a colour filter. Wherever necessary, the laser intensity is adjusted by ND filters. To suppress the anisotropy signal resulting from reorienting molecules, a half-wave plate ($\lambda/2$) rotates the horizontal probe polarization (\updownarrow) to the MA with respect to the vertical polarization (\odot) of the pump. Finally, an AOPDF (DAZZLER, Fastlite) allows to compress the pump pulse for maximum temporal resolution or to generate arbitrarily shaped pump pulses for more complex spectroscopy or coherent control experiments. Note that in this scheme most of the plane, beam-guiding mirrors are omitted. (b) The additional BBO converts the probe wavelength to 400 nm, while the 800 nm is blocked by a colour filter. This allows to generate WL with shorter wavelengths, whose intense 400 nm fundamental is blocked by a BS. Note that the 400 nm generation rotates the probe polarization about 90° , which needs to be considered by adjusting the MA.

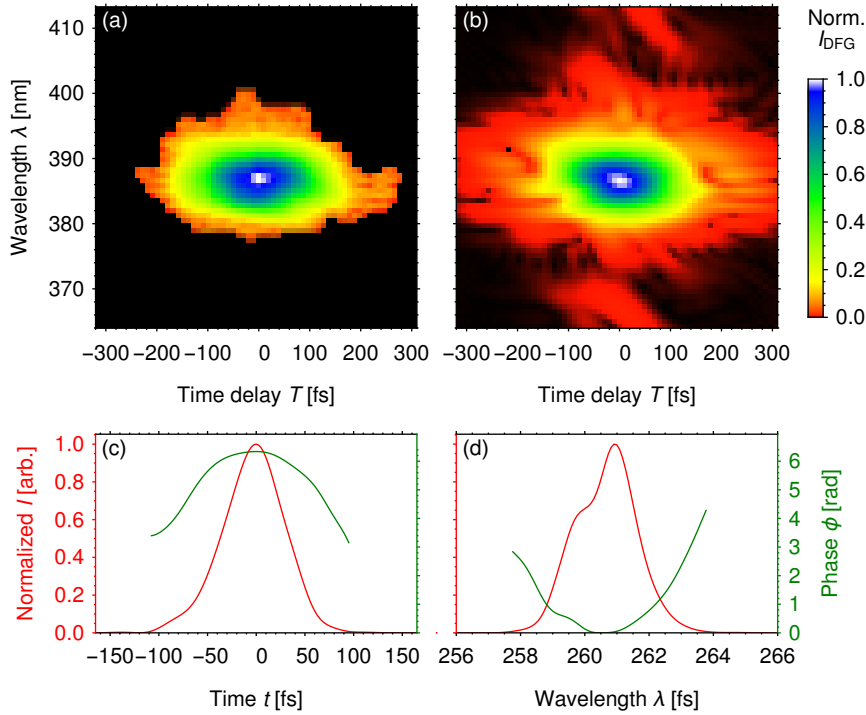


Figure 5.3.: Measured (a) and reconstructed (b) XFROG trace of the 261 nm pump pulse and the resulting temporal (c) and spectral (d) intensity (red) and phase (green). The XFROG error is 2.1 %, the temporal FWHM 72 fs and the FWHM bandwidth 2.3 nm. [3, Fig. S2] - Reproduced by permission of the PCCP Owner Societies

the 140 nJ UV pump pulses to an FWHM diameter of 27 μm (Fig. 5.5a) inside the flow cell with thin window apertures (48/UTWA2/Q/0.2, Starna GmbH). With this pump energy and beam diameter, the transient absorption measurement was operated in the non-linear, saturation regime (see Fig. 5.6 for energy dependence).

The induced photodynamics were observed with a probe pulse following each pump pulse at a delay time T , which was adjusted by directing the probe on a retroreflector mounted on a motorized delay stage (M-IMS600LM, Newport). Guided by mirrors with high reflectivity for 800 nm, the beam diameter (Galilean lens telescope), intensity (variable attenuator wheel) and polarization (zero-order half-wave plate) were adapted for supercontinuum white light (WL) generation achieved by focussing (plano-convex lens: $f = 100$ mm) the probe into a linearly moving, 5 mm thick CaF_2 plate, generating spectral components down to 310 nm (Fig. 5.1b) [187–189]. An iris in front of the focussing lens allowed to fine-tune the beam diameter. Anisotropy effects were eliminated from the measured signal by adjusting the linear probe polarization to the magic angle ($\text{MA} = 54.7^\circ$) [4, 19] (see Sec. 3) with respect to the vertical, linear pump polarization. After collimating the WL with an SM ($f = 150$ mm, diameter $d = 2$ in), it was guided towards the sample by UV-enhanced aluminum mirrors and the intense 797 nm fundamental was blocked by a custom-made filter (Laser Components GmbH). With an SM

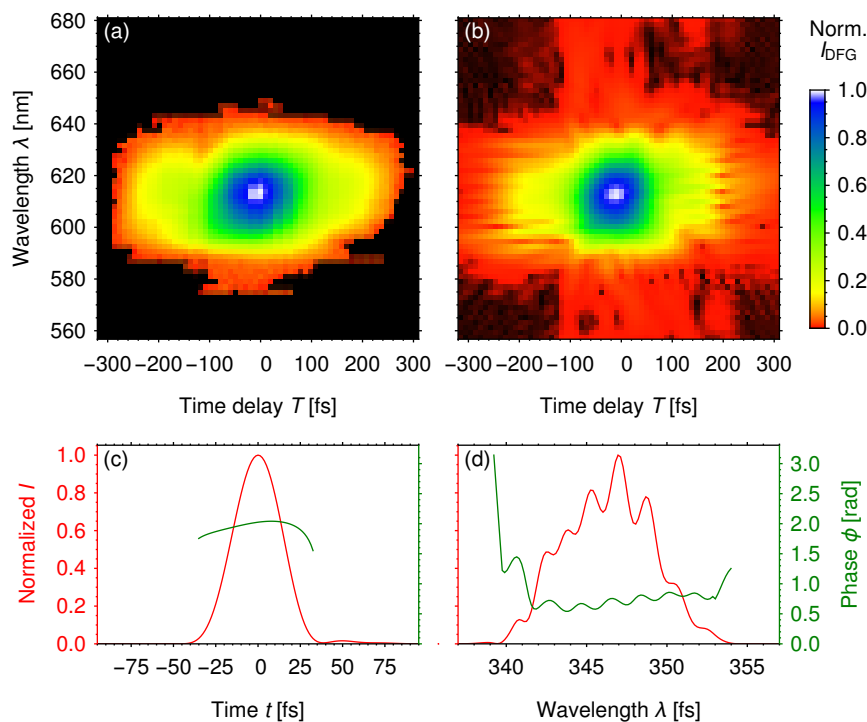


Figure 5.4.: Measured (a) and reconstructed (b) XFROG trace of the 348 nm pump pulse and the resulting temporal (c) and spectral (d) intensity (red) and phase (green). The XFROG error is 2.2 %, the temporal FWHM 34 fs and the FWHM bandwidth 6.2 nm. [3, Fig. S1] - Reproduced by permission of the PCCP Owner Societies

($f = 100$ mm), the remaining WL was focussed to an FWHM diameter of $17 \mu\text{m}$ (see Fig. 5.5b) inside the sample flow cell and spatially overlapped with the UV pump.

To extend the WL spectral range to the UV for the second measurement series (261 nm pump), the 800 nm probe light was converted to 400 nm and the residual 800 nm light was filtered out before focussing the 400 nm probe into the CaF_2 plate (Fig. 5.2b), resulting in spectral components down to 270 nm (Fig. 5.1c) [188, 190]. The 400 nm fundamental was blocked by a beamsplitter being reflective for 370 nm to 455 nm but transmissive for the rest of the 270 nm to 515 nm range. Regarding possible imperfections with regard to the linear polarization of the WL probe, note that the WP oscillations are not disturbed by polarization deviations and since the pump-selected molecular alignment redistributes within 15 ps even for the largest molecule I_3^- , only the short-time dynamics would be affected.

The WL not absorbed by the sample was collimated again by an SM ($f = 100$ mm), optionally attenuated by a neutral density (ND) filter and finally focussed with an SM ($f = 75$ mm) into a spectrograph (SP2500i, Acton). The attached two-dimensional charge-coupled device (CCD) camera (Pixis 2K, Princeton Instruments) measured the WL spectrum of each probe pulse separately at an acquisition rate of 1 kHz. Blocking every other pump pulse, either by an additional chopper placed in the pump beam or

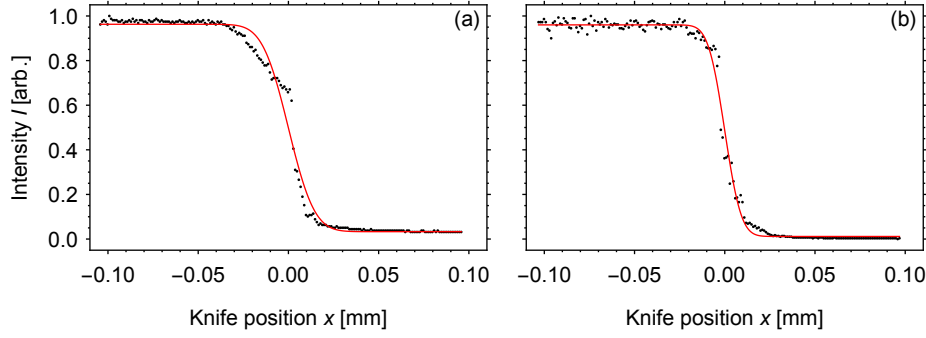


Figure 5.5.: Knife-edge scan of the 348 nm pump (a) and the (310-610) nm probe WL (b). The fitted error function (red) corresponds to a Gaussian with 27 μm spatial FWHM for the pump and 17 μm spatial FWHM for the probe. [3, Fig. S3] - Reproduced by permission of the PCCP Owner Societies

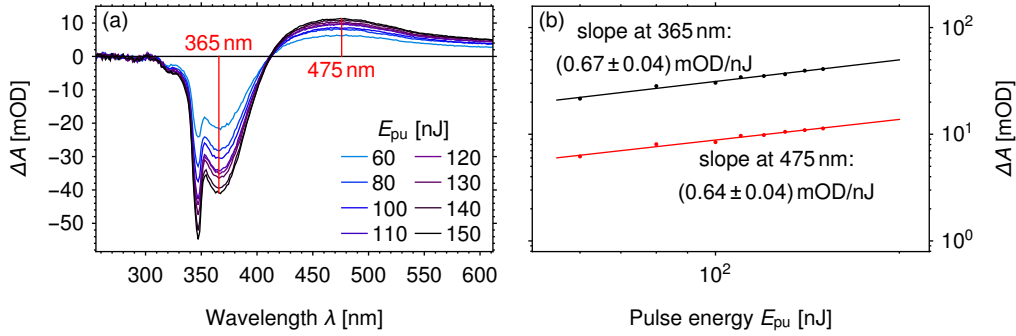


Figure 5.6.: Pump-energy dependency of the (310-610) nm difference spectrum at 3.34 ps for pumping at 348 nm (a) and the log-log slope at the GSB (365 nm) and at the PA (475 nm) (b). Since the slope is below one, the experiment is carried out in the saturation regime. [3, Fig. S4] - Reproduced by permission of the PCCP Owner Societies

by using the toggle mode of the pulse shaper, allowed to collect the dynamic spectrum $I(\lambda, T)$ and the unpumped, static reference spectrum $I_{\text{ref}}(\lambda)$ on a shot-to-shot basis. Therefore, a single difference absorption spectrum defined by (2.4) for a given delay time T could be calculated from two consecutive laser shots. For the TA data, 1000 consecutive difference absorption spectra were averaged at each delay time T , of which the first 6 ps were scanned in 300 steps with an increment of 20 fs and the remaining 2 ns were scanned with 100 steps with exponentially increasing increments. For each sample, up to 5 consecutive datasets were collected. The 2048 camera pixels were binned in groups of 8 pixels, resulting in 256 wavelength steps with 0.177 nm increment. The upper wavelength limit was given by the second-order diffraction of the spectrograph's grating, which starts to disturb the first-order diffraction at 620 nm (515 nm) for the first (second) measurement series.

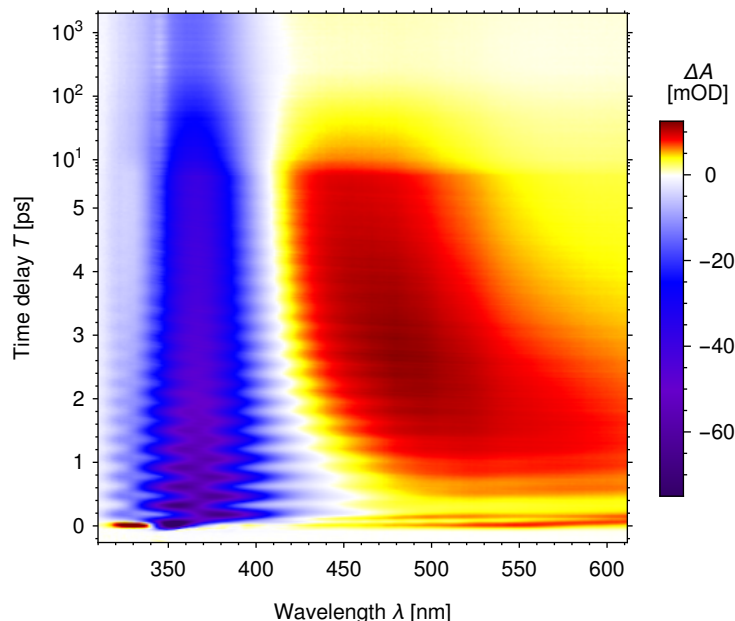


Figure 5.7.: TA data of the I_3^- dynamics in DCM after pumping at 348 nm. Note the logarithmic time scale for delays larger than 5.5 ps. The data is corrected for pump stray light and the chirp of the probe pulse according to Sec. 5.3. The negative I_3^- GSB at 366 nm is accompanied by pronounced oscillations from a ground-state vibrational WP, which travels between the turning points associated with transitions at ≈ 350 nm and ≈ 385 nm. In the red part (above 450 nm), the positive I_2^- PA rises after the excited-state WP travelled through an intermediate bond-fission state giving rise to a sharp peak right after the CA. This peak shifts to later delay times for smaller wavelengths. The I_3^- GSB and I_2^- PA decay from recombining $I_2^- + I$ fragment pairs lasts until ≈ 200 ps, then a weak permanent signal from escaped I_2^- fragments remains. For ≈ 4 ps, the I_2^- PA decay is accompanied by a blue shift due to the vibrational cooling of the hot I_2^- fragments. The short-time dynamics are detailed in the Fig. 2.1. [3, Fig. 2] - Reproduced by permission of the PCCP Owner Societies

5.3. Transient absorption signals: the case of triiodide

The different signal contributions of a trihalide system and the data fitting procedure are exemplified for the I_3^- sample pumped at 348 nm and probed in the spectral region 310 nm to 610 nm. However, before the actual fitting was applied, each of the multiple raw datasets per sample was preprocessed. First, pump stray light, which leaked into the spectrograph, was removed either by subtracting the averaged before- t_0 difference spectra or by deleting the contaminated spectral region. Second, the WL chirp was corrected by shifting the transients according to a fourth-order polynomial, which was fitted to manually selected t_0 points illustrated at the right side of Fig. 2.1. Third and finally, the different datasets of one sample were averaged after aligning their t_0 , resulting in Fig. 5.7.

The short-time dynamics start with a Gaussian-shaped coherent artefact (CA) defining time zero t_0 . In addition to the CA, a negative difference absorption signal together with

a pronounced oscillation, both centred at 366 nm, set in instantly. Since the spectral position matches the 365 nm absorption band of I_3^- and the formation of a product molecule would require some time, both effects are attributed to the GSB of the reactant I_3^- . The oscillatory behaviour is due to a vibrational WP which travels back and forth on the electronic ground-state PES. At the turning points (about 350 nm and 385 nm) the WP narrows, while it broadens at the equilibrium position (366 nm) [33].

In the red part (above 450 nm) of the TA data, right after the CA, a narrow Gaussian-shaped peak appears, attributed to the ESA of I_3^- . The non-exponential rise and decay behaviour can be explained by a WP, which moves on the excited-state PES in such a way that its corresponding signal first occurs at 600 nm or above and then shifts towards the blue (≈ 450 nm). Kühne et al. could not resolve this WP motion below 600 nm, but for wavelengths above 600 nm they observed a similar WP inducing a signal that shifts towards the red [39]. For the increasing interfragment distance along the dissociation channel, the excited state PES of I_3^- smoothly converts into the ground state PES of I_2^- . Thus, the WP pathway leads finally to the formation of I_2^- giving rise to a positive PA signal. Since the bond fission proceeds faster than the WP dephasing, the WP is still present in the diatomic fragment, resulting in an oscillatory contribution to the PA.

The long-time dynamics show the ≈ 200 ps decay of the PA and the corresponding GSB recovery, followed by a small signal remaining constant within the measured time window of 2 ns. For the first 4 ps, the PA decay is accompanied by a pronounced blue shift, which may reflect vibrational cooling due to the increasing energy gap between the electronically excited state of I_2^- and its electronic ground state with decreasing vibrational energy. Another possible explanation for the blue shift suspects the deformation of the I_2^- PES due to the iodine radical I right after bond fission. With increasing interfragment distance, the I_2^- PES and therefore also the PA would gradually change.

The measured TA data sets for each of the trihalide reactants were globally analyzed according to the procedure described in Sec. 2.3, Sec. 2.4 and Sec. 4, comprising a parallel kinetic model (yielding DADS) [53] extended with damped oscillating components (yielding OADS). In this way, both the decay dynamics and the oscillating WP propagation on the I_2^- PES can be described with high accuracy. To account for the CA and the subsequent WP motion on the excited state PES of I_3^- two Gaussian functions were included in the fit model. The temporal resolution is considered by convolving the kinetic model, the oscillating WP, and the Gaussian WP with the IRF represented by the Gaussian CA. Selected transients together with the best-fit curves are shown in Fig. 5.8, while the resulting non-linear fit parameters are listed under $I_2 + I^-$ in Tab. 5.2. The linear fit parameters of the damped oscillations and the parallel kinetic model, i.e., the OADS and DADS, are displayed in Fig. 5.9. Since OADS are complex quantities, they are represented by their amplitude and phase.

The high wavenumber $\tilde{\nu}_2 = 113.1 \text{ cm}^{-1}$ oscillation (Fig. 5.9a) with a damping lifetime of $\delta_2 = 1.08$ ps matches the symmetric stretching vibration of ground state I_3^- (see Sec. 5.5 and Tab. 5.3) and is therefore attributed to a WP travelling around a minimum on the ground-state PES of I_3^- . In the corresponding OADS (Fig. 5.9a, black) two pronounced peaks (350 nm and 385 nm) with a phase difference of π can be seen. Therefore, these signals are attributed to transitions originating from the WP's two turning points,

Table 5.2: Results of modelling the TA data for the six investigated trihalide samples. A parallel model was used consisting of decaying exponentials with lifetimes τ_i [ps] plus damped WP oscillations with wavenumbers ν_i [cm^{-1}] and damping lifetimes δ_i [ps] plus a Gaussian-shaped wavepacket with FWHM Δt_{WP} [fs] and position $t_{0,\text{WP}}$ [fs] to model the dynamics (see Sec. 4.1). The setup's temporal resolution is accounted for by convolving the model function with a Gaussian-shaped IRF with FWHM Δt_{IRF} [fs] and position $t_{0,\text{IRF}}$ [fs]. The IRF was also used to model the coherent artefact. The error of the last one or two digits, given in parentheses, was estimated by excluding one of the measured datasets before averaging and fitting. This was done for each dataset, and for each fit parameter the largest deviation was extracted.

	348 nm pump and (310-610) nm WL probe						261 nm pump and (270-515) nm WL probe					
	$\text{I}_2 + \text{I}^-$	Br_3^-	$\text{IBr} + \text{Br}^-$	$\text{ICl} + \text{Cl}^-$	$\text{I}_2 + \text{Br}^-$	Br_3^-	$\text{IBr} + \text{Br}^-$	$\text{ICl} + \text{Cl}^-$	$\text{I}_2 + \text{Br}^-$	$\text{I}_2 + \text{Cl}^-$		
τ_4	-	-	-	1(1)	-	-	-	-	-	-		
τ_3	5.4(7)	4.3(9)	3.9(4)	3.0(9)	2.9(2)	8(3)	5(2)	6(2)	8(2)	7(3)		
τ_2	91(7)	16(3)	135(16)	55(6)	101(6)	54(25)	108(32)	93(2)	120(18)	168(31)		
τ_1	∞	∞	∞	∞	∞	∞	∞	∞	∞	∞		
ν_4	-	159.4(9)	-	-	-	-	-	-	-	-		
ν_3	-	142(1)	158.3(4)	-	133.7(5)	-	-	-	-	-		
ν_2	113.1(2)	9(9)	129(2)	-	113.6(1)	161.6(3)	-	-	134.1(2)	113.1(2)		
ν_1	3.3(3)	2(7)	4(4)	173(2)	3.5(3)	3(5)	4(4)	3.1(9)	4.2(2)	4.2(8)		
δ_4	-	0.8(1)	-	-	-	-	-	-	-	-		
δ_3	-	0.54(4)	0.6(1)	-	0.55(3)	-	-	-	-	-		
δ_2	1.08(1)	1(1)	0.63(6)	-	1.01(2)	0.66(1)	-	-	0.85(3)	0.69(9)		
δ_1	1.6(1)	1.6(6)	1.0(3)	0.28(2)	1.17(5)	2.1(6)	1.5(7)	1.6(6)	1.6(2)	1.9(7)		
Δt_{IRF}	80(2)	118(2)	85.9(8)	90(5)	60(5)	99.1(3)	99.1(4)	69.2(6)	97(4)	85(3)		
$t_{0,\text{IRF}}$	14(3)	-4(1)	10(1)	-13(2)	-17(3)	-1.2(7)	0.99(7)	13(1)	-2(1)	21(6)		
Δt_{WP}	79(9)	-	-	-	118(7)	-	-	47(100)	-	-		
$t_{0,\text{WP}}$	113(2)	-	-	-	103(7)	-	-	61(4)	-	-		

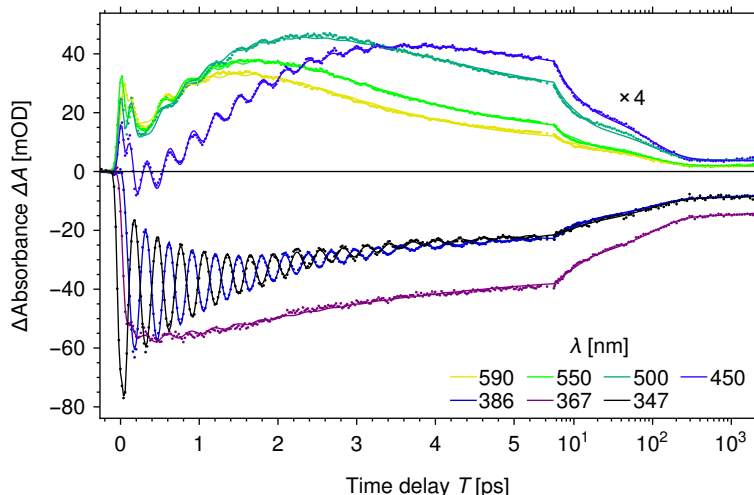


Figure 5.8.: Selected transients (dots) and best fit (solid line) after pumping I_3^- in DCM at 348 nm. Note the logarithmic time scale for delays larger than 5.5 ps. On the excited-state PES of I_3^- , the WP moves through an intermediate bond-fission state and gives rise to a sharp, Gaussian-shaped peak right after the CA above 450 nm. Subsequently, one bond breaks and the I_2^- PA rises. With the blue shift of the PA spectrum, its maximum appears at later delay times for smaller wavelengths. A weak oscillation from the I_2^- vibration sits on top of the PA, but around 450 nm the GSB and the corresponding I_3^- vibration start to overlap the PA signal. The I_3^- vibration is most pronounced at the out-of-phase WP turning points (386 nm and 347 nm), but at the GSB center wavelength (367 nm) nearly no oscillation is observed. Both PA and GSB decay biexponentially. [3, Fig. 3] - Reproduced by permission of the PCCP Owner Societies

while the low amplitude at the center wavelength (366 nm) is attributed to the WP being at a position in coordinate space that corresponds to the PES minimum. Being in phase with the low-energy turning point (385 nm), a small peak is present at ≈ 320 nm, the red edge of the D-absorption band (295 nm). Furthermore, the shoulder at ≈ 450 nm is also in phase with the low-energy turning point (385 nm), whereas for increasing probe wavelengths, the phase shifts gradually. It is not clear whether the latter oscillation signal stems from the A-/B-band of I_3^- or from the fragment I_2^- .

For the low wavenumber, three peaks can be seen in the OADS (Fig. 5.9a, red). The first one (335 nm) is blue-shifted with respect to the WP's high-energy turning point (350 nm), the second one (420 nm) is red-shifted with respect to the WP's low-energy turning point (385 nm), and the third one (560 nm) covers the region of the PA. Since the wavenumber $\tilde{\nu}_1 = 3.3 \text{ cm}^{-1}$ is small and the associated period (10.1 ps) is much longer than the damping ($\delta_1 = 1.6$ ps), the corresponding signal (Fig. 5.10) close to the WP's turning points looks more like a decaying GSB or SE rather than an oscillation. However, the decay has a non-exponential curvature, which can be expressed by a damped, low-frequency cosine function. In the PA region, the low-frequency oscillation appears like a rise followed by a decay, both of non-exponential character. Starting at 600 nm, this signal shifts to larger delay times for decreasing wavelengths due to the gradual phase shift (Fig. 5.9a, red-dashed line). Thus, the blue shift of the actual PA is modelled by a

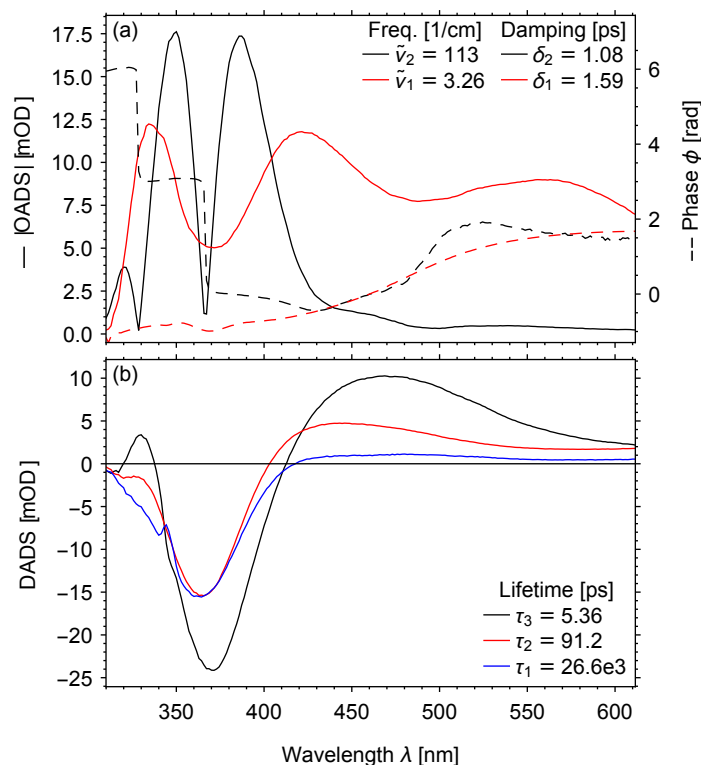


Figure 5.9.: Oscillation- and decay-associated difference spectra. (a) OADS: The $\tilde{\nu}_2 = 113 \text{ cm}^{-1}$ symmetric stretch vibration of I_3^- (black) has the largest amplitudes (solid) at the out-of-phase (dashed) WP turning points (350 nm and 385 nm) of the I_3^- C-absorption band (365 nm). The small peak at ≈ 320 nm results from the red edge of the D-absorption band (295 nm) and the weak shoulder around 450 nm might stem from the A- or B-absorption band or from the I_2^- fragment. Both signals are in phase with the signal at the red turning point (385 nm). Towards the red, the amplitude decreases and the phase shifts gradually. The low-wavenumber oscillation (red) shows three amplitude peaks (solid) and a gradually shifting phase (dashed), which results in a blue-shifting PA band (see Fig. 5.10). (b) DADS: After the initial, fast $\tau_3 = 5.4$ ps decay of the negative I_3^- GSB and the positive I_2^- PA (black), probably due to direct $\text{I}_2^- + \text{I}$ fragment recombination, an intermediate X (red), which lives for $\tau_2 = 91$ ps, is formed. The blue shift of the PA can be explained with vibrational cooling, but the blue shift of the GSB might be an artefact due to the use of a parallel fit model for a sequential process. After the intermediate X vanished, the for the measured delay of 2 ns permanent signal $\tau_1 \approx \infty$ ps from free I_2^- (blue) remains. Since X and free I_2^- have similar difference spectra, X is probably a I_2^- fragment, which is disturbed by its I partner. [3, Fig. 4] - Reproduced by permission of the PCCP Owner Societies

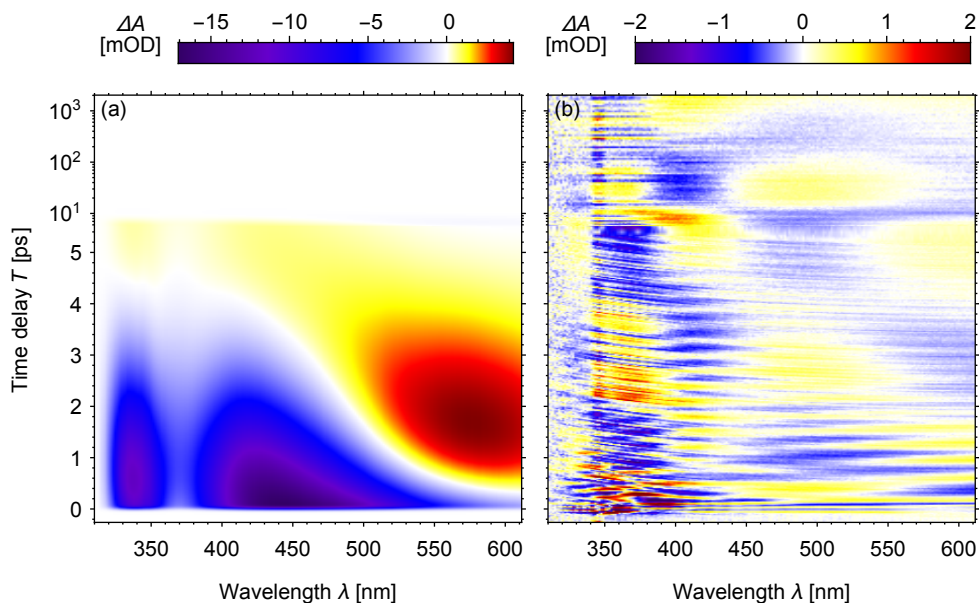


Figure 5.10.: Fitted TA data associated with the low-frequency vibration. (a) These transient signals follow a cosine curvature and therefore have a nonexponential shape. The wavelength-dependent phase $\phi(\lambda)$ of the cosine function allows the modelling of the blue shift of the PA band. (b) The fit residuals of the I_3^- sample still show some structure beyond pure noise, probably resulting from an imperfect fit of the PA blue shift. [3, Fig. 5] - Reproduced by permission of the PCCP Owner Societies

damped low-wavenumber oscillation with wavelength-dependent phase.

The further dynamics underlying the data in Fig. 5.7 can be modelled with exponential decays, yielding the DADS depicted in Fig. 5.9b. Since the largest lifetime τ_1 considerably exceeds the maximum delay time of 2 ns accessible in the measurement, the corresponding positive PA signal in the DADS (Fig. 5.9b, blue) originates from a photoproduct that is stable within the scanned time window. The exact spectral position of this PA is obscured by the overlapping GSB at 362 nm, but since the GSB is slightly blue-shifted compared to the 365 nm absorption band of I_3^- (Fig. 5.1b), the PA's maximum must be located to the low-energy side of the GSB. Matching the wavelength region of the 395 nm absorption band of I_2^- , [135, 136] this long-lived PA signal is assigned to I_2^- fragments that managed to escape their I counterpart. If a $I_2^- + I$ fragment pair stays together or meets again after separation due to diffusion processes, I_3^- can be formed by geminate recombination. Fitting the corresponding decay of the GSB and the PA yields two lifetimes ($\tau_3 = 5.4$ ps and $\tau_2 = 91$ ps) which are close to the values found in ethanol environment [(5 ± 1) ps and (75 ± 10) ps] [116].

The DADS (Fig. 5.9b, red) of the slow decay time $\tau_2 = 91$ ps is very similar to the DADS of the free I_2^- fragment (Fig. 5.9b, blue), yet the PA amplitude of the former is larger and its GSB is slightly red-shifted. Since a blue shift is expected for the observed larger PA amplitude, but a red shift occurs, the decaying PA must be narrower or its

position must be red shifted compared to the I_2^- PA. Both effects cannot be explained with vibrational cooling due to the long lifetime $\tau_2 = 91$ ps. Instead, an additional photoproduct or electronic state X is required. This hypothesis is in agreement with former observations of the 740 nm absorption band of I_2^- , where the overlapping X-state signature is more evident due to the absence of the disturbing GSB [22, 121]. For the X species, a $I_2^- + I$ contact pair that is trapped in the solvent cage was suggested, [22] assuming that the I_2^- fragment is disturbed by the nearby I partner and thus instead of the free I_2^- signal a red-shifted signal is observed. The necessity of the ET reaction (5.2) before the recombination was suggested to explain the long lifetime of the contact pair.

In contrast to this long lifetime, also a fast recombination with a time constant of $\tau_3 = 5.4$ ps exists, raising the question how some contact pairs can directly recombine while others need more time. Baratz and Ruhman suggested the formation of $I_2 + I^-$ contact pairs for which recombination is not hindered by an ET process [22]. With TA data in the UV region now at hand, the 505 nm absorption band of the assumed I_2 fragment (Fig. 5.1a) should appear as PA in the DADS of the fast decay (Fig. 5.9b, black). However, the observed PA is located in the UV and matches the 395 nm absorption band of I_2^- rather than the I_2 signal. Moreover, an oscillation with the vibrational frequency of I_2^- is present in the TA data (as discussed in Sec. 5.6) whereas an I_2 oscillation is absent, suggesting that only I_2^- is formed. An alternative explanation for the biexponential decay is an ET rate which is much faster for hot contact pairs than for cold ones. Thus, a direct recombination occurs during the first few picoseconds, whereas after cooling ($\tau_3 = 5.4$ ps) the electron is trapped and therefore the ET takes longer ($\tau_2 = 91$ ps). Such a behaviour was first observed for ion pairs in a low-dielectric solvent [191] and recently the vibrational dependence of ET rates was utilized to control different ET pathways in donor-acceptor molecules [192]. A consequence of this reaction path would be a delayed, sequential formation of the cool contact pairs, which would be mimicked in the parallel fit model by a negative absorption signal in the DADS of the preceding hot contact pairs. This signal should appear at the position of the cool I_2^- fragment, i.e., at the red edge of the GSB which should therefore be red-shifted, and indeed a red shift of the GSB to 370 nm is observed. Alternative origins for the red shift of the GSB would require an additional photoproduct or excited state for a PA or ESA at the blue edge of the GSB, or a SE at the red edge of the GSB.

5.4. Transient absorption signals of the other five trihalides

The TA signals in DCM solution were also recorded for the Br_3^- , $I Br + Br^-$, $ICl + Cl^-$, $I_2 + Br^-$, $I_2 + Cl^-$ samples, which were pumped at 348 nm or 261 nm and probed with (310–610) nm WL or with (270–515) nm WL, respectively (Fig. 5.11). All best-fit parameters are summarized in Tab. 5.2, while the corresponding OADS, DADS, and fit residuals can be found in the Figs. 5.12 to 5.16. The fit model introduced for I_3^- was also used as a starting point to fit the different TA data and yielded conclusive results, although in some cases a few modifications were necessary as outlined next. The dissociation reaction generally was faster compared to I_3^- and therefore the Gaussian-

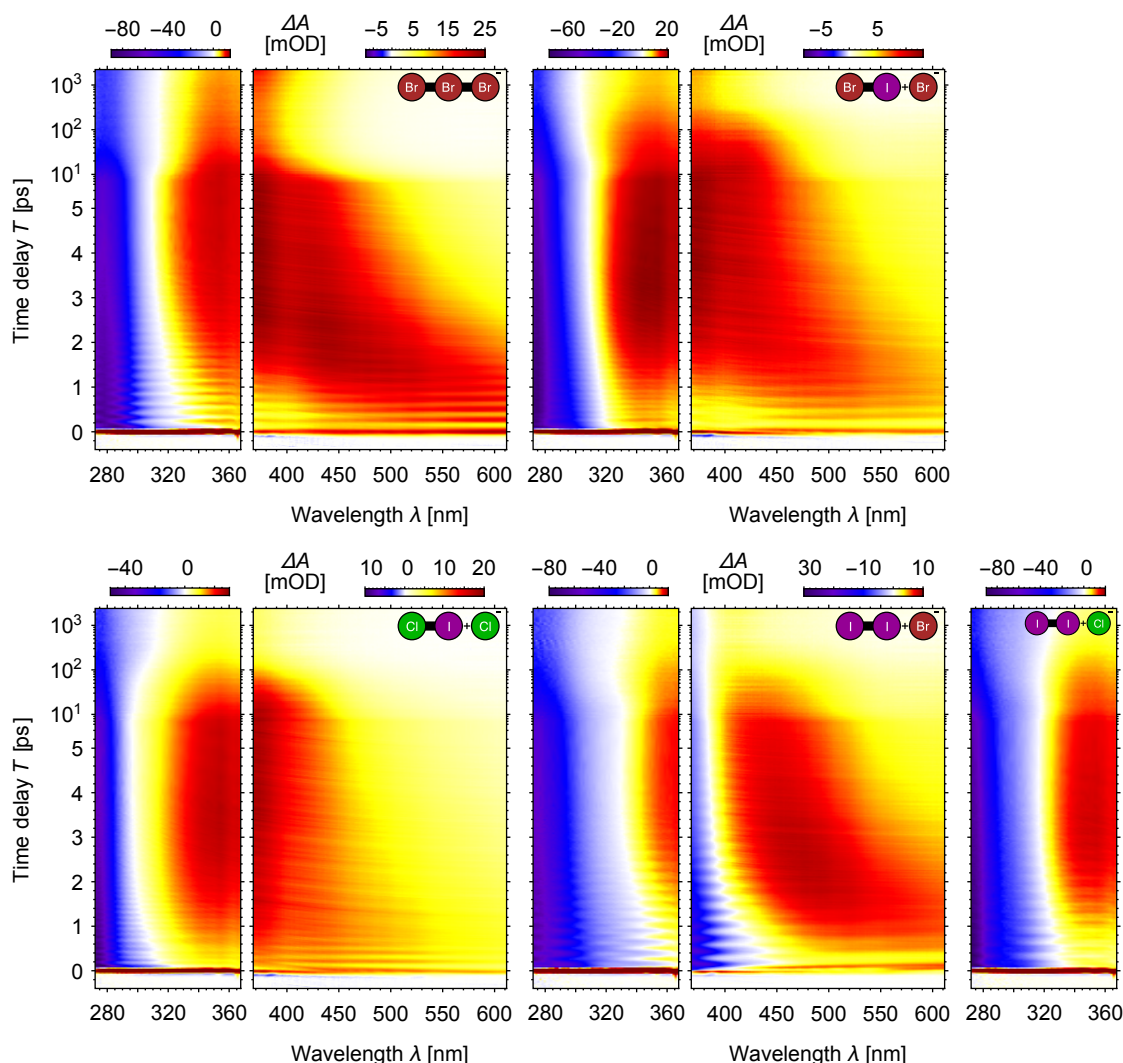


Figure 5.11.: TA data for the different trihalide samples Br_3^- , $\text{IBr} + \text{Br}^-$, $\text{ICl} + \text{Cl}^-$, $\text{I}_2 + \text{Br}^-$, and $\text{I}_2 + \text{Cl}^-$ pumped at 261 nm (narrow panels) and at 348 nm (wide panels). For the latter $\text{I}_2 + \text{Cl}^-$ only the TA data with 261 nm pump was measured. Note that the data sets do not necessarily show the same dynamics which would make it possible to just concatenate them, but due to the pump-wavelength variation a different behaviour can be probed, e.g. three-body dissociation only occurs for deep-UV excitation. Also note the logarithmic time scale for delays larger than 5.5 ps. More detailed graphs including the full wavelength range of the TA data as well as the DADS, OADS, and fit residuals are displayed in the Figs. 5.12 to 5.16. [3, Fig. 6] - Reproduced by permission of the PCCP Owner Societies

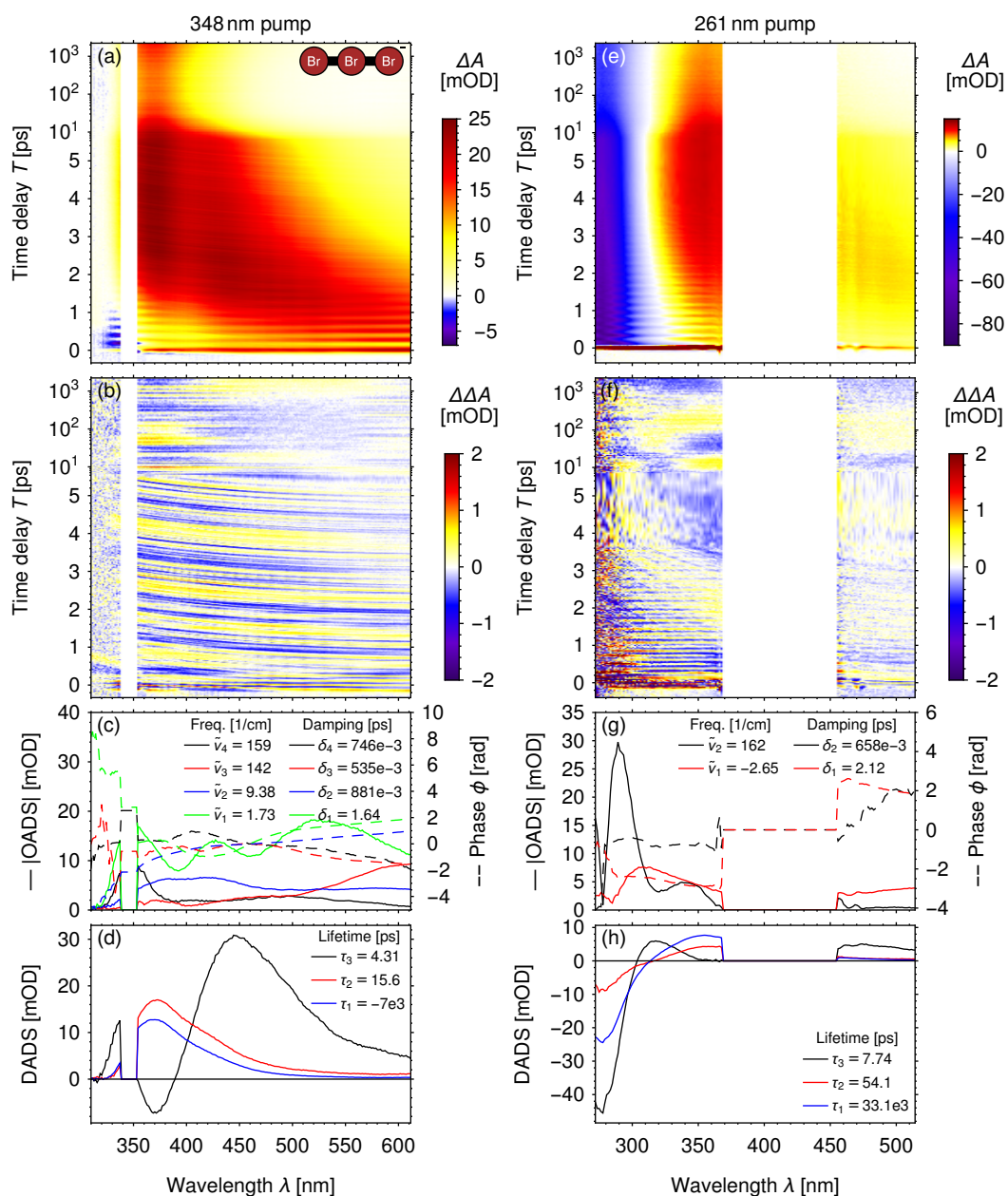


Figure 5.12.: Transient absorption data of Br_3^- pumped at 348 nm (a)-(d) and pumped at 261 nm (e)-(h). The transient absorption spectra (a), (e) were fitted similar to I_3^- , where also the weak fragment oscillations of the fit residuals (b), (f) are discussed. Like for I_3^- , the main part of the Br_3^- model function consists of a combination of damped oscillations and decaying exponentials with the corresponding OADS (c), (g) and DADS (d), (h), respectively. [3, Fig. S6] - Reproduced by permission of the PCCP Owner Societies

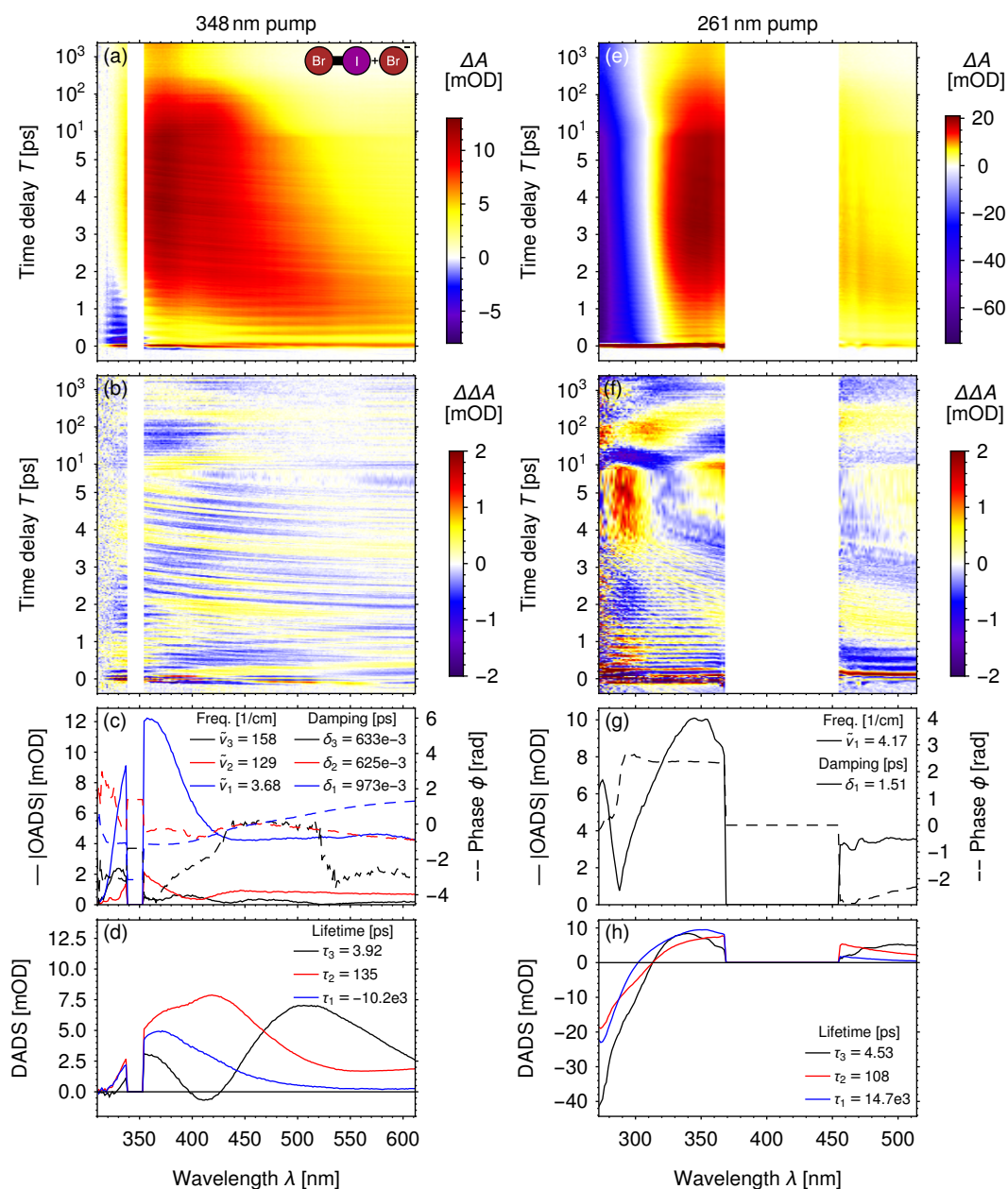


Figure 5.13.: Transient absorption data of the $\text{IBr} + \text{Br}^-$ sample pumped at 348 nm (a)-(d) and pumped at 261 nm (e)-(h). The transient absorption spectra (a), (e) were fitted similar to I_3^- , where also the weak fragment oscillations of the fit residuals (b), (f) are discussed. Like for I_3^- , the main part of the IBr_2^- model function consists of a combination of damped oscillations and decaying exponentials with the corresponding OADS (c), (g) and DADS (d), (h), respectively. [3, Fig. S7] - Reproduced by permission of the PCCP Owner Societies

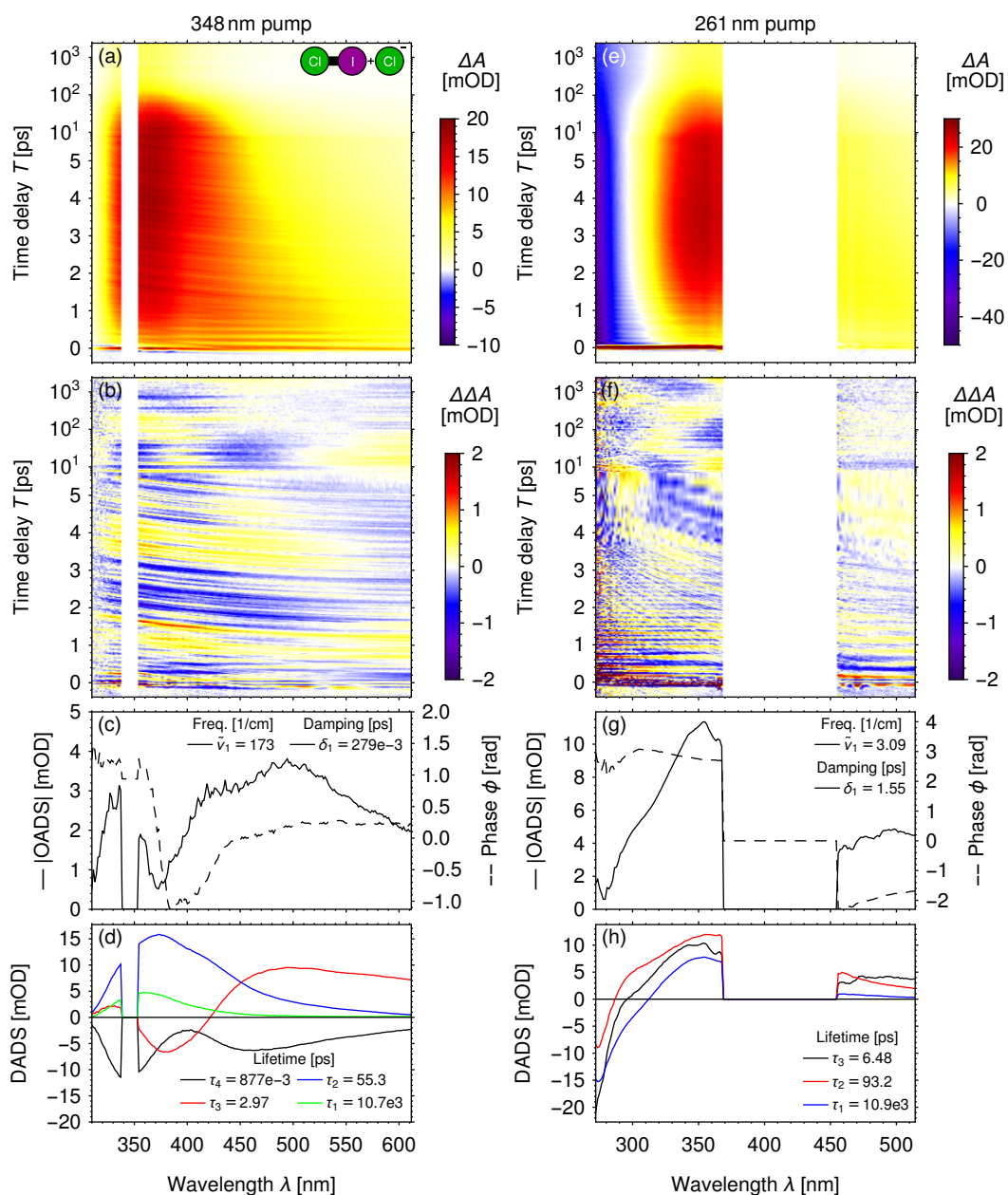


Figure 5.14.: Transient absorption data of the $\text{ICl} + \text{Cl}^-$ sample pumped at 348 nm (a)-(d) and pumped at 261 nm (e)-(h). The transient absorption spectra (a), (e) were fitted similar to I_3^- , where also the weak fragment oscillations of the fit residuals (b), (f) are discussed. Like for I_3^- , the main part of the ICl_2^- or the $\text{ICl}_2^-/\text{I}_2\text{Cl}^-$ model functions consists of a combination of damped oscillations and decaying exponentials with the corresponding OADS (c), (g) and DADS (d), (h), respectively. [3, Fig. S8] - Reproduced by permission of the PCCP Owner Societies

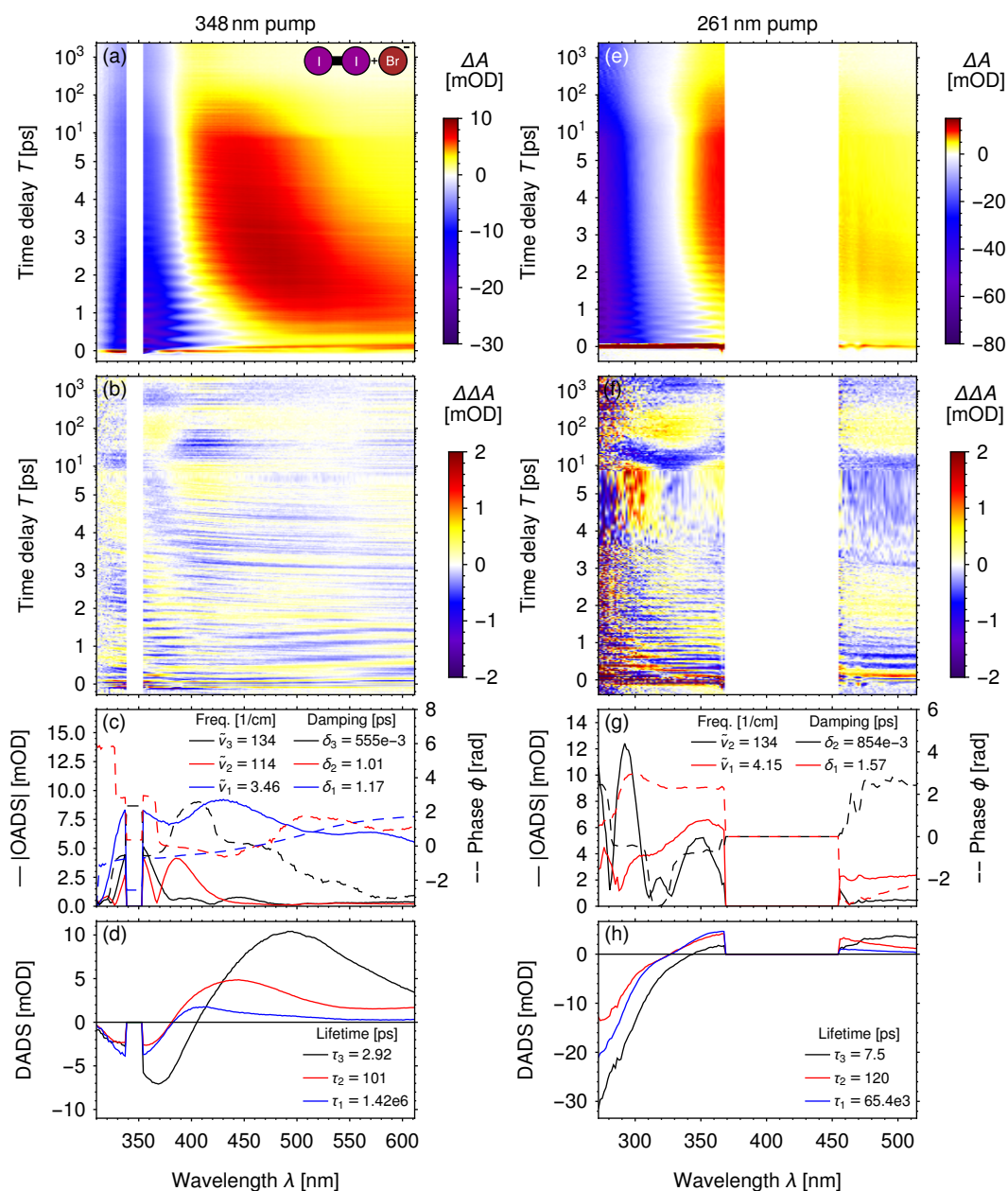


Figure 5.15.: Transient absorption data of $I_2 + Br^-$ pumped at 348 nm (a)-(d) and pumped at 261 nm (e)-(h). The transient absorption spectra (a), (e) were fitted similar to I_3^- , where also the weak fragment oscillations of the fit residuals (b), (f) are discussed. Like for I_3^- , the main part of the I_3^-/I_2Br^- model functions consists of a combination of damped oscillations and decaying exponentials with the corresponding OADS (c), (g) and DADS (d), (h), respectively. [3, Fig. S9] - Reproduced by permission of the PCCP Owner Societies

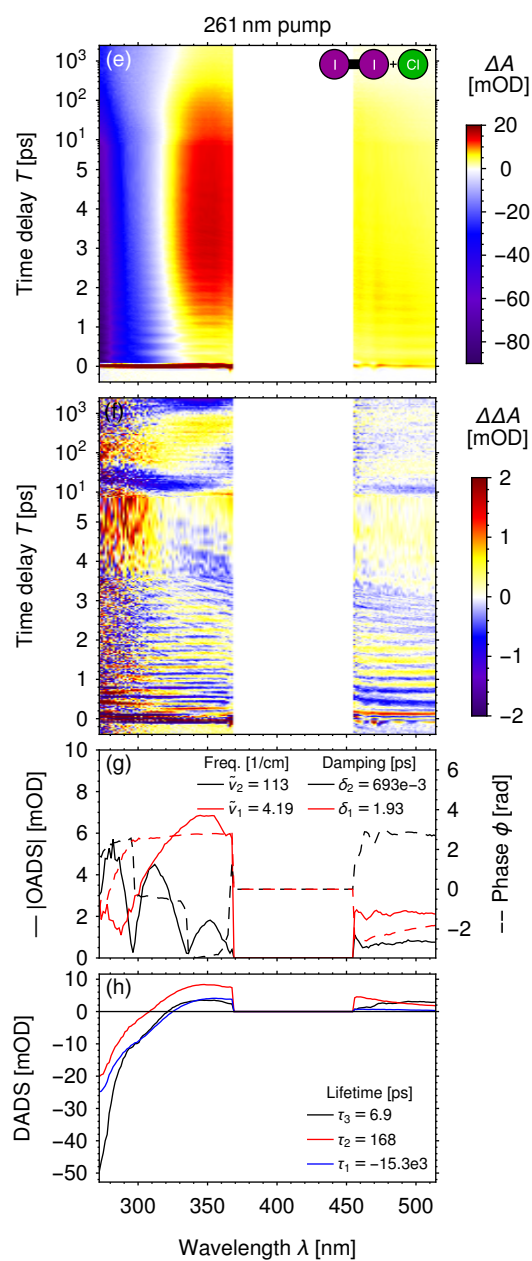


Figure 5.16.: Transient absorption data of $I_2 + Cl^-$ pumped at 261 nm. The transient absorption spectra (a) were fitted similar to I_3^- , where also the weak fragment oscillations of the fit residuals (b) are discussed. Like for I_3^- , the main part of the I_3^-/I_2Cl^- model functions consists of a combination of damped oscillations and decaying exponentials with the corresponding OADS (c) and DADS (d), respectively. [3, Fig. S10] - Reproduced by permission of the PCCP Owner Societies

shaped WP travelling through the bond-fission state could not be separated from the CA, resulting in a broader CA. Furthermore, the ICl + Cl⁻ sample pumped at 348 nm required a fourth exponential lifetime τ_4 instead of a low-wavenumber contribution, while Br₃⁻ pumped at 348 nm required two low-wavenumber components. Some of the low-wavenumber oscillations come with a conspicuous large error, making the peak-shift interpretation less reliable. Finally, the number of the fitted WP oscillations differs according to the number of reactants or fragment molecules in the sample.

Common for all measurements are three exponential lifetimes, which are interpreted in analogy to the three lifetimes of I₃⁻: The shortest lifetime τ_3 originates from an anionic dimer and represents a hot and therefore possibly fast ET and subsequent recombination with the neutral atom from the photofragmentation process. This fast ET slows down after the fragments have cooled, giving rise to a longer lifetime τ_2 that describes recombination of fragment pairs that are then trapped in the solvent cage. The third lifetime τ_1 , which is infinite with regard to the measured time window, represents permanently separated fragment pairs.

Measuring six different trihalides in an identical manner allows for a direct comparison and several inferences. Despite the fact that the fast decay τ_3 is within the error the same for all measurements except for I₂ + Br⁻ pumped at 348 nm and 261 nm, a trend can be seen. With 348 nm pump pulses τ_3 decreases for lighter elements and for non-D_{∞h}-symmetric molecular species. For the measurements with 261 nm pump pulses, all τ_3 values are larger than for 348 nm pump pulses. This slightly slower decay suggests that the larger photon energy of the 261 nm pump results in a higher vibrational excess energy transferred to the dihalide anion, and this excess energy takes longer to be distributed to the environment.

The TA data further disclose that the assumed ET with subsequent fragment recombination exhibits a much more pronounced sensitivity on the sort of involved halogen atoms for cool fragments than for hot fragments. This is evident from the data in Tab. 5.2, showing that in contrast to the very similar τ_3 lifetimes, the τ_2 lifetimes show a much stronger trihalide dependence.

For τ_2 associated with the recombination of cooled ion pairs, one might expect no changes for the pump wavelength either set to 348 nm or 261 nm as long as the same fragments are formed, because the vibrational excess energy has already been transferred to the solvent on this time scale. Yet, within the fit error, τ_2 determined for both pump wavelengths coincides only for IBr + Br⁻ and I₂ + Br⁻, but not for Br₃⁻ and ICl + Cl⁻ for which τ_2 increases for deep-UV pumping. A putative explanation is that since the fragments initially exhibit more excess energy, they can also separate further, which slows down the subsequent recombination process. Furthermore, for the ICl + Cl⁻ sample, investigating the WP oscillations in Fig. 5.17h reveals that due to the chemical equilibration, I₂Cl⁻ is present as a reactant besides the target molecule ICl₂⁻. Since the 261 nm pump is close to the I₂Cl⁻ resonance, more I₂⁻ and less ICl⁻ fragments are generated, obscuring the TA data and causing increase for the fitted τ_2 value.

The frequencies of the coherent WP motion may provide a more intuitive picture of the distributions of reactant trihalides and fragment dihalides than the overlapping absorption bands do. Therefore, the WP oscillations observed in the TA data are analysed

Table 5.3.: Calculated vibrational wavenumbers for trihalide/fragment molecules of $D_{\infty,h}$ symmetry and their IR and Raman (R) activity. In addition, published experimental values are given in parentheses.

	sym. stretch $\tilde{\nu}_1$ [cm^{-1}] (R)	bend $\tilde{\nu}_2$ [cm^{-1}] (IR)	asym. stretch $\tilde{\nu}_3$ [cm^{-1}] (IR)
I–I	219 (209) ^a	-	-
[I–I] ⁻	115 (114) ^b	-	-
Br–Br	325 (316) ^a	-	-
[Br–Br] ⁻	163 (165) ^b	-	-
Cl–Cl	553 (546) ^a	-	-
[Cl–Cl] ⁻	260 (271) ^b	-	-
[I–I–I] ⁻	115 (114)	59 (52)	142 (145) ^c
[Br–Br–Br] ⁻	166 (164)	91 (53)	190 (191) ^c
[Cl–Cl–Cl] ⁻	254 (275)	163 (165)	266 (232) ^d
[Br–I–Br] ⁻	162 (162)	76 (64)	174 (174) ^c
[Cl–I–Cl] ⁻	232 (269)	108 (127)	262 (226) ^c
[Cl–Br–Cl] ⁻	238 (278)	130 (135)	269 (225) ^c

^aRaman in DCM, cyclohexane or carbon tetrachloride [193]

^bTime-resolved resonance Raman in N_2O saturated aqueous solution [194]

^cIR and Raman in DCM [148]

^dIR and Raman in benzene/acetonitrile [195]

in great detail in Sec. 5.6, but first the characteristic wavenumbers of all possible species are determined in a theoretical investigation.

5.5. Ab-initio frequency calculations

Ab-initio frequency calculations were performed by Jan Hrušák (J. Heyrovský Institute of Physical Chemistry v.v.i., Academy of Sciences of the Czech Republic, Dolejškova 3, 182 23 Praha 8, Czech Republic) to determine the characteristic wavenumbers of the complete iodine–bromine–chlorine series of stable anionic trihalide isomers and their possible neutral or anionic diatomic photodissociation fragments. This theoretical investigation complements the calculations on different subsets of the trihalide series, which are already available in the literature [151, 152, 165, 198–200], and provides a systematic series of theoretical vibrational frequencies, which are comparable regarding to the (now higher) quality of the calculation method and the size of the used basis set.

Highly correlated quantum-chemical calculations provide a powerful tool in predicting physico-chemical properties. For small atomic clusters like in the present case quantitative agreement with the experiments can be expected if a complemented basis set is used in conjunction with the inclusion of correlation energy. In addition, heavy-elements-containing species exhibit relativistic effects, which have significant influence on the results of the calculations. One convenient way to avoid expensive solutions based on Dirac-Hartree-Fock equations is the use of pseudopotentials, by which the major rel-

Table 5.4.: Calculated vibrational wavenumbers for trihalide/fragment molecules of $C_{\infty v}$ symmetry and their IR and Raman (R) activity. In addition, published experimental values are given in parentheses.

	sym. stretch $\tilde{\nu}_1$ [cm^{-1}] (IR,R)	bend $\tilde{\nu}_2$ [cm^{-1}] (IR,R)	asym. stretch $\tilde{\nu}_3$ [cm^{-1}] (IR,R)
I–Br	272 (262) ^a	-	-
[I–Br] ⁻	139 (136) [165]	-	-
I–Cl	389 (374) ^a	-	-
[I–Cl] ⁻	193 (180) ^b	-	-
Br–Cl	442	-	-
[Br–Cl] ⁻	215	-	-
[I–I–Br] ⁻	132 (138)	68	164 (157) ^c
[I–I–Cl] ⁻	138 (155)	84 (107)	233 (324) ^c
[Br–Br–Cl] ⁻	186	109	245
[Br–I–Cl] ⁻	172 (177)	93	242 (232) ^d

^aRaman in DCM, cyclohexane or carbon tetrachloride [193]

^bAll-electron MR-CI calculation [196]

^cRaman on crystals with $(\text{CH}_3)_4\text{N}^+$ or $\text{Cu}(\text{NH}_3)_4^{2+}$ cations [197]

^dRaman in chloromethane [144]

ativistic effects (mass–velocity and Darwin terms) are easily included in a parametric way into the pseudopotentials, while at the same time the valence electrons are treated by the non-relativistic Schrödinger equation. Several relativistic pseudopotentials (or effective core potentials – RECP) were generated and successfully tested over the last three decades. These RECPs include the two major relativistic contributions to atomic properties (i.e., the mass–velocity and Darwin terms) and allow the molecular calculation being performed in a traditional non-relativistic formalism. In the present thesis, the well-established RECP parametrizations of the Stuttgart group [201–205] are applied for Br and I to replace the inner-shell electrons by the core potential. These RECP are used in conjunction with the correlation-consistent basis set of Martin and Sundermann, [206] which is contracted to approximately quintuple zeta quality and saturated with respect to the electronic correlation by four d-polarization functions, three f-polarization functions and two g-type polarization functions (15s12p4d3f2g/5s5p4d3f2g). Similar basis set contraction has been proven sufficient to achieve quantitative agreement of the calculated first-order properties of small iodine clusters [198] with the corresponding experimental values. The experimental electron affinities, equilibrium bond lengths, harmonic vibrational frequencies, dissociation and excitation energies of neutral and charged iodo clusters can be reproduced with an average accuracy of about four percent. Similarly to these calculations, the coupled-cluster CCSD(T) method was employed, [207] which was proven to be superior to the QCISD(T) method [208]. For the chlorine atom, the 1s orbital was not replaced by a RECP but the all-electron aug-cc-pV5Z basis was used [209]. All valence electrons have been correlated in the coupled-cluster calculations irrespectively if a RECP or an all-electron basis was employed. The geometry optimization and

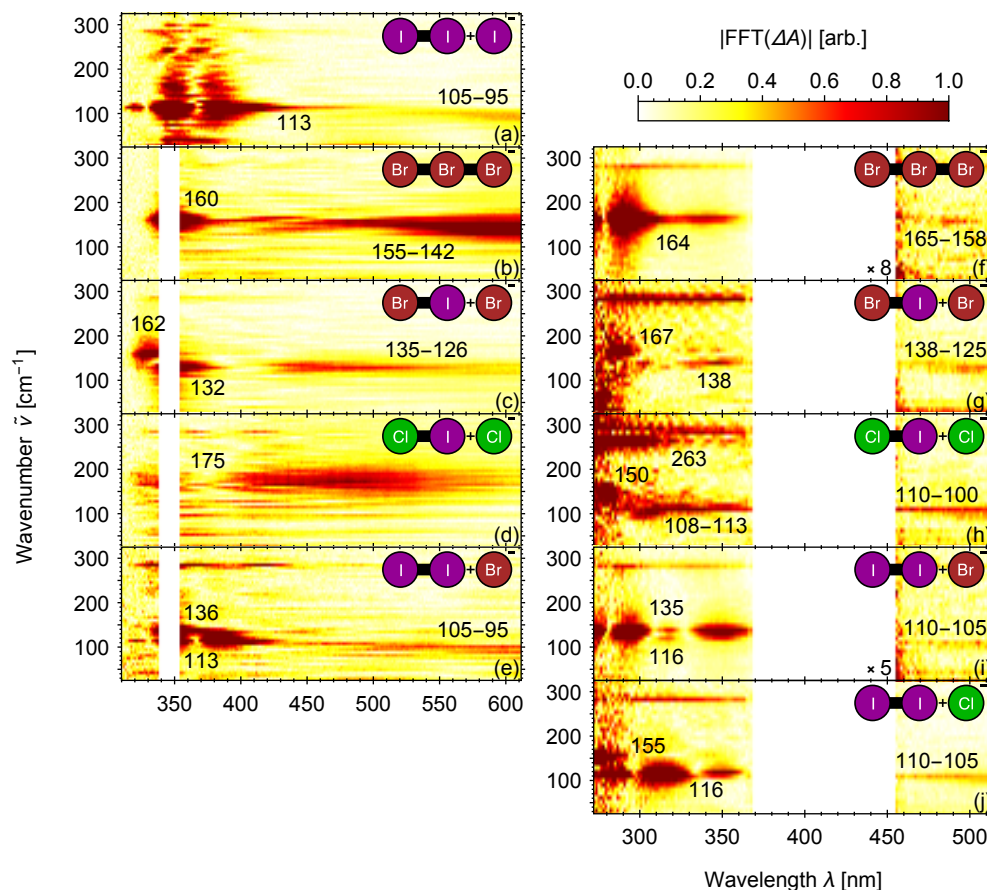


Figure 5.17.: Amplitude of the Fourier-transformed WP oscillations pumped at 348 nm [(a) to (e)] and at 261 nm [(f) to (j)]. To simultaneously consider the strong, already fitted oscillations and the weak ones remaining in the fit residuals, the former were rescaled and the sum of both was then Fourier transformed. The most prominent peaks are labelled with their respective wavenumber. [3, Fig. 7] - Reproduced by permission of the PCCP Owner Societies

the subsequent calculation of vibrational harmonics were done with the GAUSSIAN09 program [210] using numerical derivatives of the potential energy. No symmetry constraints were applied a priori in the calculations. The resulting vibrational wavenumbers are presented in Tab. 5.3 and Tab. 5.4 together with experimental values from former Raman (R) or infrared (IR) measurements.

5.6. Reactant and fragment identification

Each trihalide and each of the possible diatomic fragments has a characteristic vibrational wavenumber, which should occur in the WP oscillations if the corresponding species is present in the sample and symmetry selection rules allow its observation. Therefore, the fitted, non-oscillating background was removed and the remaining oscil-

lations were Fourier-transformed with respect to the time delay T to identify reactant mixtures, e.g. for I_2Cl^- (Fig. 5.1c), as well as possible competing fragmentation pathways. To identify also weak oscillations from the fit residuals simultaneously with the strong ones already fitted in the OADS, the latter were rescaled before the sum of both was Fourier-transformed. The resulting spectral amplitude, i.e., the absolute value of the Fourier-transformed signal, is depicted in Fig. 5.17, where panels a–e represent experiments with 348 nm pump pulses and probed with (310–610) nm WL, while for panels f–j 261 nm pump and (270–515) nm WL probe pulses were used. Signal contributions below 50 cm^{-1} are neglected, because this wavenumber region is disturbed by low-wavenumber fluctuations of the laser sources. For all samples, the 285 cm^{-1} oscillation of DCM could be observed, in some samples even the 700 cm^{-1} and 740 cm^{-1} oscillations of DCM [211–220]. Furthermore, a 490 cm^{-1} oscillation occurred in nearly every sample. This signal is considered to be an artefact, because it does not belong to DCM and its structure shows no sample dependence.

In the following, the observed vibrational dynamics will be discussed for each of the investigated trihalide samples:

(a) $\text{I}_2 + \text{I}^-$: Like in the OADS in Fig. 5.9a, two pronounced 113 cm^{-1} peaks, which match the symmetric stretch vibration of I_3^- , appear at 350 nm and 385 nm, respectively, i.e., the peaks are centered around the GSB at 366 nm and therefore correspond to the C-absorption band of I_3^- . In addition, the red edge of the D-absorption band reaches the spectral detection window and gives rise to a weak 113 cm^{-1} peak at $\approx 320\text{ nm}$. All peaks show a Lorentzian lineshape due to the exponential decay of the corresponding oscillation in the time domain.

The intense GSB and symmetric stretch oscillation increase the noise amplitude in the 330 nm to 390 nm region, which makes it difficult to identify weaker oscillations. Two small peaks at 143 cm^{-1} are found at 350 nm and 385 nm, respectively, representing the asymmetric stretch of I_3^- , which indicates that the DCM environment breaks the $\text{D}_{\infty\text{h}}$ symmetry of I_3^- and leads to a Raman-active asymmetric stretch vibration, as also observed by Gabes and Gerding [148]. Furthermore, two 163 cm^{-1} peaks appear at the same wavelengths. Since this wavenumber does not match any of the I_3^- , I_2^- or I_2 vibrations or higher harmonics, it may be assigned to a polyiodide consisting of more than three atoms [221]. The two 245 cm^{-1} peaks, which can be seen at 345 nm and 368 nm, respectively, i.e., blue-shifted with respect to the C-absorption band of I_3^- , might be assigned to the combination band previously reported at $(253 \pm 2)\text{ cm}^{-1}$ [124].

At 600 nm, a 95 cm^{-1} signal appears, which narrows and shifts to higher wavenumbers for decreasing wavelengths in the PA region until it reaches 105 cm^{-1} at $\approx 500\text{ nm}$. Such a behaviour can be explained with a vibrationally hot I_2^- fragment that oscillates in the beginning at lower wavenumbers due to the PES anharmonicity [222] and cools down to larger wavenumbers at later delay times. The cooling effect can also explain the narrowing and the blue shift of the PA band (see Sec. 5.3), which in turn might be the reason for the wavelength-dependent wavenumber shift. An alternative interpretation for the wavelength dependence is based on the filter effect of the Franck–Condon window, which limits the accessible vibrational states depending on the wavelength of the optical transition [126]. Furthermore, the I_3^- signal intensifies towards UV wavelengths and

since I_3^- and (cool) I_2^- have nearly the same fundamental wavenumber, it is not clear at which wavelength the I_2^- signal ends and the I_3^- signal starts [126]. Finally, the small interfragment distance at the beginning deforms the I_2^- PES and therefore influences the vibrational wavenumber, which will change for an increasing fragment separation [126].

(b) Br_3^- : In analogy to the $\text{I}_3^-/\text{I}_2^-$ system in (a), the 160 cm^{-1} peak which is evident in the GSB region was assigned to the symmetric stretch of Br_3^- . In the same way, also a cooling Br_2^- fragment can be identified, giving rise to the narrowing signal that shifts from 142 cm^{-1} to 155 cm^{-1} in the PA region.

(c) $\text{IBr} + \text{Br}^-$: an oscillation at 162 cm^{-1} is found, which however appears at a different wavelength position compared to the observation in (b). Therefore, it is assigned to the symmetric stretch of IBr_2^- and not to Br_3^- which could also be present in the sample due to equilibration. The asymmetric stretch of I_2Br^- , another possible side-reactant, is also ruled out, since the 162 cm^{-1} peak is absent in a sample [discussed under (e)] which clearly contains I_2Br^- . Furthermore, the 132 cm^{-1} oscillation is assigned to the IBr^- fragment instead of the symmetric stretch of I_2Br^- , for which a different signature is observed in (e). Finally, the contribution spanning from 126 cm^{-1} to 135 cm^{-1} corresponds to IBr^- and the wavenumber shift is again explained by the cooling effect.

(d) $\text{ICl} + \text{Cl}^-$: Since ICl_2^- absorbs deep in the UV at 230 nm (Fig. 5.1c), only the PA region lies in the spectral detection window. There, an oscillation at 175 cm^{-1} is observed, which originates from the ICl^- fragment. In contrast to the measurements (a) to (c), no clear wavenumber shift can be seen.

(e) $\text{I}_2 + \text{Br}^-$: For this sample, the I_3^- signature at 113 cm^{-1} and the I_2^- signature spanning from 105 cm^{-1} to 95 cm^{-1} , as known from (a), are clearly visible. Furthermore, a 136 cm^{-1} oscillation appears, which is much stronger than in (c) and consists of two out-of-phase peaks instead of only one peak. In contrast to (c), the 126 cm^{-1} to 135 cm^{-1} oscillation is barely visible. Therefore, the 136 cm^{-1} peak is assigned to I_2Br^- (symmetric stretch), a reactant which mainly gives rise to the I_2^- fragment upon photolysis as it was observed for the liquid phase [119, 120, 164].

The following oscillations have been identified in the TA data with 261 nm excitation:

(f) Br_3^- : The pronounced 164 cm^{-1} peaks located below 270 nm and at 290 nm originate from the D-absorption band of Br_3^- , while the 164 cm^{-1} peak at $\approx 342\text{ nm}$, which is also visible in (b), most likely is due to the C- or B-absorption band. In contrast to (b), here the 342 nm peak is less intense as a consequence of the lower concentration of Br_3^- , which is required to prevent saturation of the strong D-absorption band. After magnifying the VIS region by a factor of eight, a very weak signal spanning from 158 cm^{-1} to 165 cm^{-1} becomes visible, representing the coherent oscillation of the Br_2^- fragment. Thus, it seems that for pumping at 261 nm instead of 348 nm the WP dephasing is much faster or the Br_2^- fragment formation is less efficient. The latter aspect is substantiated by the possibility of a competing reaction channel, namely three-body dissociation as also observed for I_3^- pumped at 266 nm [39].

(g) $\text{IBr} + \text{Br}^-$: Like for the 348 nm pump measurement in (c), the 167 cm^{-1} oscillation is assigned to the symmetric stretch of IBr_2^- and the contribution spanning from 138 cm^{-1} to 125 cm^{-1} is associated with the IBr^- fragment. Around 350 nm, the 167 cm^{-1} peak is much weaker than in (c), because here the overall reactant concentration is reduced

to avoid saturation of the strong D-absorption band of IBr_2^- . Br_3^- would also match as putative origin of the 167 cm^{-1} peak, but it is ruled out since no corresponding signal is present in (c).

(h) $\text{ICl} + \text{Cl}^-$: The 263 cm^{-1} symmetric stretch vibration of ICl_2^- is now visible, in contrast to the data of (d), yet the 175 cm^{-1} signature of ICl^- vanished. The latter might result from pumping at 261 nm instead of 348 nm leading to a faster WP dephasing or a predominant, alternative reaction channel, e.g., three-body dissociation.

In addition, a 150 cm^{-1} peak matching the symmetric stretch wavenumber of I_2Cl^- appears. Therefore, in spite of the ICl_2^- purification due to Cl^- excess (Sec. 5.1), a low concentration of I_2Cl^- must still be present due to equilibration. Since the 261 nm pump wavelength is resonant with the I_2Cl^- absorption (Fig. 5.1c), a signal of measurable intensity may occur for such low concentrations.

Two further signals are identified, one spanning from 108 cm^{-1} to 113 cm^{-1} and the other one from 110 cm^{-1} to 100 cm^{-1} , respectively. Both signals are attributed to the I_2^- fragment, which results from the photodissociation of I_2Cl^- . I_3^- is ruled out as source of the 113 cm^{-1} signal, because the three typical 113 cm^{-1} peaks from (a) and (j) are missing, instead only one peak shifting from 108 cm^{-1} to 113 cm^{-1} can be seen in this wavelength region. Furthermore, the phase of the 108 cm^{-1} to 113 cm^{-1} oscillation is shifted about π with respect to the phase of the 110 cm^{-1} to 100 cm^{-1} oscillation, as it is expected for a WP which is trapped on the ground-state PES associated with the 395 nm absorption band of I_2^- . Like for (a), the wavenumber shift can be explained by vibrational cooling on an anharmonic PES. In the beginning, the broad, red-shifted PA spectrum of a hot I_2^- fragment causes a low-wavenumber oscillation observable far away from the absorption's band-center wavelength. While cooling down, the PA spectrum narrows and blue-shifts, and therefore the oscillation signal of increasing wavenumber moves towards the center wavelength. Such a behaviour was also observed for the 740 nm absorption band of I_2^- , [126] but the wavenumber shift was explained with the wavelength-dependent wavenumber filter effect of the Franck–Condon window and the PES-disturbing small interfragment distance at the beginning of the dissociation reaction.

(i) $\text{I}_2 + \text{Br}^-$: In analogy to the observations in (e), the strong 135 cm^{-1} peaks are assigned to the symmetric stretch of I_2Br^- , while the 110 cm^{-1} to 105 cm^{-1} contribution is associated with the I_2^- fragment. The latter is much weaker than in (e) and requires a relative magnification of five to become visible in one plot together with the other peaks. Also a weak 116 cm^{-1} contribution from I_3^- , which overlaps with the 135 cm^{-1} peaks, can be seen. This signal is weak, because the 261 nm pump wavelength is not in resonance with any of the I_3^- absorption bands.

(j) $\text{I}_2 + \text{Cl}^-$: The signature of the $\text{I}_3^-/\text{I}_2^-$ system is evident in the 116 cm^{-1} oscillation and the contributions spanning from 110 cm^{-1} to 105 cm^{-1} . Furthermore, the 155 cm^{-1} symmetric stretch vibration of I_2Cl^- already known from (c) occurs. Since no spectral feature of ICl^- is observed, I_2^- must be the main fragment of the I_2Cl^- photodissociation. Thus, although two different dihalide anion fragments are conceivable from I_2Cl^- , only the bond between the center iodine and the chlorine atom is cleaved upon deep-UV photoexcitation.

5.7. Conclusion

In agreement with former time-resolved experiments on I_3^- in the VIS-NIR range, [22] both the GSB and the PA of I_3^- show a biexponential decay ($\tau_3 = 5.4$ ps, $\tau_2 = 91$ ps) associated with fragment recombination and a permanent signal, which is assigned to the UV absorption band (395 nm) of long-lived I_2^- fragments that escaped their I partner and are therefore stable within the scanned time window of 2 ns. Despite the lack of the exact PA band position due to the overlapping GSB, the slow recombination decay $\tau_2 = 91$ ps seems to be accompanied by a blue shift of the PA band. Baratz and Ruhman observed the same behaviour much more clearly for the NIR absorption band of I_2^- (740 nm) [22] and the interpretation within this thesis follows their inference that the blue shift stems from the recombination of caged $I_2^- + I$ contact pairs, whose PA is red-shifted compared to free I_2^- due to the small interfragment distance. The existence of such long-lived contact pairs was explained by Baratz and Ruhman with the necessity of an ET process that has to take place before the actual recombination, whereas they assigned the fast decay $\tau_3 = 5.4$ ps to $I_2 + I^-$ contact pairs, which can recombine directly. Since neither the PA band nor the vibrational wavenumber of I_2 could be observed in the experiment presented in this thesis, it is suggested that no or only very few $I_2 + I^-$ contact pairs are formed and that instead the biexponential decay stems from a vibrational-dependent ET rate [191, 192] which slows down as the $I_2^- + I$ contact pairs cool down. On longer time scales, the assumed absence of $I_2 + I^-$ fragments is further supported by time-resolved X-ray liquidography experiments with 100 ps time resolution [160].

For the other trihalides (Sec. 5.4), the observations in the TA studies can be interpreted in close analogy to the case of I_3^- . All processes identified for I_3^- also occur in the other trihalides, yet with different time constants. In particular, no indication for a neutral diatomic fragment was found, but the observed absorption signals point towards a fragmentation pattern where always the bond between the center atom and the lighter halogen atom is cleaved, yielding a fragment pair of a dihalide anion and a neutral atom of the lightest involved halogen.

On short time scales, i.e., below 2 ps, vibrational WP oscillations of such a pronounced amplitude were observed that for a successful fit of the transient absorption data they needed to be considered explicitly in the model function (Sec. 4.1), which made a custom implementation of the variable projection fitting algorithm necessary (Sec. 4.2). Beside the molecular vibrations, the oscillation function, introduced in this thesis, was also capable of fitting the non-exponential and blue-shifting dynamics within the first ps (Sec. 5.3). Such a non-exponential behaviour already occurred for I_3^- in isobutyl alcohol, [121] but instead of a low-wavenumber oscillation, Ruhman and coworkers used a polynomial function for modelling the signal curvature. To extract finer details of the possible reaction pathways, the oscillations were Fourier-transformed (Sec. 5.6) and compared to ab-initio quantum-chemical calculations (Sec. 5.5) for the characteristic vibrational wavenumbers of the reactants and diatomic fragments. For all investigated trihalide reactants, only one wavenumber could be assigned to a diatomic fragment. Therefore, the analysis of the coherent WP oscillations corroborates that for every trihalide only one predominant photodissociation channel towards one anionic dihalide fragment exists. While ICl_2^-

and IBr_2^- yield vibrational signatures of the only possible dihalide (the heteronuclear ICl^- and IBr^- , respectively), the finding of only one fragment is of special relevance in the case of the asymmetric trihalides I_2Br^- and I_2Cl^- , which result both in I_2^- as sole dihalide fragment. This confirms and extends the studies on I_2Br^- [120,164] where such a behaviour was previously reported.

For all investigated trihalides, the intensity of the fragment signals is weaker for deep-UV pumping as a consequence of the increasing importance of photoinduced three-body dissociation. For ICl_2^- pumped at 261 nm, the ICl^- signature was not even detectable. Broadband probing in the UV range allowed to determine a wavelength-dependent shift of the fragment oscillation wavenumbers, as found for I_2^- in the NIR range [126]. In line with conclusions drawn for experiments with only I_3^- , [117] the increasing wavenumber observed for all samples can be explained with a cooling WP which descends in an anharmonic potential.

6. Summary

The most basic molecule to test the possibility of controlling photodissociation reactions in the liquid phase requires at least two branching dissociation pathways, i.e., competing photofragmentation patterns that give rise to different product species originating from the same precursor. In the simplest case, a molecule consisting of only three atoms connected with two distinct chemical bonds is sufficient. Promising candidates of this kind can be found in the family of the trihalides. To test whether these molecules offer besides their simple structure also two branching dissociation pathways, the ultrafast photodissociation and the subsequent fragment caging and fragment recombination of the trihalide anions I_3^- , Br_3^- , IBr_2^- , ICl_2^- , I_2Br^- and I_2Cl^- in dichloromethane (DCM) solution were studied in this thesis with transient absorption spectroscopy (Sec. 5).

To reconstruct the reaction pathway, the fragments were identified by their characteristic wavepacket (WP) vibrations that originate from the photoinduced reactant vibrations, whose dephasing rates are slower than the photodissociation process. For each investigated trihalide only one diatomic fragment and therefore only one predominant photodissociation channel was found. While the symmetric I_3^- , Br_3^- , ICl_2^- and IBr_2^- yield I_2^- , Br_2^- , ICl^- and IBr^- , respectively, the asymmetric I_2Br^- and I_2Cl^- result both in I_2^- , but not in IBr^- or ICl^- , respectively. Furthermore, no oscillation wavenumber could be assigned to a neutral diatomic fragment. Thus, except for three-body dissociation at deep-UV excitation, no branching reaction pathways were observed. In the case of I_3^- , this finding also makes the direct formation of $\text{I}_2 + \text{I}^-$ fragments pairs unlikely. Therefore, the electron transfer process $\text{I}_2^- + \text{I} \longrightarrow \text{I}_2 + \text{I}^-$ that precedes the fragment recombination $\text{I}_2 + \text{I}^- \longrightarrow \text{I}_3^-$ [22] must be able to happen on different rates to explain the observed two recombination time constants occurring for only one fragment pair $\text{I}_2^- + \text{I} \longrightarrow \text{I}_3^-$. Probably, right after the photodissociation, the electron transfer process is mediated by vibrational excess energy that is then distributed to the environment and thus leads to trapped $\text{I}_2^- + \text{I}$ contact pairs.

On more general terms, this study shows how photoproducts can be identified from vibrationally coherent oscillations in broadband transient absorption electronic spectroscopy. For this purpose, simultaneous global fitting of kinetic and oscillating components was implemented in Mathematica as detailed in Sec. 4. This approach should be applicable to a large range of molecular systems and thus help advance the further extension of vibrationally coherent time-domain spectroscopy. A drawback of accessing the vibrational signal of dissolved molecules in the time domain instead of the frequency domain is the high dephasing rate, which rapidly averages out the wave packet oscillations. Only photophysical-/chemical processes that proceed faster than the dephasing may be investigated by observing their vibrational dynamics. Fortunately, the photodissociation of the trihalides (≈ 300 fs for I_3^-) is about three times faster than the

vibrational dephasing (≈ 1 ps for I_3^-). However, the fragment recombination dynamics and the behaviour of the solvent-trapped contact pair are beyond the dephasing time window. A possible strategy to overcome this limitation is to reactivate the molecules' oscillation with a second pump pulse, also called repump, as it is done in transient resonance impulsive stimulated Raman scattering (TRISRS) [111, 117, 223].

Besides the above mentioned contributions to the photodynamics of trihalides and the data evaluation procedure of ultrafast spectroscopy, two approaches (transition-probability approach in Sec. 3.2 and response-theory approach in Sec. 3.3) for calculating magic-angle conditions in third-order spectroscopy of isotropic molecular samples were introduced in the theoretical part of this thesis (Sec. 3). Allowing for elliptical polarization and arbitrary propagation directions of each laser pulse a generalized magic-angle condition (Sec. 3.4) was developed for elliptically polarized pulses, of which the linear and circular polarizations known from the literature are limiting cases. The generality of the approach allowed the investigation of the influence of the pump and probe propagation directions onto the magic-angle configuration and made the calculation of a corrected magic angle for a noncollinear geometry possible.

In addition, magic-angle configurations were found, under which the measured third-order signal does not depend on the phase differences between the polarization components of the pump δ_{pu} and/or the probe pulse δ_{pr} . Thus, if in such a configuration e.g. a δ_{pu} -dependent signal occurs, it results either from a higher-order interaction or the electric dipole approximation is violated. Such a signal could be isolated by polarization phase cycling of the phase difference δ_{pu} .

Furthermore, the results were also transferred to 2D spectroscopy (Sec. 3.5) and third-order spectroscopy in general utilizing the universality of the response-theory approach (Sec. 3.3). A configuration for magic-angle 2D spectroscopy in box geometry was suggested that avoids the often used approximation of nearly collinear beams.

Finally, in agreement with the literature, the anisotropy and its relation to the angle α between the corresponding transition dipole moments (TDMs) was calculated (Sec. 3.6), not only for a single signal but also for multiple overlapping signal contributions on the example of a two-fold degenerate TDM.

7. Outlook for quantum control

With the results of this thesis, it is now possible to outline a potential strategy for controlling the selectivity and efficiency of the trihalides' photodissociation reaction. It became clear that the heteronuclear trihalides with two distinct chemical bonds cannot easily be purified, because they always form a chemical equilibrium with all other trihalides thinkable for the halogen atoms involved in the synthesis (see Fig. 5.1). Even the signal of I_2Cl^- , which seemed to be spectroscopically selectable, is contaminated with signal contributions from other trihalides (see Fig. 5.17j). This is a serious issue, because one cannot easily trace back the origin of an observed photodissociation fragment and thus one cannot judge about the control efficiency of a specific pulse shape. Furthermore, none of the examined trihalides showed competing reaction pathways but all of them dissociate into a major, possibly sole dihalide fragment. Nevertheless, I_2Cl^- remains a promising test candidate. Indeed, one cannot tell if the observed I_2^- fragments stem from I_2Cl^- or I_3^- , but as soon as a ICl^- signal occurs, one can assume a successful control of the I_2Cl^- photodissociation in favour of the reaction channel towards the ICl^- fragment. However, the disadvantage of observing only one natural photodissociation channel is that a control experiment cannot just aim to perturb a fragile balance but one must overcome the given, possibly strong selectivity of the photoreaction. Therefore, a trial and error control attempt will turn into the famous search for the needle in a haystack, making a more concerted strategy necessary.

At this point it is advisable to recall the photodynamics of I_3^- already known from the literature, illustrated in Fig. 2.3. The reaction starts with a pump pulse that generates a wavepacket (WP) on the excited state potential energy surface (PES). Then, this WP evolves according to the PES's shape, which offers two reaction channels, each resulting in the cleavage of another chemical bond. Due to the symmetry of I_3^- , the WP is initially placed on the top of the barrier between the two reaction channels and can therefore enter both channels simultaneously. In contrast, for trihalides lacking this kind of symmetry, e.g., I_2Cl^- , one could expect that the barrier is shifted with respect to the initial WP position and thus guides the WP into a specific direction. This would explain the natural selectivity of the photodissociation reaction and for a successful control attempt, one then needs to place the WP on the other side of the barrier or give the WP an initial momentum sufficient to overcome the barrier.

However, none of these effects can be induced directly by the pump pulse, because a laser pulse can only alter the molecules' energy, i.e., it can only shift the WP between different PES while the WP's position and motion in the coordinate space depend on the molecular properties. Nevertheless, the control goal may be achieved indirectly following the Tannor-Kosloff-Rice scheme [5,6]: First, one utilizes a laser pulse to generate a WP on a PES that is appropriate to evolve the required WP position and/or momentum. Then,

with the help of a second laser pulse, the WP is transferred to the photodissociation PES, where it can now enter the desired reaction channel. A possible intermediate PES to prepare the WP properties might be given by the I_2Cl^- ground state, for which the formation of a WP due to RISRS was already observed in the transient absorption measurement. The question whether the ground state PES can help the WP to overcome the barrier on the photodissociation PES might be answered with a theoretical study of the WP dynamics. However, prior to that one needs to calculate the shape of the involved PES, because this information is only available for I_3^- [37] but not for the other trihalides.

Assuming that the ground state PES can be used to prepare the WP, one can further speculate about the properties required for the pump pulse(s). Since the I_3^- WP oscillates between 350 nm and 385 nm and a similar bandwidth can be expected for I_2Cl^- , just shifted towards the blue, the pump should either cover the whole spectral range of the WP oscillation or at least the two colors relevant for the two WP transitions necessary for the Tannor-Kosloff-Rice scheme. With the current spectroscopic setup (see Fig. 5.2), the pump bandwidth is in the range of 2 nm to 6 nm, far below the required value. Another challenge might be the pump intensity, which needs to be higher to access higher-order non-linear effects. The current pump intensity serves for third-order spectroscopy but might be too low to efficiently support the fifth-order pump–repump control scheme. A possibility to solve both issue might be the usage of a hollow core fibre instead of a noncollinear optical parametric amplifier (NOPA) to generate the pump pulse(s).

A. femtoTools package collection

The Mathematica packages (*.m-files) that are listed in the following subsections form the femtoTools collection, which offers various functions to process, fit and plot transient absorption data and to trace Gaussian beams through optical systems. Calling

```
<<femtoTools`;
```

includes the full collection in the current Mathematica notebook (*.nb-file) if either the femtoTools folder is placed at a location that is specified in the \$Path variable or if the location of the femtoTools folder is added

```
AppendTo[$Path,"L:/Mathematica"];
```

to the \$Path variable. If the latter command is added in the `init.m` file located in

```
FileNameJoin[{$UserBaseDirectory,"Kernel","init.m"}],
```

the \$Path variable is updated automatically on each startup of Mathematica. Note that each *.m-file was automatically created from a *.nb file by switching the option `AutoGeneratedPackage` under `Format` → `Option Inspector...` → `Global Preferences` to manual. Then, Mathematica asks if it should generate an *.m-file that contains the contents of the initialization cells (right-click cell bracket → select initialization cell). To display for one package, e.g., `parVarPro`, the available functions together with a short description call

```
?"femtoTools`parVarPro`"
```

and replace the term `parVarPro` with the desired package name.

A.1. Kernel/init.m

This *.m-file defines and loads the femtoTools package collection.

```
1 (* Mathematica Package *)
2 (* :Title: femtoTools *)
3 (* :Context: femtoTools` *)
4 (* :Summary: Package collection to fit a plot transient absorption data. *)
5 (* :Keywords: fitting, variable projection, nonlinear least square *)
6 (* :Author: Sebastian Schott, IPTC Universität Würzburg *)
7 (* :Mail: sebastian.schott[at]phys-chemie.uni-wuerzburg.de *)
8 (* :Licence:
9 Copyright 2016, Sebastian Schott
10
11 Licensed under the Apache License,Version 2.0 (the "License");
12 you may not use this file except in compliance with the License.
13 You may obtain a copy of the License at
```

```

14
15   http://www.apache.org/licenses/LICENSE-2.0
16
17   Unless required by applicable law or agreed to in writing, software
18   distributed under the License is distributed on an "AS IS" BASIS,
19   WITHOUT WARRANTIES OR CONDITIONS OF ANY KIND, either express or implied.
20   See the License for the specific language governing permissions and
21   limitations under the License. *)
22   (* :Mathematica version: 10.3.1*)
23   (* :Package version: 1.0*)
24   (* :History:
25   2016-02-26: Version 1.0
26   *)
27   (* :Description:
28   To use the Mathematica package femtoTools, the parent directory of the
29   femtoTools folder needs to be in the $Path variable of Mathematica.
30   Either you copy femtoTools to a folder already present in $Path or you
31   add the location of femtotools to $Path, e.g.
32   "AppendTo[$Path,"L:/Mathematica"];". If you add the former command to
33   your "init.m" file located in
34   "FileNameJoin[{$UserBaseDirectory,"Kernel","init.m"}]",
35   the $Path variable is updated automatically on the startup of
36   Mathematica.
37   *)
38
39   <<femtoTools`io`;
40   <<femtoTools`fourier`;
41   <<femtoTools`gaussTrace`;
42   <<femtoTools`plotOptions`;
43   <<femtoTools`framePlot`;
44   <<femtoTools`imagePlot`;
45   <<femtoTools`parVarPro`;

```

A.2. parVarPro.nb

This package requires

- plotOptions

for the graphical output (e.g. Fig. 4.2) and allows to fit transient absorption data with the VPA, as explained in Sec. 4.2 and exemplified in Sec. 4.3.

```

1  (* Mathematica Package *)
2  (* :Title: parVarPro *)
3  (* :Context: femtoTools`parVarPro` *)
4  (* :Summary: Fit with the partitioned variable projection algorithm. *)
5  (* :Keywords: fitting, variable projection, nonlinear least square *)
6  (* :Mathematica version: 10.3.0*)
7  (* :Package version: 1.0*)
8  (* :Author: Sebastian Schott, IPTC Universität Würzburg *)
9  (* :Mail: sebastian.schott\[at\]phys-chemie.uni-wuerzburg.de *)
10 (* :Licence:
11 Copyright 2016, Sebastian Schott
12
13 Licensed under the Apache License, Version 2.0 (the "License");
14 you may not use this file except in compliance with the License.
15 You may obtain a copy of the License at
16
17 http://www.apache.org/licenses/LICENSE-2.0

```

```

18
19 Unless required by applicable law or agreed to in writing, software
20 distributed under the License is distributed on an "AS IS" BASIS,
21 WITHOUT WARRANTIES OR CONDITIONS OF ANY KIND, either express or implied.
22 See the License for the specific language governing permissions and
23 limitations under the License. *)
24 (* :Dependencies:
25 femtoTools`plotOptions`
26 *)
27 (* :History:
28 2016-02-26: Version 1.0
29 *)
30 (* :Description:
31 Examples of use are available in femtoTools/examples/parVarPro.nb.
32
33 The variable projection algorithm (varPro) [1] was implemented to
34 Mathematica via the built-in FindMinimum function [2] following a recent
35 Matlab implementation [3] and it was extended to the partitioned variable
36 projection algorithm (parVarPro) according to TIMP/Glotaran [4,5].
37
38 Despite the fact that the function varPro is already deprecated, it stays
39 in the package for educational reasons. The basic concept of the variable
40 projection algorithm and its Mathematica implementation is easier to
41 understand in the less complex varPro function.
42
43 ToDo:
44 - Implement error calculation for the linear and nonlinear parameters.
45
46 Features:
47 - Be as flexible as Mathematica in choosing your model function, e.g. fit
48 oscillations with a wavelength dependend phase or fit stretched-
49 exponential decays in transient absorption data.
50 - Use the analytic Jacobian or its finite difference approximation.
51 - Derivatives for analytic Jacobian are automatically calculated.
52 - Fit multiple datasets globally.
53 - Fit 1D, 2D and partitioned 2D datasets.
54 - Exploit the structure of the data to speed up the fitting procedure, e.g.
55 for transient absorption data do a chirp correction before fitting.
56 - Compact source code.
57
58 Missing features / disadvantages compared to \gls{glotaran}:
59 - Error calculation for the linear and nonlinear parameters (see ToDo).
60 - Weighting
61 - Constraints:
62   - Upper and lower bounds for nonlinear parameters.
63   - Non-negative linear parameters.
64   - Set some linear parameters equal to zero (K-matrix).
65   - Equalize some linear parameters (K-matrix).
66 - Singular value decomposition (SVD) tool set. However, Mathematica
67 implements a SVD algorithm.
68 - Mathematica is closed source.
69
70 [1] G. Golub and V. Pereyra, Inverse Problems 19, R1 (2003)
71 [2] Alexey Popkov, http://mathematica.stackexchange.com/a/16714 (2016-26-02)
72 [3] K.M. Mullen and I.H.M. van Stokkum, J. Stat. Softw. 18, 1 (2007)
73 [4] J.J. Snellenburg, S.P. Liptonok, R. Seger, K.M. Mullen,
74 and I.H.M. van Stokkum, J. Stat. Softw. 49, 1 (2012)
75 [5] D.P. O'Leary and B.W. Rust, Comput Optim Appl 54, 579 (2013)
76 *)
77
78 BeginPackage["femtoTools`parVarPro`", {"femtoTools`plotOptions`"}]
79

```

```

80 collectExp::usage = "collectExp[expr] collects together terms \
81 involving the same exponential Exp[...].\"
82
83 varPro::usage = "varPro[...] is deprecated, use parVarPro[...].
84 varPro[{dataset,...},{\[Alpha]1,...}] fits multiple datasets \
85 simultaneously using the parameters \[Alpha]1,...
86 varPro[{{x1,...},{y1,...},x,{f1[x],...}},...,{\[Alpha]1,...}] fits \
87 the linear combination of the functions f1[x],... to one-dimensional \
88 datasets y1,... depending on the variable x1,...
89 varPro[{{x1,...},{y21,y22,...},{y11,y12,...}},x,{f1[x],...}},...,{\
90 \[Alpha]1,...}] fits two-dimensional datasets.\"
91
92 parVarPro::usage = "parVarPro[{dataset,...},{\[Alpha]1,...}] fits \
93 multiple datasets simultaneously using the parameters \[Alpha]1,...
94 parVarPro[{{None,{x1,...},{y1,...}},{x},{f1[x],...}},...,{\[Alpha]\
95 1,...}] fits the linear combination of the functions f1[x],... to \
96 one-dimensional datasets y1,... depending on the variable x1,...
97 parVarPro[{{None,{x1,...},{y21,y22,...},{y11,y12,...}},{x},{f1[x],\
98 ...}},...,{\[Alpha]1,...}] fits two-dimensional datasets.
99 parVarPro[{{x21,x22,...},{x11,x12,...},{y21,y22,...},{y11,y12,...}}\
100 ,{x2,x1},{f1[x2,x1],...}},...,{\[Alpha]1,...}] partition a \
101 two-dimensional dataset to include the dependency on a second \
102 variable x2.\"
103
104 fittedModel::usage = "fittedModel[...] represents the symbolic fitted \
105 model obtained from parVarPro[...].\"
106
107 Begin[\"Private\"]
108
109 collectExp[expr_] := Collect[Expand@expr, Exp[_], Simplify];
110
111 varPro[dataset_, \[Alpha]init_, opt : OptionsPattern[]] := Module[
112   {\[Alpha]sym, d\[Phi]set,
113    \[Phi]buf, \[Phi]pinvbuf, cbuf,
114    rfunc, jfunc, cfunc,
115    fmin, \[Alpha]opt,
116    monitor, step = 0, reval = 0, jeval = 0,
117    statistic, m, q, n, yvec, ymean, ssr, \[Sigma], ctss, r2},
118
119   \[Alpha]sym = # /. {\[Alpha]sym_, _} := \[Alpha]sym & /@ \
120   \[Alpha]init;
121   d\[Phi]set = Transpose[D[#, {\[Alpha]sym}]] & /@ dataset[;; , 4];
122   cbuf = ConstantArray[{}], Length@dataset];
123
124   (*Residuals*)
125   rfunc[\[Alpha]__?NumericQ] := Join @@ Table[Module[
126     {x, y, xsym, \[Phi]vec, \[Phi], \[Phi]pinv, c, r},
127     {x, y, xsym, \[Phi]vec} = dataset[[i]];
128     \[Phi] = Compile[Evaluate[List /@ xsym], Evaluate[\[Phi]vec],
129       Parallelization -> True,
130       RuntimeAttributes -> {Listable},
131       RuntimeOptions -> \"Speed\"]@x;
132     \[Phi]pinv = PseudoInverse@\[Phi];
133     c = cbuf[[i]] = \[Phi]pinv.y;
134     r = Re[y - \[Phi].c];
135     If[VectorQ@y, r, Join @@ Transpose@r]],
136     {i, 1, Length@dataset}];
137
138   (*Jacobian*)
139   jfunc[\[Alpha]__?NumericQ] := Join @@ Table[Module[
140     {x, y, xsym, \[Phi]vec, d, \[Phi], \[Phi]pinv, c, atr, btr,
141     jtr},

```

```

142     {x, y, xsym, \[Phi]vec} = dataset[[i]];
143     d = Compile[Evaluate[List /@ xsym], Evaluate[#],
144               Parallelization -> True,
145               RuntimeAttributes -> {Listable},
146               RuntimeOptions -> "Speed"]@x & /@ d\[Phi]set[[i]];
147     \[Phi] = Compile[Evaluate[List /@ xsym], Evaluate[\[Phi]vec],
148                   Parallelization -> True,
149                   RuntimeAttributes -> {Listable},
150                   RuntimeOptions -> "Speed"]@x;
151     \[Phi]pinv = PseudoInverse@\[Phi];
152     c = (*cbuf[[i]]=*)\[Phi]pinv.y;
153     atr = #.c - \[Phi].(\[Phi]pinv.(#.c)) & /@ d;
154     btr = \
155 \[Phi]pinv\[ConjugateTranspose].(#\[ConjugateTranspose].y) - \
156 \[Phi]pinv\[ConjugateTranspose].(#\[ConjugateTranspose].(\[Phi].c)) & \
157 /@ d;
158     jtr = Re[-atr - btr];
159     If[VectorQ@y, Transpose[jtr],
160       Join @@ (Transpose[jtr, {3, 2, 1}]]],
161     {i, 1, Length@dataset}];
162
163 (*LevenbergMarquardt*)
164 {fmin, \[Alpha]opt} = FindMinimum[Null, \[Alpha]init,
165   StepMonitor :> step++,
166   EvaluationMonitor :> reval++,
167   Method -> {
168     "LevenbergMarquardt",
169     "Residual" -> rfunc @@ \[Alpha]sym,
170     "Jacobian" -> {OptionValue["Jacobian"]} /.
171       Automatic -> (jfunc @@ \[Alpha]sym),
172     EvaluationMonitor :> jeval++
173   }];
174 monitor = {"Steps" -> step, "Residual" -> reval,
175   "Jacobian" -> jeval};
176
177 (*Statistics*)
178 m = Length@Flatten@dataset[;;, 2];
179 q = Length@\[Alpha]sym;
180 n = Length@Flatten@dataset[;;, 4];
181
182 yvec = Join @@ Table[Module[
183   {y = dataset[[i, 2]}],
184   If[VectorQ@y, y, Join @@ Transpose@y]],
185   {i, 1, Length@dataset}];
186 ymean = Mean@yvec;
187
188 ssr = 2 fmin;
189 \[Sigma] = Sqrt[ssr]/Sqrt[m - n - q];
190 ctss = Total@((yvec - ymean)^2);
191 r2 = 1 - ssr/ctss;
192 statistic = {"SSR" -> ssr, "\[Sigma]" -> \[Sigma], "CTSS" -> ctss,
193   "R2" -> r2};
194
195 (*Result*)
196 {monitor, statistic, \[Alpha]opt, cbuf}
197 ];
198
199 Options[varPro] = {"Jacobian" -> Automatic(* or "FiniteDifference"*)};
200
201 parVarPro[dataset_, \[Alpha]init_, opt : OptionsPattern[]] := Module[
202   {\[Alpha]sym, d\[Phi]set,
203   \[Phi]buf, \[Phi]pinvbuf, cbuf, rbuf, ssrbuf,

```

```

204     rfunc, jfunc, cfunc,
205     absolutetiming, fmin, \[Alpha]opt,
206     monitor, step = 0, reval = 0, jeval = 0,
207     statistic, m, q, n, yvec, ymean, ssr, \[Sigma], ctss, r2},
208
209     \[Alpha]sym = # /. {\[Alpha]sym_, _} := \[Alpha]sym & /@ \
210 \[Alpha]init;
211     d\[Phi]set = Transpose[D[#, {\[Alpha]sym}]] & /@ dataset[;;, 5];
212     cbuf = ConstantArray[{}, Length@dataset];
213     rbuf = ConstantArray[{}, Length@dataset];
214     ssrbuf = {};
215
216     (*Residuals*)
217     rfunc[\[Alpha]_?NumericQ] := (AppendTo[ssrbuf, 0];
218     Join @@ Table[Module[
219         {x, xpar, xvar, y,
220          xsym, \[Phi]vec, \[Phi], \[Phi]pinv, c, r},
221         {xpar, xvar, y, xsym, \[Phi]vec} = dataset[[i]];
222         x =
223         If[xpar === None Depth[y] > 3, Flatten /@ Tuples[xvar, 1],
224          Flatten /@ Tuples[{xpar, xvar}]];
225         \[Phi] = Compile[{{xvec, _Real, 1}},
226
227             Evaluate[\[Phi]vec /.
228                 Thread[xsym -> (Indexed[xvec, #] & /@
229                  Range@Length@xsym)]],
230             Parallelization -> True,
231             RuntimeAttributes -> {Listable},
232             RuntimeOptions -> "Speed"]@x;
233         \[Phi] =
234         If[xpar === None Depth[y] > 3, {\[Phi]},
235          Partition[\[Phi], Length@xvar]];
236         \[Phi]pinv = PseudoInverse /@ \[Phi];
237         cbuf[[i]] = {}; rbuf[[i]] = {};
238         Join @@ MapThread[(
239             \[Phi] = #1; \[Phi]pinv = #2; y = #3;
240             c = \[Phi]pinv.y; AppendTo[cbuf[[i]], c];
241             r = Re[y - \[Phi].c]; AppendTo[rbuf[[i]], r];
242             ssrbuf[[-1]] += Total[r^2, \[Infinity]];
243             If[VectorQ[#3, r, Join @@ Transpose@r] &,
244              {\[Phi], \[Phi]pinv, y}]],
245          {i, 1, Length@dataset}]);
246
247     (*Jacobian*)
248     jfunc[\[Alpha]_?NumericQ] := Join @@ Table[Module[
249         {x, xpar, xvar, y, xsym, \[Phi]vec, d, \[Phi], \[Phi]pinv, c,
250          atr, btr, jtr},
251         {xpar, xvar, y, xsym, \[Phi]vec} = dataset[[i]];
252         x =
253         If[xpar === None Depth[y] > 3, Flatten /@ Tuples[xvar, 1],
254          Flatten /@ Tuples[{xpar, xvar}]];
255         d = Compile[{{xvec, _Real, 1}},
256
257             Evaluate[# /.
258                 Thread[xsym -> (Indexed[xvec, #] & /@
259                  Range@Length@xsym)]],
260             Parallelization -> True,
261             RuntimeAttributes -> {Listable},
262             RuntimeOptions -> "Speed"]@x & /@ d\[Phi]set[[i]];
263         \[Phi] = Compile[{{xvec, _Real, 1}},
264
265             Evaluate[\[Phi]vec /.

```



```

266     Thread[xsym -> (Indexed[xvec, #] & /@ Range@Length@xsym)],
267     Parallelization -> True,
268     RuntimeAttributes -> {Listable},
269     RuntimeOptions -> "Speed"@x;
270   d =
271   If[xpar === None Depth[y] > 3, {d},
272     Transpose[#, {1, 3, 2, 4}] &@
273     Partition[Transpose[d, {2, 1, 3}], Length@xvar]];
274   \[Phi] =
275   If[xpar === None Depth[y] > 3, \[Phi]],
276     Partition[\[Phi], Length@xvar]];
277   \[Phi]pinv = PseudoInverse /@ \[Phi];
278   (*cbuf[[i]]={};*)
279   Join @@ MapThread[(
280     \[Phi] = #1; \[Phi]pinv = #2; y = #3; d = #4;
281     c = \[Phi]pinv.y; (*AppendTo[cbuf[[i]], c];*)
282     atr = #.c - \[Phi].(\[Phi]pinv.(#.c)) & /@ d;
283
284     btr = \[Phi]pinv\[ConjugateTranspose].(#\
285     \[ConjugateTranspose].y) - \[Phi]pinv\[ConjugateTranspose].(#\
286     \[ConjugateTranspose].\[Phi].c) & /@ d;
287     jtr = Re[-atr - btr];
288
289     If[VectorQ@y, Transpose[jtr],
290       Join @@ (Transpose[jtr, {3, 2, 1}])] &,
291     {\[Phi], \[Phi]pinv, y, d}]],
292   {i, 1, Length@dataset}];
293
294   (*LevenbergMarquardt*)
295   {absolutetiming, {fmin, \[Alpha]opt}} =
296   FindMinimum[Null, \[Alpha]init,
297     StepMonitor -> step++,
298     EvaluationMonitor -> reval++,
299     Method -> {
300     "LevenbergMarquardt",
301     "Residual" -> rfunc @@ \[Alpha]sym,
302     "Jacobian" -> {OptionValue["Jacobian"]} /.
303     Automatic -> (jfunc @@ \[Alpha]sym),
304     EvaluationMonitor -> jeval++}
305   ] // AbsoluteTiming;
306   monitor = {
307     "Steps" -> step, "Residual" -> reval, "Jacobian" -> jeval,
308     "AbsoluteTiming" -> absolutetiming, "SSRConvergence" -> ssrbuf};
309
310   (*Statistics*)
311   m = Length@Flatten@dataset[[;; , 3]];
312   q = Length@\[Alpha]sym;
313   n = Length@Flatten@dataset[[;; , 5]];
314
315   yvec = Join @@ Table[
316     Module[{x, xpar, xvar, y, xsym, \[Phi]vec},
317       {xpar, xvar, y, xsym, \[Phi]vec} = dataset[[i]];
318       Join @@
319       Map[If[xpar === None Depth[y] > 3,
320         If[VectorQ@#, #, Join @@ Transpose@#, #] &, y]],
321     {i, 1, Length@dataset}];
322   ymean = Mean@yvec;
323
324   ssr = 2 fmin;
325   \[Sigma] = Sqrt[ssr]/Sqrt[m - n - q];
326   ctss = Chop@Total@((yvec - ymean)^2);
327   r2 = Chop[1 - ssr/ctss];

```

```

328     statistic = {"SSR" -> ssr, "\[Sigma]" -> \[Sigma], "CTSS" -> ctss,
329       "R2" -> r2};
330
331     (*Result*)
332     fittedModel[monitor, statistic, \[Alpha]opt,
333       Join[dataset, List /@ cbuf, List /@ rbuf, 2]]
334   ];
335
336   Options[parVarPro] = {"Jacobian" -> Automatic(* or "FiniteDifference"*)};
337
338   Format[fittedModel[monitor_, statistic_, \[Alpha]opt_, dataset_] :=
339     ListPlot[Log["SSRConvergence" /. monitor],
340       Epilog -> {
341         Inset[Framed[#, Background -> LightBlue] &@Column[{
342           Multicolumn[#, 2] &@Join[
343             legendForm[#, 3] & /@ monitor[;; 3]],
344             {"in " <>
345               ToString@legendForm["AbsoluteTiming" /. monitor, 3] <>
346               " s"},
347             legendForm[#, 3] & /@ statistic],
348           ""},
349         Multicolumn[legendForm[#, 3] & /@ \[Alpha]opt, 2]],
350       Scaled[{1, 1}], {1, 1}},
351     Frame -> True,
352     FrameLabel -> {"Iteration", "ln(RSS)"},
353     Joined -> True,
354     ImageSize -> 12 cm,
355     Mesh -> All, MeshStyle -> Black,
356     PlotRange -> All, PlotStyle -> Red];
357   fittedModel[monitor_, statistic_, \[Alpha]opt_, dataset_] [
358     prop_?(VectorQ[#, StringQ] &)] :=
359     fittedModel[monitor, statistic, \[Alpha]opt, dataset] & /@ prop;
360   fittedModel[monitor_, statistic_, \[Alpha]opt_, dataset_] [
361     nr_?IntegerQ] /; 0 < nr < Length@dataset := dataset[[nr]];
362   fittedModel[monitor_, statistic_, \[Alpha]opt_, dataset_] ["Data"] :=
363     dataset[;; , ; 3];
364   fittedModel[monitor_, statistic_, \[Alpha]opt_, dataset_] [
365     "DataSets"] := dataset;
366   fittedModel[monitor_, statistic_, \[Alpha]opt_, dataset_] [
367     "FitResiduals"] := dataset[;; , 7];
368   fittedModel[monitor_, statistic_, \[Alpha]opt_, dataset_] [
369     "Function"] := dataset[;; , 5];
370   fittedModel[monitor_, statistic_, \[Alpha]opt_, dataset_] [
371     "LinearParameters"] := dataset[;; , 6];
372   fittedModel[monitor_, statistic_, \[Alpha]opt_, dataset_] [
373     "NonlinearParameters"] := \[Alpha]opt;
374   fittedModel[monitor_, statistic_, \[Alpha]opt_, dataset_] ["Monitor"] :=
375     monitor;
376   fittedModel[monitor_, statistic_, \[Alpha]opt_, dataset_] [
377     "Statistic"] := statistic;
378
379   End[]
380
381   EndPackage[]

```

A.3. gaussTrace.nb

This package allows to trace Gaussian beams through optical systems.

```

1  (* Mathematica Package *)
2  (* :Title: gaussTrace *)

```

```

3 (* :Context: femtoTools`gaussTrace` *)
4 (* :Summary: Trace a Gaussian beam through an optical system consisting
5 of lenses and mirrors. *)
6 (* :Keywords: gaussian beam, ray tracing, lens, mirror *)
7 (* :Mathematica version: 10.3.0*)
8 (* :Package version: 1.0*)
9 (* :Author: Sebastian Schott, IPTC Universität Würzburg *)
10 (* :Mail: sebastian.schott[at]phys-chemie.uni-wuerzburg.de *)
11 (* :Licence:
12 Copyright 2016, Sebastian Schott
13
14 Licensed under the Apache License,Version 2.0 (the "License");
15 you may not use this file except in compliance with the License.
16 You may obtain a copy of the License at
17
18 http://www.apache.org/licenses/LICENSE-2.0
19
20 Unless required by applicable law or agreed to in writing,software
21 distributed under the License is distributed on an "AS IS" BASIS,
22 WITHOUT WARRANTIES OR CONDITIONS OF ANY KIND,either express or implied.
23 See the License for the specific language governing permissions and
24 limitations under the License. *)
25 (* :Dependencies: *)
26 (* :History:
27 2016-02-26: Version 1.0
28 *)
29 (* :Description:
30 Examples of use are available in femtoTools/examples/gaussTrace.nb.
31
32 The Gauss tracing algorithm follows the equations from Siegman [1].
33
34 [1] A.E. Siegman, Lasers (University Science Books, Sausalito, 1986)
35 *)
36
37 BeginPackage["femtoTools`gaussTrace`"]
38
39 lens::usage = "lens[p,d,h,r1,r2,n] represents a lens of thickness d, \
40 height h, left radius r1, right radius r2 and refractive index n at \
41 position p."
42
43 mirror::usage = "mirror[p,d,h,r1,r2] represents a mirror of thickness \
44 d, height h, left radius r1 and right radius r2 at position p."
45
46 stop::usage = "stop[p] represents a beam stop at position p."
47
48 abcd::usage = "abcd[n,optic] returns the ABCD matrix of an optic \
49 surrounded by a medium of refractive index n."
50
51 gaussTrace::usage = "gaussTrace[z,{p0,n0,qr0},{o1,...}] a Gaussian \
52 beam starting at position p0 in a medium of refractive index n0 with \
53 a reduced complex radius qr0 is traced through the optical system o1,...."
54
55 Begin["`Private`"]
56
57 sphericaloptic[p_, d_, h_, r1_, r2_] := Module[
58 {s1, \[Theta]1, s2, \[Theta]2},
59 s1 = If[Abs[r1] === \[Infinity],
60 {{p, -h/2}, {p, h/2}},
61 \[Theta]1 = ArcSin[h/(2 Abs@r1)];
62 Table[{p - r1, 0} +
63 r1 {Cos[\[Theta]],
64 Sin[\[Theta]}], {\[Theta], -\[Theta]1, \[Theta]1},

```

```

65     2 \[Theta]1/10]];
66 s2 = If[Abs[r2] === \[Infinity],
67   {{p + d, Sign[r1 r2] h/2}, {p + d, -Sign[r1 r2] h/2}},
68   \[Theta]2 = -Sign[r1 r2] ArcSin[h/(2 Abs@r2)];
69   Table[{p - r2, 0} + {d, 0} +
70     r2 {Cos\[Theta],
71     Sin\[Theta]}, {\[Theta], -\[Theta]2, \[Theta]2,
72     2 \[Theta]2/10}]];
73 Polygon[Join @@ {s1, s2}]
74 ];
75
76 lens /: Graphics[lens[p_, d_, h_, r1_, r2_, n_]] :=
77   Graphics[{EdgeForm[Blue], FaceForm[LightBlue],
78     sphericaloptic[p, d, h, r1, r2]}];
79
80 mirror /: Graphics[mirror[p_, d_, h_, r1_, r2_]] :=
81   Graphics[{EdgeForm[Gray], FaceForm[LightGray],
82     sphericaloptic[p, d, h, r1, r2]}];
83
84 stop /: Graphics[stop[p_]] := Graphics[];
85
86 abcd[n1_,
87   lens[p_, d_, h_, r1_, r2_,
88   n2_] := {{1, 0}, {(n1 - n2)/r2, 1}}, {{1, d/n2}, {0, 1}}, {{1,
89   0}, {(n2 - n1)/r1, 1}}];
90
91 gaussTrace[z_, {p0_, n0_, qr0_}, optic_] := Module[
92   {orientedoptic, interface, p1, mp1, qr1, p2, mp2, qr2, mi, qrp},
93
94   p2 = p0;
95   orientedoptic = Table[
96     p1 = p2; p2 = First[List @@ o];
97     If[p2 - p1 < 0, Left[o], Right[o]], {o, optic}];
98
99   interface = Join @@ (orientedoptic /. {
100     Right[lens[p_, d_, h_, r1_, r2_, n_]] := {
101     {p, {{1, 0}, {(n - n0)/r1, 1}}, {{1, (z - p)/n}, {0, 1}}},
102     {p +
103     d, {{1, 0}, {(n0 - n)/r2, 1}}, {{1, (z - p - d)/n0}, {0,
104     1}}}},
105     Left[lens[p_, d_, h_, r1_, r2_, n_]] := {
106     {p +
107     d, {{1, 0}, {(n - n0)/r2, 1}}, {{1, (z - p - d)/n}, {0,
108     1}}},
109     {p, {{1, 0}, {(n0 - n)/r1, 1}}, {{1, (z - p)/n0}, {0, 1}}}},
110     Right[mirror[p_, d_, h_, r1_, r2_]] := {
111     {p, {{1, 0}, {2/r1, 1}}, {{1, (z - p)/n0}, {0, 1}}}},
112     Left[mirror[p_, d_, h_, r1_, r2_]] := {
113     {p + d, {{1, 0}, {2/r2, 1}}, {{1, (z - p - d)/n0}, {0, 1}}}},
114     Right[stop[p_]] | Left[stop[p_]] := {
115     {p, {{1, 0}, {0, 1}}, {{1, 0}, {0, 1}}}}
116     });
117
118   {p2, mp2, qr2} = {p0, {{1, (z - p0)/n0}, {0, 1}}, qr0};
119
120   Table[
121     {p1, mp1, qr1} = {p2, mp2, qr2};
122     {p2, mi, mp2} = i;
123     qrp = Divide @@ (mp1.{qr1, 1});
124     qr2 = Divide @@ (mi.{qrp /. z -> p2, 1});
125     {qrp, {p1, p2}}, {i, interface}];
126

```

```
127 End[]
128
129 EndPackage[]
```

A.4. imagePlot.nb

This package requires

- plotOptions,
- CustomTicks

and allows to plot the two-dimensional transient absorption data in form of bitmap graphics consuming less memory and computation power when displayed on the computer screen. Beside linear time axes (e.g. Fig. 4.7a), also mixed linear–logarithmic time axes (e.g. Fig. 4.6) are supported.

```
1 (* Mathematica Package *)
2 (* :Title: imagePlot *)
3 (* :Context: femtoTools`imagePlot` *)
4 (* :Summary: Fast density plot for large datasets. *)
5 (* :Keywords: ListDensityPlot, large dataset, fast *)
6 (* :Mathematica version: 10.3.0*)
7 (* :Package version: 1.0*)
8 (* :Author: Sebastian Schott, IPTC Universität Würzburg *)
9 (* :Mail: sebastian.schott[at]phys-chemie.uni-wuerzburg.de *)
10 (* :License:
11 Copyright 2016, Sebastian Schott
12
13 Licensed under the Apache License,Version 2.0 (the "License");
14 you may not use this file except in compliance with the License.
15 You may obtain a copy of the License at
16
17 http://www.apache.org/licenses/LICENSE-2.0
18
19 Unless required by applicable law or agreed to in writing,software
20 distributed under the License is distributed on an "AS IS" BASIS,
21 WITHOUT WARRANTIES OR CONDITIONS OF ANY KIND,either express or implied.
22 See the License for the specific language governing permissions and
23 limitations under the License. *)
24 (* :Dependencies:
25 femtoTools`plotOptions`
26 CustomTicks`
27 :Author: Mark A. Caprio, Department of Physics, University of Notre Dame
28 :License: Copyright 2012, Mark A. Caprio
29 *)
30 (* :History:
31 2016-02-26: Version 1.0
32 *)
33 (* :Description:
34 Examples of use are available in femtoTools/examples/imagePlot.nb.
35 *)
36
37 BeginPackage["femtoTools`imagePlot`", {
38 "femtoTools`plotOptions`",
39 "CustomTicks`"}]
40
41 rescale::usage = "rescale[z,{min,max}] gives z rescaled to run from 0 \
```

```

42 to 0.5 over the range min to 0 and to run from 0.5 to 1 over the \
43 range 0 to max. Invalid values max<0, min>0 are set to 0."
44
45 imageTransform::usage = "imageTransform[image,{x,y},size] gives an \
46 image that is transformed to fit the scales of the x- and y-axes. \
47 Optionally, the image size can be changed."
48
49 barLegend::usage = "barLegend[{min,max},pos] generates a legend that \
50 identifies colors with the range of values between min and max. The \
51 FrameTicks and FrameLabel of the barLegend are placed according to \
52 pos (Left, Right, Bottom or Top)."
53
54 imagePlot::usage = "imagePlot[{\!\(\)*SubscriptBox[\(x\), \
55 \(\{1\}\)]\),\!\(\)*SubscriptBox[\(x\), \
56 \(\{2\}\)]\),...,\!\(\)*SubscriptBox[\(y\), \
57 \(\{1\}\)]\),\!\(\)*SubscriptBox[\(y\), \(\{2\}\)]\),...,\!\(\)*SubscriptBox[\
58 \(\{z\}\), \(\{1\}\)]\),\!\(\)*SubscriptBox[\(z\), \
59 \(\{2\}\)]\),...,\!\(\)*SubscriptBox[\(z\), \
60 \(\{21\}\)]\),\!\(\)*SubscriptBox[\(z\), \(\{22\}\)]\)}...] generates a \
61 smooth density plot with z-values defined at specified x-y-points."
62
63 imageLinLogPlot::usage = "imageLinLogPlot[{\!\(\)*SubscriptBox[\(x\), \
64 \(\{1\}\)]\),\!\(\)*SubscriptBox[\(x\), \
65 \(\{2\}\)]\),...,\!\(\)*SubscriptBox[\(y\), \
66 \(\{1\}\)]\),\!\(\)*SubscriptBox[\(y\), \(\{2\}\)]\),...,\!\(\)*SubscriptBox[\
67 \(\{z\}\), \(\{1\}\)]\),\!\(\)*SubscriptBox[\(z\), \
68 \(\{2\}\)]\),...,\!\(\)*SubscriptBox[\(z\), \
69 \(\{21\}\)]\),\!\(\)*SubscriptBox[\(z\), \(\{22\}\)]\)}...,logStart] \
70 generates a smooth density plot with z-values defined at specified \
71 x-y-points and a mixed-lin-log y-axis."
72
73 Begin["`Private`"]
74
75 rescale[z_, {min_, max_}] := Piecewise[{
76   {Rescale[Clip[z, {Min@z, 0}], {min, 0}, {0, 0.5}],
77     min <= 0 && max <= 0},
78   {Rescale[Clip[z, {0, Max@z}], {0, max}, {0.5, 1}],
79     min >= 0 && max >= 0},
80   {Clip[Rescale[Clip[z, {Min@z, 0}], {min, 0}, {0, 0.5}] +
81     Rescale[Clip[z, {0, Max@z}], {0, max}, {0.5, 1}] - 0.5, {0,
82     1}], min <= 0 && max >= 0}
83   }];
84
85 imageTransform[img_?ImageQ, {x_, y_}, size_: Automatic] := Module[
86   {xfunc, yfunc},
87   xfunc =
88     Interpolation[Transpose@{x, Range@Length@x},
89     InterpolationOrder -> 1];
90   yfunc =
91     Interpolation[Transpose@{y, Range@Length@y},
92     InterpolationOrder -> 1];
93   ImageTransformation[
94     img, {xfunc#[[1]], yfunc#[[2]]} &,
95     size /. Automatic -> Length /@ {x, y},
96     DataRange -> {{1, Length@x}, {1, Length@y}}, Padding -> "Fixed",
97     PlotRange -> {{Min@x, Max@x}, {Min@y, Max@y}}
98   ];
99
100 barLegend[{min_, max_}, pos_, opt : OptionsPattern[]] := Module[
101   {fullOpt, graphicsOpt, linTicksOpt,
102   frameLabel, frameTicks,
103   step, z, img, xyrange},

```

```

104 fullOpt = DeleteDuplicatesBy[First]@Flatten@{opt,
105     Charting`ResolvePlotTheme[OptionValue@PlotTheme, barLegend],
106     Options@barLegend};
107 graphicsOpt =
108     Complement[FilterRules[fullOpt, #], #] &@Options@Graphics;
109 linTicksOpt =
110     Complement[FilterRules[fullOpt, #], #] &@Options@LinTicks;
111
112 frameLabel = {{None, None}, {None, None}};
113 frameLabel =
114     ReplacePart[
115         frameLabel, {pos /. {Left -> {1, 1}, Right -> {1, 2},
116             Bottom -> {2, 1}, Top -> {2, 2}} -> FrameLabel /. fullOpt};
117
118 frameTicks = {{None, None}, {None, None}};
119 frameTicks =
120     ReplacePart[
121         frameTicks, {pos /. {Left -> {1, 1}, Right -> {1, 2},
122             Bottom -> {2, 1}, Top -> {2, 2}} -> (LinTicks[##,
123             TickLengthScale ->
124             If[MemberQ[{Left, Right}, pos], 16,
125             1] (TickLengthScale /. fullOpt), linTicksOpt] &)}];
126
127 step = (max - min)/512.;
128 z = Range[min, 0, step]~Join~Range[0, max, step];
129 img = Colorize[Image@If[MemberQ[{Left, Right}, pos],
130     {#} & /@ Reverse@rescale[z, {min, max}],
131     Transpose[{#} & /@ rescale[z, {min, max}]]],
132     ColorFunction -> colorData[ColorFunction /. fullOpt],
133     ColorFunctionScaling -> False];
134 xyrange = If[MemberQ[{Left, Right}, pos],
135     {{0, 1}, {min, max}},
136     {{min, max}, {0, 1}}];
137
138 Legended[#, LegendLabel /. fullOpt] &@Graphics[
139     Inset[Show[img, AspectRatio -> Full],
140         xyrange[;; , 1]], {0, 0},
141         xyrange[;; , 2]] - xyrange[;; , 1]],
142     AspectRatio -> pos /. {Left Right -> 16, Bottom Top -> 1/16},
143     FrameLabel -> frameLabel,
144     FrameTicks -> frameTicks,
145     (*ImageSize[Rule]{Automatic, ImageSize /. fullOpt}, *)
146     PlotRange -> xyrange,
147     graphicsOpt]
148 ];
149
150 Options[barLegend] = DeleteDuplicatesBy[First]@Join[
151     {ColorFunction -> "TransientAbsorption",
152     Frame -> True,
153     ImageResolution -> Automatic,
154     LegendLabel -> None,
155     PlotRangePadding -> None,
156     PlotTheme -> $PlotTheme,
157     TickDirection -> Out,
158     TickLabelStep -> 1,
159     TickLengthScale -> 2},
160     FilterRules[Options@Graphics, Except@PlotRangeClipping]];
161
162 Themes`AddThemeRules["Presentation", barLegend,
163     BaseStyle -> {FontFamily -> "Helvetica", FontSize -> 14},
164     FrameStyle -> Directive[Black, Thick],
165     ImageSize -> {Automatic, 6 cm},

```

```

166 LabelStyle -> Black,
167 TickLengthScale -> 3];
168
169 imagePlot[
170   x_?(VectorQ[#, NumberQ] &),
171   y_?(VectorQ[#, NumberQ] &),
172   z_?(MatrixQ[#, NumberQ] &),
173   opt : OptionsPattern[]
174 ] := Module[
175   {fullOpt, graphicsOpt, linTicksOpt,
176   dataRange, plotRange, frameTicks, img,
177   xint, xfunc, yint, yfunc, xs, xe, ys, ye,
178   xroi, yroi, zroi,
179   xPos, yPos},
180   fullOpt = DeleteDuplicatesBy[First]@Flatten@{opt,
181     Charting`ResolvePlotTheme[OptionValue@PlotTheme, imagePlot],
182     Options@imagePlot};
183   linTicksOpt =
184     Complement[FilterRules[fullOpt, #], #] &@Options@LinTicks;
185   graphicsOpt =
186     Complement[FilterRules[fullOpt, #], #] &@Options@Graphics;
187
188   dataRange = {{Min@x, Max@x}, {Min@y, Max@y}, {Min@z, Max@z}};
189
190   plotRange = plotRange3DOpt[PlotRange /. fullOpt];
191   plotRange =
192     MapThread[
193       Replace[#1, All Automatic Full -> #2] &, {plotRange,
194         dataRange}, 2];
195
196   frameTicks = frameTicksOpt[FrameTicks /. fullOpt];
197   frameTicks = Replace[frameTicks, {
198     True -> (LinTicks[##, ShowTickLabels -> False, linTicksOpt] &),
199     All -> (LinTicks[##, linTicksOpt] &)}, 2];
200
201   xint =
202     Interpolation[Transpose@{x, Range@Length@x},
203     InterpolationOrder -> 1];
204   xfunc =
205     Piecewise[{{1, # < Min@x}, {xint@#,
206     Min@x <= # <= Max@x}, {-1, # > Max@x}}] &;
207   yint =
208     Interpolation[Transpose@{y, Range@Length@y},
209     InterpolationOrder -> 1];
210   yfunc =
211     Piecewise[{{1, # < Min@y}, {yint@#,
212     Min@y <= # <= Max@y}, {-1, # > Max@y}}] &;
213   xs = Floor@xfunc@plotRange[[1, 1]];
214   xe = Ceiling@xfunc@plotRange[[1, 2]];
215   ys = Floor@yfunc@plotRange[[2, 1]];
216   ye = Ceiling@yfunc@plotRange[[2, 2]];
217   xroi = x[[xs ;; xe]];
218   yroi = y[[ys ;; ye]];
219   zroi = z[[ys ;; ye, xs ;; xe]];
220
221   img = imageTransform[
222     Colorize[
223       Image[rescale[zroi, plotRange[[3]]]],
224       ColorFunction -> colorData[ColorFunction /. fullOpt],
225       ColorFunctionScaling -> False],
226     {xroi, Reverse@yroi}, ImageResolution /. fullOpt];
227

```



```

228 Graphics[{Inset[Show[img, AspectRatio -> Full],
229   {Min@xroi, Min@yroi}, {0, 0}, {Max@xroi - Min@xroi,
230   Max@yroi - Min@yroi}],
231   White, FilledCurve[{
232     Line[ImageScaled /@ {{0, 0}, {0, 1}, {1, 1}, {1, 0}, {0, 0}}],
233     Line[Scaled /@ {{0, 0}, {0, 1}, {1, 1}, {1, 0}, {0, 0}}]}]},
234   FrameLabel -> ReplaceAll[FrameLabel /. fullOpt,
235     Function[barLegend[zrange_, pos_, opts___] :=
236       If[MemberQ[{Left, Right}, pos],
237         Rotate[#, -90 Degree] &@#, #] &@barLegend[
238         plotRange[[3]], pos, opts,
239         FilterRules[
240           fullOpt, {BaseStyle, ColorFunction, FrameStyle, PlotTheme}]]],
241   FrameTicks -> frameTicks,
242   PlotRange -> plotRange[;; 2]],
243   graphicsOpt]
244 ];
245
246 Options[imagePlot] = DeleteDuplicatesBy[First]@Join[
247   {AspectRatio -> 1,
248   ColorFunction -> "TransientAbsorption",
249   Frame -> True,
250   ImageResolution -> Automatic,
251   PlotRangePadding -> None,
252   PlotTheme -> $PlotTheme,
253   TickDirection -> Out,
254   TickLengthScale -> 1},
255   FilterRules[Options@Graphics, Except@PlotRangeClipping]];
256
257 Themes`AddThemeRules["Presentation", imagePlot,
258   BaseStyle -> {FontFamily -> "Helvetica", FontSize -> 14},
259   FrameStyle -> Directive[Black, Thick],
260   ImageSize -> 12 cm,
261   LabelStyle -> Black,
262   TickLengthScale -> 2];
263
264 imageLinLogPlot[
265   x_?(VectorQ[#, NumberQ] &),
266   y_?(VectorQ[#, NumberQ] &),
267   z_?(MatrixQ[#, NumberQ] &),
268   logStart_?NumberQ,
269   opt : OptionsPattern[]
270 ] := Module[{fullOpt, imagePlotOpt, linTicksOpt, frameTicks},
271   fullOpt = DeleteDuplicatesBy[First]@Flatten@{opt,
272     Charting`ResolvePlotTheme[OptionValue@PlotTheme,
273     imageLinLogPlot],
274     Options@imageLinLogPlot};
275   linTicksOpt =
276     Complement[FilterRules[fullOpt, #], #] &@Options@LinTicks;
277   imagePlotOpt =
278     Complement[FilterRules[fullOpt, #], #] &@Options@imagePlot;
279   frameTicks = frameTicksOpt[FrameTicks /. fullOpt];
280   frameTicks[[1]] = Replace[frameTicks[[1]], {
281     True -> (linLogTicks[##, logStart, ShowTickLabels -> False,
282     linTicksOpt] &),
283     All -> (linLogTicks[##, logStart, linTicksOpt] &)}, 1];
284   imagePlot[x, linLogAxis[y, logStart], z, FrameTicks -> frameTicks,
285     imagePlotOpt]
286 ];
287
288 Options[imageLinLogPlot] = Options[imagePlot];
289

```

```

290 Themes`AddThemeRules["Presentation", imageLinLogPlot,
291   Charting`ResolvePlotTheme["Presentation", imagePlot]];
292
293 End[]
294
295 EndPackage[]

```

A.5. framePlot.nb

This package requires

- plotOptions,
- CustomTicks

and allows to plot one-dimensional data with mixed linear–logarithmic coordinates (e.g. Fig. 5.8) or two different ordinates (e.g. Fig. 5.3c and d).

```

1  (* Mathematica Package *)
2  (* :Title: framePlot *)
3  (* :Context: femtoTools`framePlot` *)
4  (* :Summary: ListPlot wrapper using custom PlotRangeClipping and FrameTicks. *)
5  (* :Keywords: ListPlot, Frame*)
6  (* :Mathematica version: 10.3.0*)
7  (* :Package version: 1.0*)
8  (* :Author: Sebastian Schott, IPTC Universität Würzburg *)
9  (* :Mail: sebastian.schott[at]phys-chemie.uni-wuerzburg.de *)
10 (* :Licence:
11 Copyright 2016, Sebastian Schott
12
13 Licensed under the Apache License,Version 2.0 (the "License");
14 you may not use this file except in compliance with the License.
15 You may obtain a copy of the License at
16
17   http://www.apache.org/licenses/LICENSE-2.0
18
19 Unless required by applicable law or agreed to in writing,software
20 distributed under the License is distributed on an "AS IS" BASIS,
21 WITHOUT WARRANTIES OR CONDITIONS OF ANY KIND,either express or implied.
22 See the License for the specific language governing permissions and
23 limitations under the License. *)
24 (* :Dependencies:
25 femtoTools`plotOptions`
26 CustomTicks`
27   :Author: Mark A. Caprio, Department of Physics, University of Notre Dame
28   :License: Copyright 2012, Mark A. Caprio
29 *)
30 (* :History:
31 2016-02-26: Version 1.0
32 *)
33 (* :Description: *)
34
35 BeginPackage["femtoTools`framePlot`", {
36   "femtoTools`plotOptions`",
37   "CustomTicks`"}]
38
39 frameListPlot::usage = "frameListPlot[{{x1,y1},...},...] generates \
40 a framed ListPlot using a custom PlotRangeClipping."
41

```

```

42 frameListLinLogPlot::usage = \
43 "frameListLinLogPlot[{{x1,y1},...},...] generates a framed ListPlot \
44 with a mixed-lin-log x-axis."
45
46 yyShow::usage = "yyShow[p1,p2] combines plot p1 with y-axis frame on \
47 the left and plot p2 with y-axis frame on the right."
48
49 Begin["`Private`"]
50
51 frameListPlot[data_, opt : OptionsPattern[]] := Module[
52   {fullOpt, linTicksOpt, listPlotOpt, frameTicks, plot},
53   fullOpt = DeleteDuplicatesBy[First]@Flatten@{opt,
54     Charting`ResolvePlotTheme[OptionValue@PlotTheme, frameListPlot],
55     Options@frameListPlot};
56   linTicksOpt =
57     Complement[FilterRules[fullOpt, #], #] &@Options@LinTicks;
58   listPlotOpt =
59     Complement[FilterRules[fullOpt, #], #] &@Options@ListPlot;
60
61   frameTicks = frameTicksOpt[FrameTicks /. fullOpt];
62   frameTicks = Replace[frameTicks, {
63     True -> (LinTicks[##, ShowTickLabels -> False, linTicksOpt] &),
64     All -> (LinTicks[##, linTicksOpt] &)}, 2];
65
66   plot = ListPlot[data,
67     FrameTicks -> frameTicks,
68     PlotRangeClipping -> False,
69     listPlotOpt];
70   If[PlotRangeClipping /. fullOpt,
71     Show[plot, Graphics[{White, FilledCurve[{
72       Line[ImageScaled /@ {{0, 0}, {0, 1}, {1, 1}, {1, 0}, {0, 0}}],
73       Line[Scaled /@ {{0, 0}, {0, 1}, {1, 1}, {1, 0}, {0, 0}}]}]}],
74     plot]
75   ];
76
77 Options[frameListPlot] = DeleteDuplicatesBy[First]@Join[
78   {Frame -> True,
79     PlotRange -> All,
80     PlotRangePadding -> {None, Automatic},
81     TickDirection -> Out,
82     TickLengthScale -> 1},
83   Options@ListPlot];
84
85 Themes`AddThemeRules[Automatic, frameListPlot,
86   Charting`ResolvePlotTheme[Automatic, ListPlot]];
87 Themes`AddThemeRules["Presentation", frameListPlot,
88   BaseStyle -> {FontFamily -> "Helvetica", FontSize -> 14},
89   FrameStyle -> Directive[Black, Thick],
90   ImageSize -> 12 cm,
91   LabelStyle -> Black,
92   TickLengthScale -> 2];
93
94 frameListLinLogPlot[data_, logStart_?NumberQ,
95   opt : OptionsPattern[]] := Module[
96   {fullOpt, linTicksOpt, frameListPlotOpt, frameTicks, plot},
97   fullOpt = DeleteDuplicatesBy[First]@Flatten@{opt,
98     Charting`ResolvePlotTheme[OptionValue@PlotTheme,
99     frameListLinLogPlot],
100    Options@frameListLinLogPlot};
101   linTicksOpt =
102     Complement[FilterRules[fullOpt, #], #] &@Options@LinTicks;
103   frameListPlotOpt =

```

```

104     Complement[FilterRules[fullOpt, #], #] &@Options@frameListPlot;
105
106     frameTicks = frameTicksOpt[FrameTicks /. fullOpt];
107     frameTicks[[2]] = Replace[frameTicks[[1]], {
108       True -> (linLogTicks[##, logStart, ShowTickLabels -> False,
109         linTicksOpt] &),
110       All -> (linLogTicks[##, logStart, linTicksOpt] &)}, 1];
111
112     frameListPlot[
113       Transpose@{linLogAxis#[[;;, 1]], logStart}, #[[;;, 2]] & /@
114       If[Depth@data > 3, data, {data}],
115       FrameTicks -> frameTicks,
116       frameListPlotOpt]
117   ];
118
119 Options[frameListLinLogPlot] = Options[frameListPlot];
120
121 Themes`AddThemeRules[Automatic, frameListLinLogPlot,
122   Charting`ResolvePlotTheme[Automatic, frameListPlot]];
123 Themes`AddThemeRules["Presentation", frameListLinLogPlot,
124   Charting`ResolvePlotTheme["Presentation", frameListPlot]];
125
126 yyShow[fgraphin_, ggraphin_, opt : OptionsPattern[] := Module[
127   {linTicksOpt, graphicsOpt,
128     clipping, fgraph, ggraph,
129     frange, grange, frameTicks},
130   linTicksOpt =
131     Complement[FilterRules[{opt}, #], #] &@Options@LinTicks;
132   graphicsOpt =
133     Complement[FilterRules[{opt}, #], #] &@Options@Graphics;
134   clipping = {White, FilledCurve[{
135     Line[ImageScaled /@ {{0, 0}, {0, 1}, {1, 1}, {1, 0}, {0, 0}}],
136     Line[Scaled /@ {{0, 0}, {0, 1}, {1, 1}, {1, 0}, {0, 0}}]}}];
137   {fgraph, ggraph} =
138     DeleteCases[#, clipping, \[Infinity]] & /@ {fgraphin, ggraphin};
139   {frange,
140     grange} = (PlotRange /. AbsoluteOptions[#, PlotRange])[[
141     2]] & /@ {fgraph, ggraph};
142   frameTicks = frameTicksOpt[OptionValue@FrameTicks];
143   frameTicks = Replace[frameTicks, {
144     True -> (LinTicks[##, ShowTickLabels -> False, linTicksOpt] &),
145     All -> (LinTicks[##, linTicksOpt] &)}, 2];
146   frameTicks[[1, 2]] = Replace[frameTicks[[1, 2]],
147     f_Function -> f[grange[[1]], grange[[2]],
148     TickPostTransformation -> (Rescale[#, grange, frange] &)];
149   Show[
150     fgraph,
151     ggraph /. Graphics[graph_, s___] -> Graphics[
152       GeometricTransformation[graph,
153         RescalingTransform[{{0, 1}, grange}, {{0, 1}, frange}], s],
154     Graphics[clipping],
155     FrameTicks -> frameTicks,
156     graphicsOpt]
157   ];
158
159 Options[yyShow] = DeleteDuplicatesBy[First]@Join[
160   {TickDirection -> Out,
161     TickLengthScale -> 1},
162   Options@Graphics];
163
164 End[]
165

```

A.6. plotOptions.nb

This package requires

- CustomTicks.

and defines the basic plot options for all other plot packages.

```

1  (* Mathematica Package *)
2  (* :Title: plotOptions *)
3  (* :Context: femtoTools`plotOptions` *)
4  (* :Summary: Basic plot options for custom plot functions. *)
5  (* :Keywords: *)
6  (* :Mathematica version: 10.3.0*)
7  (* :Package version: 1.0*)
8  (* :Author: Sebastian Schott, IPTC Universität Würzburg *)
9  (* :Mail: sebastian.schott[at]phys-chemie.uni-wuerzburg.de *)
10 (* :Licence:
11 Copyright 2016, Sebastian Schott
12
13 Licensed under the Apache License,Version 2.0 (the "License");
14 you may not use this file except in compliance with the License.
15 You may obtain a copy of the License at
16
17   http://www.apache.org/licenses/LICENSE-2.0
18
19 Unless required by applicable law or agreed to in writing,software
20 distributed under the License is distributed on an "AS IS" BASIS,
21 WITHOUT WARRANTIES OR CONDITIONS OF ANY KIND,either express or implied.
22 See the License for the specific language governing permissions and
23 limitations under the License. *)
24 (* :Dependencies:
25 CustomTicks`
26   :Author: Mark A. Caprio, Department of Physics, University of Notre Dame
27   :License: Copyright 2012, Mark A. Caprio
28 *)
29 (* :History:
30 2016-02-26: Version 1.0
31 *)
32 (* :Description:
33 http://mathematica.stackexchange.com/questions/45501/plotlegends-and-imagesize
34 *)
35
36 BeginPackage["femtoTools`plotOptions`", {"CustomTicks`"}]
37
38 colorData::usage = "colorData[\"scheme\"] gives a function that \
39 generates colors in the named color scheme when applied to parameter \
40 values."
41
42 cm::usage = "Converts cm to printer points."
43
44 frameTicksOpt::usage = "frameTicksOpt[expr] preprocesses all possible \
45 FrameTicks settings."
46
47 insetLegend::usage = "insetLegend[plot] converts a legend into an \
48 inset. This workaround is required to guarantee the correct size of \
49 exported eps/pdf/?... files. Depracated: Size bug relates to Printout \
50 environment. Workaround: \

```

```

51 SetOptions[$FrontEnd,PrintingStyleEnvironment\[Rule](*\Printout\*)\Working"]
52 Working"]"
53
54 legendForm::usage = "legendForm[expr,n] prints real numbers (n-digit \
55 precision) in a compact notation, which is suitable for PlotLegend."
56
57 linLogAxis::usage = "linLogAxis[{\!\(\)*SubscriptBox[\(x\), \
58 \(\{1\}\)\),\!\(\)*SubscriptBox[\(x\), \(\{2\}\)\),..},logStart] generates a \
59 lin-log-mixed axis by taking the decadic logarithm of \
60 \!\(\)*SubscriptBox[\(x\), \(\{n\}\)]\}>logStart."
61
62 linLogTicks::usage = "linLogTicks[min,max,logStart] generates \
63 lin-log-mixed tick marks starting the decadic log part at logStart \
64 (based on CustomTicks)."
65
66 plotRange3D0pt::usage = "plotRange3D0pt[expr] preprocesses all \
67 possible 3D PlotRange settings."
68
69 Begin["`Private`"]
70
71 colorData["TransientAbsorption"] := Module[
72   {darkPurple = RGBColor[0.2, 0, 0.4],
73    purple = RGBColor[0.4, 0, 0.8],
74    darkRed = RGBColor[0.5, 0, 0]},
75   Blend[{darkPurple, purple, Blue, White, Yellow, Red,
76    darkRed}, #] &];
77
78 (*Matlab FROG code from Trebino's group: \
79 http://frog.gatech.edu/code.html*)
80 colorData["FROG"] := Module[
81   {n = 255, step1, step2, step3, frogcolmap},
82
83   step1 = Floor[0.15*n];
84   step2 = Floor[0.50*n];
85   step3 = Floor[0.95*n];
86
87   frogcolmap = ConstantArray[0, {n, 3}];
88   frogcolmap[[1 ;; step1, 1]] = 1.;
89   frogcolmap[[1 ;; step1, 2]] = (Range[1., step1]/step1)^0.7;
90   frogcolmap[[1 ;; step1, 3]] = 0.;
91
92   frogcolmap[[step1 ;; step2,
93    1]] = ((step2 - Range[step1, step2])/(step2 - step1))^0.7;
94   frogcolmap[[step1 ;; step2, 2]] = 1.;
95   frogcolmap[[step1 ;; step2, 3]] = 0.;
96
97   frogcolmap[[step2 ;; step3, 1]] = 0.;
98   frogcolmap[[step2 ;; step3,
99    2]] = ((step3 - Range[step2, step3])/(step3 - step2))^0.8;
100   frogcolmap[[step2 ;; step3,
101    3]] = ((Range[step2, step3] - step2)/(step3 - step2))^0.8;
102
103   frogcolmap[[step3 ;; n,
104    1]] = ((Range[step3, n] - step3)/(n - step3))^1.0;
105   frogcolmap[[step3 ;; n, 2]] = frogcolmap[[step3 ;; n, 1]];
106   frogcolmap[[step3 ;; n, 3]] = 1.;
107
108   frogcolmap = Join[ConstantArray[0, {n + 1, 3}], frogcolmap];
109   Blend[RGBColor @@@ frogcolmap, #] &];
110
111 (*Glotaran documentation: \
112 http://timpgui.org/wiki/doku.php?id=color_and_line_convention*)

```

```

113 colorData["Glotaran"] := {
114   Black, Red, Blue, Green, Magenta, Cyan, Yellow,
115   RGBColor[{0, 139, 0}/255.], Orange, RGBColor[{150, 75, 0}/255.],
116   RGBColor[{128, 128, 128}/255.], RGBColor[{148, 0, 211}/255.],
117   RGBColor[{64, 224, 208}/255.], RGBColor[{128, 0, 0}/255.],
118   RGBColor[{75, 0, 130}/255.], Black};
119
120 cm = 72/2.54;
121
122 frameTicksOpt[frameTicksInit_] := Module[{frameTicks = frameTicksInit},
123   frameTicks =
124     Replace[frameTicks, # -> {#, #} & /@ {None, Automatic, True, All}];
125   frameTicks =
126     Replace[frameTicks, # -> {#, #} & /@ {None, Automatic, True, All},
127     1];
128   frameTicks[;;, 1] =
129     Replace[frameTicks[;;, 1], Automatic -> All, 1];
130   frameTicks[;;, 2] =
131     Replace[frameTicks[;;, 2], Automatic -> True, 1];
132   frameTicks];
133
134 insetLegend[plot_Legended] := Show[
135   plot[[1]],
136   Graphics[Inset[plot[[2, 1]],
137     Scaled@plot[[2, 2, 1]] /. {Left -> 0, Right -> 1, Bottom -> 0,
138     Top -> 1},
139     plot[[2, 2, 2]]]]
140   ];
141
142 legendForm[expr_, n_] :=
143   EngineeringForm[expr, n,
144     NumberFormat -> (Row[{StringTrim[#1, "."],
145     If[#3 == "", "", "e"], #3}] &)];
146
147 linLogAxis[axis_?VectorQ, logStart_] := Module[
148   {linpart, logpart},
149   {linpart, logpart} = SplitBy[axis, logStart <= # &];
150   Join[linpart, (Log[10, logpart] - Log[10, First@logpart] +
151     First@logpart)]
152   ];
153
154 linLogTicks[min_, max_, logStart_, opt : OptionsPattern[]] := Join[
155   LinTicks[min, logStart, opt],
156   Select[
157     LogTicks[0, max,
158     opt] /. {a_, b_, c_, d_} := {a - Log[10, logStart] + logStart,
159     b, c, d},
160     #[[1]] > logStart &]
161   ];
162 Options[linLogTicks] = Options[LinTicks];
163
164 plotRange3DOpt[plotRangeInit_] := Module[{plotRange = plotRangeInit},
165   plotRange =
166     Replace[plotRange, # -> {#, #, #} & /@ {All, Automatic, Full}];
167   plotRange =
168     Replace[plotRange, z_?NumericQ := {Automatic, Automatic, {-z, z}}];
169   plotRange =
170     Replace[plotRange,
171     z_?(VectorQ[#, NumericQ] &) := {Automatic, Automatic, z}];
172   plotRange = Replace[plotRange,
173     xy_?(Length[#] == 2 &) := {First@xy, Last@xy, Automatic}];
174   plotRange =

```

```

175     Replace[plotRange, # -> {#, #} & /@ {All, Automatic, Full}, 1];
176     plotRange];
177
178 End[]
179
180 EndPackage[]

```

A.7. fourier.nb

This packages provides the Fourier transformation tools, which were used to prepare the data for Fig. 5.17 and to unwrap the spectral phase in, e.g., Fig. 5.9a.

```

1  (* Mathematica Package *)
2  (* :Title: fourier *)
3  (* :Context: femtoTools`fourier` *)
4  (* :Summary: Basic tools to process Fourier transformed data. *)
5  (* :Keywords: centered fftc, fft shift, unwrap phase, blank phase*)
6  (* :Mathematica version: 10.3.0*)
7  (* :Package version: 1.0*)
8  (* :Author: Sebastian Schott, IPTC Universität Würzburg *)
9  (* :Mail: sebastian.schott[at]phys-chemie.uni-wuerzburg.de *)
10 (* :Licence:
11 Copyright 2016, Sebastian Schott
12
13 Licensed under the Apache License,Version 2.0 (the "License");
14 you may not use this file except in compliance with the License.
15 You may obtain a copy of the License at
16
17 http://www.apache.org/licenses/LICENSE-2.0
18
19 Unless required by applicable law or agreed to in writing,software
20 distributed under the License is distributed on an "AS IS" BASIS,
21 WITHOUT WARRANTIES OR CONDITIONS OF ANY KIND,either express or implied.
22 See the License for the specific language governing permissions and
23 limitations under the License. *)
24 (* :Dependencies: *)
25 (* :History:
26 2016-02-26: Version 1.0
27 *)
28 (* :Description: *)
29
30 BeginPackage["femtoTools`fourier`"]
31
32 fftShift::usage = "fftShift[list] shifts the elements of a \
33 one-dimensional list to place the first element at the center."
34
35 ifftShift::usage = "ifftShift[list] undoes the result of fftShift."
36
37 fftc::usage = "fftc[list] finds the zero-frequency-centered discrete \
38 Fourier transform of a zero-time-centered list of complex numbers."
39
40 ifftc::usage = "ifftc[list] finds the zero-time-centered discrete \
41 Fourier transform of a list of zero-frequency-centered complex \
42 numbers."
43
44 fftcAxis::usage = "fftcAxis[list] converts a zero-time-centered axis \
45 into a zero-frequency-axis and vice versa."
46
47 blankPhase::usage = "blankPhase[spectrum,threshold] extracts the \
48 phase from a complex spectrum and removes the datapoints with \

```



```

49 amplitude<threshold*Max[amplitude]"
50
51 unwrap::usage = "unwrap[phase] to remove/reduce phase jumps."
52
53 Begin["`Private`"]
54
55 fftShift[list_] := RotateLeft[list, Ceiling[Length[list]/2]];
56 ifftShift[list_] := RotateLeft[list, Floor[Length[list]/2]];
57
58 fftc[list_] := fftshift@Fourier@ifftshift@list;
59 ifftc[list_] := fftshift@InverseFourier@ifftshift@list;
60
61 fftcAxis[tn_] := Module[
62   {T, dt, F, df},
63   T = tn[[-1]] - tn[[1]]; dt = T/(Length[tn] - 1);
64   F = 1/dt; df = 1/T;
65   Range[-F/2, F/2, df]
66   ];
67
68 blankPhase[spectrum_?MatrixQ, threshold_] := Module[
69   {wavelength, amplitude, phase, blanked},
70   wavelength = spectrum[;;, 1];
71   amplitude = Abs@spectrum[;;, 2];
72   phase = Arg@spectrum[;;, 2];
73   blanked =
74     Select[Transpose@{wavelength, amplitude, phase}, #[[2]] >
75       threshold Max@amplitude &];
76   Transpose@{blanked[;;, 1], blanked[;;, 3]}
77   ];
78 blankPhase[spectrum_?(VectorQ[#, MatrixQ[#] &] &), threshold_] :=
79   blankPhase[#, threshold] & /@ spectrum;
80
81 unwrap[Phase_, Cutoff_: N[\[Pi]]] :=
82   Module[{p, dp, dps, dpcorr, PhaseCorr},
83     p = Phase;
84     (*Incremental phase variations*)
85     dp = Differences[p];
86     (*Equivalent phase variations in[-pi,pi]*)
87     dps = Mod[dp + \[Pi], 2 \[Pi]] - \[Pi];
88     (*Preserve variation sign for pi vs.-pi; Numerical precision of #1==
89     N[-\[Pi]]?*)
90     dps = MapIndexed[
91       If[#1 == N[-\[Pi]] && dp[[First@#2]] > 0, \[Pi], #1] &, dps];
92     (*Incremental phase corrections*)
93     dpcorr = dps - dp;
94     (*Ignore correction when incr.variation is<CUTOFF*)
95     dpcorr =
96       MapIndexed[If[Abs[dp[[First@#2]]] < Cutoff, 0, #1] &, dpcorr];
97     (*Integrate corrections and add to Phase to produce smoothed phase \
98     values*)
99     p[[2 ;;]] = p[[2 ;;]] + Accumulate[dpcorr];
100     (*Offset correction*)
101     p - p[[Round[Length@Phase/2]]]
102     ];
103
104 End[]
105
106 EndPackage[]

```

A.8. io.nb

This packages allows to format and export transient absorption data for Glotaran.

```
1  (* Mathematica Package *)
2  (* :Title: io *)
3  (* :Context: femtoTools`io` *)
4  (* :Summary: Custom file format io functions. *)
5  (* :Keywords: *)
6  (* :Mathematica version: 10.3.0*)
7  (* :Package version: 1.0*)
8  (* :Author: Sebastian Schott, IPTC Universität Würzburg *)
9  (* :Mail: sebastian.schott[at]phys-chemie.uni-wuerzburg.de *)
10 (* :Licence:
11 Copyright 2016, Sebastian Schott
12
13 Licensed under the Apache License,Version 2.0 (the "License");
14 you may not use this file except in compliance with the License.
15 You may obtain a copy of the License at
16
17 http://www.apache.org/licenses/LICENSE-2.0
18
19 Unless required by applicable law or agreed to in writing,software
20 distributed under the License is distributed on an "AS IS" BASIS,
21 WITHOUT WARRANTIES OR CONDITIONS OF ANY KIND,either express or implied.
22 See the License for the specific language governing permissions and
23 limitations under the License. *)
24 (* :Dependencies: *)
25 (* :History:
26 2016-02-26: Version 1.0
27 *)
28 (* :Description: *)
29
30 BeginPackage["femtoTools`io`"]
31
32 export::usage = "export[\"file.ascii\",{x,y,z},\"Glotaran\"] exports \
33 2D data to a file in the Glotaran format."
34
35 Begin["`Private`"]
36
37 export[File_, {x_?VectorQ, y_?VectorQ, z_?MatrixQ}, "Glotaran",
38 precision_: 5] := Module[{header, data},
39 header = {
40 {"Header"},
41 {"Created by femtotools (Mathematica 10)"},
42 {"Time explicit"},
43 {"intervalnr " <> ToString[Length[x]]}
44 };
45 (* SetPrecision[... ,5] precise enough? *)
46 data =
47 SetPrecision[Prepend[Prepend[z, y] // Transpose, x], precision];
48 Export[File, header~Join~data, "Table"];
49
50 End[]
51
52 EndPackage[]
```

Glossary

AOPDF acousto-optic programmable dispersive filter.

BBO barium borate.

BS beam splitter.

CA coherent artefact.

CAADS CA-associated difference spectra.

CCD charge-coupled device.

CD circular dichroism.

CTSS corrected total sum of squares.

DADS decay associated difference spectra.

DCM dichloromethane.

DE differential equation.

EADS evolution-associated difference spectra.

ESA excited state absorption.

ET electron transfer.

FWHM full width at half maximum.

Glotaran global and target analysis.

GSB ground state bleach.

IR infrared.

IRF instrumental response function.

LEPS London–Eyring–Polanyi–Sato.

MA magic angle.

ND neutral density.

NIR near-infrared.

NOPA noncollinear optical parametric amplifier.

OADS oscillation-associated difference spectra.

ORD optical rotatory dispersion.

PA product absorption.

PEC potential energy curve.

PES potential energy surface.

RECP relativistic effective core potential.

RMS root mean square.

SADS species-associated difference spectra.

SE stimulated emission.

SHG second harmonic generation.

SM spherical mirror.

SSR sum squared residual.

SVD singular-value decomposition.

SVEA slowly-varying envelope approximation.

TA transient absorption.

TDM transition dipole moment.

Ti:Sa titanium-sapphire.

TIMP tim package.

TRISRS transient resonance impulsive stimulated Raman scattering.

UV ultra-violet.

VIS visible.

VPA variable projection algorithm.

WL white light.

WP wavepacket.

XADS X associated difference spectra.

Bibliography

- [1] A. Steinbacher, H. Hildenbrand, S. Schott, J. Buback, M. Schmid, P. Nuernberger, and T. Brixner. *Generating laser-pulse enantiomers*. *Opt. Express*, **25**, 21735–21752 (2017). doi:10.1364/OE.25.021735.
- [2] J. Knorr, P. Sokkar, S. Schott, P. Costa, W. Thiel, W. Sander, E. Sanchez-Garcia, and P. Nuernberger. *Competitive solvent-molecule interactions govern primary processes of diphenylcarbene in solvent mixtures*. *Nat Commun*, **7**, 12968 (2016). doi:10.1038/ncomms12968.
- [3] S. Schott, L. Röss, J. Hrušák, P. Nuernberger, and T. Brixner. *Identification of photofragmentation patterns in trihalide anions by global analysis of vibrational wavepacket dynamics in broadband transient absorption data*. *Phys. Chem. Chem. Phys.*, **18**, 33287–33302 (2016). doi:10.1039/C6CP06729H.
- [4] S. Schott, A. Steinbacher, J. Buback, P. Nuernberger, and T. Brixner. *Generalized magic angle for time-resolved spectroscopy with laser pulses of arbitrary ellipticity*. *J. Phys. B: At. Mol. Opt. Phys.*, **47**, 124014 (2014). doi:10.1088/0953-4075/47/12/124014.
- [5] D. J. Tannor and S. A. Rice. *Control of selectivity of chemical reaction via control of wave packet evolution*. *J. Chem. Phys.*, **83**, 5013–5018 (1985). doi:10.1063/1.449767.
- [6] D. J. Tannor, R. Kosloff, and S. A. Rice. *Coherent pulse sequence induced control of selectivity of reactions: Exact quantum mechanical calculations*. *J. Chem. Phys.*, **85**, 5805–5820 (1986). doi:10.1063/1.451542.
- [7] P. Brumer and M. Shapiro. *Control of unimolecular reactions using coherent light*. *Chem. Phys. Lett.*, **126**, 541–546 (1986). doi:10.1016/S0009-2614(86)80171-3.
- [8] U. Gaubatz, P. Rudecki, M. Becker, S. Schiemann, M. Külz, and K. Bergmann. *Population switching between vibrational levels in molecular beams*. *Chem. Phys. Lett.*, **149**, 463–468 (1988). doi:10.1016/0009-2614(88)80364-6.
- [9] D. Meshulach and Y. Silberberg. *Coherent quantum control of two-photon transitions by a femtosecond laser pulse*. *Nature*, **396**, 239–242 (1998). doi:10.1038/24329.
- [10] T. Brixner and G. Gerber. *Quantum control of gas-phase and liquid-phase femtochemistry*. *ChemPhysChem*, **4**, 418–438 (2003). doi:10.1002/cphc.200200581.

- [11] P. Nuernberger, G. Vogt, T. Brixner, and G. Gerber. *Femtosecond quantum control of molecular dynamics in the condensed phase*. Phys. Chem. Chem. Phys., **9**, 2470–2497 (2007).
- [12] A. Assion, T. Baumert, M. Bergt, T. Brixner, B. Kiefer, V. Seyfried, M. Strehle, and G. Gerber. *Control of chemical reactions by feedback-optimized phase-shaped femtosecond laser pulses*. Science, **282**, 919–922 (1998). doi:10.1126/science.282.5390.919.
- [13] P. Nuernberger, D. Wolpert, H. Weiss, and G. Gerber. *Femtosecond Quantum Control of Molecular Bond Formation*. PNAS, **107**, 10366–10370 (2010). doi:10.1073/pnas.0913607107.
- [14] U. Banin, A. Waldman, and S. Ruhman. *Ultrafast photodissociation of I_3^- in solution: Direct observation of coherent product vibrations*. J. Chem. Phys., **96**, 2416–2419 (1992). doi:10.1063/1.462041.
- [15] J. J. Snellenburg, S. P. Laptanok, R. Seger, K. M. Mullen, and I. H. M. van Stokkum. *Glutaran: a Java-Based Graphical User Interface for the R-Package TIMP*. J. Stat. Softw., **49**, 1–22 (2012).
- [16] G. Golub and V. Pereyra. *Separable nonlinear least squares: the variable projection method and its applications*. Inverse Prob., **19**, 52278–R1 (2003). doi:10.1088/0266-5611/19/2/201.
- [17] I. H. M. van Stokkum, C. C. Jumper, J. J. Snellenburg, G. D. Scholes, R. van Grondelle, and P. Malý. *Estimation of damped oscillation associated spectra from ultrafast transient absorption spectra*. J. Chem. Phys., **145**, 174201 (2016). doi:10.1063/1.4966196.
- [18] *Mathematica, Version 10.3*. Wolfram Research, Inc., Champaign, Illinois (2015).
- [19] H. E. Lessing and A. Von Jena. *Separation of Rotational Diffusion and Level Kinetics in Transient Absorption Spectroscopy*. Chem. Phys. Lett., **42**, 213–217 (1976). doi:10.1016/0009-2614(76)80349-1.
- [20] B. O’Regan and M. Grätzel. *A low-cost, high-efficiency solar cell based on dye-sensitized colloidal TiO_2 films*. Nature, **353**, 737–740 (1991). doi:10.1038/353737a0.
- [21] A. Hagfeldt, G. Boschloo, L. Sun, L. Kloo, and H. Pettersson. *Dye-Sensitized Solar Cells*. Chem. Rev., **110**, 6595–6663 (2010). doi:10.1021/cr900356p.
- [22] A. Baratz and S. Ruhman. *UV photolysis of in solution – Multiple product channels detected by transient hyperspectral probing*. Chem. Phys. Lett., **461**, 211–217 (2008). doi:10.1016/j.cplett.2008.07.001.
- [23] F. Träger. *Springer handbook of lasers and optics*. Springer handbooks. Springer, New York, NY (2007).

- [24] S. Mukamel. *Principles of nonlinear optical spectroscopy*. Oxford University Press, New York, 1st edition (1995).
- [25] M. Cho. *Two-Dimensional Optical Spectroscopy*. CRC Press, Boca Raton, FL (2009).
- [26] D. J. Tannor. *Introduction to Quantum Mechanics: A Time-Dependent Perspective*. University Science Books, Sausalito (2007).
- [27] E. C. M. Chen and W. E. Wentworth. *Negative ion states of the halogens*. J. Phys. Chem., **89**, 4099–4105 (1985). doi:10.1021/j100265a035.
- [28] J. G. Dojahn, E. C. M. Chen, and W. E. Wentworth. *Characterization of Homonuclear Diatomic Ions by Semiempirical Morse Potential Energy Curves. 1. The Halogen Anions*. J. Phys. Chem., **100**, 9649–9657 (1996). doi:10.1021/jp953601z.
- [29] P. M. Morse. *Diatomic Molecules According to the Wave Mechanics. II. Vibrational Levels*. Phys. Rev., **34**, 57–64 (1929). doi:10.1103/PhysRev.34.57.
- [30] H. Kobeissi. *On testing diatomic vibration-rotation wavefunction for high levels*. J. Comput. Phys., **61**, 351–358 (1985). doi:10.1016/0021-9991(85)90069-5.
- [31] J. P. Dahl and M. Springborg. *The Morse oscillator in position space, momentum space, and phase space*. J. Chem. Phys., **88**, 4535–4547 (1988). doi:10.1063/1.453761.
- [32] S.-H. Dong, R. Lemus, and A. Frank. *Ladder operators for the Morse potential*. Int. J. Quantum Chem., **86**, 433–439 (2002).
- [33] P. Vöhringer. *Kohärente Photochemie am Beispiel des Triiodid-Ions: Quantendynamik und Femtosekundenspektroskopie*. Habilitationsschrift, Univ. Karlsruhe (1998).
- [34] S. Sato. *On a New Method of Drawing the Potential Energy Surface*. The Journal of Chemical Physics, **23**, 592–593 (1955). doi:10.1063/1.1742043.
- [35] R. Nakanishi, N. Saitou, T. Ohno, S. Kowashi, S. Yabushita, and T. Nagata. *Photodissociation of gas-phase I₃⁻: Comprehensive understanding of nonadiabatic dissociation dynamics*. J. Chem. Phys., **126**, 204311 (2007). doi:10.1063/1.2736691.
- [36] A. S. P. Gomes, L. Visscher, H. Bolvin, T. Saue, S. Knecht, T. Fleig, and E. Eliav. *The electronic structure of the triiodide ion from relativistic correlated calculations: A comparison of different methodologies*. J. Chem. Phys., **133**, 064305 (2010). doi:10.1063/1.3474571.
- [37] I. Benjamin, U. Banin, and S. Ruhman. *Ultrafast photodissociation of I₃⁻ in ethanol: A molecular dynamics study*. J. Chem. Phys., **98**, 8337–8340 (1993). doi:doi:10.1063/1.464539.

- [38] G. Ashkenazi, R. Kosloff, S. Ruhman, and H. Tal-Ezer. *Newtonian propagation methods applied to the photodissociation dynamics of I_3^-* . J. Chem. Phys., **103**, 10005–10014 (1995). doi:10.1063/1.469904.
- [39] T. Kühne, R. Küster, and P. Vöhringer. *Femtosecond photodissociation of triiodide in solution: Excitation energy dependence and transition state dynamics*. Chem. Phys., **233**, 161–178 (1998). doi:10.1016/S0301-0104(97)00354-6.
- [40] M. T. Zanni, B. J. Greenblatt, A. V. Davis, and D. M. Neumark. *Photodissociation of gas phase I_3^- using femtosecond photoelectron spectroscopy*. J. Chem. Phys., **111**, 2991–3003 (1999). doi:10.1063/1.479660.
- [41] R. P. Feynman, R. B. Leighton, and M. Sands. *The Feynman Lectures on Physics*. Basic Books, New York, new millennium edition (2011).
- [42] D. L. Andrews and T. Thirunamachandran. *On three-dimensional rotational averages*. J. Chem. Phys., **67**, 5026–5033 (1977). doi:doi:10.1063/1.434725.
- [43] D. P. Craig and T. Thirunamachandran. *Molecular Quantum Electrodynamics*. Courier Dover Publications (1998).
- [44] R. W. Boyd. *Nonlinear Optics*. Academic Press, Burlington, 3rd edition (2008).
- [45] R. M. Hochstrasser. *Two-dimensional IR-spectroscopy: polarization anisotropy effects*. Chem. Phys., **266**, 273–284 (2001). doi:10.1016/S0301-0104(01)00232-4.
- [46] R. C. Jones. *A New Calculus for the Treatment of Optical Systems*. J. Opt. Soc. Am., **31**, 488–493 (1941). doi:10.1364/JOSA.31.000488.
- [47] T. Brixner. *Poincaré representation of polarization-shaped femtosecond laser pulses*. Appl. Phys. B, **76**, 531–540 (2003). doi:10.1007/s00340-003-1137-3.
- [48] T. Brixner and G. Gerber. *Femtosecond polarization pulse shaping*. Opt. Lett., **26**, 557–559 (2001). doi:10.1364/OL.26.000557.
- [49] M. Ninck, A. Galler, T. Feurer, and T. Brixner. *Programmable common-path vector field synthesizer for femtosecond pulses*. Opt. Lett., **32**, 3379–3381 (2007). doi:10.1364/OL.32.003379.
- [50] A. E. Siegman. *Lasers*. University Science Books, Sausalito (1986).
- [51] R. W. Boyd and D. J. Gauthier. *Chapter 6 - “Slow” and “fast” light*. In E. Wolf, editor, *Progress in Optics*, volume 43, pages 497–530. Elsevier (2002).
- [52] J.-C. Diels and W. Rudolph. *Ultrashort Laser Pulse Phenomena: Fundamentals, Techniques, and Applications on a Femtosecond Time Scale (Optics and Photonics Series)*. Academic Press Inc., 2nd edition (2006).

- [53] I. H. M. van Stokkum, D. S. Larsen, and R. van Grondelle. *Global and target analysis of time-resolved spectra*. *Biochim. Biophys. Acta, Bioenerg.*, **1657**, 82–104 (2004). doi:10.1016/j.bbabi.2004.04.011.
- [54] D. C. Johnston. *Stretched exponential relaxation arising from a continuous sum of exponential decays*. *Phys. Rev. B*, **74**, 184430 (2006). doi:10.1103/PhysRevB.74.184430.
- [55] C. Consani, F. Koch, F. Panzer, T. Unger, A. Köhler, and T. Brixner. *Relaxation dynamics and exciton energy transfer in the low-temperature phase of MEH-PPV*. *J. Chem. Phys.*, **142**, 212429 (2015). doi:10.1063/1.4918645.
- [56] A. Hipke. *Ultrafast Dynamics of the Novel, Intrinsically Chiral Model Bisporphyrin beta,beta' Linked Bis[Tetraphenylporphyrinato-Zinc(II)]*. Masterarbeit, Universität Würzburg (2011).
- [57] D. P. O’Leary and B. W. Rust. *Variable projection for nonlinear least squares problems*. *Comput. Optim. Appl.*, **54**, 579–593 (2013). doi:10.1007/s10589-012-9492-9.
- [58] K. M. Mullen and I. H. M. van Stokkum. *TIMP: An R Package for Modeling Multi-way Spectroscopic Measurements*. *J. Stat. Softw.*, **18**, 1–46 (2007).
- [59] T. Ypma. *Historical Development of the Newton–Raphson Method*. *SIAM Rev.*, **37**, 531–551 (1995). doi:10.1137/1037125.
- [60] C. F. Borges. *A full-Newton approach to separable nonlinear least squares problems and its application to discrete least squares rational approximation*. *Electron. Trans. Numer. Anal.*, **35**, 57–68 (2009).
- [61] H. O. Hartley. *The Modified Gauss-Newton Method for the Fitting of Non-Linear Regression Functions by Least Squares*. *Technometrics*, **3**, 269–280 (1961). doi:10.1080/00401706.1961.10489945.
- [62] K. Levenberg. *A method for the solution of certain non-linear problems in least squares*. *Quart. Appl. Math.*, **2**, 164–168 (1944). doi:10.1090/qam/10666.
- [63] D. W. Marquardt. *An Algorithm for Least-Squares Estimation of Nonlinear Parameters*. *J. Soc. Indust. Appl. Math.*, **11**, 431–441 (1963).
- [64] G. H. Golub and C. F. Van Loan. *Matrix Computations*. 3rd edition (1996).
- [65] C.-K. Min, T. Joo, M.-C. Yoon, C. M. Kim, Y. N. Hwang, D. Kim, N. Aratani, N. Yoshida, and A. Osuka. *Transient absorption anisotropy study of ultrafast energy transfer in porphyrin monomer, its direct meso–meso coupled dimer and trimer*. *J. Chem. Phys.*, **114**, 6750–6758 (2001). doi:10.1063/1.1357438.

- [66] S. N. Goldie and G. J. Blanchard. *Orientational and Vibrational Relaxation Dynamics of Perylene and 1-Methylperylene in n-Alcohols: Probing the Balance between van der Waals and Hydrogen-Bonding Interactions*. J. Phys. Chem. A, **103**, 999–1006 (1999). doi:10.1021/jp9845219.
- [67] P. Toele, H. Zhang, and M. Glasbeek. *Femtosecond Fluorescence Anisotropy Studies of Excited-State Intramolecular Double-Proton Transfer in [2,2′-bipyridyl]-3,3′-diol in Solution*. J. Phys. Chem. A, **106**, 3651–3658 (2002). doi:10.1021/jp0134446.
- [68] V. B. Borisov, U. Liebl, F. Rappaport, J.-L. Martin, J. Zhang, R. B. Gennis, A. A. Konstantinov, and M. H. Vos. *Interactions between Heme d and Heme b595 in Quinol Oxidase bd from Escherichia coli: A Photoselection Study Using Femtosecond Spectroscopy*. Biochemistry, **41**, 1654–1662 (2002). doi:10.1021/bi0158019.
- [69] M. Theisen, M. Linke, M. Kerbs, H. Fidder, M. E.-A. Madjet, A. Zacarias, and K. Heyne. *Femtosecond polarization resolved spectroscopy: A tool for determination of the three-dimensional orientation of electronic transition dipole moments and identification of configurational isomers*. J. Chem. Phys., **131**, 124511 (2009). doi:10.1063/1.3236804.
- [70] M. Linke, A. Lauer, T. von Haimberger, A. Zacarias, and K. Heyne. *Three-Dimensional Orientation of the Qy Electronic Transition Dipole Moment within the Chlorophyll a Molecule Determined by Femtosecond Polarization Resolved VIS Pump-IR Probe Spectroscopy*. J. Am. Chem. Soc., **130**, 14904–14905 (2008). doi:10.1021/ja804096s.
- [71] G. R. Fleming. *Chemical Applications of Ultrafast Spectroscopy*, volume 13 of *International Series of Monographs on Chemistry*. Oxford University Press, USA, New York (1986).
- [72] D. C. Arnett, C. C. Moser, P. L. Dutton, and N. F. Scherer. *The First Events in Photosynthesis: Electronic Coupling and Energy Transfer Dynamics in the Photosynthetic Reaction Center from Rhodobacter sphaeroides*. J. Phys. Chem. B, **103**, 2014–2032 (1999). doi:10.1021/jp984464j.
- [73] D. M. Jonas, M. J. Lang, Y. Nagasawa, T. Joo, and G. R. Fleming. *Pump-Probe Polarization Anisotropy Study of Femtosecond Energy Transfer within the Photosynthetic Reaction Center of Rhodobacter sphaeroides R26*. J. Phys. Chem., **100**, 12660–12673 (1996). doi:10.1021/jp960708t.
- [74] I. Hwang, U. Selig, S. S. Y. Chen, P. E. Shaw, T. Brixner, P. L. Burn, and G. D. Scholes. *Photophysics of delocalized excitons in carbazole dendrimers*. J. Phys. Chem. A, **117**, 6270–6278 (2013). doi:10.1021/jp4006845.
- [75] T. G. Goodson. *Optical Excitations in Organic Dendrimers Investigated by Time-Resolved and Nonlinear Optical Spectroscopy*. Acc. Chem. Res., **38**, 99–107 (2005). doi:10.1021/ar020247w.

- [76] M. Lim, T. A. Jackson, and P. A. Anfinrud. *Binding of CO to myoglobin from a heme pocket docking site to form nearly linear Fe–C–O*. *Science*, **269**, 962–966 (1995).
- [77] M. Lim, T. A. Jackson, and P. A. Anfinrud. *Orientalional distribution of CO before and after photolysis of MbCO and HbCO: A determination using time-resolved polarized mid-IR spectroscopy*. *J. Am. Chem. Soc.*, **126**, 7946–7957 (2004).
- [78] P. Nuernberger, K. F. Lee, A. Bonvalet, L. Bouzahir-Sima, J.-C. Lambry, U. Liebl, M. Joffre, and M. H. Vos. *Strong Ligand–Protein Interactions Revealed by Ultrafast Infrared Spectroscopy of CO in the Heme Pocket of the Oxygen Sensor FixL*. *J. Am. Chem. Soc.*, **133**, 17110–17113 (2011). doi:10.1021/ja204549n.
- [79] Z. Liu, C. Tan, X. Guo, J. Li, L. Wang, A. Sancar, and D. Zhong. *Determining complete electron flow in the cofactor photoreduction of oxidized photolyase*. *PNAS*, **110**, 12966–12971 (2013). doi:10.1073/pnas.1311073110.
- [80] A. Lukacs, A. P. M. Eker, M. Byrdin, K. Brettel, and M. H. Vos. *Electron Hopping through the 15 Å Triple Tryptophan Molecular Wire in DNA Photolyase Occurs within 30 ps*. *J. Am. Chem. Soc.*, **130**, 14394–14395 (2008). doi:10.1021/ja805261m.
- [81] J. Lindner and P. Vöhringer. *Femtosecond vibrational spectroscopies and applications to hydrogen-bond dynamics in condensed phases*. *Bunsen Magazin*, **6**, 180–197 (2011).
- [82] M. Cho. *Two-dimensional circularly polarized pump–probe spectroscopy*. *J. Chem. Phys.*, **119**, 7003–7016 (2003). doi:10.1063/1.1599344.
- [83] C. Cohen-Tannoudji, B. Diu, and F. Laloë. *Quantenmechanik 02: Band 2*. Gruyter, 4., durchgesehene und verbesserte auflage. edition (2010).
- [84] K. Oda, M. Hita, S. Minemoto, and H. Sakai. *All-Optical Molecular Orientation*. *Phys. Rev. Lett.*, **104**, 213901 (2010). doi:10.1103/PhysRevLett.104.213901.
- [85] A. Mukerjee, T. J. Sørensen, A. P. Ranjan, S. Raut, I. Gryczynski, J. K. Vishwanatha, and Z. Gryczynski. *Spectroscopic Properties of Curcumin: Orientation of Transition Moments*. *J. Phys. Chem. B*, **114**, 12679–12684 (2010). doi:10.1021/jp104075f.
- [86] F. Filsinger, J. Küpper, G. Meijer, L. Holmegaard, J. H. Nielsen, I. Nevo, J. L. Hansen, and H. Stapelfeldt. *Quantum-state selection, alignment, and orientation of large molecules using static electric and laser fields*. *J. Chem. Phys.*, **131**, 064309 (2009). doi:10.1063/1.3194287.
- [87] H. Stapelfeldt and T. Seideman. *Colloquium: Aligning molecules with strong laser pulses*. *Rev. Mod. Phys.*, **75**, 543–557 (2003). doi:10.1103/RevModPhys.75.543.

- [88] F. Rosca-Pruna and M. J. J. Vrakking. *Experimental Observation of Revival Structures in Picosecond Laser-Induced Alignment of I₂*. *Phys. Rev. Lett.*, **87**, 153902 (2001). doi:10.1103/PhysRevLett.87.153902.
- [89] I. Wolfram Research. *Mathematica Edition: Version 8.0*. Wolfram Research, Inc., Champaign, Illinois (2010).
- [90] P. Nuernberger, T. Vieille, C. Ventalon, and M. Joffre. *Impact of Pulse Polarization on Coherent Vibrational Ladder Climbing Signals*. *J. Phys. Chem. B*, **115**, 5554–5563 (2011). doi:10.1021/jp1113762.
- [91] C. K. Johnson and C. Wan. *Anisotropy Decays Induced by Two-Photon Excitation*. In J. R. Lakowicz, editor, *Topics in Fluorescence Spectroscopy: Nonlinear and Two-Photon-Induced Fluorescence*, volume 5, pages 43–85. Springer (1997).
- [92] J. J. Sakurai and J. Napolitano. *Modern quantum mechanics*. Addison-Wesley, Boston [u.a.], 2. ed., international ed. edition (2011).
- [93] S. S. Andrews. *Using Rotational Averaging To Calculate the Bulk Response of Isotropic and Anisotropic Samples from Molecular Parameters*. *J. Chem. Educ.*, **81**, 877–885 (2004). doi:10.1021/ed081p877.
- [94] D. L. Andrews and N. P. Blake. *Three-dimensional rotational averages in radiation-molecule interactions: an irreducible cartesian tensor formulation*. *J. Phys. A: Math. Gen.*, **22**, 49–60 (1989). doi:10.1088/0305-4470/22/1/011.
- [95] W. M. McClain, D. Tian, and W. A. Ghoul. *Comparison of numerical and analytical orientation average methods in polymer light scattering*. *J. Chem. Phys.*, **87**, 4986–4994 (1987). doi:10.1063/1.452813.
- [96] G. Wagnière. *The evaluation of three-dimensional rotational averages*. *J. Chem. Phys.*, **76**, 473–480 (1982). doi:10.1063/1.442747.
- [97] D. L. Andrews and W. A. Ghoul. *Eighth rank isotropic tensors and rotational averages*. *J. Phys. A: Math. Gen.*, **14**, 1281–1290 (1981). doi:10.1088/0305-4470/14/6/008.
- [98] M. T. Zanni, N.-H. Ge, Y. S. Kim, and R. M. Hochstrasser. *Two-dimensional IR spectroscopy can be designed to eliminate the diagonal peaks and expose only the crosspeaks needed for structure determination*. *PNAS*, **98**, 11265–11270 (2001). doi:10.1073/pnas.201412998.
- [99] K.-K. Lee, K.-H. Park, S. Park, S.-J. Jeon, and M. Cho. *Polarization-Angle-Scanning 2dir Spectroscopy of Coupled Anharmonic Oscillators: A Polarization Null Angle Method*. *J. Phys. Chem. B*, **115**, 5456–5464 (2011). doi:10.1021/jp1102274.

- [100] A. F. Fidler, V. P. Singh, P. D. Long, P. D. Dahlberg, and G. S. Engel. *Probing energy transfer events in the light harvesting complex 2 (LH2) of Rhodospira rubra with two-dimensional spectroscopy*. J. Chem. Phys., **139**, 155101 (2013). doi:10.1063/1.4824637.
- [101] G. S. Schlau-Cohen, A. Ishizaki, T. R. Calhoun, N. S. Ginsberg, M. Ballottari, R. Bassi, and G. R. Fleming. *Elucidation of the timescales and origins of quantum electronic coherence in LH2*. Nat. Chem., **4**, 389–395 (2012). doi:10.1038/nchem.1303.
- [102] H. Maekawa, G. Ballano, C. Toniolo, and N.-H. Ge. *Linear and Two-Dimensional Infrared Spectroscopic Study of the Amide I and II Modes in Fully Extended Peptide Chains*. J. Phys. Chem. B, **115**, 5168–5182 (2011). doi:10.1021/jp105527n.
- [103] J. Réhault and J. Helbing. *Angle determination and scattering suppression in polarization-enhanced two-dimensional infrared spectroscopy in the pump-probe geometry*. Opt. Express, **20**, 21665–21677 (2012). doi:10.1364/OE.20.021665.
- [104] L. Chuntonov and J. Ma. *Quantum Process Tomography Quantifies Coherence Transfer Dynamics in Vibrational Exciton*. J. Phys. Chem. B, **117**, 13631–13638 (2013). doi:10.1021/jp4075493.
- [105] J. J. Rodriguez and S. Mukamel. *Dissecting Two-Dimensional Ultraviolet Spectra of Amyloid Fibrils into Beta-Strand and Turn Contributions*. J. Phys. Chem. B, **116**, 8830–8835 (2012). doi:10.1021/jp303956w.
- [106] C. Y. Wong and G. D. Scholes. *Biexcitonic Fine Structure of CdSe Nanocrystals Probed by Polarization-Dependent Two-Dimensional Photon Echo Spectroscopy*. J. Phys. Chem. A, **115**, 3797–3806 (2011). doi:10.1021/jp1079197.
- [107] S. Westenhoff, D. Paleček, P. Edlund, P. Smith, and D. Zigmantas. *Coherent Picosecond Exciton Dynamics in a Photosynthetic Reaction Center*. J. Am. Chem. Soc., **134**, 16484–16487 (2012). doi:10.1021/ja3065478.
- [108] J. M. Womick and A. M. Moran. *Nature of Excited States and Relaxation Mechanisms in C-Phycocyanin*. J. Phys. Chem. B, **113**, 15771–15782 (2009). doi:10.1021/jp908093x.
- [109] J. N. Moore, P. A. Hansen, and R. M. Hochstrasser. *Iron-carbonyl bond geometries of carboxymyoglobin and carboxyhemoglobin in solution determined by picosecond time-resolved infrared spectroscopy*. PNAS, **85**, 5062–5066 (1988).
- [110] J. R. Lakowicz. *Principles of Fluorescence Spectroscopy*. Springer, New York, N.Y., 3 edition (2006).
- [111] S. Hess, H. Bürsing, and P. Vöhringer. *Dynamics of fragment recoil in the femtosecond photodissociation of triiodide ions in liquid solution*. J. Chem. Phys., **111**, 5461–5473 (1999). doi:10.1063/1.479807.

- [112] G. B. Shaw, C. L. Brown, and J. M. Papanikolas. *Investigation of Interligand Electron Transfer in Polypyridyl Complexes of Os(II) Using Femtosecond Polarization Anisotropy Methods: Examination of Os(bpy)₃²⁺ and Os(bpy)₂(mab)₂²⁺*. J. Phys. Chem. A, **106**, 1483–1495 (2002). doi:10.1021/jp012924u.
- [113] Y. Liang, O. Schalk, and A.-N. Unterreiner. *Transient Anisotropy in Degenerate Systems: Experimental Observation in a Cd-porphyrin*. EPJ web conf., **41**, 05014 (2013). doi:10.1051/epjconf/20134105014.
- [114] V. Pereyra and G. Scherer, editors. *Exponential Data Fitting and its Applications*. Bentham Science, Sharjah (2012).
- [115] U. Banin, R. Kosloff, and S. Ruhman. *Femtosecond Chemical Dynamics in Solution: Photodissociation of I₃⁻*. Isr. J. Chem., **33**, 141–156 (1993). doi:10.1002/ijch.199300019.
- [116] U. Banin and S. Ruhman. *Ultrafast photodissociation of I₃. Coherent photochemistry in solution*. J. Chem. Phys., **98**, 4391–4403 (1993). doi:doi:10.1063/1.465066.
- [117] U. Banin and S. Ruhman. *Ultrafast vibrational dynamics of nascent diiodide fragments studied by femtosecond transient resonance impulsive stimulated Raman scattering*. J. Chem. Phys., **99**, 9318–9321 (1993). doi:doi:10.1063/1.465501.
- [118] U. Banin, A. Bartana, S. Ruhman, and R. Kosloff. *Impulsive excitation of coherent vibrational motion ground surface dynamics induced by intense short pulses*. J. Chem. Phys., **101**, 8461–8481 (1994). doi:10.1063/1.468108.
- [119] E. Gershgoren, E. Gordon, D. Star, and S. Ruhman. *Role of Symmetry Breaking in Transfer of Vibrational Coherence from Reactant to Product*. In P. P. F. Barbara, P. J. G. Fujimoto, W. H. K. P. D, and P. W. Zinth, editors, *Ultrafast Phenomena X*, number 62 in Springer Series in Chemical Physics, pages 207–208. Springer Berlin Heidelberg (1996).
- [120] E. Gershgoren, E. Gordon, and S. Ruhman. *Effect of symmetry breaking on vibrational coherence transfer in impulsive photolysis of trihalide ions*. J. Chem. Phys., **106**, 4806–4809 (1997). doi:doi:10.1063/1.473479.
- [121] E. Gershgoren, U. Banin, and S. Ruhman. *Caging and Geminate Recombination following Photolysis of Triiodide in Solution*. J. Phys. Chem. A, **102**, 9–16 (1998). doi:10.1021/jp972138i.
- [122] Z. Wang, T. Wasserman, E. Gershgoren, J. Vala, R. Kosloff, and S. Ruhman. *Geminate recombination of I₃⁻ in cooled liquid and glassy ethanol*. Chem. Phys. Lett., **313**, 155–161 (1999). doi:10.1016/S0009-2614(99)00974-4.
- [123] Z. Wang, T. Wasserman, E. Gershgoren, and S. Ruhman. *Vibrational dephasing of I₃⁻ in cooled ethanol solutions — where is the inhomogeneity?* J. Mol. Liq., **86**, 229–236 (2000). doi:10.1016/S0167-7322(99)00144-0.

- [124] E. Gershgoren, J. Vala, R. Kosloff, and S. Ruhman. *Impulsive Control of Ground Surface Dynamics of I_3^- in Solution*. J. Phys. Chem. A, **105**, 5081–5095 (2001). doi:10.1021/jp0039518.
- [125] E. Gershgoren, Z. Wang, S. Ruhman, J. Vala, and R. Kosloff. *Investigating pure vibrational dephasing of I_3^- in solution: Temperature dependence of T_2^* for the fundamental and first harmonic of ν_1* . J. Chem. Phys., **118**, 3660–3667 (2003). doi:10.1063/1.1539844.
- [126] T. Kühne and P. Vöhringer. *Vibrational relaxation and geminate recombination in the femtosecond-photodissociation of triiodide in solution*. J. Chem. Phys., **105**, 10788–10802 (1996). doi:doi:10.1063/1.472887.
- [127] S. Hess and P. Vöhringer. *Instantaneous Product Anisotropies in the fs-Photolysis of Triiodide*. In *Ultrafast Phenomena XI*, number 63 in Springer Series in Chemical Physics, pages 600–602. Springer Berlin Heidelberg (1998).
- [128] T. Kühne and P. Vöhringer. *Transient Anisotropy and Fragment Rotational Excitation in the Femtosecond Photodissociation of Triiodide in Solution*. J. Phys. Chem. A, **102**, 4177–4185 (1998). doi:10.1021/jp973154i.
- [129] T. Koslowski and P. Vöhringer. *Is solvated I_3^- angular?* Chem. Phys. Lett., **342**, 141–147 (2001). doi:10.1016/S0009-2614(01)00567-X.
- [130] H. Bürsing, J. Lindner, S. Hess, and P. Vöhringer. *Real-time probing of vectorial properties of ultra-fast photodissociations in liquids*. Appl. Phys. B, **71**, 411–417 (2014). doi:10.1007/s003400000344.
- [131] Q. R. Stottlemeyer. *Investigation of the behavior of the aqueous I_3-I_2-I system following intense irradiation*. Master thesis, California Institute of Technology (1954).
- [132] L. I. Grossweiner and M. S. Matheson. *The Kinetics of the Dihalide Ions from the Flash Photolysis of Aqueous Alkali Halide Solutions*. J. Phys. Chem., **61**, 1089–1095 (1957). doi:10.1021/j150554a013.
- [133] P. Fournier de Violet, R. Bonneau, and J. Joussot-Dubien. *Laser flash photolysis of iodine-iodide mixture in hydroxylic solvent. Evidence for the existence of the radical anion I* . Chem. Phys. Lett., **28**, 569–572 (1974). doi:10.1016/0009-2614(74)80107-7.
- [134] A. Barkatt and M. Ottolenghi. *Laser Flash-Photolysis of Aqueous Triiodide Solutions*. Mol. Photochem., **6**, 253–261 (1974).
- [135] J. H. Baxendale, P. Sharpe, and M. D. Ward. *Absorption in the far red by I_2^- and Br_2^-* . Int. J. Radiat. Phys. Chem., **7**, 587–588 (1975). doi:10.1016/0020-7055(75)90027-3.

- [136] T. Shida, Y. Takahashi, H. Hatano, and M. Imamura. *Electronic structures of I₂⁻ and I₄⁻ ions in γ -irradiated rigid solutions*. Chem. Phys. Lett., **33**, 491–494 (1975). doi:10.1016/0009-2614(75)85758-7.
- [137] T. J. Dunn, J. N. Sweetser, I. A. Walmsley, and C. Radzewicz. *Experimental determination of the dynamics of a molecular nuclear wave packet via the spectra of spontaneous emission*. Phys. Rev. Lett., **70**, 3388–3391 (1993). doi:10.1103/PhysRevLett.70.3388.
- [138] M. H. Vos, F. Rappaport, J.-C. Lambry, J. Breton, and J.-L. Martin. *Visualization of coherent nuclear motion in a membrane protein by femtosecond spectroscopy*. Nature, **363**, 320–325 (1993). doi:10.1038/363320a0.
- [139] S. Ruetzel, M. Diekmann, P. Nuernberger, C. Walter, B. Engels, and T. Brixner. *Multidimensional spectroscopy of photoreactivity*. PNAS, **111**, 4764–4769 (2014). doi:10.1073/pnas.1323792111.
- [140] J. A. Cina, P. A. Kovac, C. C. Jumper, J. C. Dean, and G. D. Scholes. *Ultrafast transient absorption revisited: Phase-flips, spectral fingers, and other dynamical features*. J. Chem. Phys., **144**, 175102 (2016). doi:10.1063/1.4947568.
- [141] L. Zhu, K. Takahashi, M. Saeki, T. Tsukuda, and T. Nagata. *Photodissociation of gas-phase I₃: product branching in the visible and UV regions*. Chem. Phys. Lett., **350**, 233–239 (2001). doi:10.1016/S0009-2614(01)01288-X.
- [142] A. A. Hoops, J. R. Gascooke, A. E. Faulhaber, K. E. Kautzman, and D. M. Neumark. *Two- and three-body photodissociation of gas phase I₃⁻*. J. Chem. Phys., **120**, 7901–7909 (2004). doi:10.1063/1.1691017.
- [143] P. A. D. de Maine. *Iodine Complexes in Inert Solvents. III. Iodine Complexes with Methanol, Ethanol, or Diethyl Ether in Carbon Tetrachloride*. J. Chem. Phys., **26**, 1192–1199 (1957). doi:10.1063/1.1743491.
- [144] A. Maki and R. Forneris. *Infrared and Raman spectra of some trihalide ions: ICl₂, IBr₂⁻, I₂⁻, I₂Br⁻, and BrICl⁻*. Spectrochim. Acta, Part A, **23**, 867–880 (1967). doi:10.1016/0584-8539(67)80014-X.
- [145] P. Klaeboe. *The Raman spectra of some iodine, bromine, and iodine monochloride charge-transfer coomplexes in solution*. J. Am. Chem. Soc., **89**, 3667–3676 (1967). doi:10.1021/ja00991a001.
- [146] W. Kiefer and H. J. Bernstein. *The UV-laser excited resonance raman spectrum of the I₃⁻ ion*. Chem. Phys. Lett., **16**, 5–9 (1972). doi:10.1016/0009-2614(72)80442-1.
- [147] K. Kaya, N. Mikami, Y. Udagawa, and M. Ito. *Resonance Raman effect of I₃⁻ ion by ultraviolet laser excitation*. Chem. Phys. Lett., **16**, 151–153 (1972). doi:10.1016/0009-2614(72)80479-2.

- [148] W. Gabes and H. Gerding. *Vibrational spectra and structures of the trihalide ions*. J. Mol. Struct., **14**, 267–279 (1972). doi:10.1016/0022-2860(72)85172-X.
- [149] A. E. Johnson and A. B. Myers. *Emission cross sections and line shapes for photodissociating triiodide in ethanol: Experimental and computational studies*. J. Chem. Phys., **102**, 3519–3533 (1995). doi:10.1063/1.468577.
- [150] A. E. Johnson and A. B. Myers. *Solvent Effects in the Raman Spectra of the Triiodide Ion: Observation of Dynamic Symmetry Breaking and Solvent Degrees of Freedom*. J. Phys. Chem., **100**, 7778–7788 (1996). doi:10.1021/jp953052x.
- [151] G. A. Landrum, N. Goldberg, and R. Hoffmann. *Bonding in the trihalides (X_3^-), mixed trihalides (X_2Y^-) and hydrogen bihalides (X_2H^-). The connection between hypervalent, electron-rich three-center, donor–acceptor and strong hydrogen bonding?* J. Chem. Soc., Dalton Trans., pages 3605–3613 (1997). doi:10.1039/a703736h.
- [152] Y. Ogawa, O. Takahashi, and O. Kikuchi. *Ab initio MO study of structure and stability of heteronuclear trihalide anions X_2Y^- ($X, Y = Cl, Br, \text{ or } I$) in the gas phase and in solution*. J. Mol. Struct. THEOCHEM, **429**, 187–196 (1998). doi:10.1016/S0166-1280(97)00351-5.
- [153] H. Sato, F. Hirata, and A. B. Myers. *Theoretical Study of the Solvent Effect on Triiodide Ion in Solutions*. J. Phys. Chem. A, **102**, 2065–2071 (1998). doi:10.1021/jp9732827.
- [154] R. M. Lynden-Bell, R. Kosloff, S. Ruhman, D. Danovich, and J. Vala. *Does solvation cause symmetry breaking in the I_3^- ion in aqueous solution?* J. Chem. Phys., **109**, 9928–9937 (1998). doi:doi:10.1063/1.477659.
- [155] C. J. Margulis and D. F. Coker. *Modeling solvation of excited electronic states of flexible polyatomic molecules: Diatomics-in-molecules for I_3 in argon clusters*. J. Chem. Phys., **114**, 6744–6749 (2001). doi:10.1063/1.1357799.
- [156] C. J. Margulis, D. F. Coker, and R. M. Lynden-Bell. *Symmetry breaking of the triiodide ion in acetonitrile solution*. Chem. Phys. Lett., **341**, 557–560 (2001). doi:10.1016/S0009-2614(01)00548-6.
- [157] F. S. Zhang and R. M. Lynden-Bell. *Solvent-Induced Symmetry Breaking*. Phys. Rev. Lett., **90**, 185505 (2003). doi:10.1103/PhysRevLett.90.185505.
- [158] F. S. Zhang and R. M. Lynden-Bell. *Interactions of triiodide cluster ion with solvents*. Eur. Phys. J. D, **34**, 129–132 (2005). doi:10.1140/epjd/e2005-00133-6.
- [159] K. H. Kim, J. H. Lee, J. Kim, S. Nozawa, T. Sato, A. Tomita, K. Ichiyanagi, H. Ki, J. Kim, S.-i. Adachi, and H. Ihee. *Solvent-Dependent Molecular Structure of Ionic Species Directly Measured by Ultrafast X-Ray Solution Scattering*. Phys. Rev. Lett., **110**, 165505 (2013). doi:10.1103/PhysRevLett.110.165505.

- [160] K. H. Kim, J. Kim, J. H. Lee, and H. Ihee. *Topical Review: Molecular reaction and solvation visualized by time-resolved X-ray solution scattering: Structure, dynamics, and their solvent dependence*. *Struct. Dyn.*, **1**, 011301 (2014). doi:10.1063/1.4865234.
- [161] I. Josefsson, S. K. Eriksson, N. Ottosson, G. Öhrwall, H. Siegbahn, A. Hagfeldt, H. Rensmo, O. Björneholm, and M. Odellius. *Collective hydrogen-bond dynamics dictates the electronic structure of aqueous I₃⁻*. *Phys. Chem. Chem. Phys.*, **15**, 20189–20196 (2013). doi:10.1039/C3CP52866A.
- [162] S. K. Eriksson, I. Josefsson, N. Ottosson, G. Öhrwall, O. Björneholm, H. Siegbahn, A. Hagfeldt, M. Odellius, and H. Rensmo. *Solvent Dependence of the Electronic Structure of I⁻ and I₃⁻*. *J. Phys. Chem. B*, **118**, 3164–3174 (2014). doi:10.1021/jp500533n.
- [163] N. K. Jena, I. Josefsson, S. K. Eriksson, A. Hagfeldt, H. Siegbahn, O. Björneholm, H. Rensmo, and M. Odellius. *Solvent-Dependent Structure of the I₃⁻ Ion Derived from Photoelectron Spectroscopy and Ab Initio Molecular Dynamics Simulations*. *Chem. Eur. J.*, **21**, 4049–4055 (2015). doi:10.1002/chem.201405549.
- [164] P. Salén, M. Liu, and P. v. d. Meulen. *Femtosecond Photo-induced Dissociation of the Trihalide Anions I₃⁻ and I₂Br⁻ in Solution*. In P. T. Kobayashi, P. T. Okada, P. T. Kobayashi, P. K. A. Nelson, and P. S. D. Silvestri, editors, *Ultrafast Phenomena XIV*, number 79 in Springer Series in Chemical Physics, pages 499–501. Springer Berlin Heidelberg (2005).
- [165] A. Sanov, T. Sanford, L. J. Butler, J. Vala, R. Kosloff, and W. C. Lineberger. *Photodissociation Dynamics of Gas-Phase BrICl⁻ and IBr₂⁻ Anions*. *J. Phys. Chem. A*, **103**, 10244–10254 (1999). doi:10.1021/jp9920803.
- [166] P. E. Crider, A. W. Harrison, and D. M. Neumark. *Two- and three-body photodissociation dynamics of diiodobromide (I₂Br⁻) anion*. *J. Chem. Phys.*, **134**, 134306 (2011). doi:doi:10.1063/1.3571474.
- [167] R. Mabbs, K. Pichugin, E. Surber, and A. Sanov. *Time-resolved electron detachment imaging of the I⁻ channel in I₂Br⁻ photodissociation*. *J. Chem. Phys.*, **121**, 265–272 (2004). doi:doi:10.1063/1.1756869.
- [168] M. T. Zanni, B. J. Greenblatt, A. V. Davis, and D. M. Neumark. *Photodissociation dynamics of I₃⁻ using femtosecond photoelectron spectroscopy*. volume 3271, pages 196–207 (1998). doi:10.1117/12.308408.
- [169] H. Choi, R. T. Bise, A. A. Hoops, and D. M. Neumark. *Photodissociation dynamics of the triiodide anion (I₃⁻)*. *J. Chem. Phys.*, **113**, 2255–2262 (2000). doi:doi:10.1063/1.482040.

- [170] P. Gilch, I. Hartl, Q. An, and W. Zinth. *Photolysis of Triiodide Studied by Femtosecond Pump-Probe Spectroscopy with Emission Detection*. *J. Phys. Chem. A*, **106**, 1647–1653 (2002). doi:10.1021/jp0108521.
- [171] Y. Nishiyama, M. Terazima, and Y. Kimura. *Photo-dissociation and recombination of triiodide in room temperature ionic liquids*. *Chem. Phys. Lett.*, **491**, 164–168 (2010). doi:10.1016/j.cplett.2010.03.093.
- [172] Y. Nishiyama, M. Terazima, and Y. Kimura. *Ultrafast Relaxation and Reaction of Diiodide Anion after Photodissociation of Triiodide in Room-Temperature Ionic Liquids*. *J. Phys. Chem. B*, **116**, 9023–9032 (2012). doi:10.1021/jp212299c.
- [173] J. Jortner and A. Treinin. *Intensities of the absorption bands of halide ions in solution*. *Trans. Faraday Soc.*, **58**, 1503–1510 (1962). doi:10.1039/TF9625801503.
- [174] W. Gabes and D. Stufkens. *Electronic absorption spectra of symmetrical and asymmetrical trihalide ions*. *Spectrochim. Acta, Part A*, **30**, 1835–1841 (1974). doi:10.1016/0584-8539(74)80134-0.
- [175] A. I. Popov and R. F. Swensen. *Studies on the Chemistry of Halogens and of Polyhalides. V. Spectrophotometric Study of Polyhalogen Complexes in Acetonitrile and in Ethylene Dichloride*. *J. Am. Chem. Soc.*, **77**, 3724–3726 (1955). doi:10.1021/ja01619a015.
- [176] A. E. Gillam. *The absorption spectra of solutions of iodide bromide, cyanogen iodine, and cyanogen bromide*. *Trans. Faraday Soc.*, **29**, 1132–1139 (1933). doi:10.1039/TF9332901132.
- [177] D. Meyerstein and A. Treinin. *Charge-transfer complexes of iodine and inorganic anions in solution*. *Trans. Faraday Soc.*, **59**, 1114 (1963). doi:10.1039/tf9635901114.
- [178] E. Eyal and A. Treinin. *A Spectrophotometric Study of the System $I_2 + Br^-$* . *J. Am. Chem. Soc.*, **86**, 4287–4290 (1964). doi:10.1021/ja01074a012.
- [179] S. Coudreau, D. Kaplan, and P. Tournois. *Ultraviolet acousto-optic programmable dispersive filter laser pulse shaping in KDP*. *Opt. Lett.*, **31**, 1899–1901 (2006). doi:10.1364/OL.31.001899.
- [180] S. Weber, M. Barthélemy, and B. Chatel. *Direct shaping of tunable UV ultra-short pulses*. *Appl. Phys. B*, **98**, 323–326 (2010). doi:10.1007/s00340-009-3745-z.
- [181] N. Krebs, R. A. Probst, and E. Riedle. *Sub-20 fs pulses shaped directly in the UV by an acousto-optic programmable dispersive filter*. *Opt. Express*, **18**, 6164–6171 (2010). doi:10.1364/OE.18.006164.
- [182] N. Krebs, I. Pugliesi, J. Hauer, and E. Riedle. *Two-dimensional Fourier transform spectroscopy in the ultraviolet with sub-20 fs pump pulses and 250–720*

- nm supercontinuum probe*. *New J. Phys.*, **15**, 085016 (2013). doi:10.1088/1367-2630/15/8/085016.
- [183] S. Linden, H. Giessen, and J. Kuhl. *XFROG - A new method for amplitude and phase characterization of weak ultrashort pulses*. *Phys. Status Solidi B*, **206**, 119–124 (1998).
- [184] S. Linden, J. Kuhl, and H. Giessen. *Amplitude and phase characterization of weak blue ultrashort pulses by downconversion*. *Opt. Lett.*, **24**, 569–571 (1999). doi:10.1364/OL.24.000569.
- [185] R. Trebino. *Frequency-resolved optical gating: The measurement of ultrashort laser pulses*. Springer, New York (2002).
- [186] P. Nuernberger, G. Vogt, R. Selle, S. Fechner, T. Brixner, and G. Gerber. *Generation of shaped ultraviolet pulses at the third harmonic of titanium-sapphire femtosecond laser radiation*. *Appl. Phys. B*, **88**, 519–526 (2007). doi:10.1007/s00340-007-2725-4.
- [187] G. Buntinx, R. Naskrecki, and O. Poizat. *Subpicosecond Transient Absorption Analysis of the Photophysics of 2,2'-Bipyridine and 4,4'-Bipyridine in Solution*. *J. Phys. Chem.*, **100**, 19380–19388 (1996). doi:10.1021/jp960900v.
- [188] C. Nagura, A. Suda, H. Kawano, M. Obara, and K. Midorikawa. *Generation and Characterization of Ultrafast White-Light Continuum in Condensed Media*. *Appl. Opt.*, **41**, 3735–3742 (2002). doi:10.1364/AO.41.003735.
- [189] U. Megerle, I. Pugliesi, C. Schrieffer, C. Sailer, and E. Riedle. *Sub-50 fs Broadband Absorption Spectroscopy with Tunable Excitation: Putting the Analysis of Ultrafast Molecular Dynamics on Solid Ground*. *Appl. Phys. B*, **96**, 215–231 (2009). doi:10.1007/s00340-009-3610-0.
- [190] A. L. Dobryakov, S. A. Kovalenko, A. Weigel, J. L. Pérez-Lustres, J. Lange, A. Müller, and N. P. Ernsting. *Femtosecond pump/supercontinuum-probe spectroscopy: Optimized setup and signal analysis for single-shot spectral referencing*. *Rev. Sci. Instrum.*, **81**, 113106 (2010). doi:10.1063/1.3492897.
- [191] K. G. Spears, X. Wen, and R. Zhang. *Electron Transfer Rates from Vibrational Quantum States*. *J. Phys. Chem.*, **100**, 10206–10209 (1996). doi:10.1021/jp960444a.
- [192] M. Delor, P. A. Scattergood, I. V. Sazanovich, A. W. Parker, G. M. Greetham, A. J. H. M. Meijer, M. Towrie, and J. A. Weinstein. *Toward control of electron transfer in donor-acceptor molecules by bond-specific infrared excitation*. *Science*, **346**, 1492–1495 (2014). doi:10.1126/science.1259995.
- [193] J. W. Anthonsen. *Raman investigations of charge-transfer complexes of dioxane with iodine, bromine, chlorine, iodine bromide, iodine chloride and bromine*

- chloride*. Spectrochim. Acta, Part A, **32**, 963–970 (1976). doi:10.1016/0584-8539(76)80280-2.
- [194] G. N. R. Tripathi, R. H. Schuler, and R. W. Fessenden. *Time-resolved resonance raman spectra of dihalide radical anions in aqueous solution*. Chem. Phys. Lett., **113**, 563–568 (1985). doi:10.1016/0009-2614(85)85032-6.
- [195] J. C. Evans and G. Y.-S. Lo. *Vibrational Spectra of the Cl_3^- Ion and Evidence for the Existence of Cl_5^-* . J. Chem. Phys., **44**, 3638–3639 (1966). doi:10.1063/1.1727279.
- [196] P. E. Maslen, J. Faeder, and R. Parson. *Ab initio calculations of the ground and excited states of I_2^- and ICl^-* . Chem. Phys. Lett., **263**, 63–72 (1996). doi:10.1016/S0009-2614(96)01162-1.
- [197] J. Breckenridge and T. Surles. *Preparation and Raman spectra of some metal-ammine trihalide compounds*. Inorg. Nucl. Chem. Letters, **9**, 1131–1135 (1973). doi:10.1016/0020-1650(73)80019-4.
- [198] D. Danovich, J. Hrušák, and S. Shaik. *Ab initio calculations for small iodo clusters. Good performance of relativistic effective core potentials*. Chem. Phys. Lett., **233**, 249–256 (1995). doi:10.1016/0009-2614(94)01451-Z.
- [199] Y. Ogawa, O. Takahashi, and O. Kikuchi. *Ab initio MO study of structure and stability of X_3^- ($X = F, Cl, Br, I$) in solution*. J. Mol. Struct. THEOCHEM, **424**, 285–292 (1998). doi:10.1016/S0166-1280(97)00155-3.
- [200] B. Braïda and P. C. Hiberty. *Application of the Valence Bond Mixing Configuration Diagrams to Hypervalency in Trihalide Anions: A Challenge to the Rundle-Pimentel Model*. J. Phys. Chem. A, **112**, 13045–13052 (2008). doi:10.1021/jp803808e.
- [201] P. Fuentealba, H. Preuss, H. Stoll, and L. Von Szentpály. *A proper account of core-polarization with pseudopotentials: single valence-electron alkali compounds*. Chem. Phys. Lett., **89**, 418–422 (1982). doi:10.1016/0009-2614(82)80012-2.
- [202] A. Bergner, M. Dolg, W. Küchle, H. Stoll, and H. Preuß. *Ab initio energy-adjusted pseudopotentials for elements of groups 13–17*. Mol. Phys., **80**, 1431–1441 (1993). doi:10.1080/00268979300103121.
- [203] P. Fuentealba, L. von Szentpály, H. Preuss, and H. Stoll. *Pseudopotential calculations for alkaline-earth atoms*. J. Phys. B: At. Mol. Phys., **18**, 1287 (1985). doi:10.1088/0022-3700/18/7/010.
- [204] G. Igel-Mann, H. Stoll, and H. Preuss. *Pseudopotentials for main group elements (IIIa through VIIa)*. Mol. Phys., **65**, 1321–1328 (1988). doi:10.1080/00268978800101811.

- [205] W. Küchle, M. Dolg, H. Stoll, and H. Preuss. *Ab initio pseudopotentials for Hg through Rn*. Mol. Phys., **74**, 1245–1263 (1991). doi:10.1080/00268979100102941.
- [206] J. M. L. Martin and A. Sundermann. *Correlation consistent valence basis sets for use with the Stuttgart–Dresden–Bonn relativistic effective core potentials: The atoms Ga–Kr and In–Xe*. J. Chem. Phys., **114**, 3408–3420 (2001). doi:10.1063/1.1337864.
- [207] K. Raghavachari, G. W. Trucks, J. A. Pople, and M. Head-Gordon. *A fifth-order perturbation comparison of electron correlation theories*. Chem. Phys. Lett., **157**, 479–483 (1989). doi:10.1016/S0009-2614(89)87395-6.
- [208] J. Hrušák, S. Ten-no, and S. Iwata. *Quadratic configuration interaction versus coupled-cluster theory: Importance of orbital relaxation phenomena in CuH and CuF*. J. Chem. Phys., **106**, 7185–7192 (1997). doi:10.1063/1.473680.
- [209] D. E. Woon and T. H. D. Jr. *Gaussian basis sets for use in correlated molecular calculations. III. The atoms aluminum through argon*. J. Chem. Phys., **98**, 1358–1371 (1993). doi:10.1063/1.464303.
- [210] M. J. Frisch, G. W. Trucks, H. B. Schlegel, G. E. Scuseria, M. A. Robb, J. R. Cheeseman, G. Scalmani, V. Barone, B. Mennucci, G. A. Petersson, H. Nakatsuji, M. Caricato, X. Li, H. P. Hratchian, A. F. Izmaylov, J. Bloino, G. Zheng, J. L. Sonnenberg, M. Hada, M. Ehara, K. Toyota, R. Fukuda, J. Hasegawa, M. Ishida, T. Nakajima, Y. Honda, O. Kitao, H. Nakai, T. Vreven, J. A. Montgomery, Jr., J. E. Peralta, F. Ogliaro, M. Bearpark, J. J. Heyd, E. Brothers, K. N. Kudin, V. N. Staroverov, R. Kobayashi, J. Normand, K. Raghavachari, A. Rendell, J. C. Burant, S. S. Iyengar, J. Tomasi, M. Cossi, N. Rega, J. M. Millam, M. Klene, J. E. Knox, J. B. Cross, V. Bakken, C. Adamo, J. Jaramillo, R. Gomperts, R. E. Stratmann, O. Yazyev, A. J. Austin, R. Cammi, C. Pomelli, J. W. Ochterski, R. L. Martin, K. Morokuma, V. G. Zakrzewski, G. A. Voth, P. Salvador, J. J. Dannenberg, S. Dapprich, A. D. Daniels, Ö. Farkas, J. B. Foresman, J. V. Ortiz, J. Cioslowski, and D. J. Fox. *Gaussian 09, Revision D.01*. Gaussian, Inc., Wallingford CT (2013).
- [211] P. Pringsheim and B. Rosen. *Über den Ramaneffekt*. Z. Phys., **50**, 741–755 (1928). doi:10.1007/BF01339409.
- [212] S. Bhagavantam and S. Venkateswaran. *The Raman Spectra of Some Organic Halogen Compounds*. Proc. R. Soc. London, Ser. A, **127**, 360–373 (1930). doi:10.1098/rspa.1930.0064.
- [213] B. Trumpy. *Ramaneffekt und Konstitution der Moleküle. VI*. Z. Phys., **88**, 226–234 (1934). doi:10.1007/BF01351870.
- [214] C. Corin and G. B. B. M. Sutherland. *The Infra-Red Absorption Spectrum of Methylene Chloride*. Proc. R. Soc. London, Ser. A, **165**, 43–53 (1938). doi:10.1098/rspa.1938.0043.

- [215] E. K. Plyler and W. S. Benedict. *INFRARED SPECTRA OF EIGHTEEN HALOGEN-SUBSTITUTED METHANES*. J. Research Natl. Bur. Standards, **Vol: 47**, 202–220 (1951). doi:10.6028/jres.047.026.
- [216] H. L. Welsh, M. F. Crawford, T. R. Thomas, and G. R. Love. *Raman Spectroscopy of Low Pressure Gases and Vapors*. Can. J. Phys., **30**, 577–596 (1952). doi:10.1139/p52-053.
- [217] T. Shimanouchi and I. Suzuki. *Infrared spectra and force constants of CH₂Cl₂, CHDCl₂, and CD₂Cl₂*. J. Mol. Spectrosc., **8**, 222–235 (1962). doi:10.1016/0022-2852(62)90023-1.
- [218] B. F. E. Palma, E. A. Piotrowski, S. Sundaram, and F. F. Cleveland. *Substituted methanes: Part XXXIV. Raman and infrared spectral data and calculated thermodynamic properties for CH₂Cl₂, CHDCl₂, and CD₂Cl₂*. J. Mol. Spectrosc., **13**, 119–131 (1964). doi:10.1016/0022-2852(64)90061-X.
- [219] T. Shimanouchi. *Tables of molecular vibrational frequencies*. National Bureau of Standards, Washington (1972).
- [220] G. A. Vorob'eva and S. P. Timonin. *A comparison of the Raman spectra of substituted methanes in the liquid and gaseous state*. J. Appl. Spectrosc., **18**, 629–632 (1973). doi:10.1007/BF00609326.
- [221] K. R. Loos and A. C. Jones. *Structure of triiodide ion in solution. Raman evidence for the existence of higher polyiodide species*. J. Phys. Chem., **78**, 2306–2307 (1974). doi:10.1021/j100615a028.
- [222] M. T. Zanni, A. V. Davis, C. Frischkorn, M. Elhanine, and D. M. Neumark. *Femtosecond stimulated emission pumping: Characterization of the I₂⁻ ground state*. J. Chem. Phys., **112**, 8847–8854 (2000). doi:10.1063/1.481499.
- [223] U. Banin, R. Kosloff, and S. Ruhman. *Vibrational relaxation of nascent diiodide ions studied by femtosecond transient resonance impulsive stimulated Raman scattering (TRISRS); experiment and simulation*. Chemical Physics, **183**, 289–307 (1994). doi:10.1016/0301-0104(94)00099-9.

Danksagung

Mein Dank geht an Prof. Dr. Tobias Brixner für die Aufnahme in seine Arbeitsgruppe, für seine Anleitung und Unterstützung und für die vielfältigen Möglichkeiten Neues zu lernen.

Ich bedanke mich bei Prof. Dr. Patrick Nürnberger für sein immer offenes Ohr und die vielen ergiebigen Diskussionen.

Meinen Bachelorstudentinnen Lea Reß, Julia Heilmüller und Anja Hasenkopf und meinen Praktikanten Dr. Martin Pfeffermann und Andreas Tröster danke ich für ihre wertvollen Beiträge zur Laborarbeit, Datenauswertung und -interpretation.

Meinem Kooperationspartner Dr. Jan Hrušák danke ich für seine theoretischen Rechnungen zu den Trihalden und bei Dr. Johannes Knorr bedanke ich mich für die gute Zusammenarbeit bei der Weiterentwicklung des Transienten Absorptionssetups.

Prof. Dr. Mark Caprio danke ich für das Mathematica-Paket CustomTicks und die zur Verwendung benötigte Software-Lizenz.

Ein großes Dankeschön richte ich an alle Kollegen im Arbeitskreis und Mitarbeitern am Lehrstuhl für ihre Hilfsbereitschaft und die tolle Arbeitsatmosphäre.

Meinen Korrekturlesern Dr. Frank Daeche, Heiko Hildenbrand, Lea Reß und Julia Heilmüller danke ich für die zeitintensive Fehlersuche.

Mein besonderer Dank geht an meine Freunde und meine Familie für ihre immerwährende Unterstützung.